

ADVERTIMENT. La consulta d'aquesta tesi queda condicionada a l'acceptació de les següents condicions d'ús: La difusió d'aquesta tesi per mitjà del servei TDX (www.tesisenxarxa.net) ha estat autoritzada pels titulars dels drets de propietat intel·lectual únicament per a usos privats emmarcats en activitats d'investigació i docència. No s'autoritza la seva reproducció amb finalitats de lucre ni la seva difusió i posada a disposició des d'un lloc aliè al servei TDX. No s'autoritza la presentació del seu contingut en una finestra o marc aliè a TDX (framing). Aquesta reserva de drets afecta tant al resum de presentació de la tesi com als seus continguts. En la utilització o cita de parts de la tesi és obligat indicar el nom de la persona autora.

ADVERTENCIA. La consulta de esta tesis queda condicionada a la aceptación de las siguientes condiciones de uso: La difusión de esta tesis por medio del servicio TDR (www.tesisenred.net) ha sido autorizada por los titulares de los derechos de propiedad intelectual únicamente para usos privados enmarcados en actividades de investigación y docencia. No se autoriza su reproducción con finalidades de lucro ni su difusión y puesta a disposición desde un sitio ajeno al servicio TDR. No se autoriza la presentación de su contenido en una ventana o marco ajeno a TDR (framing). Esta reserva de derechos afecta tanto al resumen de presentación de la tesis como a sus contenidos. En la utilización o cita de partes de la tesis es obligado indicar el nombre de la persona autora.

WARNING. On having consulted this thesis you're accepting the following use conditions: Spreading this thesis by the TDX (www.tesisenxarxa.net) service has been authorized by the titular of the intellectual property rights only for private uses placed in investigation and teaching activities. Reproduction with lucrative aims is not authorized neither its spreading and availability from a site foreign to the TDX service. Introducing its content in a window or frame foreign to the TDX service is not authorized (framing). This rights affect to the presentation summary of the thesis as well as to its contents. In the using or citation of parts of the thesis it's obliged to indicate the name of the author



Universitat Politècnica de Catalunya

Department of Geotechnical Engineering and
Geosciences

PhD Thesis

**LANDSLIDES IN RESERVOIRS.
A COUPLED THERMO-HYDRO-
MECHANICAL APPROACH**

by

Núria Mercè Pinyol i Puigmartí

Supervised by:

Eduardo E. Alonso Pérez de Ágreda
Jean Vaunat

AGRADECIMIENTOS

Cuando llegué al Departamento no sabía prácticamente nada ni de Mecánica del Suelo ni de Geotecnia. Ahora, con la tesis finalizada, me doy cuenta que, aunque me queda mucho, algo he aprendido. Y si es así, es gracias a las personas que afortunadamente he encontrado en este Departamento. Aprovecho estas líneas para darles mi agradecimiento.

Debo empezar por Eduardo Alonso, aunque no le gusta que le dé las gracias. Él ha sido como un Maestro para mí del que sólo cabe aprender. Le agradezco su interés durante largas discusiones por transmitir sus conocimientos hasta el último detalle sin dejar cabos sueltos.

Agradezco a Sebastià Olivella su ayuda y confianza. Con él empecé la tesina de la carrera y desde entonces siempre ha dado respuesta a todas las dudas que le he planteado, rápidamente por el pasillo o durante horas peleando con Code_Bright con admirable paciencia.

A Jean Vaunat le agradezco su dedicación especialmente los primeros años, sin duda los más duros. Sus ánimos fueron clave a mitad de doctorado cuando miras atrás y ves que el avance de la tesis es dudoso y lo que queda por hacer, inalcanzable.

Agradezco también a otros profesores su amable predisposición a ayudar con sus aclaraciones y comentarios: Jordi Corominas, Enrique Romero, Ignasi Carol, Xavier Sánchez, Antonio Gens, Antoni Lloret, Josep Suriol y José Moya.

Y al profesor Alexander Puzrin de la ETH (Zurich) por su atenta revisión de parte del trabajo realizado en esta Tesis, su amabilidad y acertados consejos.

Agradezco el apoyo económico del Departament d'Educació y Universitats de la Generalitat de Catalunya por la beca recibida, así como también la ayuda del Centro Internacional de Métodos Numéricos de Ingeniería y, en particular, de su director Eugenio Oñate, que han permitido mi formación y el desarrollo de esta Tesis.

Al personal del Departamento, Mar, Eva, Mari Carmen, Víctor, Óscar, Albert i Joan, gracias por su trato amable e interés en facilitar los trámites administrativos o resolver los problemas informáticos. Y a Raúl, gracias por su ayuda en la preparación de figuras.

Quiero ahora agradecer a mis compañeros de doctorado todos los momentos compartidos. A los que me dieron la bienvenida con útiles consejos y ánimos: Beti, Alexandra, Fermín, Juan, Iván Berdugo, Ernesto, Marcelo y Kanta. Y a los que han ido avanzando conmigo: Héctor, Sergio Samat, Rodrigo, Ricardo, Benoit, Rafaela, Mauricio, Dani, Vladimir, José Manuel Gesto, Analice, Samuel, Tere, Abel, Diego y Anna (una amiga a la que espero haber dado la bienvenida y ayuda que yo recibí). Quiero dar un reconocimiento especial a Nubia por nuestras discusiones siempre enriquecedoras en esos descansos que nos permiten seguir trabajando hasta que termina el día.

A Davoud Ebrahimi, Maria Nikolinakou y Rita Sousa les agradezco su ayuda y compañía durante mi estancia en Boston donde me hicieron sentir como en casa.

Y finalmente, un especial agradecimiento a mi familia por sus ánimos, paciencia y comprensión durante estos años.

ABSTRACT

Landsliding is an important problem when facing the design, construction and operation of dams and reservoirs. Impoundment of the slope toes as well as the rapid drawdown may trigger the movement of first-time landslides or reactivate ancient landslides often located in reservoir sites. This Thesis deals with the particular case of landslides around reservoirs defined as a mobilized mass that slides on a well-defined shearing surface without experiencing a major degradation.

In the first part of the Thesis the mechanism of rapid drawdown is discussed as a fully coupled flow-deformation problem for saturated/unsaturated conditions.

Additional risk appears when landslide accelerates and is able to enter the reservoir at high speed creating impulsive waves. The discussion on the different phenomena leading to the fast acceleration is today very active. Probably the lack of well-documented cases makes the advancement of knowledge difficult. The mechanism to explain the rapid acceleration of landslides favoured in this Thesis is based on thermal effects on the sliding surface that induce the generation of pore water pressure and therefore, the reduction of the frictional strength. The governing equations (mass and heat balance equations and constitutive equations) formulated in the shear band have been written and integrated together with the motion equation of the slide. With the aim of finding practical criteria to decide the actual risk of slide acceleration due the phenomena analysed, a closed-form solution has been obtained for the case of planar landslides under the hypothesis of incompressible water, solid particles and porous media. For a rational range of the most relevant parameters, comparison between analytical and numerical (relaxing the assumptions introduced in the analytical development) solutions shows a remarkable similarity and reveals that the closed-form solution is accurate enough for practical applications.

The thermo-hydro-mechanical approach discussed is applied in the case of Vaiont landslide. The stability of this landslide before the failure is first discussed by means of a simple explanation introducing the internal strength of the mobilized rock. The analysis is consistent with the available data (slide geometry, residual strength, material properties and laboratory tests). When the self-feeding mechanism of pore pressure generation due to heat resulting from the frictional work is introduced in the dynamic analysis of the Vaiont model, the high velocity actually observed is predicted.

Sensitivity and scale analysis have been performed for the case of a planar landslide and for the geometry of Vaiont. Three parameters have been found important to explain the acceleration of the motion: the thickness of the shearing band, its permeability and its stiffness. In fact, permeability and thickness can be related since both depend on the particle size distribution. Calculated results indicate that the permeability of the shear band is a key parameter. A threshold of permeability established around 10^{-8} to 10^{-10} m/s marks the transition for a potentially risky slide (when the permeability is lower) to a safe one (for higher values of permeability).

For very large landslides, critical combinations of band permeability and band thickness result in a substantial increase in temperature. At high calculated values of temperature (hundreds or even thousands of °C), the analysis presented is not applicable. Evaporation or advance constitutive equations including rock melting should be included.

In a final chapter a recent large landslide located in Canelles reservoir is analyzed. The slide is regarded as a potential risk for the operation of the dam and the reservoir. Some of the developments made in the Thesis, namely the solution of rapid drawdown and the thermal coupled model for fast landsliding, are applied to Canelles. The chapter describes the methodology adopted which can be applied in similar cases.

RESUMEN

La ocurrencia de deslizamientos es uno de los principales problemas presentes durante el diseño, construcción y explotación de presas y embalses. La inundación del pie de los taludes, así como el desembalse rápido, pueden provocar primeras roturas o reactivar antiguos deslizamientos, existentes con frecuencia en el entorno de los embalses. Esta Tesis se centra en el caso particular de los deslizamientos en las márgenes de embalses en los que una masa de terreno desliza sobre una superficie de corte bien definida sin que se observe una intensa degradación del material movilizado.

En la primera parte de la Tesis se discute el desembalse rápido como un problema acoplado de flujo y deformación en condiciones saturadas/no saturadas.

Un riesgo adicional aparece cuando el deslizamiento acelera e invade el embalse a gran velocidad, generando una ola. La discusión de los fenómenos responsables de la aceleración de los deslizamientos sigue actualmente activa. Probablemente la falta de casos bien documentados dificulta el avance en su conocimiento. En esta Tesis se considera como fenómeno responsable de la aceleración del deslizamiento el efecto del calor en la banda de corte, lo que induce la generación de presión de agua y, por consiguiente, la reducción de la resistencia friccional. Se definen las ecuaciones del problema (balance de masa y calor y ecuaciones constitutivas) en la banda de corte y se integran junto a la ecuación del movimiento. Con objeto de encontrar criterios prácticos para cuantificar el riesgo de aceleración debido al fenómeno analizado, se ha obtenido una solución analítica para el caso de deslizamientos planos bajo las hipótesis de incompresibilidad del agua, partículas sólidas y medio poroso. La comparación entre la solución analítica y la numérica (sin considerar las hipótesis impuestas en el desarrollo analítico), cuando se varían los parámetros más relevantes dentro de un rango razonable, indica que la solución analítica es suficientemente precisa para aplicaciones prácticas.

El desarrollo termo-hidro-mecánico presentado se aplica al caso del deslizamiento de Vaiont. En primer lugar se explica la situación de estabilidad previa a la rotura introduciendo la resistencia de la roca movilizada. El análisis es coherente con la información disponible (geometrías del deslizamiento, resistencia residual, propiedades de los materiales y ensayos de laboratorio). Cuando el mecanismo de generación de presión de agua debido al calor resultante del trabajo friccional se incluye en el análisis dinámico del modelo del deslizamiento de Vaiont, se predice bien la alta velocidad observada.

Se han realizado análisis de sensibilidad y de efecto escala tanto para el caso de deslizamiento plano como para la geometría de Vaiont. Se han encontrado tres parámetros relevantes para explicar la aceleración del movimiento: el espesor de la banda de corte, su permeabilidad y su rigidez. De hecho, la permeabilidad y el espesor de la banda de corte están directamente relacionados dado que ambos dependen de la granulometría del material. Los resultados obtenidos indican que la permeabilidad de la banda es el parámetro clave. Un umbral de permeabilidad establecido entre 10^{-8} y 10^{-10}

m/s, marca la transición entre deslizamientos potencialmente acelerados (cuando la permeabilidad es baja) y deslizamientos seguros (permeabilidades mayores a 10^{-10} m/s).

En el caso de deslizamientos de grandes dimensiones, combinaciones críticas de la permeabilidad y espesor de la banda de corte resultan en un incremento substancial de la temperatura. Los altos valores resultantes de los cálculos (cientos o miles de °C) invalidan el análisis aquí presentado. Fenómenos como la evaporación o la fusión de la roca deberían ser incluidos en estos casos.

En el último Capítulo se analiza el deslizamiento de Canelles ocurrido recientemente. El deslizamiento pone en riesgo el buen funcionamiento de la presa y del embalse. Algunos de los desarrollos descritos en la Tesis, como son la solución del desembalse rápido y el modelo termo-hidro-mecánico para el análisis de la aceleración de los deslizamientos se han aplicado al caso de Canelles. El capítulo describe la metodología adoptada, que puede ser aplicada en casos similares.

TABLE OF CONTENTS

CHAPTER 1 Introduction and Organization of the Thesis

1.1	INTRODUCTION	1
1.1.1	Direct implication of reservoir operation.....	2
1.1.2	First-time and ancient landslides.....	5
1.1.3	Consequences of landslides in reservoir sites	9
1.1.4	Acceleration of landslides in reservoir sites	9
1.1.5	Case histories.....	11
	Potentially dangerous landslides.....	12
	Catastrophic landslides	15
1.2	THESIS LAYOUT	24

CHAPTER 2 Rapid Drawdown in Slopes and Embankments

2.1	INTRODUCTION	28
2.2	HISTORICAL PERSPECTIVE	33
2.2.1	Undrained analysis.....	34
2.2.2	Flow methods	35
2.3	DRAWDOWN IN A SIMPLE SLOPE.....	36

2.3.1	Instantaneous drawdown	38
2.3.2	Progressive drawdown ($v = 0.5$ m/day)	43
2.4	SOME DESIGN RULES REVISITED.....	44
2.5	COUPLED ELASTO-PLASTIC ANALYSIS OF DRAWDOWN	50
2.6	GLEN SHIRA DAM CASE HISTORY	54
2.7	CONCLUSIONS	69
2.8	APPENDIX COUPLED FLOW-DEFORMATION FORMULATION FOR SATURATED/UNSATURATED CONDITIONS.....	71

CHAPTER 3 Rapid Landslides. Thermo-hydro-mechanical Approach

3.1	INTRODUCTION	78
3.1.1	Previous works on rapid landslide considering thermal effects	79
3.1.2	Heating effects in saturated porous media.....	80
	Laboratory testing.....	80
	A field heating experiment.....	88
3.1.3	Additional thermo-mechanical features.....	90
	Effect on compressibility.....	90
	Elastoplastic thermal strains	90
	Changes in preconsolidation pressure with temperature	93
3.1.4	Residual shearing behaviour. Shearing rate effects.....	93
3.1.5	Thickness of shear bands	102
3.2	PROBLEM APPROACH AND GOVERNING EQUATIONS	104
3.2.1	Shear strains and heat generation in the shear band	104
3.2.2	Balance equations inside and outside the shear band.....	106
	Heat balance equation.....	107
	Mass balance equations.....	108
	Dynamic equilibrium equation	111

CHAPTER 4 Fast Planar Slide. A Closed-form Thermo-hydro-mechanical Solution

4.1	INTRODUCTION	113
4.2	THE MOTION EQUATION FOR A PLANAR LANDSLIDE	114

4.3	NUMERICAL SOLUTION	115
4.4	ANALYTICAL SOLUTION	119
4.5	SUMMARY OF ASSUMPTIONS	122
4.6	SOLVED CASE.....	123
4.7	SENSITIVITY ANALYSIS.....	132
4.7.1	Effect of permeability and shear band thickness	132
4.7.2	Effect of the position of dissipation boundary (parameter Y) in the analytical solution	134
4.7.3	Effect of depth of sliding surface	136
4.8	CONCLUSIONS	136
	APPENDIX 4.1 FINITE DIFFERENCE APPROXIMATION OF SYSTEM OF EQUATIONS (4.3)	137

CHAPTER 5 Static Equilibrium and Run-out Analysis of Vaiont Landslide

5.1	INTRODUCTION	143
5.2	FUNDAMENTAL INFORMATION ON VAIONT.....	144
5.2.1	Geological setting.....	146
5.2.2	The sliding surface.....	149
5.2.3	Monitoring data before the slide.....	150
5.2.4	Water pressures and rainfall.....	151
5.3	AN EVOLUTIVE TWO-WEDGE STABILITY MODEL.....	152
5.3.1	Internal shearing	155
5.3.2	Motion equations.....	158
5.4	STATIC EQUILIBRIUM AT FAILURE AND SAFETY FACTORS	161
5.5	LANDSLIDE RUNOUT.....	166
5.6	DISCUSSION	170
5.7	CONCLUSIONS	171

CHAPTER 6 Thermo-hydro-mechanical and Dynamic Analysis of Vaiont Landslide

6.1	INTRODUCTION	173
6.2	DYNAMICS OF VAIONT SLIDING GEOMETRY	174
6.2.1	Balance equations	175

6.2.2	Dynamic equilibrium of the two wedges.....	177
6.3	COMPUTED RESULTS	181
6.4	SCALE EFFECTS	187
6.5	DISCUSSION	190
6.6	CONCLUSIONS	194
APPENDIX 6.1 FLOWCHART AND COMPUTER PROGRAM FOR THE DYNAMIC ANALYSIS OF THE INFINITE PLANAR AND TWO-WEDGE SLIDES		196
APPENDIX 6.2 PARAMETERS OF THE BALANCE EQUATIONS FOR THE DYNAMIC ANALYSIS OF TWO INTERACTING WEDGES.....		210

CHAPTER 7 Canelles Landslide

7.1	BACKGROUND.....	215
7.1.1	Description of the failure	216
	Geological setting and location of the sliding plane	217
7.2	LABORATORY TESTS	225
7.3	WATER LEVEL AND PIEZOMETER MEASUREMENTS.....	226
7.3.1	Water level elevation.....	226
7.3.2	Piezometers	226
7.4	PORE WATER PRESSURE CALCULATION	230
7.5	SAFETY FACTOR CALCULATION.....	238
7.6	ANALYSIS OF RAPID SLIDING.....	239
7.7	CONCLUSIONS	242

CHAPTER 8 Conclusions and Future Research245

REFERENCES.....249

CHAPTER 1

Introduction and Organization of the Thesis

1.1 INTRODUCTION

In the design, construction and operation of dams and reservoir sites, instabilities of banks and ancient landslides by reservoir impoundment are one of most important issue to face. Most of dams and reservoirs are located in natural valleys frequently resulting from fluvial or glacial erosion whose banks are potentially instable and there is a high risk that engineering projects activate or reactivate landslides. In addition, it is common to find valleys whose geologic structure is a syncline involving stratification layers parallel or subparallel to the topographic slope. This situation favours the motion of landslides into reservoirs. In these cases, potential sliding planes are generally located in layers that exhibit smaller shear strength than the surrounding strata.

There is a wide variety of landslides depending on the materials involved, morphology, rate of movement, triggering mechanism and type of run-out. Several authors have work on their definition and classification (Nemcok, 1972; Varnes, 1978; Hutchinson, 1988, among others). A European classification used by Dikay *et al.*, (1996) distinguished between:

- *Fall*, that usually denotes the free-fall movement of material from a steep slope or cliff;
- *Topple*, which is very similar to a fall in many respects, but normally involving a pivoting action rather than complete separation at the base of the failure;

- *Slide*, in which a mass moves over a well-defined failure surface where relative displacements are concentrated;
- *Lateral spreading*, characterized by the low-angle slopes involved and its unusual form and rate of movement;
- *Flow*, that behaves as a fluidised mass in which water or air are significantly involved;
- *Complex*, which involves changes of behaviour during downslope motion. It may be described by two or more of the previously described movements.

The work presented in this Thesis focuses on the third group of movements: slides that move with a relatively light degradation of the mobilized body. In particular, the Thesis concentrates on landslides around reservoirs or rivers.

1.1.1 Direct implication of reservoir operation

Reservoir operation implies two unfavourable effects for the stability of banks and slopes:

- (a) The submergence of the toe of a potential landslide
- (b) The rapid drawdown condition

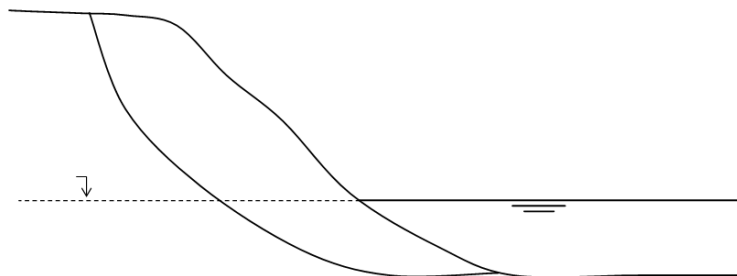


Figure 1.1 Slope partially submerged.

Regarding the first point, considerer in Figure 1.1 a slope partially submerged. The groundwater profile will be affected by the position of the reservoir water level whether the slope is fed by the stored water or the opposite. Considerer a potential failure surface and the horizontal free water level within the slope indicated in the Figure 1.1. This particular case results in hydrostatic profiles of pore water pressure associated to a stationary state due to reservoir level. The progressive inundation of the toe of the slope implies an increment of pore water pressure acting along the sliding surface that contributes to reduce the effective stress and therefore, to reduce the frictional strength. This reduction of effective stress is partially compensated by a total stress increment due to the load of the water weight against the slope surface. This

total stress increment along the sliding surface can not be easily calculated. However, given the geometry of the failure surface and the slope, it can “a priori” be estimated that pore water increment may not be completely compensated by the increase in total stress induced by water loading on the exposed surface and, therefore, a reduction of the effective stress takes place. Under these conditions, resisting forces decrease. However, this negative effect may be compensated by the beneficial increment of the hydrostatic forces acting on the exposed slope, which oppose the slide motion.

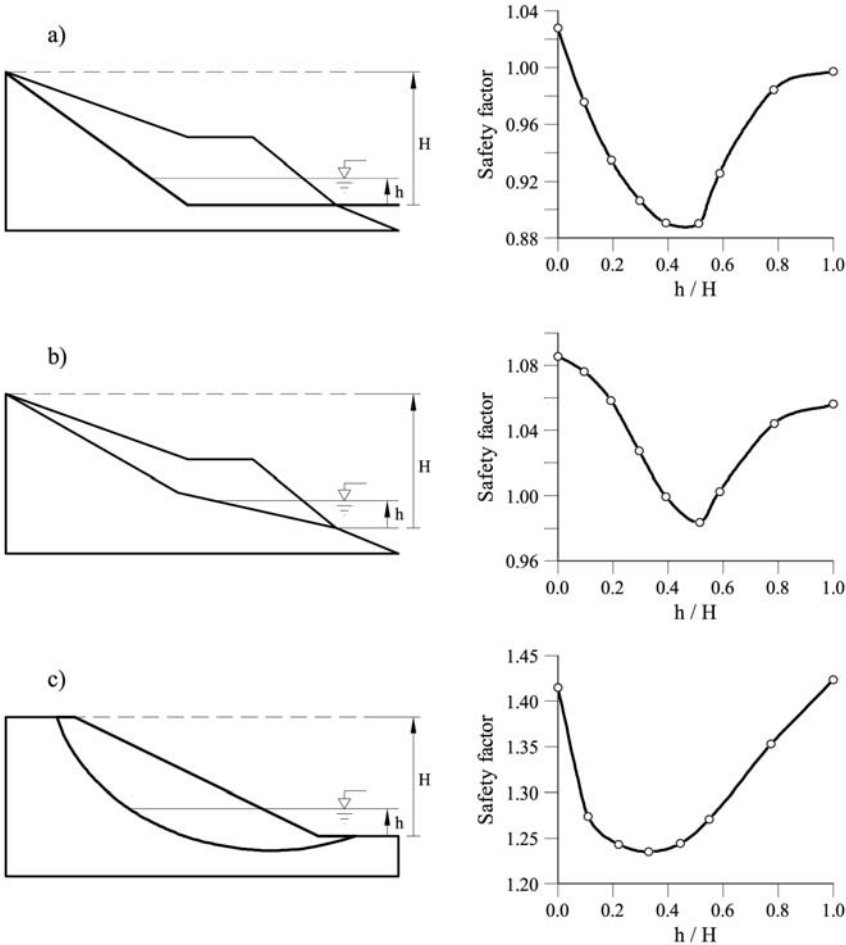


Figure 1.2 Evolution of safety factor (Morgenstern – Price method) when the water level in the reservoir increases. h_w : water level above the elevation of the exit point of the sliding surface. H : maximum value of h_w , when the entire slope is submerged. Case (a): geometry of Vaiont and ($c' = 0$; $\phi' = 12^\circ$); Case (b): geometry modified from Case (a) and ($c' = 0$; $\phi' = 15^\circ$); Case (c): conventional slope and circular failure surface ($c' = 0$; $\phi' = 30^\circ$).

In fact, the resulting changes of safety factor, when the external level changes depend on a number of factors, including slope and failure surface geometry. More will be said on this topic when analyzing reservoir drawdown in Chapter 2. The interesting result is that a minimum safety factor is typically calculated for an intermediate water level. Consider the simple case represented in Figure 1.2. The three cases shown were solved by means of a commercial slope stability program for soil slopes (GEO-SLOPE

2004 developed by GEO/SLOPE International Ltd. Calgary, Alberta, Canada). The Morgenstern-Price method (Morgenstern and Price, 1965) has been used. In all cases, the distribution of pore pressure inside the slide follows a horizontal water table and no suction effects have been considered. Minimum safety factors are obtained when water level reaches a value varying between $1/3$ to $1/2$ of the slope height. Note that slopes with a lower planar or sub-planar failure surface (cases “a” and “c” in Fig. 1.2) are especially sensitive to submerging the toe if compared with a failure surface dipping in the direction of the slope itself (case “b”).

The second critical situation met during reservoir operation, rapid drawdown, is a classical scenario in slope stability, which arises when totally or partially submerged slopes experience a reduction of the external water level. This is a common situation in riverbanks, subjected to changing river levels. Flooding conditions are critical in this case because river levels reach peak values and the rate of decreasing water level tends to reach maximum values also.

Rapid drawdown conditions have been extensively analysed in the field of dam engineering because reservoir water levels fluctuate widely due to operational reasons. Drawdown rates of 0.1 m/day are common. Drawdown velocities of 0.5 m/day are quite significant. One meter/day and higher rates are rather exceptional. However, reverse pumping storage schemes or dam flow discharges when reservoir level is low may lead to such fast water level changes in reservoir levels.

Sherard *et al.* (1963) in their book on earth and earth-rock dams describe several upstream slope failures attributed to rapid drawdown conditions. Interestingly, in most of the reported failures the drawdown did not reach the maximum water depth but approximately half of it (from maximum reservoir elevation to approximately mid-dam level). Drawdown rates in those cases were not exceptional at all (10 or 15 cm/day). A Report on Deterioration of Dams and Reservoirs (ICOLD, 1980) reviews causes of deterioration and failures of embankment dams. Thirty-three cases of upstream slips were collected and a third of them were attributed to an excessively rapid drawdown of the reservoir. A significant case was San Luis dam, in California (USCOLD, 1980). San Luis dam is one of the largest earthfill dams in the world (100 m high; 5500 m long; 70 million m³ of compacted embankment). An upstream slide developed in 1981 after 14 years of successful operation of the dam because of a drawdown, which was more intense than all the previous ones. In this case, the average drawdown rate was around 0.2 m/day and the change in reservoir level reached 55 m. Lawrence Von Thoen (1985) described this case.

There is a long history of contributions, which probably starts with the analysis of Casagrande (1940), with the purpose of understanding and providing prediction tools for drawdown conditions. The main purpose of those contributions has been the prediction of pore water pressures inside the slope. Geotechnical publications place also emphasis on the determination of safety factor, although this is generally a

relatively straightforward exercise (if the analysis is performed under drained conditions) if the spatial and time distribution of pore water pressures are already known.

The drawdown problem is discussed in detail in Chapter 2. The drawdown condition in a slope is analysed as a fully coupled flow-deformation problem for saturated/unsaturated conditions. Some fundamental concepts are first discussed in a qualitative manner and, later, explored in more detail in synthetic examples, solved under different hypothesis, including the classical approaches. Some design rules, which include a few fundamental parameters for the drawdown problem, have also been solved in a rigorous manner to illustrate the limitations of simplified procedures. An interesting case history will also be discussed in detail.

The relevance of rapid drawdown is discussed again in Chapter 7 where a very large landslide (35 millions m³ approximately) was triggered by a rapid drawdown on the left margin of Canelles reservoir (Catalonia, Spain).

1.1.2 First-time and ancient landslides

From a geotechnical perspective, it is important to distinguish between first-time failures and reactivation of ancient landslides. The first type develops in “intact” sites. These types of slides are difficult to analyze, especially when brittle materials are involved in the potential failure surface. It is the case of hard soils or soft argillaceous rocks, in particular those having a high plasticity, the strength operating in practice is especially difficult to predict. In fact, materials exhibit a shearing softening behaviour from a peak value, associated with a low value of shearing displacement, to a low residual strength value, reached when clay particles orient in the direction of shearing. Drained ring shearing tests and reversal direct shear tests allow the estimation of the residual strength, which is mainly determined by particle size and the mineralogy of the soil. A simple but wrong conclusion in the analysis of first-time slides in brittle materials would be that the available strength is defined by the maximum peak strength reached when the slide starts to move. However, field evidence show that the available strength is intermediate between peak and residual conditions. Progressive failure phenomenon seems to have an important role to explain the failure mechanism. Early classical studies on this topic were published by Skempton (1967), Bjerrum (1967) and Bishop (1967, 1971). More recent contributions have been published by Cooper (1998), Potts *et al.* (1990), Dounias *et al.* (1996) and Mesri and Shahien (2003).

In contrast, in ancient landslides a pre-existing slide surface has been subjected to an increasing history of accumulated relative displacement. Hence, it is expected that on the sliding surface cohesion will be insignificant and the frictional angle will be close or equal to residual values.

It is widely accepted that ancient landslides exhibit a low safety factor close to conditions of strict equilibrium ($SF = 1$). ICOLD (2002) reports that in at least 75% of

cases in which old landslides (active or inactive) are disturbed (by an excavation or by submerging the slide toe) slide reactivation or an increase in the rates of motion are observed. A simple explanation is that once the first slide occurred in the past it reached a new but strict equilibrium. Therefore, small changes in the resistant and destabilizing actions applied on the landslide body, such as excavation, erosion, weathering, changes in pore water distribution within the slope or even chemical changes, may induce the reactivation of the slide.

It is also a frequent observation when dealing with ancient landslides, especially in consolidated clayey strata, that a very low value of friction angle, even lower than the residual friction determined in ring shearing tests under the relevant effective normal stress, is obtained in joints and shearing zones. This low value is determined when testing directly the shearing surface and it is consistent with the value required to explain the instability by back-analysis.

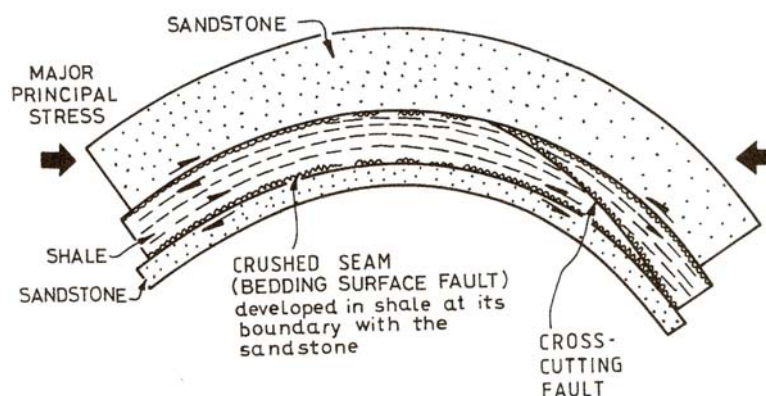


Figure 1.3 Usual way in which bedding surface faults are formed in mudrocks (Fell *et al.* 2005).

Several reasons have been invoked to explain this result. A first explanation is provided by previous tectonical or morphological processes. In some situations, folding or tilting sedimentary strata having different stiffness leads to relative displacement between interbedded contacts. This idea was represented by Fell *et al.* (2005) by means of Figure 1.3. Residual conditions are reached at the interface between weak and hard bedding contacts.

In addition, tectonical processes occurred at a level of stress higher than the present stress intensity. Since the residual shearing strength envelope is not linear with normal effective stress (Picarelli, 1990; Stark and Eid, 1994), the actual friction angle acting on the pre-existing slip surface corresponds to the minimum value previously reached, despite the lower current applied normal stress. This concept was schematically explained by Alonso (2000) by means Figure 1.4 reproduced here.

Another geological process inducing the development of residual strength in weak bedding contacts is the valley relief associated with river excavation that especially affects dam and reservoirs sites (Burland *et al.*, 1977).

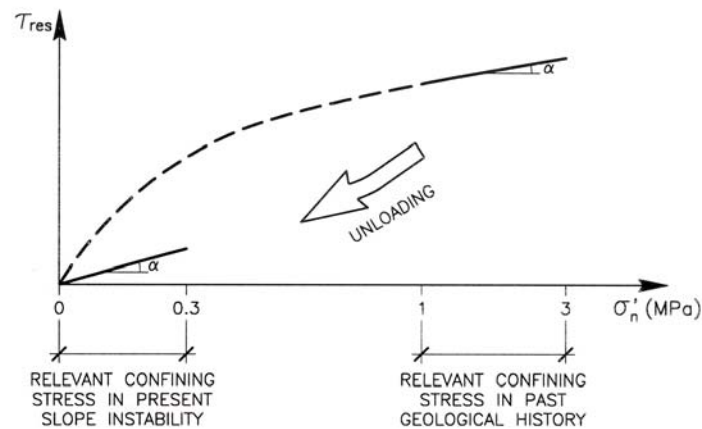


Figure 1.4 Residual strength envelope in residual conditions on sliding surfaces (Alonso, 2000).

Weathering and changes in mineralogy of the material located in the slide surface may also lead to a significant reduction of the available shearing strength. In particular, sliding surfaces are prone to exhibit changes in their mineralogy whenever they become preferential paths for water flow which leads the dissolution of salts and other minerals. Different authors have shown the negative effects of chemical alteration and weathering on the friction angle. Hawkins *et al.* (1988) observed that the loss in calcite content leads to a reduction of 25% of friction angle; Rodríguez-Ortiz and Prieto (1980) reported the effect of sulphate content when evaluated the stability of natural slopes and their mineralogy; Chigira (1989) noted that the oxidation of pyrite in mudstone transforming chlorite into smectite was a cause of landslide; Elnaggar and Flint (1976) highlighted the mineralogical and geomechanical changes on the shear zone of an ancient landslide as a result of groundwater interactions in fissured claystone. (The last two mentioned works were provided by Hamel, 2004).

Another interesting case is the Cortes landslide (Valencia, Spain). It was located on the left bank of Júcar River, upstream but very close of the Cortes arch-gravity dam (Alonso *et al.*, 1993). The excavation of the upper part of the landslide in order to ensure its stabilization allowed the direct observation of the striated shearing zone. It was shown to be a few millimetres thick, striated layer of greenish colour in contrast with the brown colour of the surrounding marl that constituted the thicker strata where the failure surface was located. Mineralogical analyses by X-ray diffraction were made on samples of the thin greenish layer and, for comparison, on samples taken a few millimetres apart, within the thick marl layer. The main layer was described as an argillaceous dolomitic layer (Fig. 1.5a). However, in the thin greenish layer, the dolomite was almost absent (Fig. 1.5b). This change in mineralogy affected the

mechanical features of the material. Direct shearing tests on the actual sliding surface aligned carefully with the middle plane of the shear box provided a friction angle equal to 17° , five degrees lower than the residual friction obtained in reconstituted clayey dolomitic samples tested in the ring shear test.

The mentioned considerations about the strength available along the slide surface are important because they make it necessary to test the strength on intact samples taken on the sliding surface. In the cases mentioned before, the usual ring shear test on reconstituted samples of the material around the sliding surface will overestimate the residual strength.

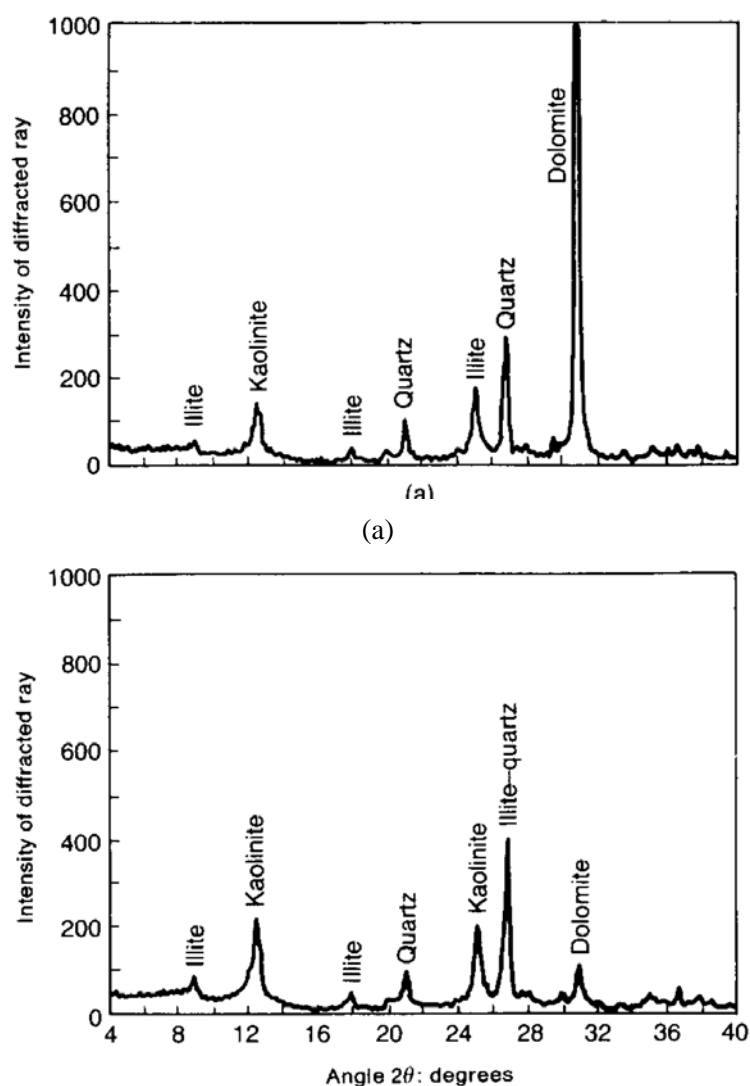


Figure 1.5 Diffractograms of two neighbouring samples within the marl layer of Cortes slide: (a) main body of the layer, brown and beige; (b) striated sliding surface, grey and green (θ = angle of diffracted ray) (Alonso *et al.*, 1993).

1.1.3 Consequences of landslides in reservoir sites

In general, slope instabilities imply a risk that should be prevented for its dangerous consequences: damage in roads, buildings, foundations, etc. However, slope instabilities around reservoirs, being them induced or not by the stored water, include additional risks:

- Damage to the dam or its foundation with catastrophic consequence
- s.
- Partial or complete blockage of the storage water and the formation of natural dams that induce a reduction of the volume of the reservoir and a non controlled increase in the upstream water level. The failure of such dams can be disastrous because of the risk of dam overtopping.
- Depending on their velocity, they can generate a destructive wave when the landslide hits the reservoir water. The wave will propagate and may induce a dam failure or a dam overtopping with dangerous consequences.

1.1.4 Acceleration of landslides in reservoir sites

The risk associated with landslides in reservoirs attracted wide attention in 1963 when the catastrophic failure of the left bank slope in Vaiont reservoir in Italy caused more than 2000 deaths and a mayor destruction (Hedron and Patton, 1985; Müller, 1964). The case is reviewed often in the literature mainly because of the difficulty of determining the causes of its great acceleration. The slide reached a velocity around 25 - 30 m/s (100 km/h), an estimation based on the height of the ensuing wave.

The risk of landslide acceleration may become one of the most challenging problems to face for people in charge of reservoir and dam operation. The question of what speed can reach a specific landslide and its consequences does not have an easy response. The analysis of the whole phenomena requires assessing the following phenomena (Fig. 1.6):

- Triggering of the landslide.
- Run-out.
- Impact of the landslide against the reservoir and generation of a destructive wave.
- Wave propagation.
- Impact on dam and facilities around the reservoir.

Most of the models developed so far to describe the wave generation and propagation take into account the hydro-dynamic of the water body, making assumptions on the falling mass, although they do not analyze in detail the landslide run-out (Harbitz *et al.*, 1993; Noda, 1970; Biscarini, 2010; Capone, 2009; Walder *et al.*,

2003). Pastor *et al.* (2009) presented a model able to describe all mentioned phases, from landslide triggering to wave propagation, considering the coupled interaction between the avalanche of a fluidized soil and the water body.

The risk of a landslide reaching a high velocity depends basically on the differences between resistant and destabilizing actions applied on the unstable body. There are different factors that may lead to the acceleration of landslides:

- Resistant actions (shear strength) decrease due to strength softening (typically in brittle materials) and rate effects on residual strength.
- Generation of compressive pore water pressures on saturated sliding surfaces in undrained or partially drained conditions. It typically occurs in loose granular soils (which are prone to flow liquefaction).
- Generation of water pressure due to fragmentation or crushing of particles formed by shearing in granular materials (Sassa *et al.*, 1996; Wang and Sassa; 2002).
- Pore water pressure generation by thermal effects due to frictional shearing at the shear band.

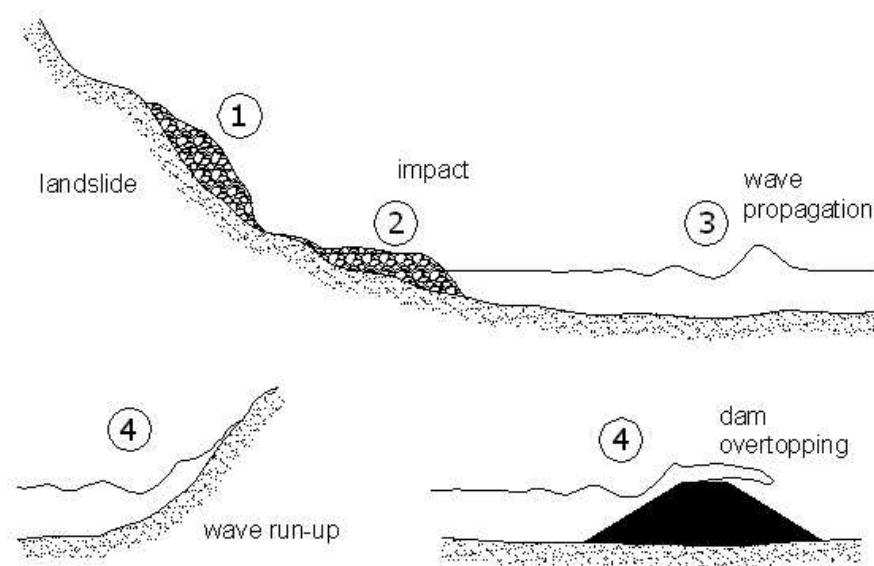


Figure 1.6 Principal phases in the phenomenon of landslide-induced wave and consequences (Capone, 2009)

The discussion on the basic phenomena leading to the fast acceleration of a landslide is today very active and each case should be analysed separately. In this work, the fourth cause mentioned, the relevance of thermal effects on the sliding surface and its role to increase the local pore water pressure, has been favoured as a rational

mechanism to explain the slide acceleration in clayey materials. Chapter 3 presents an introductory explanation of the phenomena with the purpose of developing a theoretical model of the problem. The developed formulation is applied in the following chapters to synthetic and real cases. A closed form solution for the case of a planar landslide is presented in Chapter 4 under some specific assumptions. Numerical and analytical solutions will be compared and a sensitivity analysis aiming at practical conclusions will also be described.

Before closing this introductory part, a number of case histories will be briefly presented. They illustrate the magnitude and dangerous consequences of landslides that accelerate and invade reservoirs and rivers. The occurrence of such events is not frequent and there is a lack of well-documented case histories. Most of the cases described below may be criticized for being too descriptive but they strongly convey the risk of these rare events.

1.1.5 Case histories

In this Section, the causes, features and consequences of landslides around reservoirs are exemplified by means of the description of some published real cases. This section is not intended as an exhaustive review of landslide occurrences in the vicinity of reservoirs. Rather, a few representative cases are described.

Two important cases of non-catastrophic landslides in Spain associated with reservoirs, Cortes landslide (Valencia) and Canelles landslide (Catalonia) are not mentioned here. They will be described in subsequent chapters. Cortes landslide is analysed in Chapter 4. Despite the fact that it was stabilized before it could accelerate, an analysis of its potential acceleration under the simplification of a planar motions is made in Chapter 4. Canelles landslide is currently a potentially dangerous case for the operation of the reservoir. The landslide was first observed in summer 2006. The case is presented in Chapter 7. A thermo-hydro-mechanical analysis was developed for this case in order to estimate the maximum velocity of the slide. The results have been used to estimate the generation and propagation of waves within the reservoir. This part of the work, which is outside the scope of this Thesis, has been performed by the Instituto de Hidráulica Ambiental of Universidad de Cantabria (Spain).

In the following description of catastrophic landslides, the most famous and well-documented Vaiont landslide is not mentioned because two chapters of this Thesis are focussed on it. Chapter 5 summarizes the relevant data available and the most relevant features of the motion previous to the catastrophic failure. This information allows establishing the main hypothesis and assumptions made in the model presented for Vaiont Landslide. In Chapter 6, a dynamic analysis of Vaiont landslide is presented. The objective was to explain the high velocity reached by including thermal effects. However, the most interesting contribution of the analysis performed is the derivation of some practical criteria to decide the actual risk of slide acceleration. Results cannot

be accepted as a well proven criteria but they are believed to be a first step in that direction.

The landslides collected here are divided in two groups: those which may rationally be viewed as potentially dangerous and those which actually failed at high speed and resulted in a catastrophic situation.

Potentially dangerous landslides

Aknes Landslide, Norway

Aknes is a large rockslide continuously creeping located above a fjord in Norway, in the vicinity of several communities and tourist places (Ganerød *et al.*, 2008) with an estimated volume of 35-40 millions of m³ and dimensions of 800 m across-slope and 1000 m down slope (Fig. 1.7)

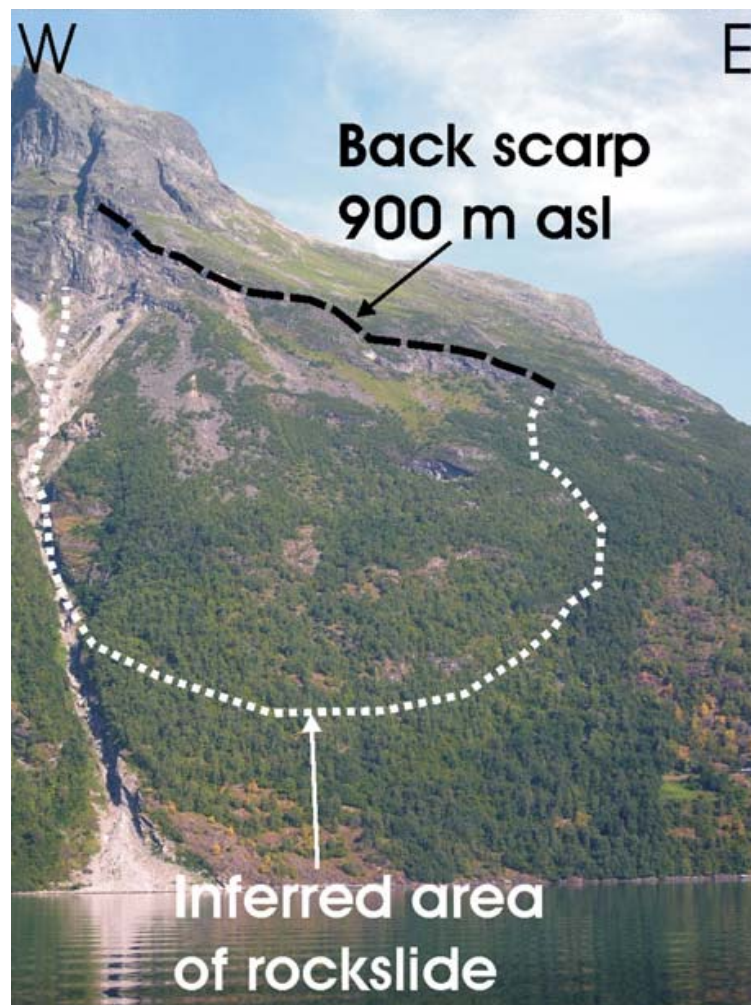


Figure 1.7 Overview of Aknes landslides over the fjord in Norway (Ganerød *et al.*, 2008).

The unstable mass is defined by a back scarp, a basal shear zone, 50 m deep and a toe zone where the basal sliding surface daylight on the slope surface. Figure 1.8 shows the geological model of the Aknes rockslide presented by Ganerød *et al.* (2008). It was obtained by geological surveys using different techniques (structural maps, geomorphologic interpretation, penetrating radar, seismic refraction, 2D resistivity profiling and sonic logging of p-waves). The rockslide can be divided into an upper part (subdomains 1 and 2, Fig. 1.8) that experience extension and a lower part (subdomains 3 and 4) that deforms by compression. The upper boundary zone of the rockslide is seen as a back scarp that is controlled by, and it is parallel to, the pre-existing steep foliation planes of gneiss. The foliation in the lower part seems to control the development of the basal sliding surface which daylights at different levels. The sliding surfaces are subparallel to the topographic slope and are located along mica-rich layers in the foliation. (Ganerød *et al.*, 2008).

The shear strength of the material involved in the sliding surface of Aknes landslides has been reported by Grøneng *et al.* (2009). Samples from gouge material, unfilled rock joints and intact rock were tested. Gouge material (9-19% clay content) tested in triaxial test exhibited a friction angle between 18 and 35° depending on the mineralogy. Samples containing the lowest percentages of quartz and highest percentage of mica shown the lowest shear strength. Rock joints shear strength was evaluated by empirical methods (Barton and Choubey, 1978) resulting a friction angle of 24°. The tested intact gneiss showed a shearing strength defined by 19-25 MPa of cohesion and 57-89° of friction angle.

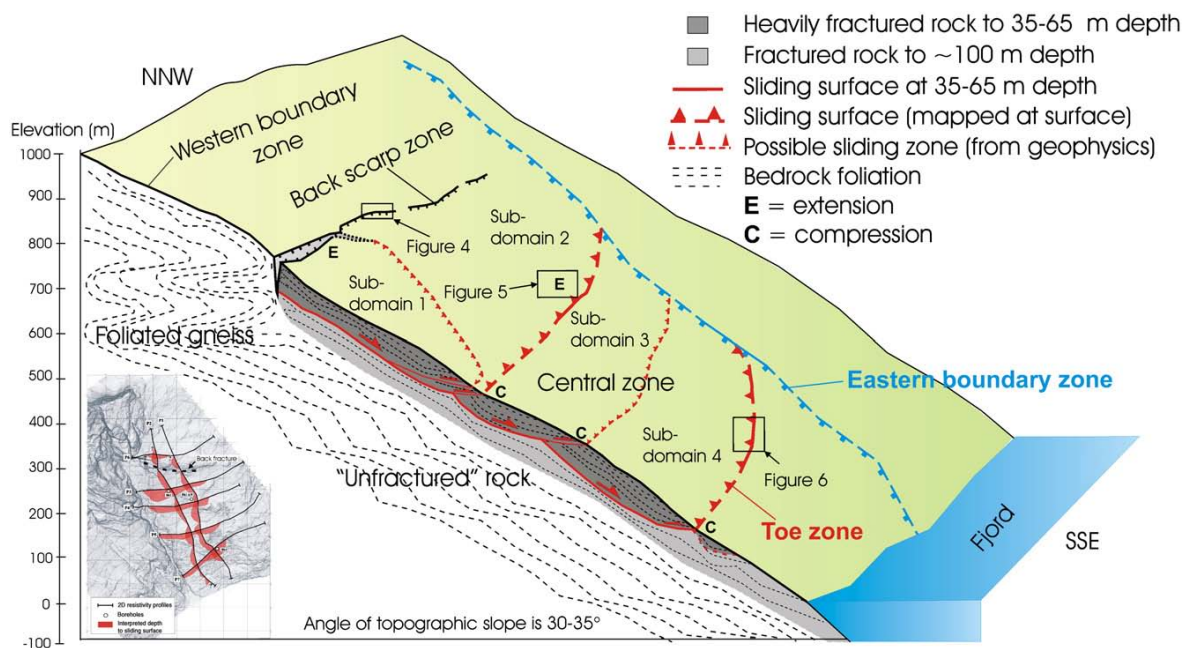


Figure 1.8 Geological model of Aknes landslides (Ganerød *et al.*, 2008).

Maoping Landslide, China

Maoping landslide is the largest ancient landslide located on the left bank of the Qingjiang river (one of the major tributaries of the Yangtze river). It is located 66 km upstream of Geheyan dam and it was reactivated by the impoundment of the reservoir (2.9 billions m³) in April 1993.

The Maoping landslide was geologically investigated before reservoir inundation and its displacements are being controlled and correlated with reservoir level and rainfall. A total of 34 landslides (in total 0.16 billions of m³ in volume) were identified on both banks of the reservoir.

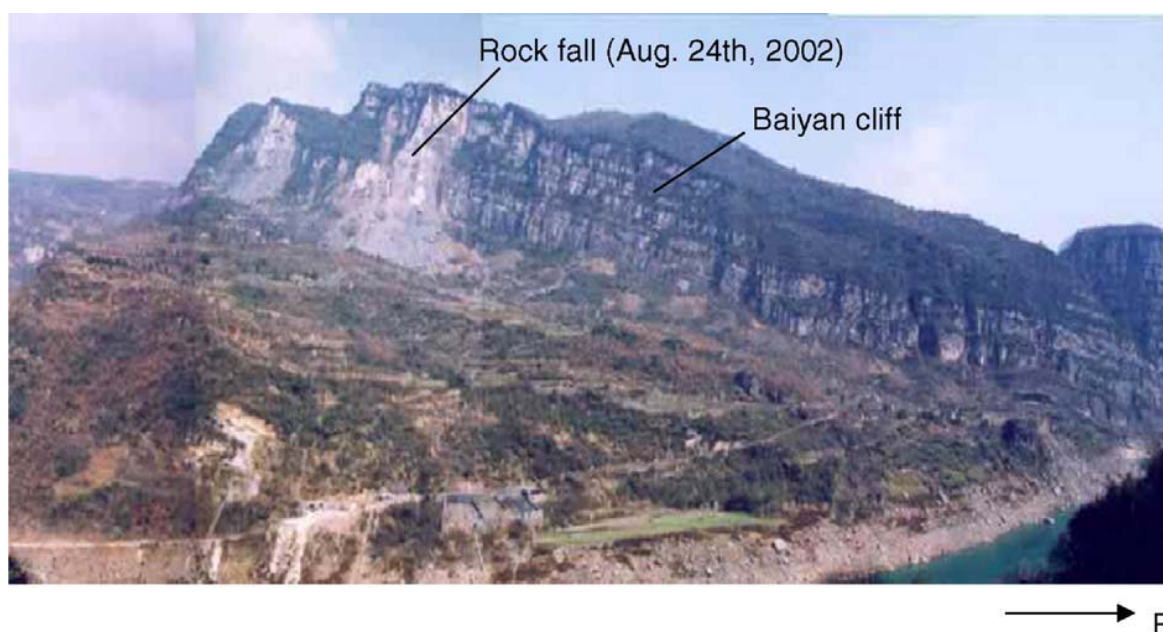


Figure 1.9 Overview of Moaping landslide (Qi *et al.*, 2006)

The reactivation of the Moaping landslide required the relocation of a small village located on the valley slope. Qi *et al.* (2006) is used as a main source for the summary presented here. The volume of the landslide is estimated in 23.5 millions m³. Figure 1.9 shows an overview of the landslide. The thickness of the slides varies from 5 to 89 m, increasing from the rear to the front and from the west to the east.

The mobilized mass includes three main layers. The first layer is constituted by a detritic soil (10-20 m thick) occasionally containing limestone blocks. The second layer (5-15 m thick) is constituted by quartz sandstone blocks, often overlaid by a layer of 2 – 8 m thick of coal soil and gray white detritus and fragments. The third layer (20-40 m) is bedrock-like disintegrated blocks of sandstone. The sliding plane was developed along a bedding surface in the sandstone, which is inter layered by shales with a dipping angle of 15 – 20°, except for the front part (having a length of 180 m) where it is near horizontal. However the sliding zone has a different appearance when one

compares the west and eastern parts. This difference seems to be the result of different sliding processes and sliding sequences in the history of the landslide. The formation process of the Moaping landslide was a result of three major landslides shown in Figure 1.10. The landslide previous history is complex but the fundamental information is that it is a presently reactivation of an ancient landslide.

Stability analyses based on strength parameters obtained in the laboratory (Qi *et al.*, 2006) were carried out before and during the reservoir impoundment. Drained strength parameters were obtained in consolidated quick tests on saturated samples which gives a doubtful reliability to the results.

Cracks and settlements were first observed in the ground and houses after reservoir impoundment. During the raining seasons, cracks opened. According to observations the maximum accumulated horizontal displacement of the slide reached 2840 mm, in the period March, 1993 to October, 2005.

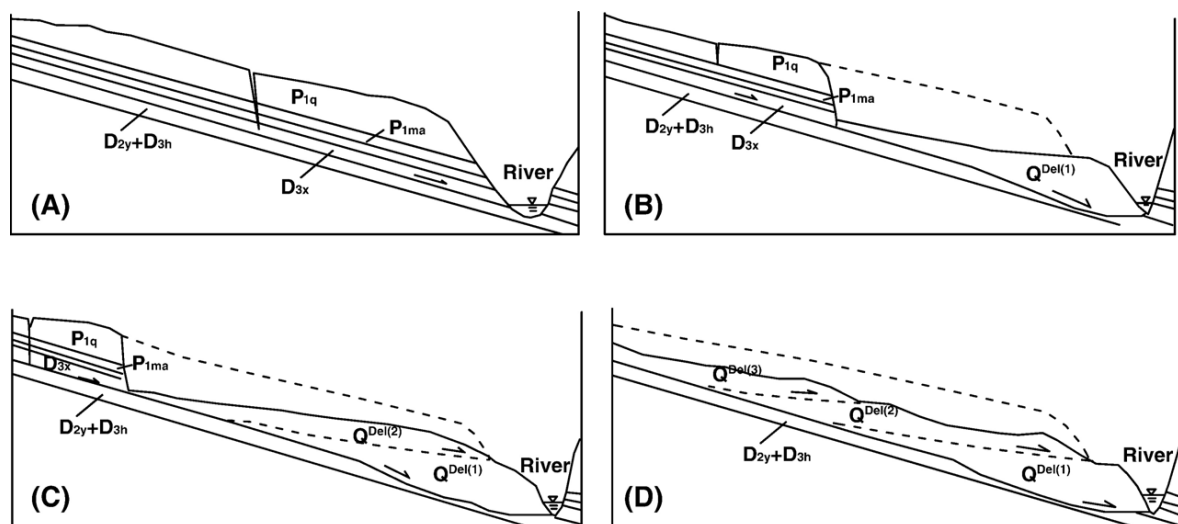


Figure 1.10 Formation process of the Moaping landslide (after Bureau of Investigation and Survey, Changjiang Water resources Commission, 1993. From Qi *et al.*, 2006)

Catastrophic landslides

San Juan de Grijalva Landslide, Mexico, 2007

In November 4, 2007, a catastrophic landslide took place in the left margin of the Grijalva river located in the south-eastern province of Chiapas, Mexico. It was a translational movement with a length of 1200 m, 610 m wide and a depth of 70 m. The volume was around 50 million m³. The run-out of the landslide was about 800 m.

The impact of the slide against the water of the river generated a wave which was reported to be 50 m high (Alcántara-Ayala *et al.*, 2008) or 15 m high (Hernández-Madrugal *et al.*, 2010) depending on the source. The landslide-generated wave destroyed the San Juan de Grijalva village. A lake was formed due to a landslide-induced dam,

which flooded 21 villages upstream. The landslide and its subsequent consequences killed nineteen people and six more were reported missing.

The landslide was registered in a seismic station located at a distance of 16 km. Such records indicated that the mass movement took place during approximately 80 seconds (Alcántara-Ayala *et al.*, 2008). Before the slide, the topography of valley was characterized by a 5 – 20° slope on the upper hillside, and a 20 – 40° slope on the adjacent right bank of the Grijalva River. At first sight, such geometry of the sliding surface leads to the deceleration of the landslide.

A 80 m high and 1170 m wide dam was created across the Grijalva River. This dam created a lake having a surface of 49 km². Figure 1.11 shows a photograph of the natural dam induced by the landslide.



Figure 1.11 San Juan de Grijalva landslide blocking the river (Alcántara-Ayala *et al.*, 2008).

The geological setting includes alternating conglomerates, sands, silts, clays and marls of Eocene and Miocene age, which overlie Jurassic and Cretaceous rocks (Hernández-Madrigal *et al.*, 2010) (Fig 1.12). Alcántara-Ayala *et al.* (2008) mentioned that the slide surface was located on a clay strata dipping toward the river.

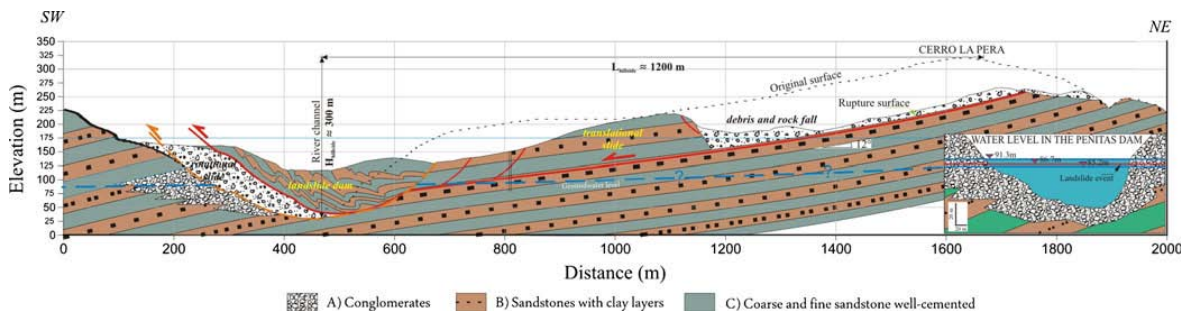


Figure 1.12 Geological cross-section of San Juan Grijalva landslide (Hernández-Madrigal *et al.*, 2010).

Three factors are invoked as triggering causes for the landslide (Hernández-Madrigal *et al.*, 2010): the intense precipitation that took place in the previous months (the cumulative rainfall in the preceding 30 days was 67% of the average annual rainfall), an earthquake which occurred 5 days before the landslide, and the water level drawdown of the Grijalva River due to the release of water from the Peñitas dam located 14 km downstream. Figure 1.13 shows the water level at the Peñitas reservoir (which controls the level of the river upstream). The landslide occurred almost at the end of the final drawdown. The drawdown velocity at the end of drawdown period was 1.47 m/day, 4.2 times greater than the average drawdown rate of 0.35 m/day.

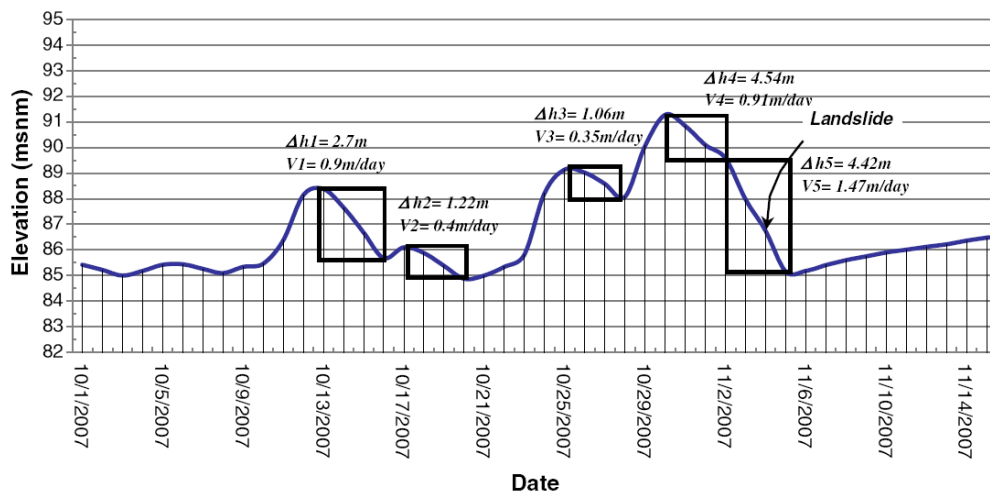


Figure 1.13 Water level at the Peñitas dam before San Juan de Grijalva landslide occurred in November 4, 2007 (Hernández-Madrigal *et al.*, 2010).

A channel was excavated in the natural dam to restore partially the natural flow conditions of Grijalva river.

Qianjiangping Landslide, China (2003)

Qianjiangping landslide occurred after the first impoundment of the Three Gorges Reservoir in 14th July, 2003. It was located in the left bank of the Qinggan River, a

tributary of the Yangtze River. It happened when the reservoir reached a water height of 135 m. Erosion by the river, quarrying of shale in the landslide toe and previous heavy rain seem to be additional combined causes leading to the instability (Wang *et al.* 2004).



(a)



(b)

Figure 1.13 View of the Qianjiangping landslide: (a) from the upstream side; (b) front view. (Wang *et al.*, 2004).

Figure 1.14 shows the landslide from the upstream side and a frontal view of the landslide. The landslide had a tongue-like shape and has a length of 1200 m and a width of 1000 m. The average thickness of the sliding mass was about 20 m, thinner in the upper part and thicker in lower part. The total volume was estimated to be more than 20 millions of m^3 . It displaced forward around 250 m. Figure 1.15 shows a representative section of the slide. It was a typical translational rockslide.

The landslide caused loss of life and serious damage with important economical cost. Thirteen people lost their lives on the slope banks and eleven fishermen died while working on boats in the nearby area. The casualties on the river were a consequence of the high velocity of the slide which triggered a 30 m high wave. Witness accounts showed that it took few minutes to complete the whole sliding process (Wang *et al.*, 2004). The slide velocity was not given despite the available data on the wave height.

The landslide completely blocked the Qinggan River and formed a lake upstream. To prevent that the water level in the impounding area reached a dangerous level with possible damage downstream in case of dam breaching, a channel diversion was excavated (Dai *et al.*, 2004).

The displaced block was constituted by layers of weathered sandstone and shale. According to Dai *et al.* (2004), the slip surface was located in a thin layer of clayey soil having a thickness of several centimetres. The bedrock below the sliding surface was constituted by sandstone and siltstone layers interbedded with intact shale if compared with the overlying material.

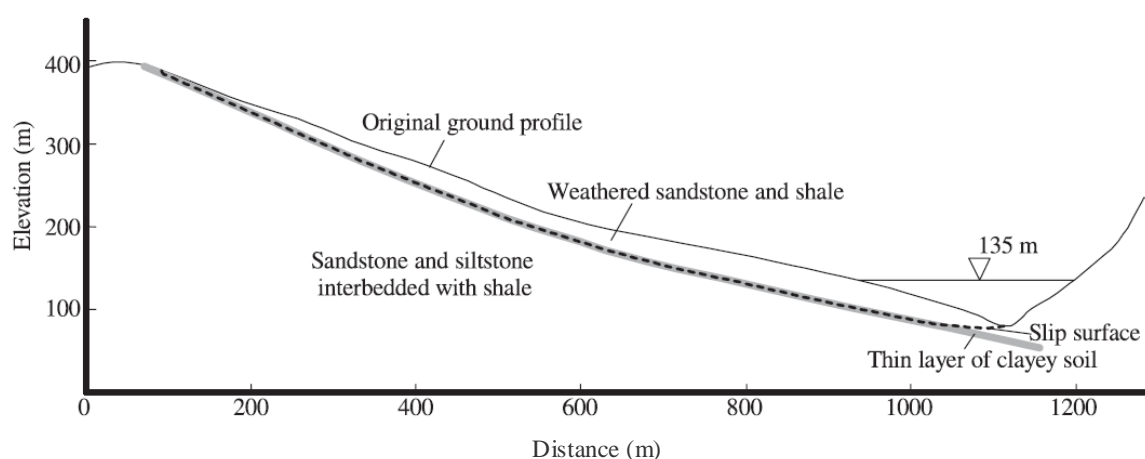


Figure 1.15 Qianjiangping landslide representative section (Dai *et al.*, 2004).

The sliding surface could be uncovered in the upper part of the landslide (Wang *et al.*, 2004). According with their interpretation, Figure 1.16a shows the original situation, previous to the 2003 landslide. The photograph 1.16a shows a striated surface which indicates the initial sliding direction (red arrows). Figure 1.16b

corresponds to new striations that follows the sliding direction of the 2003 landslide (indicated by the blue arrow). The pre-existing shearing surface is associated with an older geological event (probably during intense folding in a Cretaceous Period) (Wang *et al.*, 2004). The existence of widely distributed striation on the sliding surface as well as other geomorphological indications leads to accept that the sliding surface was mobilized prior to the landslide in 2003. However, since the “old” and “new” directions of sliding are not the same, it would be interesting to evaluate if the shearing strength along the mobilized shear surface remains in residual conditions when the shearing direction changes.

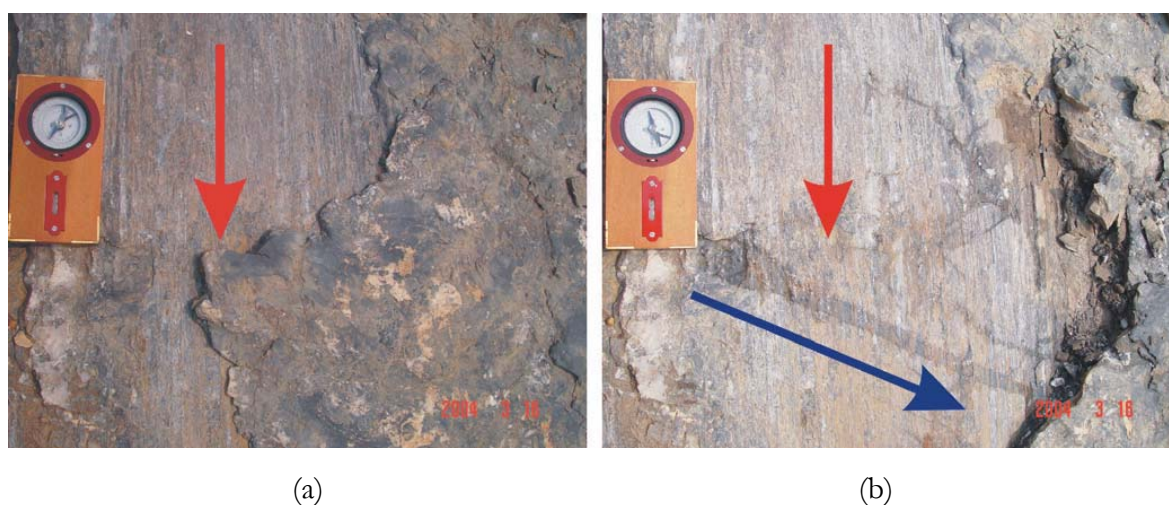


Figure 1.16 Photographs from the same site of the upper part of the Qianjiangping landslide sliding surface showing the pre-existing scratches that underlie the sliding surface of the July 2003 event (blue narrow shows the sliding direction, red arrows show the strike direction of the pre-existing scratches) (Wang *et al.*, 2004).

A more detailed exploration of the sliding zone is presented by Wang *et al.* (2008). Two horizontal tunnels were excavated with the purpose of reaching the sliding zone. Two different materials were found: a layer of black silt with calcite blocks ($w_L = 30\%$; $PI = 2$) on the top, while the lower strata was a yellow clay ($w_L = 49\%$; $PI = 40$). Figure 1.17 shows a photograph of the sliding zone taken in one of the horizontal investigation tunnels. Samples of the two types of materials were tested by direct shearing imposing different rates of displacement (Wang *et al.*, 2008). A mobilized residual friction angles (reached after more than 2000 mm of relative displacement) equal to 26° and 20° were obtained for the reconstituted black silt and the yellow clay samples, respectively. Undrained rapid ring shear tests indicated that a rate of displacement around 10 mm/sec induces a drop of the strength of around 10° on the black silty soil. The rate of shearing did not affect the yellow clay.

A fundamental question rises from the description of Qianjiangping landslide: ¿What was the cause of the rapid loss of shearing resistance necessary to achieve the high rate of acceleration? The representative cross-section shown in Figure 1.15 does

not explain the development of a high velocity. Several alternative reasons could be possibly advanced, but an accurate analysis and further testing may be required. A drop of strength as the displacement increases could explain such acceleration. However, if it is true that the sliding surface is in residual conditions, the loss of strength with displacement increment is unlikely. Wang *et al.* (2004) mentioned the presence of crystalline calcite on the sliding zone, acting as a cement deposited after the folding of sedimentary strata that mobilized the sliding surface. Crystalline calcite is characterized by brittle fracture and this phenomena could explain the sudden loss of strength.

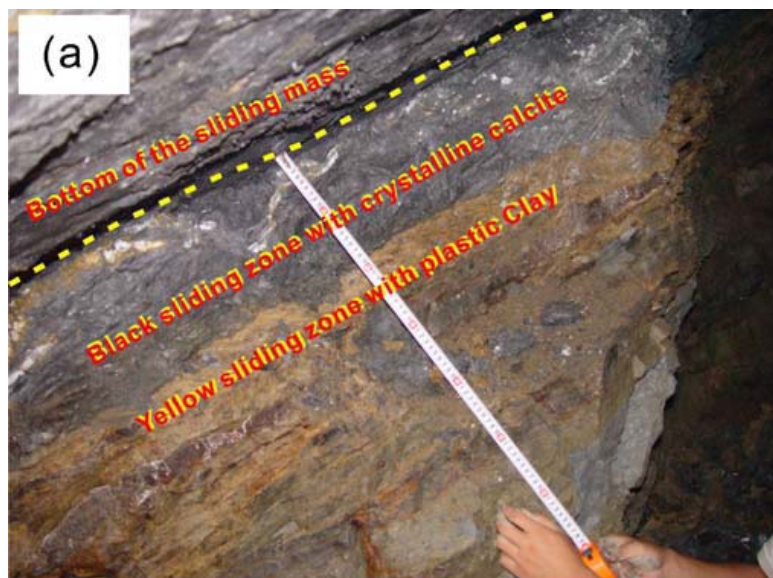


Figure 1.17 Photographs of sliding zone of Qianjiangping landslide taken from horizontal tunnel. (Wang *et al.*, 2004).

A more complex mechanism is described by Wang *et al.* (2008). They explain that the effect of shearing rate is the actual reason for the strength softening behaviour. None of the authors considers the effect of heating induced by frictional work at the sliding surface. This approach, developed in this Thesis, explains the build-up of pore pressure by the movement of the slide. The shearing displacement generates frictional work that dissipates in heat. Temperature increments lead to the dilatation of solid particles and water that, in a saturated porous media, and always depending on properties such as stiffness and permeability, leads to build-up pore water pressure. As a result, the effective normal strength reduces and, accordingly, the available frictional strength. Checking this hypothesis requires a specific thermo-hydro-mechanical analysis of the landslide.

La Josefina Landslide, Ecuador (1993)

On March 29, 1993, a massive rockslide dammed the Río Paute in Cuenca, Ecuador. Its situation is shown in Figure 1.18. The slide was 1500 m long and 600 m

wide. The volume of the moving mass was estimated to be around 20 million m³ (Harden, 2004) of igneous rocks overlain by colluvial deposits.

Aerial photographs taken before the failure and the observation of a headscarp approximately 80 m high, led to the conclusion that the movement was a reactivation of an ancient landslide. It was probably triggered by heavy rain and mine excavations at the toe.

The regions upstream and downstream from the landslide were densely populated. Seventy two people were reported killed or missing (Chamot, 1993) and the economic losses were devastating.

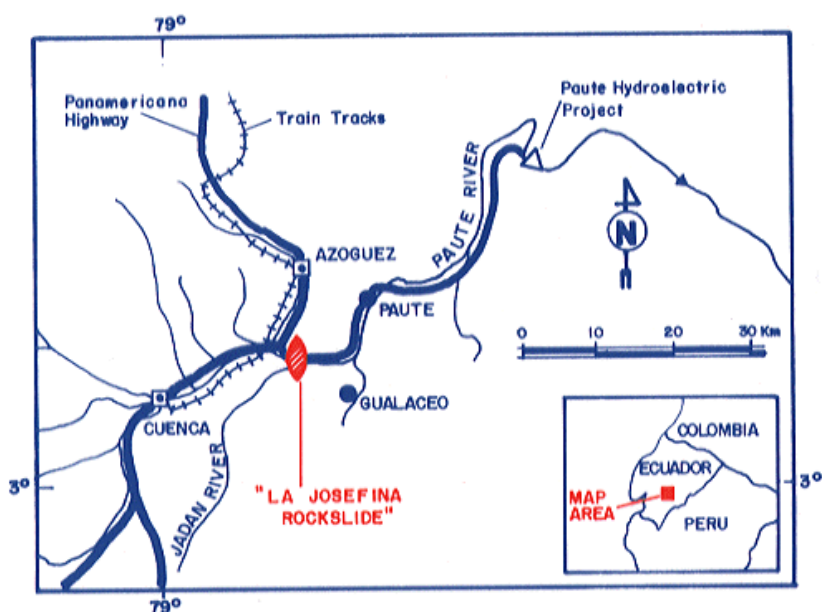


Figure 1.18 Location map for La Josefina rockslide (Plaza-Netos and Zevallos, 1994).

The slide formed a 100 m high natural dam on the Río Paute at its junction with the Río Jadan (Fig. 1.19). The impoundment behind this dam flooded the upstream valley for a length of 10 km, submerging agricultural land, houses and industries. The final stored water volume of the natural dam was 200 million m³. The lake reached a depth of 83 m. After 33 days, the dam failed, resulting in a peak discharge of 10000 m³/s. The resulting debris flow and mudflow flooded the valley downstream entering into the Amaluza Reservoir behind the dam with the same name. Reservoir authorities manage to lower 31 m the reservoir level. In spite of this precaution, severe damage on the powerhouse turbines occurred due to the high concentration of suspended soils in the water and also on houses and industries located around the affected site (Schuster *et al.*, 2002).

The failure of the landslide-induced dam led to a decrease in the water level of the Josefina lake at a relatively high velocity and several landslides occurred on the

surrounding slopes due to the rapid drawdown. The most important one was Zhizhio slide (Schuster *et al.*, 2002). No additional information on these landslides has been found.

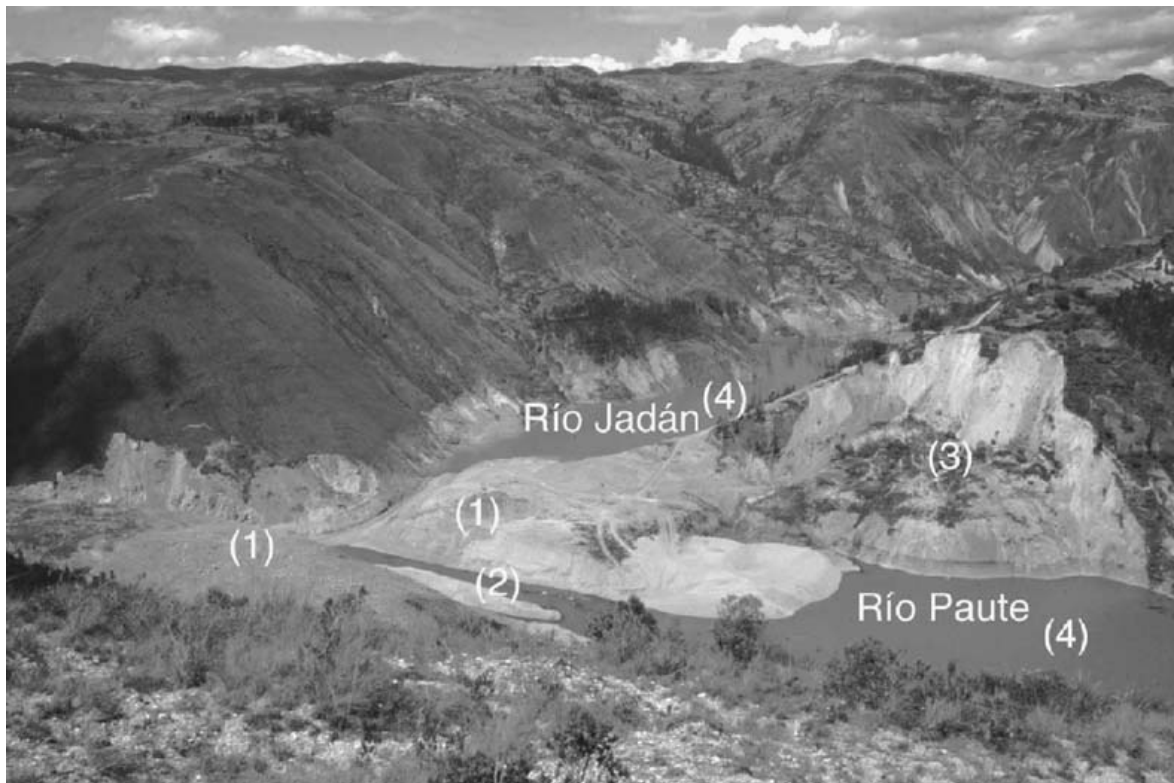


Figure 1.19 The landslide scar and dam in 1994, 1 year after the dam was ruptured. The photograph was taken from near the top of the slide, looking southward; the flow of the Paute River is from right (west) to left (east). Numbered features are (1) deposits from the March 29, 1993 landslide, (2) channel excavated to release impounded water, (3) a post-rupture slope failure at Zhizhio, and (4) remnant lakes a year after the dam rupture (photo by Harden, 2004).

Gros Ventre landslide, United States (1925)

The Gros Ventre landslide is located in Bridger-Teton National Forest, Wyoming, U.S.A. The landslide occurred on June 23, 1925, after several weeks of heavy rain. The landslide created a huge dam across the Gros Ventre River, which stored the water and formed a lake. Approximately 38 millions m³ of primarily sedimentary rock slid down the north face of Sheep Mountain, crossed over the Gros Ventre river and raced up the opposing mountainside a distance of 100 m (Fig. 1.20). The landslide created a large dam over 60 m high and 400 m wide across the Gros Ventre River. On May 18 1927, a portion of the landslide dam failed, resulting in a massive flood that reached a height of 2 m 40 km downstream. The small town of Kelly, 10 km downstream, was destroyed and six people were killed.



Figure 1.20 Gros Ventre landslide overview (Shelton, 1966).

1.2 THESIS LAYOUT

The Thesis is organized in eight chapters. Each chapter contains its own summary, introduction and conclusions. A common list with the cited references is presented in Chapter 8. The main contents of each chapter are introduced here as follows:

- *Chapter 2* presents an analysis of the drawdown problem on slopes as a fully coupled flow-deformation problem for saturated/unsaturated conditions. Classical procedures developed to determine the flow regime within the slope and the resulting stability conditions are reviewed at the beginning of this chapter. Later some fundamental concepts are discussed and explored in more detail by the analysis of synthetic examples under different hypothesis. Sensitivity analyses are presented. The chapter is closed with the discussion of a comprehensive case history.
- *Chapter 3* includes an analysis of rapid landslides using a thermo-hydro-mechanical approach. Previously an introductory section is presented to discuss earlier works published on rapid landslides and their causes. It serves to highlight some relevant aspects of direct implication for the analysis described later.
- *Chapter 4* applies the theory developed in the previous chapter. The governing equations of the thermo-hydro-mechanical problem for landslides are integrated conveniently for the case of a planar landslide. A practical closed

form is obtained for the case of incompressible fluid, solid particles and soil skeleton. A case study, based on a well known translational slide (Cortes slide, Spain) has been solved. Numerical and analytical solutions are compared.

- *Chapter 5* focuses in the Vaiont landslide. First, a review and analysis of the available information is presented. Once convenient hypothesis are assumed according to the previous review, a static and dynamic equilibrium of Vaiont is presented. A model of two interacting evolutive wedges represents the landslide. The approach gives a simple explanation to the stability of the slide, before failure. Rock strength degradation of the mobilized mass as motion develops, has also been included. This degradation, even if it is intense, was unable to explain the very high estimated landslide velocities.
- *Chapter 6* introduces the thermo-hydro-mechanical formulation in the dynamic analysis of Vaiont landslide presented in Chapter 5. The model predicts the high velocity observed and is consistent with other data. Sensitivity analyses of the more relevant parameters and the issue of scale effects are presented and discussed.
- *Chapter 7* presents a study of an ancient landslide reactivated in the left bank of the Canelles reservoir. A methodology to analyze the landslide, based on field works, laboratory testing and in situ measurements, is described for the case of Canelles landslide occurred in summer 2006. The analysis made involves the consideration of the drawdown problem (discussed in Chapter 1) and the analysis of its potential acceleration taking into account thermal effects (Chapter 3).
- *Chapter 8* provides some general conclusions and suggestions for future research.

The fundamental contributions of this Thesis have been published in the following journal papers:

- Alonso, E.E. and Pinyol, N.M. (2010) Criteria for rapid sliding I. A review of Vaiont case. *Engineering Geology*. Article in press. Available online, doi:10.1016/j.enggeo.2010.04.018
- Pinyol, N.M. and Alonso, E.E. (2010) Criteria for rapid sliding II. Thermo-hydro-mechanical and scale effects in Vaiont case. *Engineering Geology*. Article in press. Available online, doi:10.1016/j.enggeo.2010.04.017
- Pinyol, N.M. and Alonso, E.E. (2008) Fast planar slides. A closed form thermo-hydro-mechanical solution. *International Journal for Numerical and Analytical Methods in Geomechanics* 34, 27-52.

Pinyol, N.M., Alonso, E.E. and Olivella, S. (2008) Rapid drawdown in slopes and embankments. *Water Resources Research* 44, W00D03, 22pp. Special issues on: Hydrology and Mechanical Coupling in Earth Sciences and Engineering: Interdisciplinary Perspectives.

CHAPTER 2

Rapid Drawdown in Slopes and Embankments

The rapid drawdown condition arises when submerged slopes experience a rapid reduction of the external water level. Classical procedures developed to determine the flow regime within the slope and the resulting stability conditions are reviewed in this chapter. They are grouped in two classes: the “stress-based” undrained approach, recommended for impervious materials, and the flow approach, which is specified for rigid pervious materials (typically a granular soil).

Field conditions often depart significantly from these simplified cases and involve materials of different permeability and compressibility arranged in a complex geometry. The drawdown problem is discussed in this chapter as a fully coupled flow-deformation problem for saturated/unsaturated conditions. Some fundamental concepts are first discussed in a qualitative manner and later, explored in more detail in synthetic examples, solved under different hypothesis, including the classical approaches. Some design rules, which include a few fundamental parameters for the drawdown problem have also been solved in a rigorous manner to illustrate the limitations of simplified procedures.

The last part of this chapter is devoted to the discussion of a comprehensive case history. In Shira earthdam pore pressures were recorded at different points inside the embankment during a controlled drawdown. Predictions of four calculation procedures (instantaneous drawdown, pure flow, coupled flow-elastic and coupled flow-elastoplastic, all of them for saturated/unsaturated conditions) are compared with

measured pressure records. Only the coupled analysis provides a consistent and reasonable solution.

The role of the different soil properties in explaining the phenomena taking place during drawdown is finally discussed.

2.1 INTRODUCTION

As an introduction to the remaining chapter, consider, in qualitative terms, the nature of the drawdown problem in connection with Figure 2.1a, b.

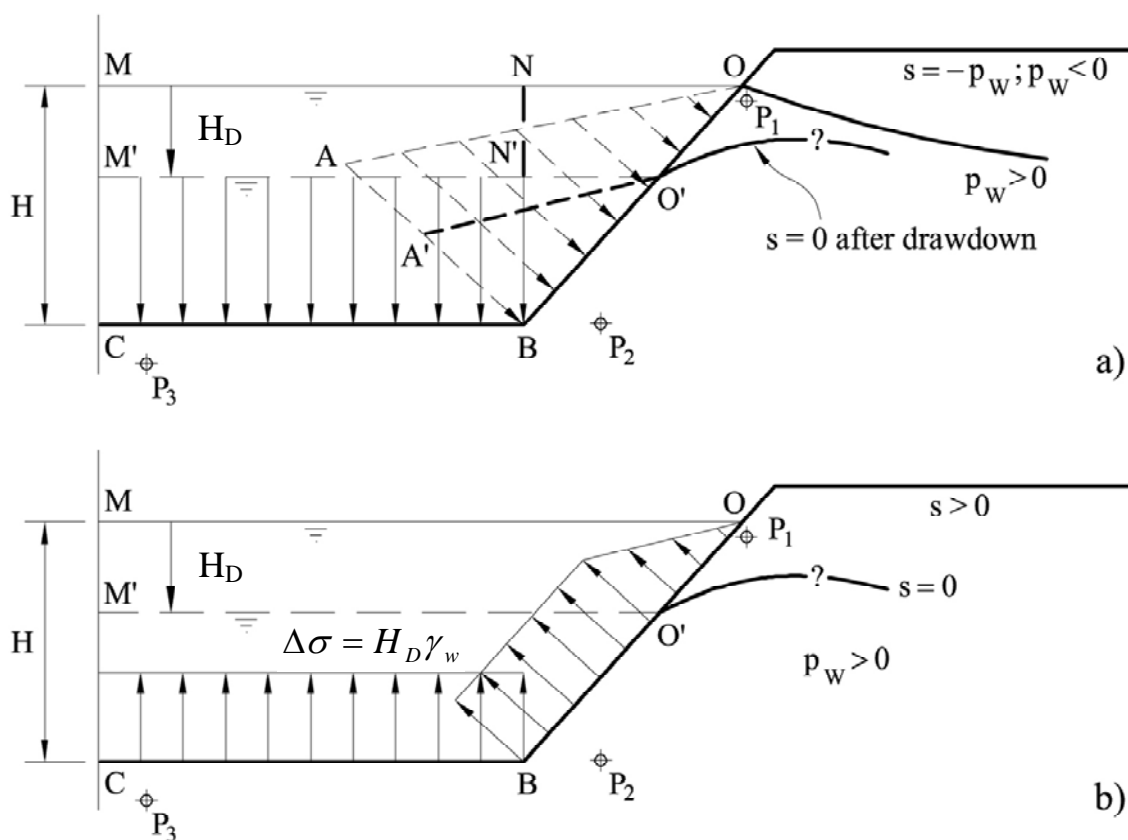


Figure 2.1 The drawdown scenario: (a) Hydrostatic stresses acting against the exposed slope surface; (b) Change in applied stresses on the exposed boundaries induced by a drawdown H_D .

The position of the water level MO (height H) provides the initial conditions of the slope CBO. Pore water pressures in the slope are positive below a zero pressure line ($p_w = 0$). Above this line, pore water pressures are negative and suction is defined as $s = -p_w$. A drawdown of intensity H_D takes the free water to a new level M' N' O' during a time interval t_{DD} . This change in level implies:

- A change in total stress conditions against the slope. Initial hydrostatic stresses (OAB against the slope surface; MNBC against the horizontal lower surface) change to O'A' B and M'N'B C. The stress difference is plotted in Figure 2.1b.

The slope OB is subjected to a stress relaxation of constant intensity ($\Delta\sigma = H_D \gamma_w$) in the lower part (BO') and a linearly varying stress distribution in its upper part (O'O). The bottom horizontal surface CB experiences a uniform decrease of stress of intensity, $H_D \gamma_w$.

- A change in hydraulic boundary conditions. In its new state, water pressures against the slope are given by the hydrostatic distribution O'A'B on the slope face and by the uniform water pressure value $p_w = (H-H_D) \gamma_w$ on the horizontal lower surface.

The change in boundary total stresses result in a new stress distribution within the slope. This stress change will induce, in general, a change in pore pressure. The sign and intensity of these pore pressures depend on the constitutive (stress-strain) behaviour of the soil skeleton. An elastic soil skeleton will result in a drop of pore pressure equal to the change in mean (octahedral) stress. If dilatancy (of positive or negative sign) is present, due to shear effects, additional pore water pressures will be generated. Changes in total stress-induced pore pressures are, in fact, simultaneous to the dissipation process due to the new unbalanced hydraulic boundary conditions. A transient flow will establish. Therefore, as the permeability of the soil increases (always in relation with the speed of water level change), pore pressures will dissipate faster. They may dissipate in "real time" if the soil permeability is large enough. Then the effect of stress-induced pore pressures apparently disappears. Otherwise, in an "undrained" condition (high speed of water level changes or very low permeability) changes in pore pressure will be induced exclusively by total stress changes.

Skempton (1954) and Henkel (1960) provided expressions for the development of pore pressures (p_w) under undrained conditions before modern constitutive equations, based on critical state concepts, were born. The Henkel expression:

$$\Delta p_w = B(\Delta\sigma_{oct} + a\Delta\tau_{oct}) \quad (2.1)$$

in terms of changes in mean ($\Delta\sigma_{oct}$) and shear ($\Delta\tau_{oct}$) octahedral stresses is useful for the discussion. Coefficient B is given by:

$$B = \left(\frac{1}{1 + n \frac{K'_{skel}}{K_w}} \right) \quad (2.2)$$

where n is the soil porosity; K'_{skel} , the bulk modulus of the soil skeleton, and K_w , the bulk modulus of water. K_w is close to $K_w = 2100$ MPa and, therefore, in practically all cases involving natural or compacted materials in riverbank and embankment dam engineering, $K'_{skel} \ll K_w$ and $B = 1$. Even for an exceptionally stiff soil material ($K'_{skel} \cong$

K_{ij}) the value of B is close to 1. This is a well-known result but it is often read, in connection with drawdown analysis, that in cases of rigid materials the (stress) uncoupled flow analysis is sufficiently accurate, implying that no stress-related changes in pore pressures are generated. It is clear that this is never the case in practice. Only if the "rigid" material happens to be pervious and for a different reason, the stress coupling seems to be absent. This will be discussed further in the paper.

The change in hydraulic boundary conditions adds a new transient scenario and pore pressures will dissipate in time, trying to reach stationary conditions under the new boundary conditions.

Consider three representative points (P_1 , P_2 and P_3) of the slope sketched in Figure 2.1 and their expected evolution of pore pressures in qualitative terms in Figure 2.2a,b,c. A given time, t_{DD} , in the t axis marks the end of the drawdown operation. It will be seen, when reviewing in the next section the available methods for drawdown analysis, that two wide classes of procedures have been developed.

The first class highlights the effect of changing boundary stress in order to calculate the pore water pressures immediately after a (sudden) drawdown. The second class of procedures uses pure Darcy-type flow, and they are said to be valid for rigid (!) and pervious materials. It is also common, at present, to find flow-based stress uncoupled analysis in practical applications and, therefore, a distinction of the results likely to be found in case of stress coupled or uncoupled (pure flow) analysis is useful for discussion.

A Point P_1 , close to the upper part of the slope, will experience a limited change in stress due to the unloading represented in Figure 2.1. Therefore, no major differences should be found when comparing coupled or uncoupled analysis, even if the soil is impervious. In a pervious case, it has already been argued, no differences in practice will be found. Note also that the upper points in the slope may develop negative pore water pressures (suction).

At the other extreme of the slope, Point P_3 , "bottom of the sea" conditions exist, if the slope face BO is far away. Because of the one-dimensional nature of this situation, it is well-known that pore pressures in the soil, at any depth, will follow the changing water level and the situation will be always in equilibrium with the new hydraulic boundary condition. However, in order to reproduce this elementary result with a computational tool, it is necessary to use a fully coupled hydromechanical approach. Otherwise, a change in water level will trigger a transient flow condition because no information on the instantaneous change in pore water pressure is available in an uncoupled model.

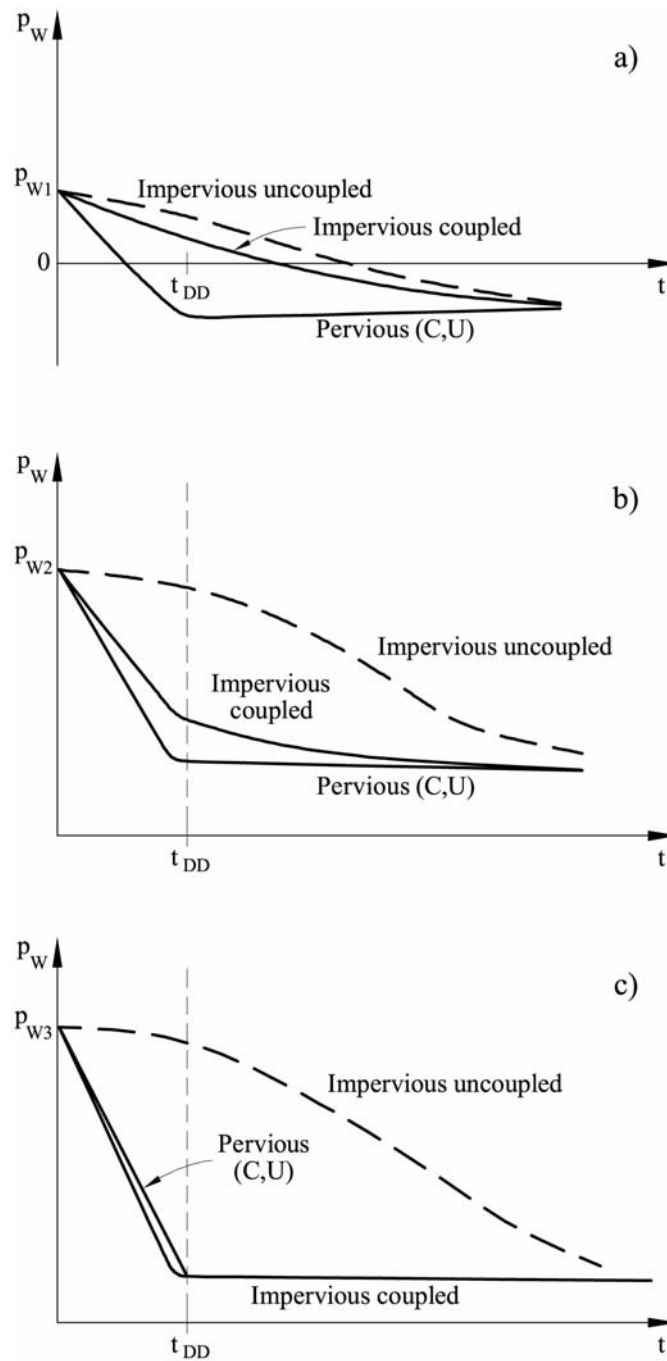


Figure 2.2 Change in pore water pressures in Points (a) P_1 ; (b) P_2 ; and (c) P_3 for coupled or uncoupled analysis and pervious or impervious fill.

Predicting the behaviour of Point P_2 , near the toe of the slope is more difficult. Mean and shear stresses are high and they experience significant gradients. New pore pressures generated after unloading are far from being in equilibrium among them and with respect to the new hydraulic head imposed at the boundary. In fact, in a fully coupled approach, the transient process of pore water pressure dissipation has several origins. They are: the rate of water lowering (this is a boundary condition), the

heterogeneous distribution of "instantaneous" pore water pressures after drawdown and the "source" or "storage" terms provided by both, the changing saturation in some parts of the domain and the deformation of the soil skeleton. Figure 2.2b shows that the response of Point P₂ in a coupled analysis will depend on the permeability of the soil. The uncoupled analysis will be unable to introduce stress effects, however. Only in a highly pervious soil, both analyses would provide the same answer. The problem has, however, an additional difficulty because soil stiffness, which controls the "storage or source" term associated with changes in effective stress, will also dictate the rate of the process.

A reference to the usual expression of time to reach a given degree of consolidation, U , in one-dimensional consolidation problems, provides a clue on the effect of soil stiffness:

$$t = \frac{L^2 T(U)}{k E_m} \gamma_w \quad (2.3)$$

where L is a reference length associated with the geometry of the consolidation domain; T is the time factor; k , the soil permeability, E_m , the confined stiffness modulus, and γ_w , the water specific unit weight.

Soft materials (E_m low) will react with high consolidation times, all the remaining factors being maintained. Figure 2.3b indicates this effect. Permeability and stiffness control the rate of pore pressure dissipation in this case, in the manner indicated. However, if more advanced soil models are introduced, the simple trends given in Figure 2.3 may change.

The changing boundary condition and the soil permeability essentially control the transient behaviour of the uncoupled model (Fig. 2.3a). Note that a comparison of Figures 2.3a and 2.3b does not provide clear indication of the relative position of the pressure dissipation curves. Therefore, it is difficult to define "a priori" the degree of conservatism associated with either one of the two approaches. Of course, it is expected that the fully coupled approach should provide answers close to actual field conditions.

The remaining part of the chapter covers these aspects in more detail. In order to do so, a comprehensive formulation for a fully hydro-mechanical coupling, valid for saturated and unsaturated conditions will be presented. Soil behaviour will be characterised by an elastoplastic critical state model for saturated and unsaturated conditions, formulated in the domain of net stresses (excess of total stress over air pressure) and suction. This type of model goes beyond previous known attempts to

analyse drawdown effects. Then a review will be made of some simple existing rules to estimate drawdown effects on slopes.

Despite the long list of developments and publications associated with drawdown analysis, almost no comparison between field measurements and calculations exist. For this reason, it was appropriate to perform an analysis of an interesting published field case and to compare model results and measurements.

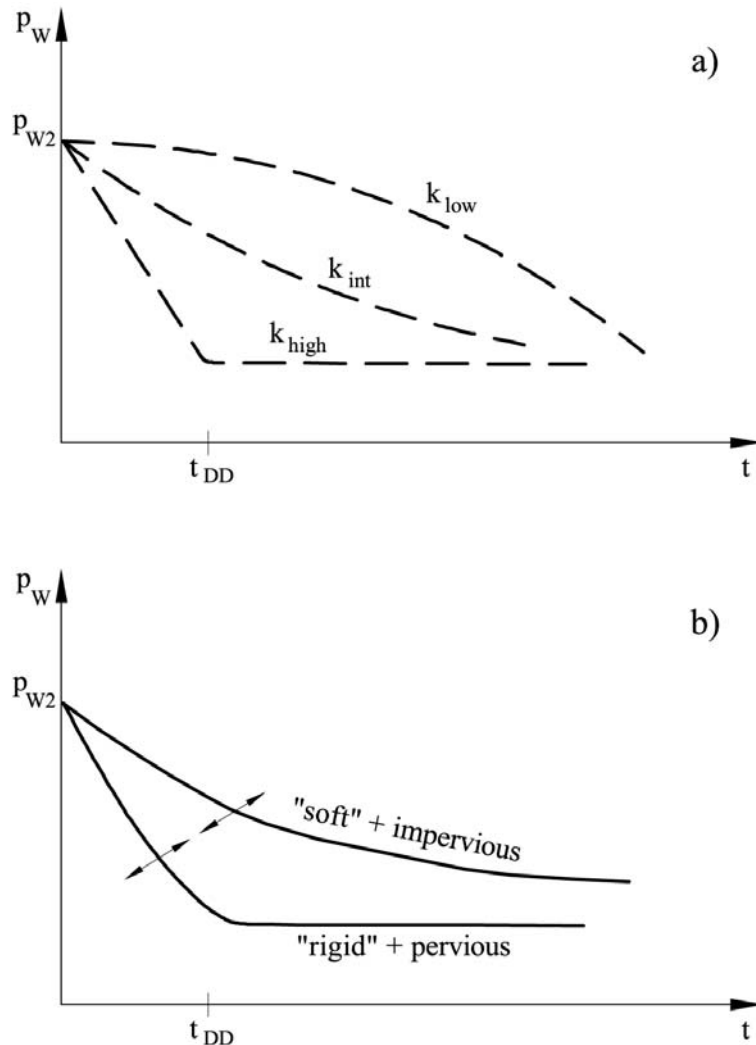


Figure 2.3 Change in pore water pressures in point P_2 for (a) uncoupled analysis; (b) coupled analysis.

2.2 HISTORICAL PERSPECTIVE

The literature describes two approaches to predict the pore water pressure regime after drawdown: the undrained analysis and the flow methods.

2.2.1 Undrained analysis

The aim is the determination of pore water pressures immediately after drawdown in impervious soils. Skempton (1954) derived first his well-known expression in terms of soil parameters A and B , and suggested that the following expression:

$$\frac{\Delta u}{\Delta \sigma_1} = \bar{B} = B \left[1 - (1 - A) \left(1 - \frac{\Delta \sigma_3}{\Delta \sigma_1} \right) \right] \quad (2.4)$$

could be useful in drawdown analysis. In his wording:

The “overall” coefficient \bar{B} is a useful parameter, especially in stability calculations involving rapid drawdown, and it can be measured directly in the laboratory for the relevant values of stress-changes in a particular problem.

Note that in Equation (2.4) if \bar{B} is known, the only unknown to determine the change in pore pressure is the change in major principal stresses. Bishop (1954) followed this recommendation and assumed that the major principal stress in any point within the slope is the vertical stress. He proposed also that the change in weight, statically computed in a column of soil and water above a reference point, would provide $\Delta \sigma_1$. Finally he suggested $\bar{B} = 1$ as an appropriate value in practice. Bishop’s approach has been criticized because it may lead to unacceptable large negative pore water pressures under the dam (Baker *et al.*, 1992).

Morgenstern (1962) accepted Bishop’s proposal based on a correspondence between Bishop’s method and pore pressures measured in two dams subjected to rapid drawdown (Alcova and Glen Shira dams). It is not clear that results of Glen Shira dam follow Bishop recommendation, however, and more will be said about this case later. Morgenstern published plots providing safety factors after drawdown in terms of drawdown ratio (H_D/H in Fig. 2.1) for different values of slope angle, effective cohesion and effective friction. The dam geometry was simple: a homogeneous triangular dam on an impervious base. Much later, Lane and Griffiths (2000) solve a similar case in terms of geometry, but failure conditions are calculated by means of a (c', ϕ) reduction procedure built into a finite element program, which uses a Mohr-Coulomb failure criterion. They do not solve any flow equation in their program and it is not clear how they could derive the pore water pressures induced by total stress unloading.

Lowe and Karafiath (1980) and Baker *et al.* (1992) performed undrained analyses to calculate the safety factors of slopes under rapid drawdown conditions. The analysis is applicable to relatively impervious soils and it does not require a determination of pore pressures after drawdown (which is required for a drained analysis of the type performed by Morgenstern). Instead, the idea is to find the distribution of undrained

strengths for the particular stress state just before drawdown. However, the emphasis in this paper lies on the determination of pore pressures after drawdown so that general effective stress analysis could be performed. No more reference to this type of undrained approach for safety factor calculation will be made here.

2.2.2 Flow methods

Casagrande (1940) developed a procedure to find the time required to reach a certain “proportion of drainage” of the upstream shell of dams having an impervious clay core. By assuming a straight saturation line, he was able to derive some analytical expressions. Later Reinius (1954) demonstrated the use of flow nets to solve slow drawdown problems. This contribution was based on earlier work published in Sweden. The key idea is that:

[...] the flow net at slow drawdown is determined by dividing the time in intervals and assuming the reservoir water level to be stationary and equal to the average value during the interval.

He also computed, based on the Swedish friction circle method of analysis, safety factors during drawdown and plotted them in terms of a coefficient: k/nv which integrates the soil permeability (k), the porosity (n) and the velocity of lowering the reservoir level, v . He also explained, in the following terms, the pore water pressure generation due to rapid drawdown:

When the reservoir is lowered rapidly, the total stresses decrease. If the soil does not contain air bubbles and the water content remains unchanged, the effective stresses in the soil also remains unchanged provided that the compressibility of the water is neglected. Hence the neutral stresses must decrease.

A similar statement may be found in Terzaghi and Peck (1948). Examples of flow net construction for drawdown conditions may be found in Cedergren (1967).

Finite difference approximations and, later, finite element techniques were used in the 60's and 70's to calculate the flow regime under drawdown conditions. The major problem was to predict the location of the phreatic surface during drawdown. When Dupuit-type of assumptions -horizontal flow- are made (Brahma and Harr, 1962; Stephenson 1978) the location of the zero-pressure surface comes automatically from the analysis. When solving the Laplace equation by finite elements (Desai, 1972, 1977), some remeshing procedures were devised. A more recent example of a determination of the free surface is given in Cividini and Gioda (1984).

In parallel, the liquid water flow equation for unsaturated porous media was being solved by means of finite difference or finite element approximations (Rubin, 1968; Richards and Chan, 1969; Freeze, 1971; Cooley, 1971; Neumann, 1973; Akai *et al.*, 1979; Hromadka and Guymon, 1980, among others). These developments made it

obsolete the involved numerical techniques required to approximate the free surface through the saturated flow equation. Berilgen (2007) published a recent contribution to the drawdown problem. The author uses two commercial programs for transient/flow and deformation analysis respectively. He reports a sensitivity analysis involving simple slope geometry, two saturated values of permeability, two drawdown rates and five drawdown ratios (H_D/H in Fig. 2.2a). Safety factors are calculated by a (c' , ϕ') reduction method built into the mechanical finite element program. The author emphasizes that the undrained rapid drawdown case and the fully drained case (high permeability) are rough approximations for other intermediate situations likely to be found in practice.

It turns out that the position of the zero pressure line depends also on unsaturated flow properties, such as the water retention curve and the relative permeability, which are outside the formulation for saturated conditions. However, few applications of these developments have been described in connection with the drawdown problem. Pauls *et al.* (1999) reports a case history. A stress-uncoupled finite element program was used to analyse the pore pressure evolution in a river bank as a result of a flooding situation. Consistently, predicted pore pressures remained well above the measured piezometric data. One possible explanation, not given in the original paper, is the uncoupled nature of the computational code used. In fact, no riverbank failures were observed in this case despite the calculated safety factors, lower than one.

Difficulties for the development of consistent, fully coupled hydromechanical codes for saturated/unsaturated soils, hampered by the issue of the effective stress principle and the development of consistent constitutive equations for unsaturated conditions, have prevented a more advanced and realistic analysis of the classical drawdown problem. This paper relies on one of the existing complete formulations in this regard. The solved cases use the finite element program CODE_BRIGTH (DIT-UPC, 2002) developed at the Department of Geotechnical Engineering and Geosciences of UPC. The code solves in a fully coupled manner thermal, mechanical and flow (air and water) problems in porous media. It may handle a variety of mechanical constitutive laws but the results presented here correspond either to elastic conditions or to elastoplastic constitutive models (BBM; Alonso *et al.*, 1990; Rockfill model; Oldecop and Alonso, 2001). The formulation used in CODE_BRIGTH is briefly described in the Appendix.

2.3 DRAWDOWN IN A SIMPLE SLOPE

Consider the case sketched in Figure 2.1. A fully submerged simple slope will experience a drawdown condition when the water level acting against the slope surface is lowered. The actual geometry of the slope analyzed is given in Figure 2.4. The figure

indicates the position of three singular points used in the discussion: A point at midslope (P_A), a point at the slope toe (P_B) and a point away from the slope (P_C) which is representative of “bottom of the sea” conditions. Three auxiliary vertical profiles will assist in the analysis of results. Critical failures surfaces obtained in drawdown stability analysis are typically close to points P_A and P_B and this provides a motivation to analyze the response of those locations. Two cases are considered, either an instantaneous drawdown or a drawdown at a reasonable speed in dam engineering applications: 0.5 m/day.

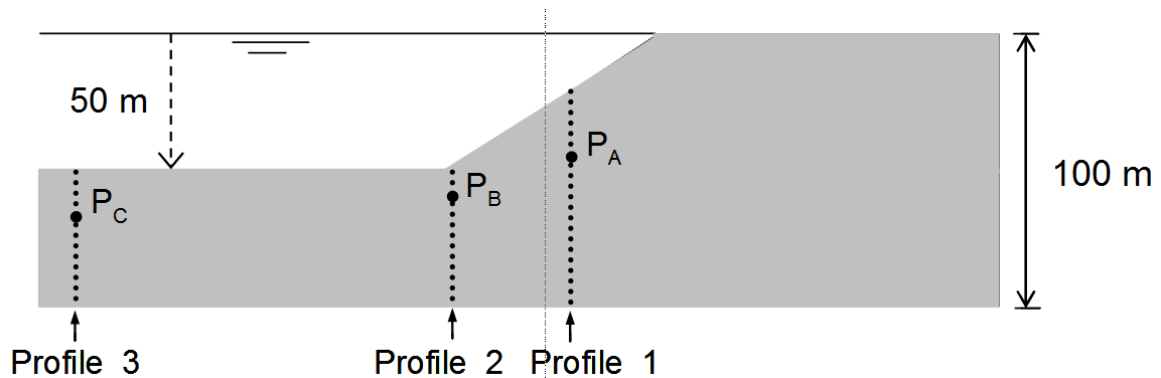


Figure 2.4 Geometry of the slope. Labels indicate the position of three singular points mentioned in the discussion.

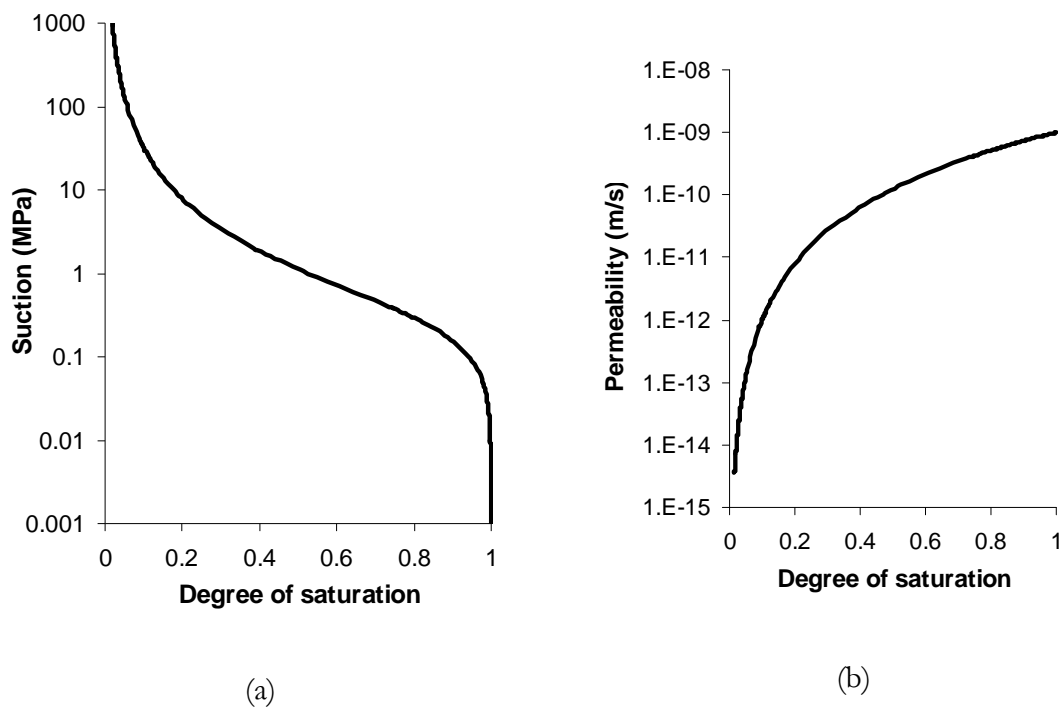


Figure 2.5 Retention curve and relative permeability function for the analysis of a simple slope.

An elastic constitutive law will characterize the soil. Therefore, stability conditions are not an issue here. Concerning the hydraulic description, Figure 2.5 indicates the water retention curve and the relative permeability law adopted in calculations. The retention curve (Fig. 2.5) has been defined by means of a Van Genuchten model and the relative permeability varies with the degree of saturation following a cubic law ($k_{rel} = k_{sat} S_r^3$). A constant saturated permeability $k_{sat} = 10^{-10}$ m/s was also used in all calculations. This is a low value, typical of an impervious material in engineering applications.

2.3.1 Instantaneous drawdown

The initial water level in the slope is horizontal and it is located at the maximum level in the reservoir. Therefore, the initial pore pressures in the soil follow a hydrostatic pattern (Fig. 2.6). Drawdown is then simulated by removing instantaneously all the water in the reservoir. The water level ($p_w = 0$) is maintained at the level of the toe of the slope. The inclined slope surface maintains a “seepage condition”: water may flow out whenever $p_w > 0$ in the soil but it remains impervious otherwise. All the remaining boundary surfaces remain impervious.

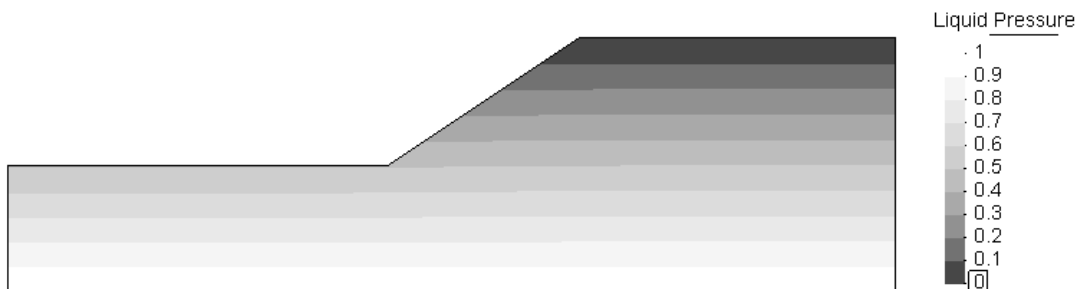


Figure 2.6 Initial pore water pressure distribution before drawdown

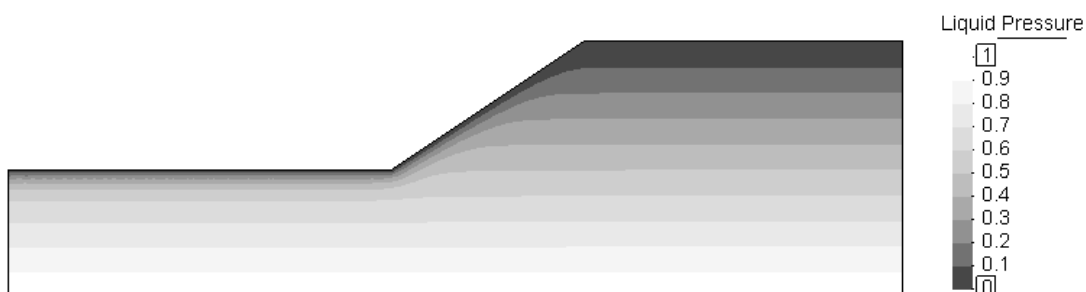


Figure 2.7 Pore water pressure distribution after immediate drawdown in an uncoupled analysis.

Changes in pore water pressure developed immediately after the drawdown will be exclusively due to total stress changes. Therefore, if an uncoupled analysis is run, the pore water pressures inside the slope will maintain their initial values immediately after drawdown. This is shown in Figure 2.7. The only difference between Figures 2.6 and 2.7 lies in the boundaries where the new boundary conditions after drawdown were imposed.

In a coupled analysis, the magnitude of pore pressure changes depends on the stress – strain behaviour of the soil skeleton. In the analysis presented here several elastic soil moduli are considered ($E = 10000$ MPa, 1000 MPa and 100 MPa). The first case corresponds to a stiff material (a soft clayey rock, for instance). The second case is an upper limit for a very rigid compacted and low porosity material. The third case is a reasonable assumption for a well compacted well graded soil.

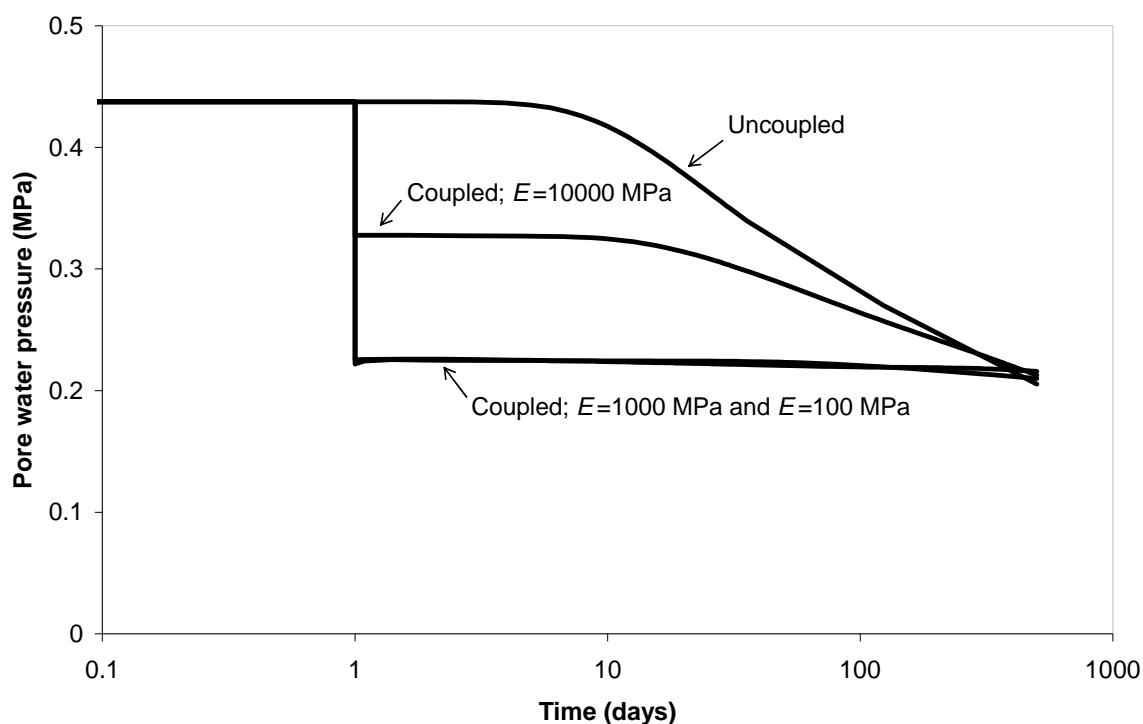


Figure 2.8 Pore water pressure evolution after instantaneous drawdown in the point P_A (see Fig. 2.4).

Figures 2.8 to 2.10 show the calculated time evolution of pore pressure after the instantaneous drawdown in the three reference points (Fig. 2.4). At day 1 in the plots, instantaneous drawdown is simulated. In the case of uncoupled analysis, no immediate effect of the drawdown is obtained, as expected. In the coupled analysis, the instantaneous pore pressure drop depends on the compressibility of the soil skeleton.

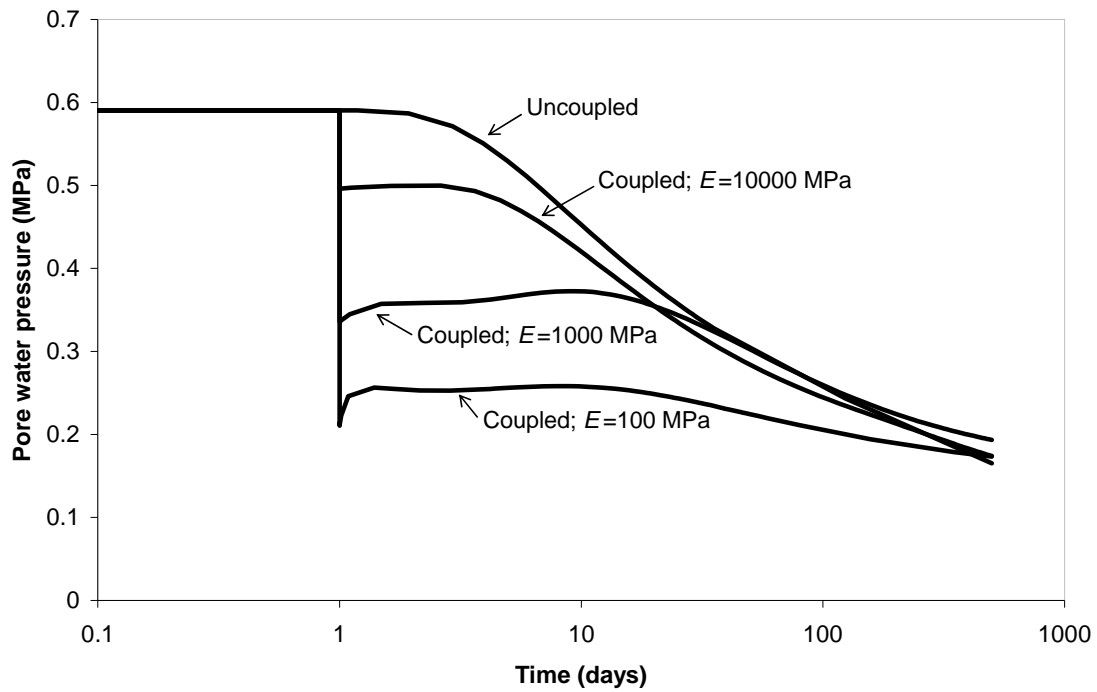


Figure 2.9 Pore water pressure evolution after instantaneous drawdown in the point P_B (see Fig. 2.4).

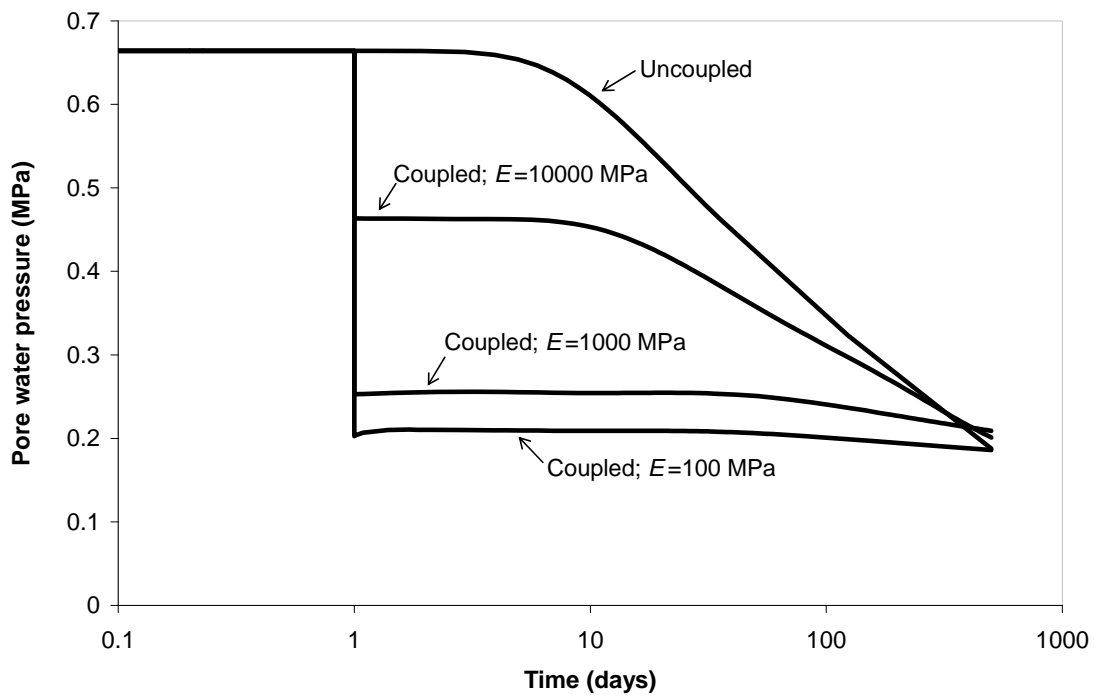


Figure 2.10 Pore water pressure evolution after instantaneous drawdown in the point P_C (see Fig. 2.4).

The stiffer the soil, the more limited the stress-induced change in pore water pressure. Immediately after drawdown a dissipation process begins. The rate of pore water pressure dissipation is controlled by the initial conditions after drawdown but also by the permeability and stiffness of the soil. Note that in an uncoupled analysis the calculated dissipation rates are higher, because the implicit assumption is an infinitely rigid soil. Eventually, all cases result in the same long term solution.

Note that the coupled analysis leads systematically to lower water pressures than the uncoupled (pure flow) approximation during the first stages of the dissipation. This is due to the effect of the initial state after drawdown, controlled by the change in stress. However, since pressures dissipate faster the stiffer the soil, this situation changes after some time and the water pressure records may cross at some particular time, which depends on the position of the considered point in the slope. Note also that full steady state conditions were not reached at the end of the simulation period.

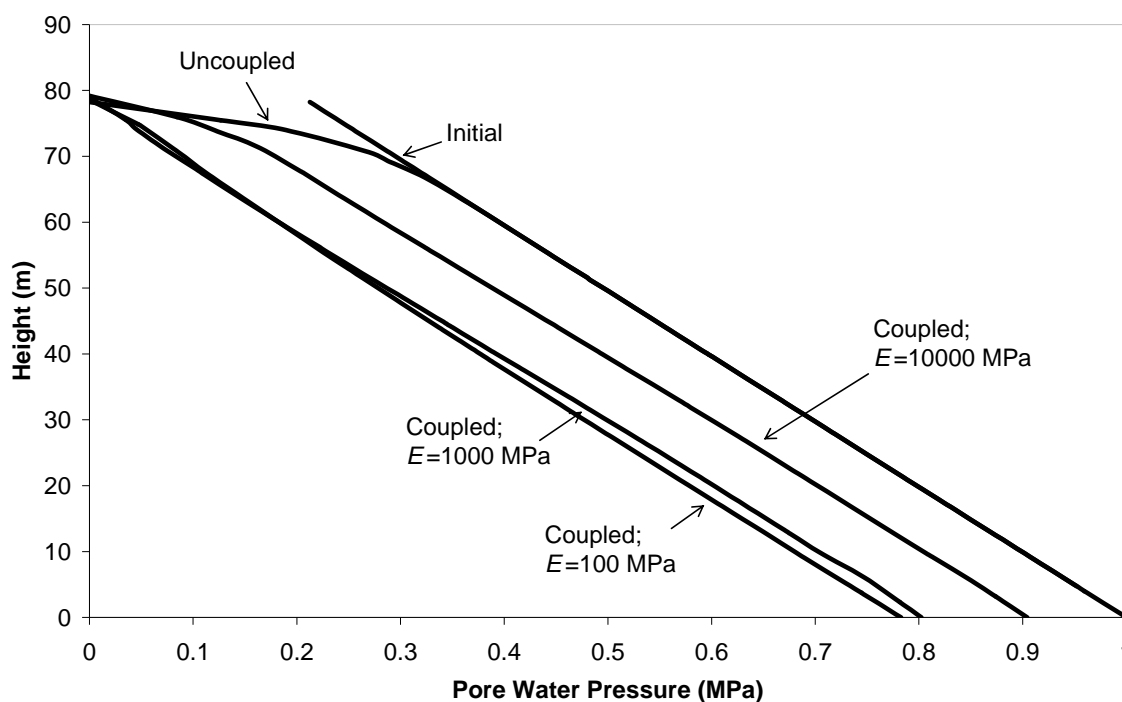


Figure 2.11 Pore water pressure immediately after instantaneous drawdown along Profile 1 (see Fig. 2.4).

Figures 2.11 to 2.13 show the pore pressure distribution along the three vertical profiles indicated in the Figure 2.4 immediately after the instantaneous drawdown. The drop of pore pressure due to total stress reduction is practically constant with height, especially in Profiles 1 and 2, where stress conditions are more regular. The toe of the slope has a more complex stress distribution and this is reflected in a more irregular

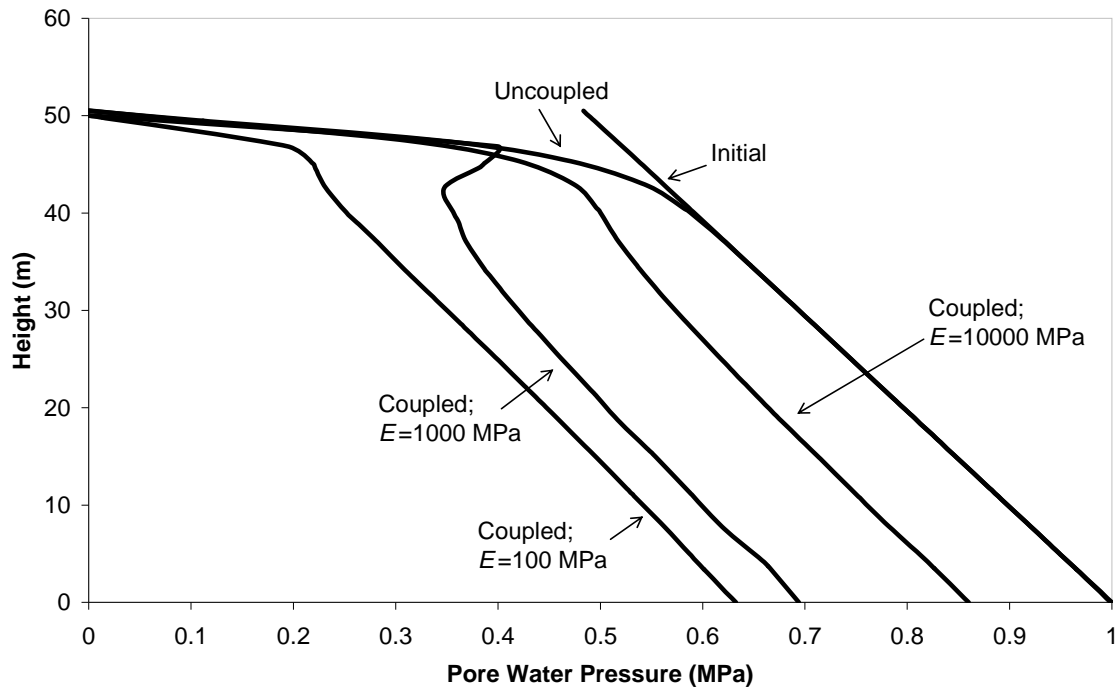


Figure 2.12 Pore water pressure immediately after instantaneous drawdown along Profile 2 (see Fig. 2.4).

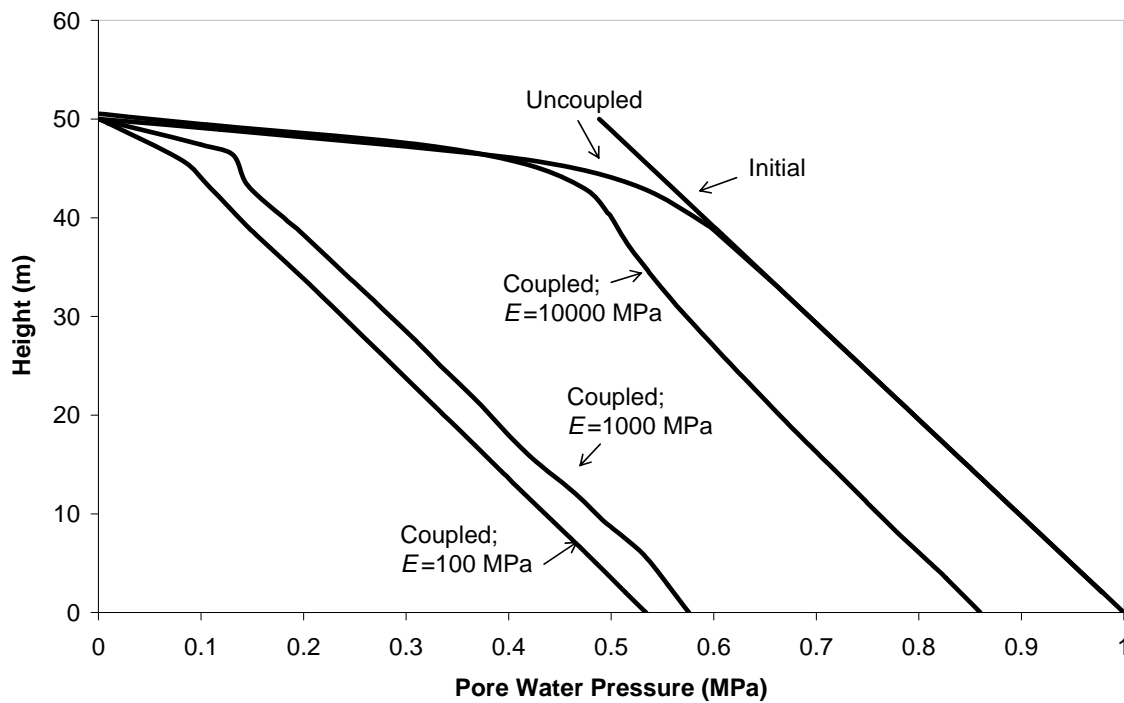


Figure 2.13 Pore water pressure immediately after instantaneous drawdown along Profile 2 (see Fig. 2.4).

distribution of pore pressures after drawdown, especially in points close to the slope boundary.

The trends in the three profiles are, however, similar. Note that for a compacted soil, typical in earthdam materials ($E = 100 \text{ MPa}$), the uncoupled, pure flow analysis provides an extremely unrealistic answer.

2.3.2 Progressive drawdown ($v = 0.5 \text{ m/day}$)

Conditions of the analysis remain unchanged except for the drawdown rate. This is, however, an important parameter and results depend markedly of this rate. Consider first the case of the “bottom of the sea” conditions (Fig. 2.14). All the coupled analyses lead essentially to the same response. This is because variations in the instantaneous response are erased by the simultaneous dissipation of pressures. For the stiffer materials considered ($E = 1000, 10000 \text{ MPa}$), water pressures remain slightly above the most common cases in soils. However, the pure flow analysis is far from the correct answer. .

Similar results were obtained for the three reference points. Only the case of the mid slope point is plotted in Figure 2.15.

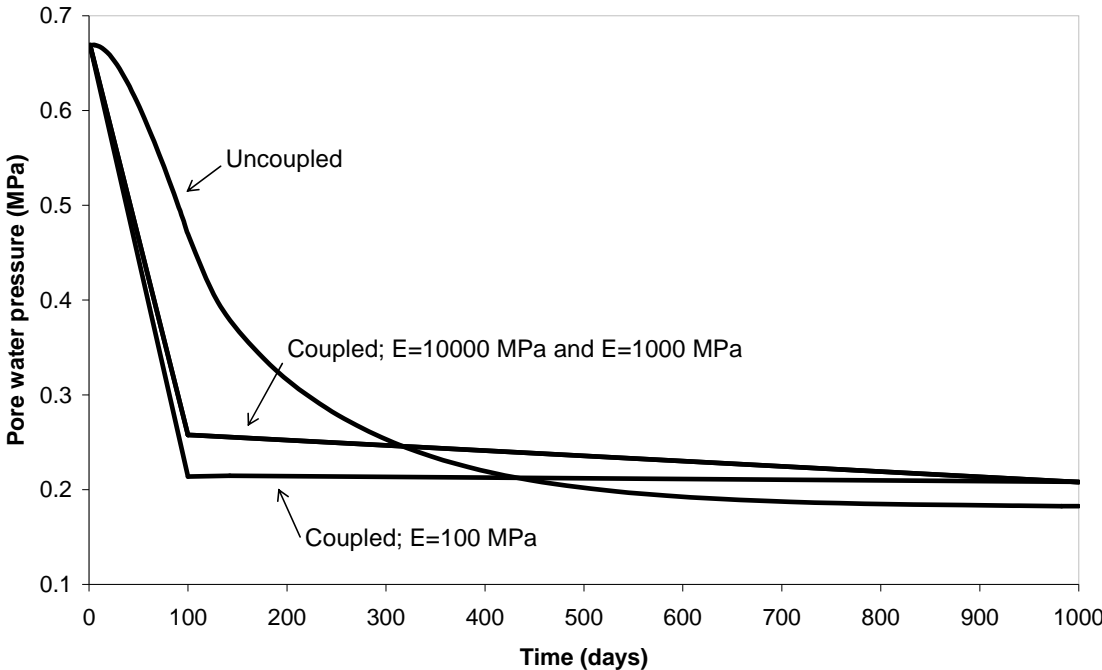


Figure 2.14 Pore water pressure evolution after progressive drawdown in the point P_C (see Fig. 2.4).

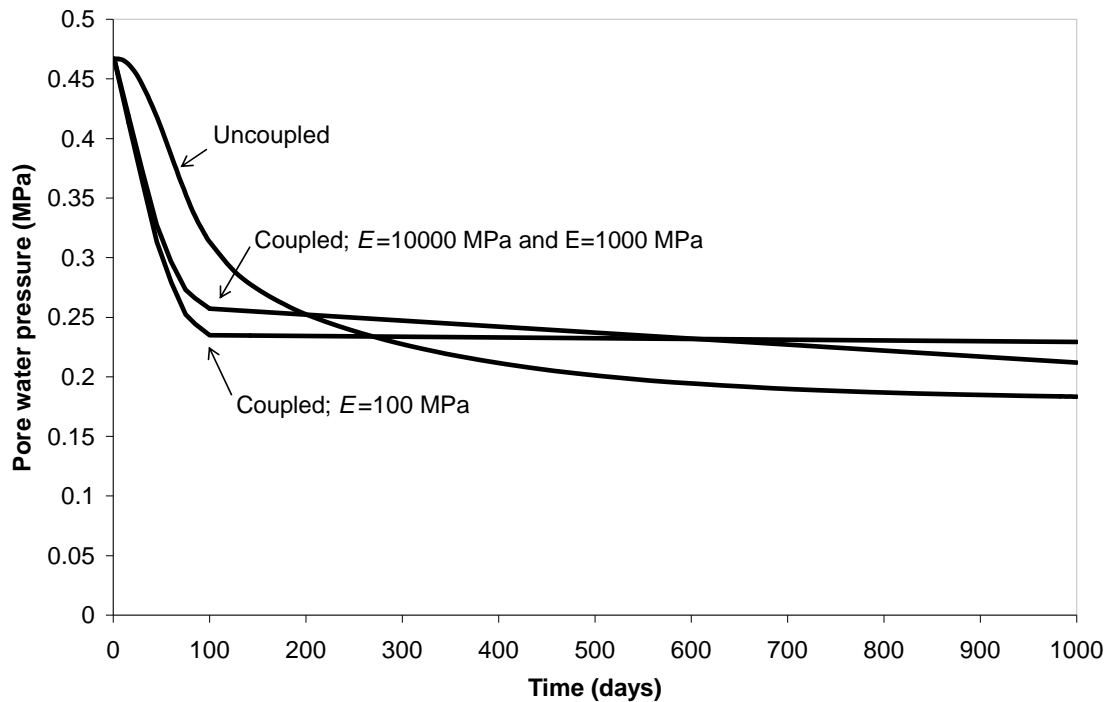


Figure 2.15 Pore water pressure evolution after progressive drawdown in the point P_A (see Fig. 2.4).

It may be argued that the pure flow analysis is a conservative approach if viewed in terms of slope safety against failure. However, this is a result which depends on the particular case considered and cannot be generalized, as shown below.

The set of calculated results in Figures 2.14 and 2.15 correspond to the “impervious” case qualitatively shown in Figure 2.2. If the soil permeability is increased, the differences between coupled and uncoupled analysis reduce and eventually they vanish because the high dissipation rates mask the stress-induced response of pore pressure change. However, it is by no means easy to decide “a priori” where is the threshold permeability, which justifies the use of an uncoupled analysis. The solved cases, presented in the remaining of the paper, provide additional information on this issue.

2.4 SOME DESIGN RULES REVISITED

Let us consider now the case of relatively pervious materials. Mechanical coupling in these cases is not relevant for the reasons mentioned before and the common recommendation is to base the analysis on the determination of flow nets by means of numerical, analytical or graphical procedures. However, the drawdown implies that an initially saturated soil becomes progressively unsaturated. The distribution of pore

water pressures in the slope depends now on some key properties of the unsaturated soil, and, in particular, on the water retention characteristics.

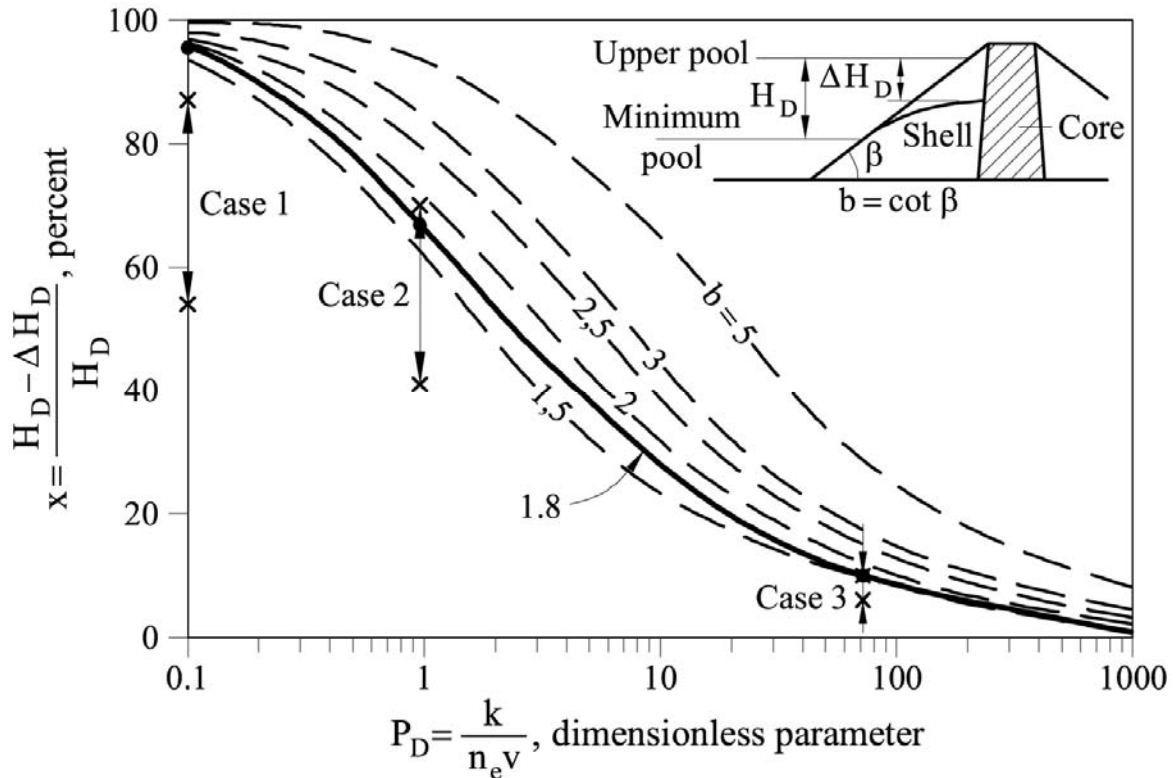


Figure 2.16 Chart for determining height of saturation at core face. Free draining upstream shell subject to drawdown (US Corps of Engineers, 1970).

Some approximate procedures have been proposed to estimate the pore pressures in a slope during drawdown. Figure 2.16 illustrates one case, in connection with the stability analysis of earthdams (US Corps of Engineers, 1970). The idea of the chart is to facilitate a procedure to locate the position of the free surface after drawdown. This is achieved by providing the lowering of the seepage line at the interface between the impervious dam core and the upstream shell (ΔH_D).

This distance is a function of the total drawdown drop (H_D), the soil permeability, k , the velocity of drawdown, v , the effective – or “drained”- porosity, n_e , and the slope geometry, given by the slope angle, β .

With the purpose of showing the effect of correctly modelling the saturated-unsaturated transition, a few cases directly inspired in the geometry and conditions considered in this design plot have been calculated. The cases analysed correspond to the three points marked in Figure 2.16 for the slope angle $b = \cot(\beta) = 1.8$. A set of soil properties, matching the conditions of these three points are given in Table 2.1.

Table 2.1 Soil properties for the analysis of the drawdown of an upstream shell

Parameter	Symbol	Value			Unit
		Case 1	Case 2	Case 3	
Young Moduli	E	100	100	100	MPa
Saturated permeability	κ_{sat}	$5 \cdot 10^{-8}$	10^{-6}	10^{-4}	m/s
Retention curve parameters (Van Genuchten)	P_0	2 – 0.05	0.2 – 0.007	0.05 – 0.005	MPa
	λ	0.2	0.2	0.2	-
	$S_{r\max}$	1	1	1	-
	$S_{r\min}$	0	0	0	-
Effective porosity	n_e	0.09	0.18	0.24	-

Drawdown velocity was fixed at 0.5 m/day. A common soil porosity $n = 0.2$ was also selected. Three saturated soil values of permeability, $k_{sat} = 5 \cdot 10^{-8}$ m/s, $k_{sat} = 10^{-6}$ m/s and $k_{sat} = 10^{-4}$ m/s correspond to a relatively impervious shell (typically a mixture of gravel, sand, silt and some clay), a partially draining material (typically a compacted well graded mixture) and a free draining material (typically a gravelly sand). The effective porosity for these three cases is indicated in Table 1. The n_e values selected reflect the type of soil associated with the three cases analyzed. The additional soil property, not considered in Figure 2.16, is the water retention of the soil. The effect of a reasonable variation of this property was investigated. To do so, a Van Genuchten representation of the water retention curve is selected. By changing parameter P_0 , associated with the air entry value, different soil retention capabilities are simulated. The second parameter of the retention curve, λ , was kept constant at the value given in the table. All the calculations have been performed in a coupled mode, using an elastic soil modulus $E = 100$ MPa.

Figures 2.17 to 2.19 indicate the calculated distribution of water pressures, below the saturation line, for the extreme cases analyzed. These plots provide the possibility of calculating ΔH_D and the range of calculated values has been indicated in the caption of each figure. These values are also plotted on Figure 2.16.

At first sight, the results in Figures 2.17-2.19 may look contrary to expectations, since the height of the phreatic surface decreases when the air entry value increases. This is a result valid for the particular permeability selected when comparing the effect of alternative water retention curves. Therefore, it makes sense only when the range of water retention curves analyzed is limited since all of them should provide essentially the same saturated permeability. The calculated result is better explained if one considers also the distribution of degree of saturation within the slope. In Figure 2.20,

the degree of saturation along a vertical profile in the middle of the slope is represented for the two extreme cases having a common saturated permeability $k_{sat} = 10^{-6}$ m/s (Case 2).

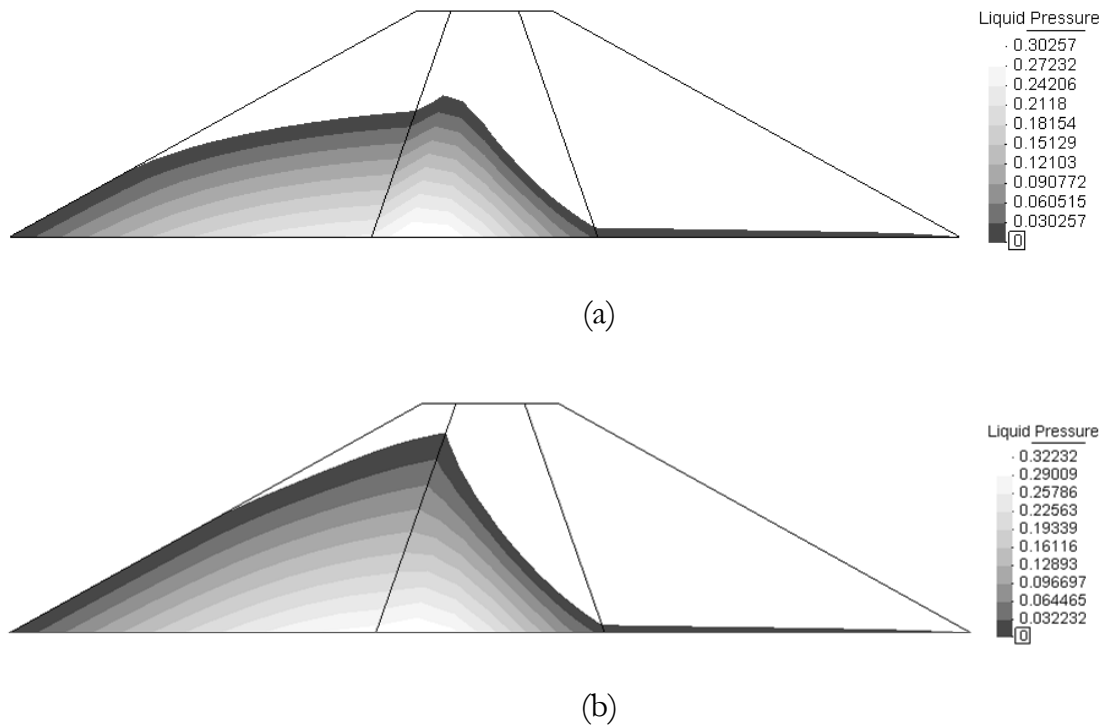


Figure 2.17 Pore pressure distribution after total drawdown for Case 1: a) $P_0 = 2$ MPa, $\Delta H_D = 22$ m; b) $P_0 = 0.05$ MPa, $\Delta H_D = 6$ m.

For a given soil permeability, the amount of water to be drained during drawdown is similar for both cases. Above the phreatic line ($s > 0$), if P_0 is low, even for low suction (close to the value of P_0) the degree of saturation decreases significantly (this is determined by the retention curve, Fig. 2.21) and the amount of drained water from the unsaturated zone is higher. In the other case (higher P_0), the zone above the phreatic line is almost saturated (Fig. 2.20) although pore water pressures remain negative. Then the phreatic line may reach a lower elevation for the same amount of drained water. Therefore, if P_0 decreases, the phreatic line ($p_w = s = 0$) remains at higher elevation (the saturated zone of the slope is larger).

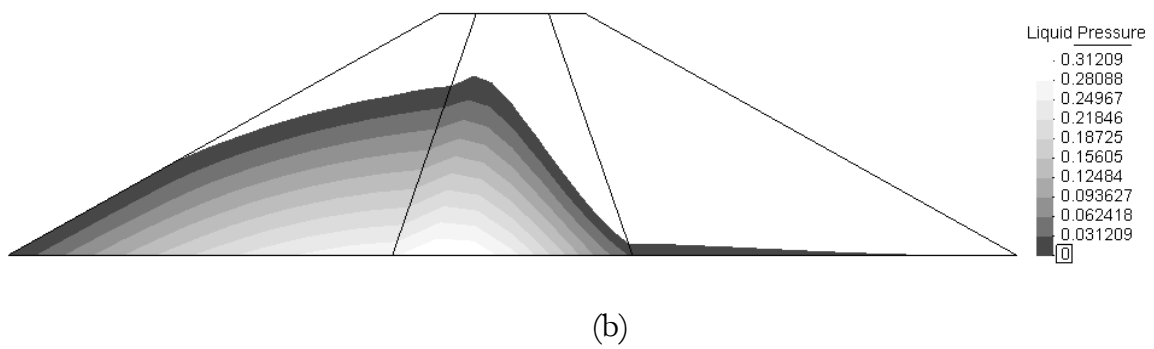
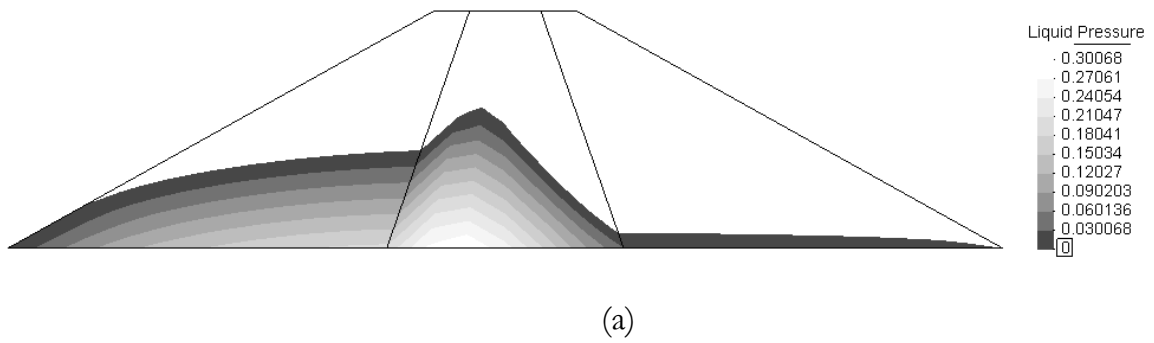


Figure 2.18 Pore pressure distribution after total drawdown for Case 2. (a) $P_0 = 0.2$ MPa, $\Delta H_D = 29$ m; (b) $P_0 = 0.007$ MPa, $\Delta H_D = 15$ m

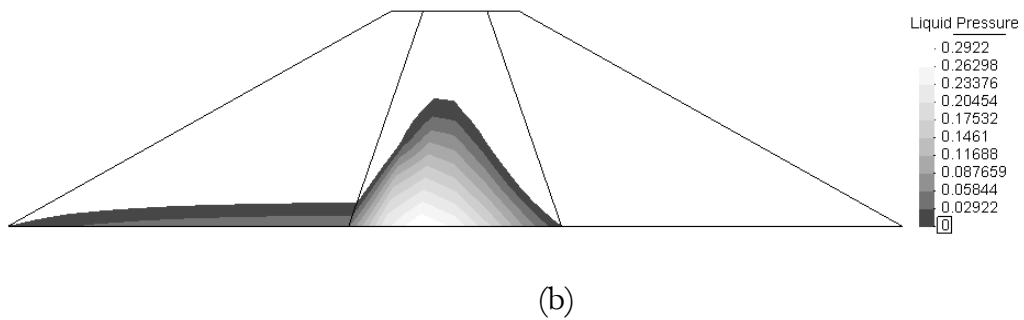
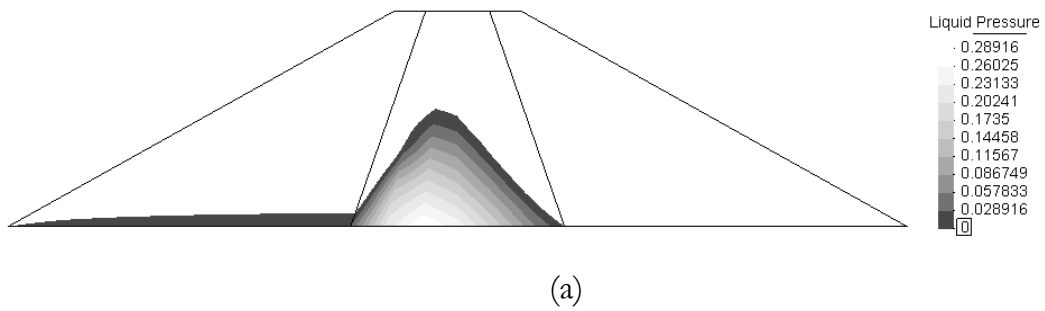


Figure 2.19 Pore pressure distribution after total drawdown for Case 2. (a) $P_0 = 0.05$ MPa, $\Delta H_D = 47$ m; (b) $P_0 = 0.005$ MPa, $\Delta H_D = 45$ m.

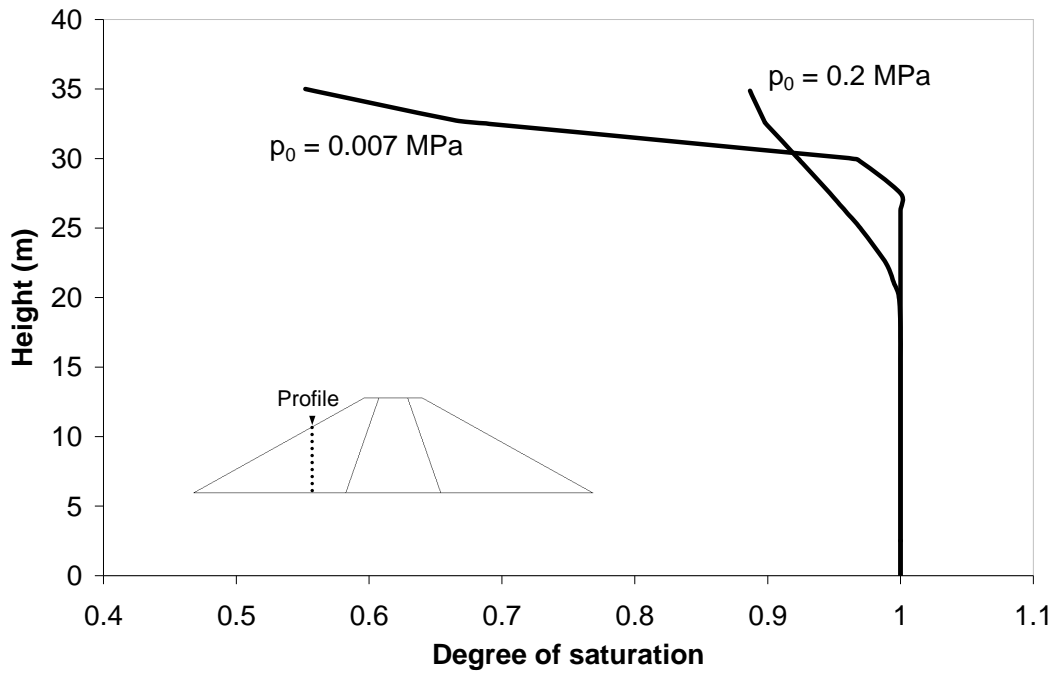


Figure 2.20 Degree of saturation after total drawdown along the profile indicated in the figure for the Case 2 ($k_{sat} = 10^{-6}$ m/s).

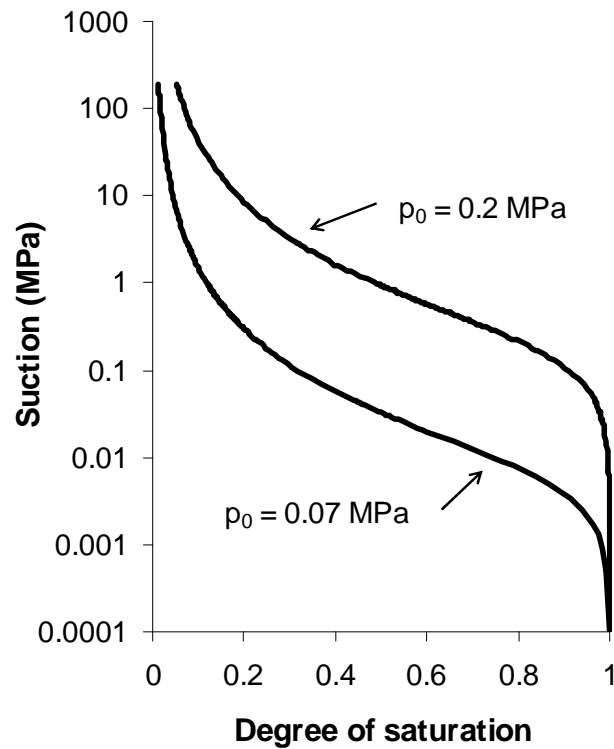


Figure 2.21 Retention curves considered in Case 2.

If only positive pore water pressures are considered in stability calculations, higher P_0 may lead to higher safety factors against slope failure than the case of a lower air entry value. For the particular case of $k_{sat} = 10^{-6}$ m/s again, the safety factor calculated by means of a Morgenstern-Price method against an imposed failure surface through the middle of the slope has been calculated. A Mohr-Coulomb failure criterion (strength parameters $\phi' = 28^\circ$ and $c' = 0$) has been considered. For the case of $P_0 = 0.2$ MPa, a safety factor equal to 1.25 is obtained. If P_0 is reduced to 0.007 MPa, the calculated safety factor is 1.48. However, this conclusion may change if a more comprehensive description of soil strength, valid for saturated and unsaturated conditions is introduced in the analysis, a subject that is outside the purpose of this Chapter.

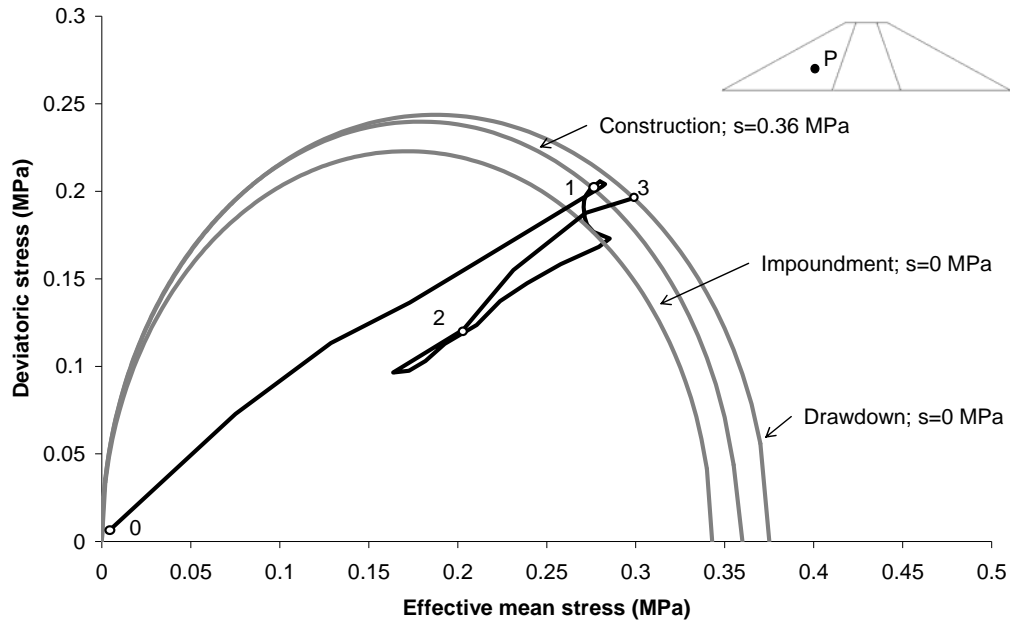
The results obtained have been included in Figure 2.16. The largest discrepancies with the Manual recommendations are obtained for low values of the index P_D (more impervious materials, always with respect to drawdown velocity). Recommendations are too conservative in these cases. The fact to be stressed is that the set of parameters included in the design procedure implied in Figure 2.16 is incomplete, even if couplings effects are disregarded. Only in the case of very pervious materials, drawdown predictions of the chart reproduced in Figure 2.16 seem to be accurate.

2.5 COUPLED ELASTO-PLASTIC ANALYSIS OF DRAWDOWN

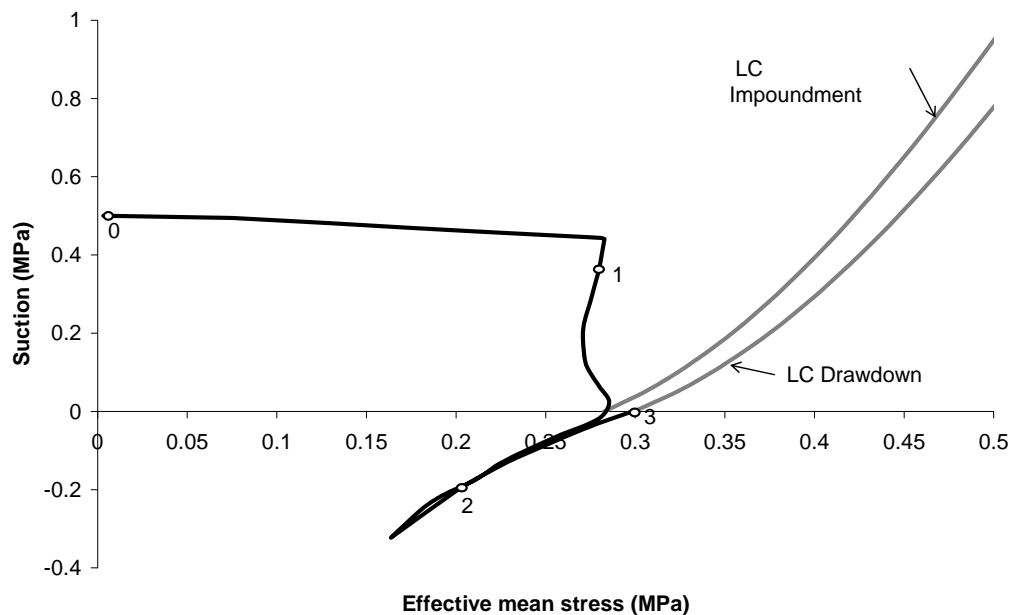
All the coupled analyses reported so far describe the soil by means of an elastic constitutive law. In principle, drawdown may be viewed as an unloading scenario. However, the particular geometry of the problem and the no uniformity of applied boundary stresses may result in significant shearing. In addition, the progressive reduction in pore water pressures implies a parallel increase in confining stresses. If yielding conditions are reached, plastic deformations will take place and additional local sources of water will develop. They will modify the pore pressure response of the slope.

In order to show some aspects of the elastoplastic response of the soil during drawdown, the dam geometry analyzed in the previous section was considered again. Dam materials (core and shell) are now simulated by means of elastoplastic models. To facilitate the selection of parameters and to reproduce, as much as possible, a real situation, the mathematical description of the two materials involved were borrowed from previous work by the author on Beliche dam (Pinyol, 2004; Alonso *et al.*, 2005). The shell material is equivalent to the “inner rockfill” of Beliche whereas the clay core of the example analyzed here reproduces also Beliche’s core. The shell will be described by a “rockfill model” presented in Oldecop and Alonso (2001) and Alonso *et al.* (2005). The clay core is described by means of the BBM (Alonso *et al.*, 1990;

Appendix). Code_Bright handles both models. Material parameters were derived from the backanalysis of large scale laboratory tests and are given in Tables 2.2 and 2.3.



(a)



(b)

Figure 2.22 Stress-suction path followed by point P (indicated in the inset) during: 0-1 Construction; 1-2 Impoundment; and 2-2 Drawdown. Yield surfaces reached at the end of each stage are plotted. (a) Effective mean stress – deviatoric stress path and (b) Effective mean stress – suction path.

The analysis performed reproduces construction, impoundment and drawdown stages. Figure 2.22 shows the stress-suction path followed by a representative point located inside of the upstream rockfill shoulder. For the simulation of dam construction the weight of the whole dam is applied, in a single stage, in a ramp manner. A low initial isotropic yield stress, p_o^* , is assumed for the compacted materials. Therefore, the weight load applied induces immediately the yielding of the dam. Plastic deformations will accumulate during the construction stage (step 0-1 in Fig. 2.22). During construction, suction decreases due to the reduction of porosity (from $s = 0.5$ MPa, initial value, to the calculated value, $s = 0.26$ MPa).

Table 2.2 Mechanical parameters for rockfill.

Definition of parameter	Symbol	Units	Beliche dam Inner shell
I. ELASTIC BEHAVIOUR			
Elastic modulus	E	MPa	150
Poisson's ratio	ν	-	0.2
II. PLASTIC BEHAVIOUR			
Plastic virgin instantaneous compressibility	$\lambda^i - \kappa$	-	0.025
Virgin clastic compressibility for saturated conditions	λ_0^d	-	0.028
Parameter to describe the rate of change of clastic compressibility with total suction	α_s	-	0.010
Slope of critical state strength envelope for dry conditions	M_{dry}	-	1.75
Slope of critical state strength envelope for saturated conditions	M_{sat}	-	1.20
Parameter that controls the increase in cohesion with suction	k_s	-	0
Threshold yield mean stress for the onset of clastic phenomena	p_y	MPa	0.01
Parameter that defines the non-associativeness of plastic potential	α	-	0.2
III. INITIAL STATE FOR DAM MODEL			
Initial suction	s_0	MPa	20
Initial mean yield stress	p_o^*	MPa	0.02

Table 2.3 Parameters for the mechanical models used for the clay core

Definition of parameter	Symbol	Units	Beliche dam
			Clay core
I. ELASTIC BEHAVIOUR			
Elastic modulus	E	MPa	100
Poisson's ratio	ν	-	0.4
II. PLASTIC BEHAVIOUR			
Virgin compressibility for saturated conditions	$(\lambda(0) - \kappa)$	-	0.020
Parameter that establishes the minimum value of the compressibility coefficient for high values of suction	r	-	0.7
Parameter that controls the rate of increase in stiffness with suction	β	MPa ⁻¹	1.2
Reference stress	p^c	MPa	0.02
Slope of critical state strength line	M	-	0.88
Parameter that controls the increase in cohesion with suction	k_s	-	0.1
Parameter that defines the non-associativeness of plastic potential	α	-	0.2
III. INITIAL STATE FOR DAM MODEL			
Initial suction	s_0	MPa	0.5
Initial yield mean net stress	p_0^*	MPa	0.02

During the impoundment step 1-2, total stresses and pore pressures change. Because of saturation a compressive strain (collapse) develops in the rockfill and additional irreversible volumetric deformation are accumulated. The final size of the yield envelope is determined by the isotropic yield stress reached at zero suction. Path 1-2 essentially implies an elastic unloading in the deviatoric plane. Mean and deviatoric stresses reduce simultaneously, following a path parallel to the initial construction path. Water pressures change from negative values (soil under suction) to positive ones. Note also that the strength parameter (M) is not constant during this path. In fact strength envelopes in the rockfill model depend on the current suction and they are defined in terms of two extreme values (M_{dry} and M_{wet}) given in Table 2.2.

During drawdown (at a velocity of 0.5 m/s) point P experiences a sudden reversal in its stress path (Fig. 2.22). Both mean and the deviatoric stresses increase again simultaneously and follow a path parallel to the initial construction path (Fig. 2.22). The shape of this path depends on the permeability and the compressibility of the material. In the case represented in Figure 2.22, when the end of the drawdown is close (Point 2), the current yield surface is reached and new plastic deformations take place. The plastic reduction of the porosity will release some water, which will be dissipated at the expense of an increase in pore water pressure. In the case analyzed this is a minor effect because yielding at the final drawdown stage is very limited. The next discussion on a case record (Shira dam) will provide additional insight into these phenomena.

2.6 GLEN SHIRA DAM CASE HISTORY

Glen Shira Lower Dam is a part of a pumping storage scheme in Northern Scotland. The reservoir was expected to experience fast drawdown rates and this situation prompted the field experience reported by Paton and Semple (1961). Probably this is one of the best-documented case histories concerning the effect of drawdown on earthdams. The maximum cross section of the dam is presented in Figure 2.22. The 16 m high embankment has a centred thin reinforced concrete wall. The homogeneous embankment is made of compacted moraine soil. A rockfill shell covers the upstream slope of the compacted moraine to increase stability. Published grain size distributions of the moraine soil indicate a well-graded material having a maximum size of 15 cm. Plasticity is not reported for this soil. It was apparently compacted wet of optimum at an average water content $w = 15\%$. The attained average dry density was 19.8 kN/m^3 , which is a relatively high value for a granular mixture. A friction angle $\phi' = 26^\circ$ is reported.

For the rockfill a porosity of $n = 0.4$, a dry density of 16.7 kN/m^3 and a friction angle $\phi' = 45^\circ$ are mentioned in the paper.

Five porous stone piezometer disks, previously calibrated against mercury columns, were located in the places shown in Figure 2.22. They were connected to Bourdon gauges through thin polyethylene tubing. The authors conclude in their paper that the possibility of instrumental error are “*of minor order and can be neglected*”.

No significant pore water pressures were recorded during construction. Positive pore pressures were measured only after reservoir filling.

A total water level drawdown of 9.1 meters in four days was applied to Glen Shira dam. This maximum drawdown was imposed in four stages of rapid (7.2 m/day) water lowering followed by short periods of constant water level. Details of changing water

level in the reservoir and the measured pore water pressures are indicated in the set of figures prepared to analyze this case.

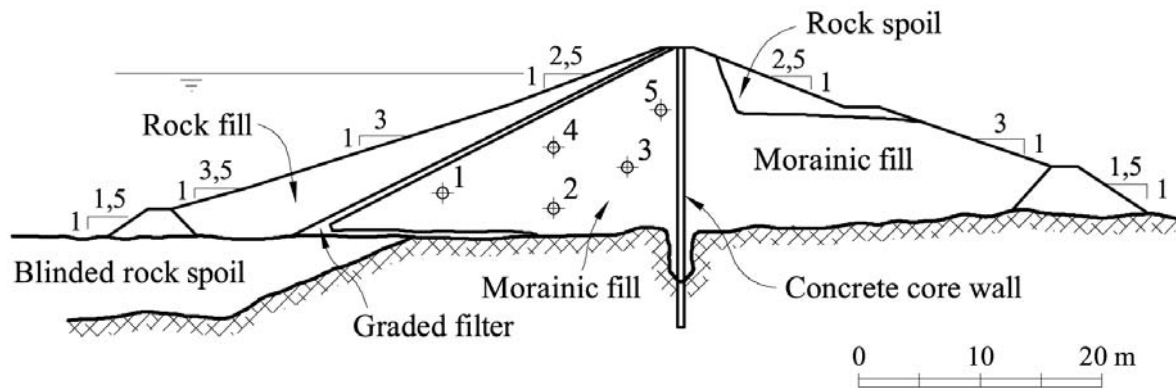


Figure 2.23 Maximum cross section of Shira Dam. The position of Piezometers 1 to 5 is indicated (Patton and Semple, 1961).

Measured pore pressures have been compared with calculated values in Figures 2.24 to 2.28. The following hypotheses, ordered in the sense of increasing complexity, were made to perform calculations:

- 1) A pure flow analysis for saturated/unsaturated conditions that follows the changing hydraulic boundary conditions actually applied to the upstream slope. Table 2.5 provides the hydraulic parameters used in calculations. These parameters are common to the remaining analyses described below.
- 2) An instantaneous drawdown of the maximum intensity, followed by pore water pressure dissipation. This is a coupled analysis which attempts to reproduce the classical hypothesis behind the undrained methods, briefly described in the introduction of the Chapter. The procedure does not correspond strictly to Bishop's method because in the analyses reported here the correct change in total stresses is actually applied. The soil was simulated as an elastic material. (Properties are given below, in Table 2.5).
- 3) A coupled analysis (saturated/unsaturated), following the applied upstream changes in hydrostatic pore pressures. The soil is considered elastic (properties are given in Table 2.4).
- 4) A coupled analysis (saturated/unsaturated) following the applied upstream changes in hydrostatic pore pressures. The soil is considered elasto-plastic following the BBM model, Alonso *et al.* (1990) (properties are given in Table 2.4). The elastic parameters of this model are taken from the previous elastic model.

The case of Shira dam is especially interesting because the permeability of the compacted moraine fill (around 10^{-8} m/s; see below) is an intermediate value between impervious clay and a free draining material. One may wonder to what extent the classical hypothesis for drawdown analysis (undrained or pure flow) approximates the actual behaviour. This aspect will be discussed later.

The following ideas have guided the selection of parameters. The elastic (unloading-reloading) elastic moduli of compacted moraine and rockfill are typical of a stiff soil. In fact, well graded granular mixtures become rather stiff when compacted. The virgin compressibility, $\lambda(0) - \kappa$, is approximately one order of magnitude higher than the elastic compressibility. Parameters r and β controls the shape of the yield LC curve of BBM. The moraine soil is assumed to gain limited stiffness as suction increases (parameter r). Also, the increase in stiffness with suction is fast for relatively low values of suction and remains fairly constant thereafter (parameter β). The slope of the critical state strength line reflects the friction angles provided in the paper. Zero cohesion is assumed throughout the analysis, irrespective of suction (parameter k_j). A small reference stress (p^c) is assumed. Associated flow conditions were assumed in both materials (parameter $\alpha = 1$). Rockfill properties were assumed to be similar to the compacted moraine, except for the higher friction angle.

The dam was built in a single step. A more detailed representation of dam construction plays a minor role in the analysis of drawdown. The following “as compacted” initial suction and saturated yield stress were imposed: $s_0 = 0.01$ MPa and $p_o^* = 0.01$ MPa. Given the low value of p_o^* , which reflects the isotropic yield state after compaction, dam conditions at the end of construction correspond to a normally consolidated state. The dam was then impounded until steady state conditions were reached. The presence of the impervious concrete membrane results in a simple initial state: all points upstream of the concrete wall maintain hydrostatic water pressure conditions. This initial state correspond to day 5 in the plots presented later

The information given in the original paper provided data to approximate hydraulic parameters. Two saturated permeabilities are mentioned for compacted specimens in the laboratory ($1.6 \cdot 10^{-8}$ m/s, when compacted at optimum water content and $1.6 \cdot 10^{-7}$ m/s when compacted wet of optimum). However, the dry densities reached in the field (19.8 kN/m³) are higher than the optimum laboratory B.S. compaction (19.2 kN/m³) and this leads to a reduction in permeability. A saturated permeability value $k_{sat} = 1.6 \times 10^{-8}$ m/s was therefore selected for field conditions.

Table 2.4 Parameters for the mechanical models used for the analysis of Shira dam.

Definition of parameter	Symbol	Units	Type of soil	
			Moraine	Rockfill
I. ELASTIC BEHAVIOUR				
Elastic modulus	E	MPa	100	100
Poisson's ratio	ν	-	0.2	0.2
II. PLASTIC BEHAVIOUR				
Virgin compressibility for saturated conditions	$\lambda(0) - \kappa$	-	0.020	0.020
Parameter that establishes the minimum value of the compressibility coefficient for high values of suction	r	-	0.8	0.8
Parameter that controls the rate of increase in stiffness with suction	β	MPa ⁻¹	6.5	6.5
Reference stress	p^c	MPa	0.01	0.01
Slope of critical state strength line	M	-	1.4 (35°)	1.85 (45°)
Parameter that controls the increase in cohesion with suction	k_s	-	0	0
Parameter that defines the non-associativeness of plastic potential	α	-	1	1
III. INITIAL STATE FOR DAM MODEL				
Initial suction	s_0	MPa	0.01	0.01
Initial yield mean net stress	p_0^*	MPa	0.01	0.01

Table 2.5 Hydraulic parameters used for the analysis of Shira dam.

Definition of parameter	Symbol	Units	Type of soil	
			Moraine	Rockfill
I. PERMEABILITY				
Saturated permeability	k_{sat}	m/s	$1.6 \cdot 10^{-8}$	$1.0 \cdot 10^{-4}$
Relative permeability	k_{rel}	-	$k_{sat} (S_w)^2$	$k_{sat} (S_w)^2$
II. WATER RETENTION				
Van Genuchten parameter describing air entry value	P_0	MPa	0.05	0.01
Van Genuchten parameter describing mid slope of retention curve	λ	-	0.2	0.4

Water retention properties for the moraine were derived following a simplified procedure, which makes use of the grain size distribution. Since the moraine soil is a granular material, capillary effects will dominate the water retention properties. On the other hand, pore size distributions may be approximated if grain size distributions are known. An example is given, for a beach sand, in Alonso and Romero (2002). The idea is that the pore size distribution follows the shape of the grain size distribution. However, the pore diameter is a fraction of the equivalent grain size. In the sand reported by Alonso and Romero (2002) this fraction is approximately 0.25. It is probably lower in a well-graded material although this ratio was accepted to derive the pore size distribution from the known average value of the grading curve for the moraine soil. The next step is to use Laplace equation to derive the suction emptying a given pore size. This leads immediately to the water retention curve. The estimated curve is given in Figure 2.29. The Van Genuchten expression fitted to the derived water retention curve corresponds to parameters (see also Table 2.6): $P_0 = 0.05$ MPa and $\lambda = 0.2$. The rockfill retention curve was approximated with a significantly lower air entry value (lower P_0) and an increased facility to desaturate (higher λ) when suction is applied. Finally, a cubic law, in terms of the degree of saturation, defined the relative permeability.

The known history of the final stages of reservoir filling and drawdown history of the reservoir levels is indicated in Figures 2.24 to 2.28

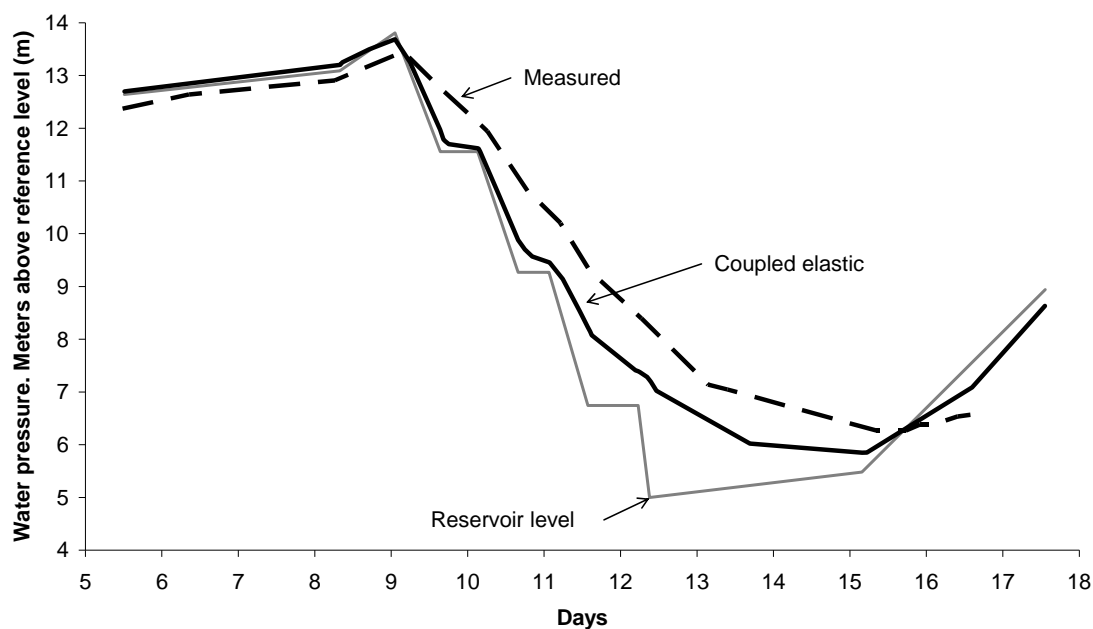


Figure 2.24 Measured and calculated pore pressures in Piezometer 1 (Coupled saturated/unsaturated analysis; elastic soil properties).

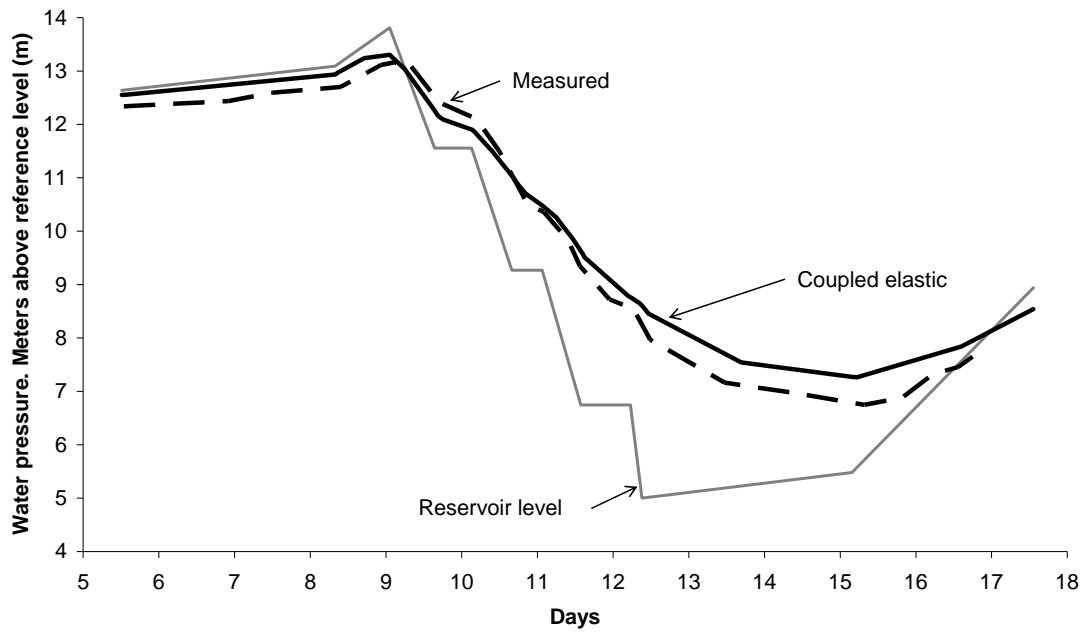


Figure 2.25 Measured and calculated pore pressures in Piezometer 2 (Coupled saturated/unsaturated analysis; elastic soil properties).

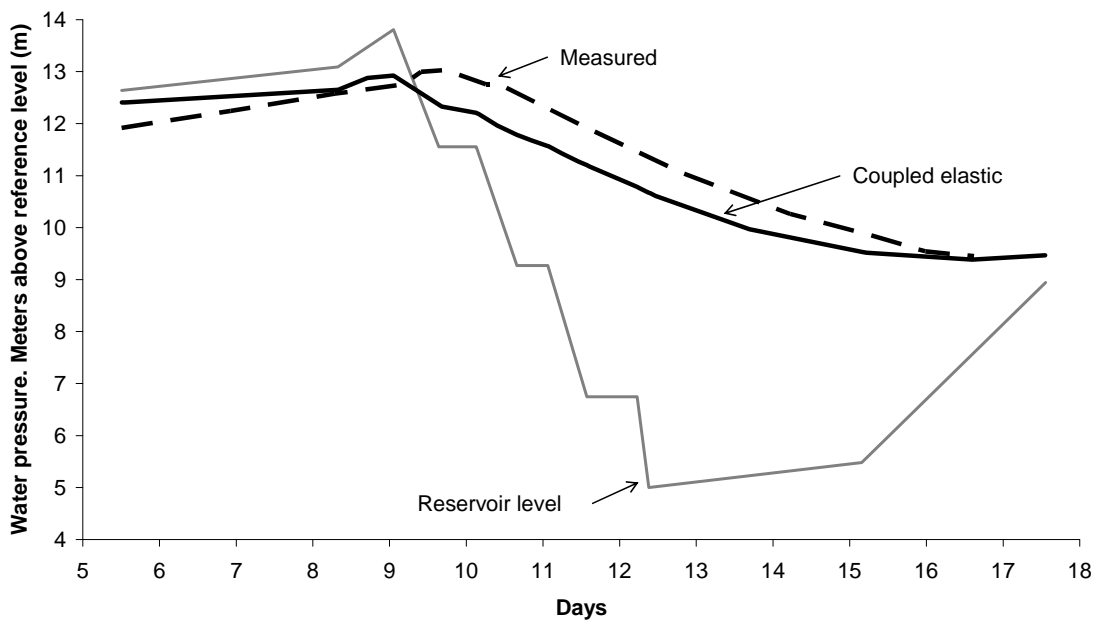


Figure 2.26 Measured and calculated pore pressures in Piezometer 2 (Coupled saturated/unsaturated analysis; elastic soil properties).

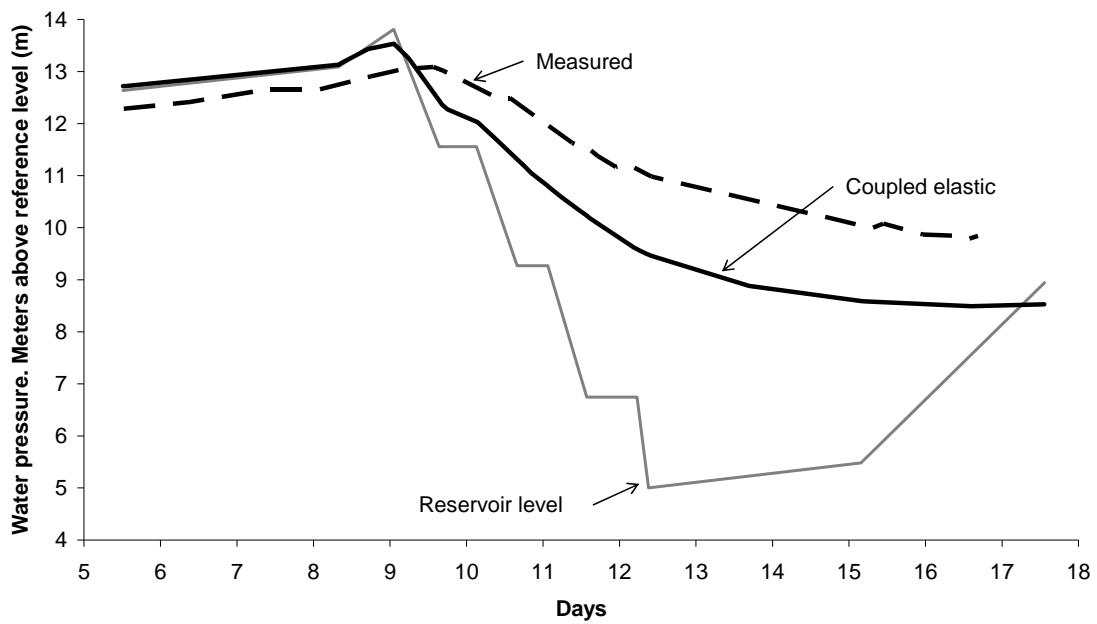


Figure 2.27 Measured and calculated pore pressures in Piezometer 4 (Coupled saturated/unsaturated analysis; elastic soil properties).

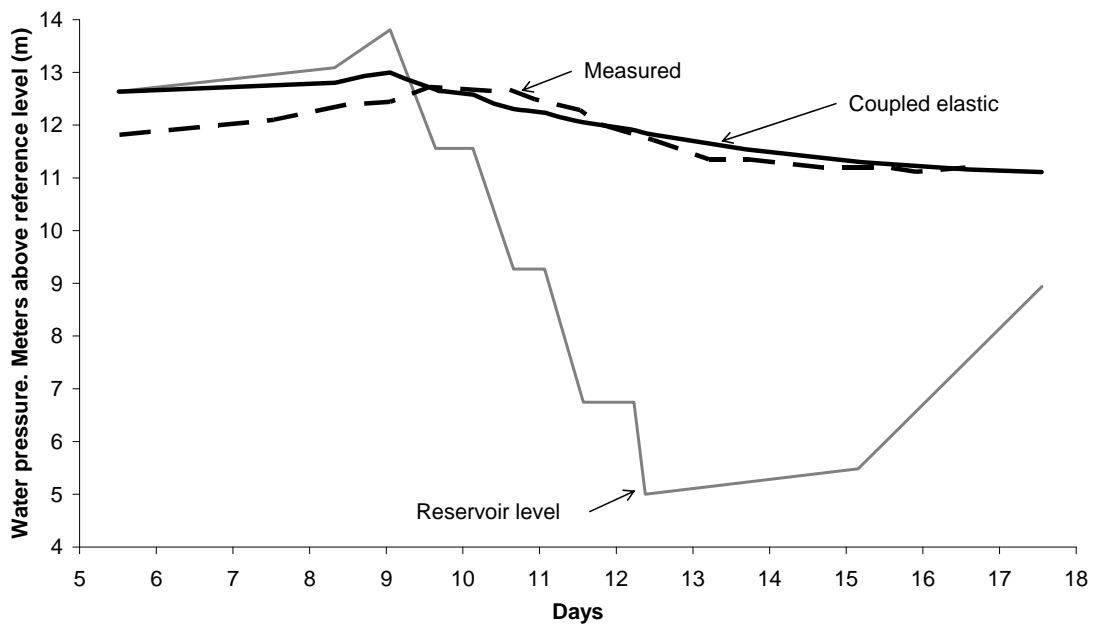


Figure 2.28 Measured and calculated pore pressures in Piezometer 5 (Coupled saturated/unsaturated analysis; elastic soil properties).

These five figures include a comparison between the calculated evolution of pore pressures and the corresponding measurements of the five piezometers. The analysis

corresponds to Case 2 of the list of four cases described above: a coupled flow-elastic deformation for saturated/unsaturated conditions. The agreement is satisfactory. The pattern of recorded pore pressures and the smoothing effect introduced by the soil stiffness and permeability (specially noteworthy in Piezometers 1 and 2) are well captured by the model. A better agreement between measurements and calculations probably requires the consideration of certain field heterogeneity in permeability and/or soil stiffness.

Paton and Semple (1961) plotted also contours of piezometric head during drawdown. Two examples are given in Figures 2.30b and 2.31b. They correspond to drawdown drops of 4.85 and 8.8 m. The reservoir level reaches 9.15 and 5.2 m respectively (with respect to the zero reference level which in this paper is placed at the dam base: point 0 in Fig. 2.30 and 2.31). The authors used the data recorded on the five piezometers to interpolate the curves shown in the figure. They made the hypothesis of a zero water pressure at the shell-rockfill interphase. The computed distribution of heads inside the dam shell, for the same amount of drawdown, is also plotted in Figures 2.20a and 2.21a. The agreement is quite acceptable, although some discrepancies exist, which, in part could be attributed to the limited accuracy of the interpolation made.

Table 2.6 Shira dam. Instantaneous drawdown. Comparison of coupled and simplified (Bishop) analysis

Piezometer	Initial pressure (horizontal water table) (kPa)	Calculated instantaneous pressure drop (Code_Bright) (kPa)	Bishop hypothesis ($\Delta u = \bar{B} \cdot \Delta \sigma_v$) $\bar{B} = 1$ (kPa)
1	96	42	42
2	106	22	12
2	67	10	1
4	56	17	12
5	22	6	0

There was also an interest in comparing the performance of the different methods of analysis listed above. Figures 2.32 to 2.36 illustrate this comparison. Consider first the hypothesis of instantaneous drawdown (9.5 m of water level drawdown, instantaneously). The calculated pressure drop is indicated in the figures by means of a vertical bar. A (coupled) dissipation process is then calculated and the progressive

decay in pore pressures is also plotted. If compared with the actual pore pressures measured at the end of the real drawdown period, the hypothesis of instantaneous drawdown leads obviously to an extremely pessimistic and unrealistic situation. (The end point of the instantaneous drawdown at $t = 9$ days is to be compared with the pore pressure recorded at the end of the drawdown period at $t = 12.4$ days).

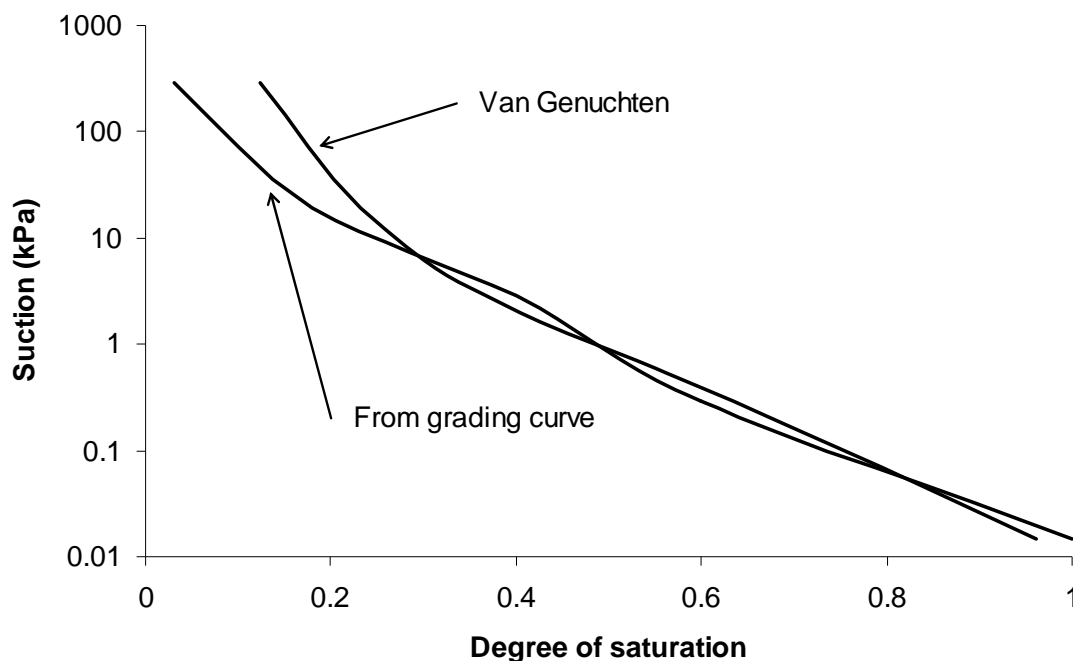


Figure 2.29 Water retention curve derived from average grading of moraine material and Van Genuchten approximation.

It is also interesting to compare the results of the fully coupled analysis of the instantaneous drawdown with the approximated method of analysis suggested by Skempton/Bishop. Table 2.6 shows the comparison. The change in vertical stress ($\Delta\sigma_v$) has two contributions: the change in free water elevation above a given point and the decrease in total specific weight of the rockfill material covering the moraine shell. An effective saturated porosity of 0.2, after drainage, was assumed to calculate the drop in total specific weight. Bishop hypothesis leads systematically to a higher pore pressure drop than the more accurate analysis. This is specially the case for the piezometers located deep inside the fill. Discrepancies are due to the simplified stress distribution assumed in the approximate method.

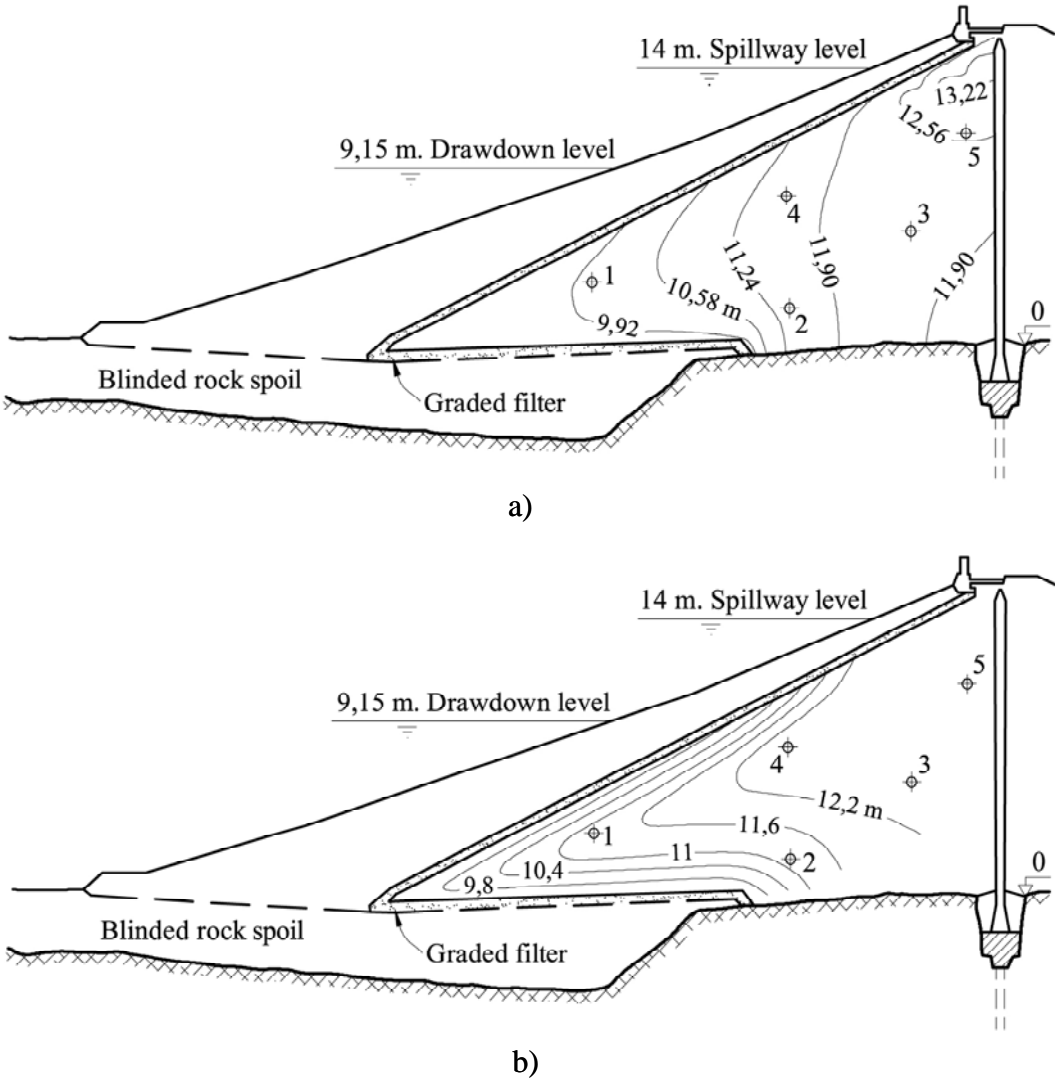


Figure 2.30 Distribution of pore pressures inside the shell for a drawdown 14 to 9.15 m. (a) Computed results (coupled analysis); (b) Interpolated values plotted by Paton and Semple (1961).

Consider now the opposite calculation method: a pure flow analysis. In this case, Figures 2.32 to 2.36 indicate that the predicted pore pressures are the lowest ones if compared with the remaining methods of analysis. Calculated water pressures follow closely the history of reservoir levels. The “damping” effect associated with soil compressibility is absent. When the water level is increased, at the end of the drawdown test, the pure flow analysis indicates, against the observed behaviour, a fast recovery of pore pressures within the embankment.

Coupled analyses are closer to actual measurements. This is true in absolute terms but also in the trends observed when boundary conditions (changes in reservoir level) are modified.

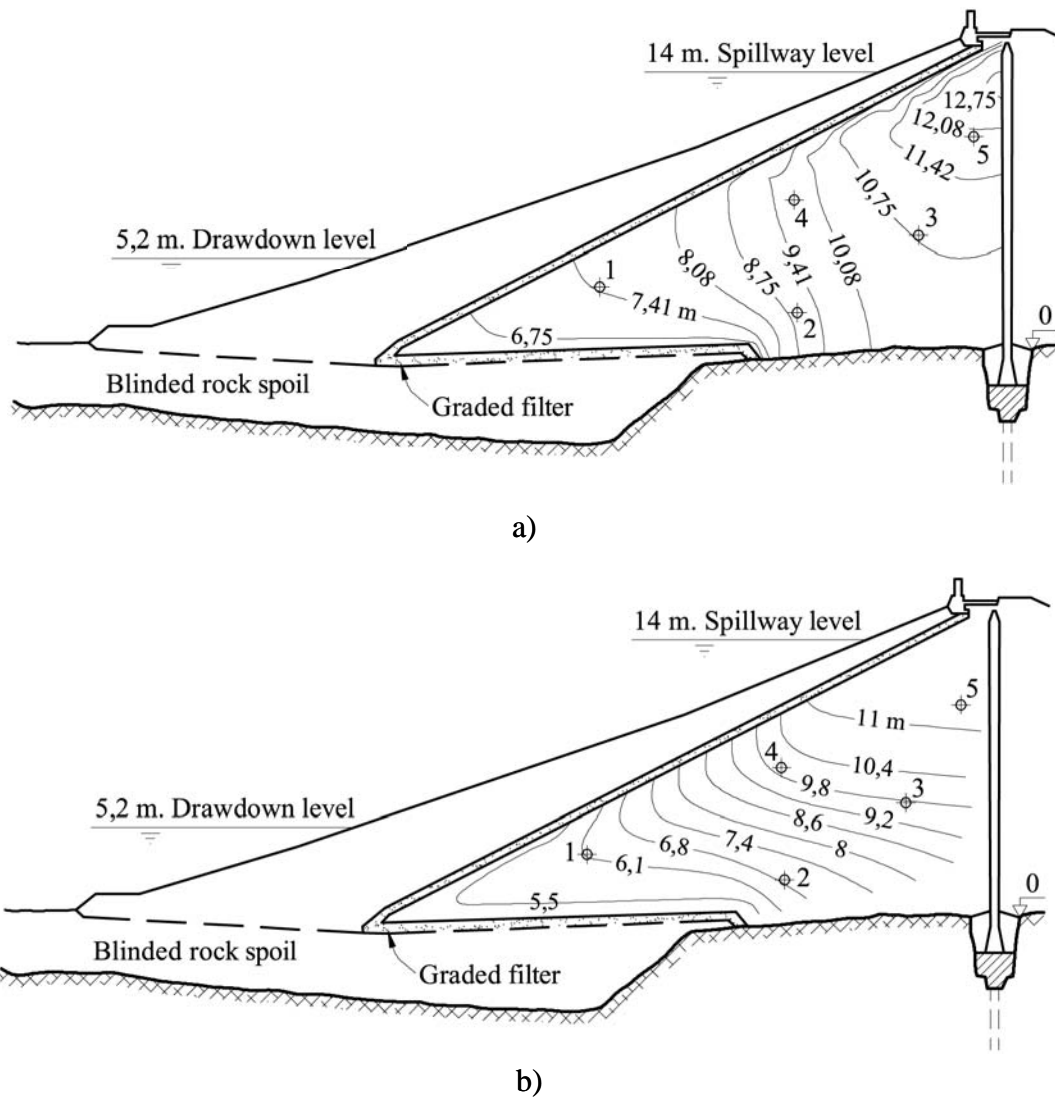


Figure 2.31 Distribution of pore pressures inside the shell for a drawdown 14 to 9.15 m. (a) Computed results (coupled analysis); (b) Interpolated values plotted by Paton and Semple (1961).

Construction of Shira Dam leaves most of the embankment under normally consolidated conditions. This is a consequence of the low initial yield stress, p_0^* , adopted in the analysis. p_0^* is related to the energy of compaction, but a detailed discussion of this topic is outside the limits of this Chapter. Granular materials, and certainly rockfill, tend to yield under low stresses after compaction. Therefore, the accumulation of layers over a given point will induce plastic straining. The stress paths in points relatively away from the slope surfaces follow K_0 – type of conditions. Figure 2.37 indicates the stress path of points located in the position of Piezometers 1 and 2. Plotted in the figure are also the yield surfaces at the end of construction. The maximum size of the yield surface corresponds to these construction stages. Once the dam is completed, reservoir impoundment leads to a reversal of the stress path, which

enters into the elastic zone. Drawdown leads to a new sharp reversal in the stress path and the increase in deviatoric stresses. However, the end of the drawdown path remains inside the elastic locus in the two cases represented in Figure 2.37. The possibility of inducing additional plastic straining during drawdown depends on the geometry of the dam cross section and on the constitutive behaviour of the materials involved. Shira dam has a stable geometry because of the low upstream slope (2 to 1) and shear stresses inside the dam are relatively small. In addition, the granular shell material has a high friction angle (45°). However, under different circumstances, plastic straining may develop during drawdown, and, in this case, pore pressures will probably increase because the yield point, located in the “wet” (compression) side of the yield locus (see Fig. 2.37) implies that additional local sources of local are available for dissipation.

Note also the differences in calculated stress paths for Piezometers 1 and 2 during drawdown. Piezometer 2 is located deep inside the embankment, at a high elevation and therefore pore pressure changes are small: the effective mean stress remains constant and the stress path moves vertically upwards. However, the change in deviatoric stresses is also small and the final stress point is far from reaching critical state conditions. Piezometer 2, on the contrary, is close to the upstream shell, at a lower elevation. Changes in pore pressure and deviatoric stress are large in this position and the stress path moves approximately parallel to the initial construction path and approaches yielding conditions in compression.

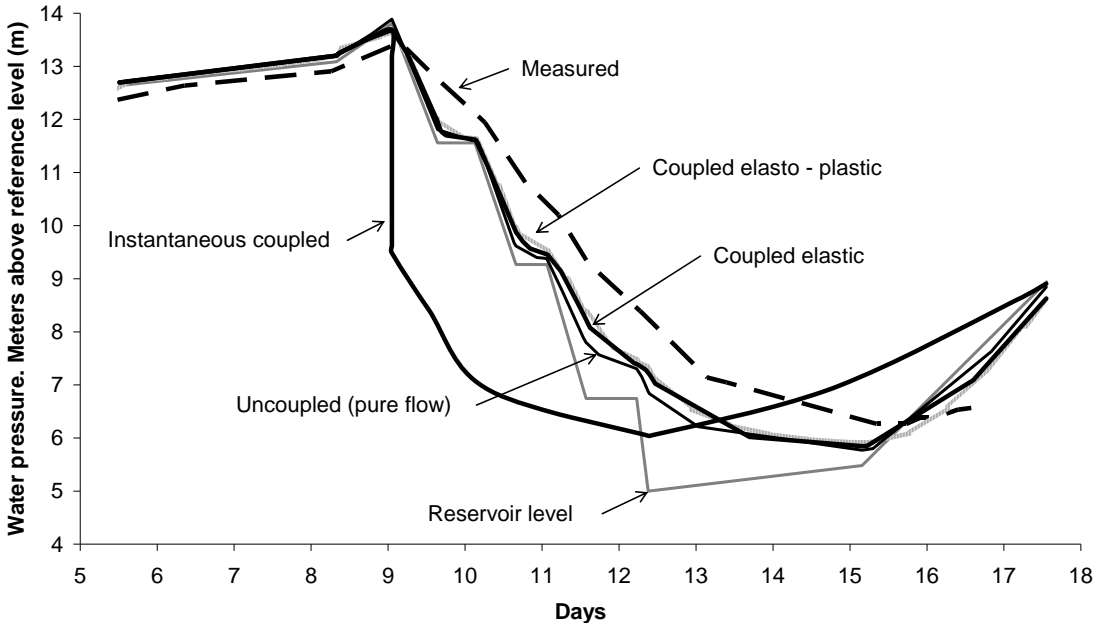


Figure 2.32 Comparison of measured pore pressures in Piezometer 1 and different calculation procedures.

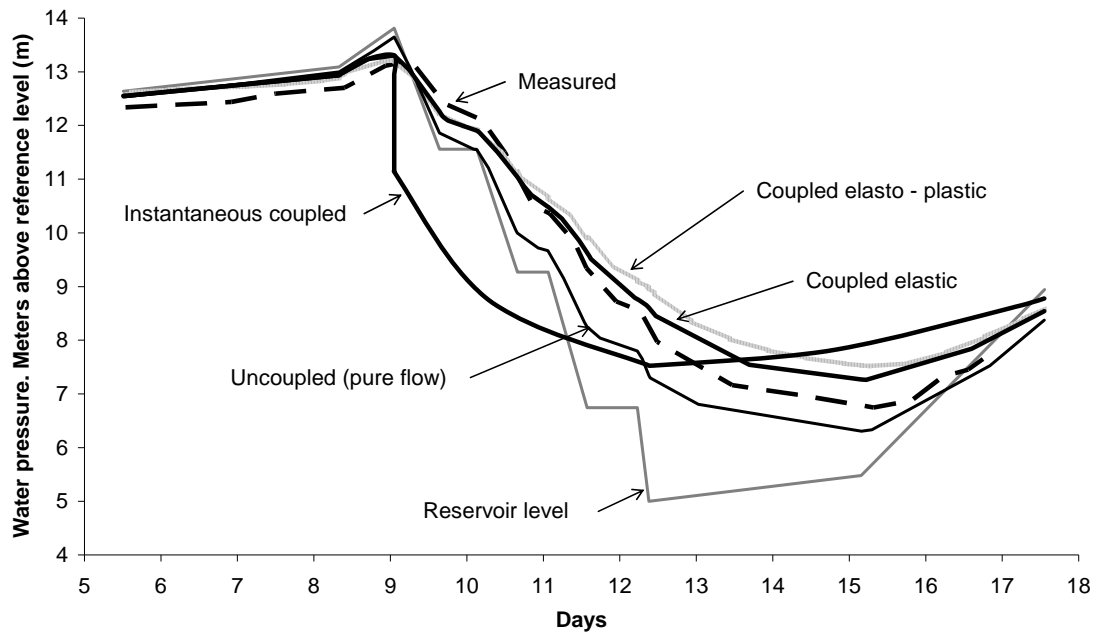


Figure 2.33 Comparison of measured pore pressures in Piezometer 2 and different calculation procedures.

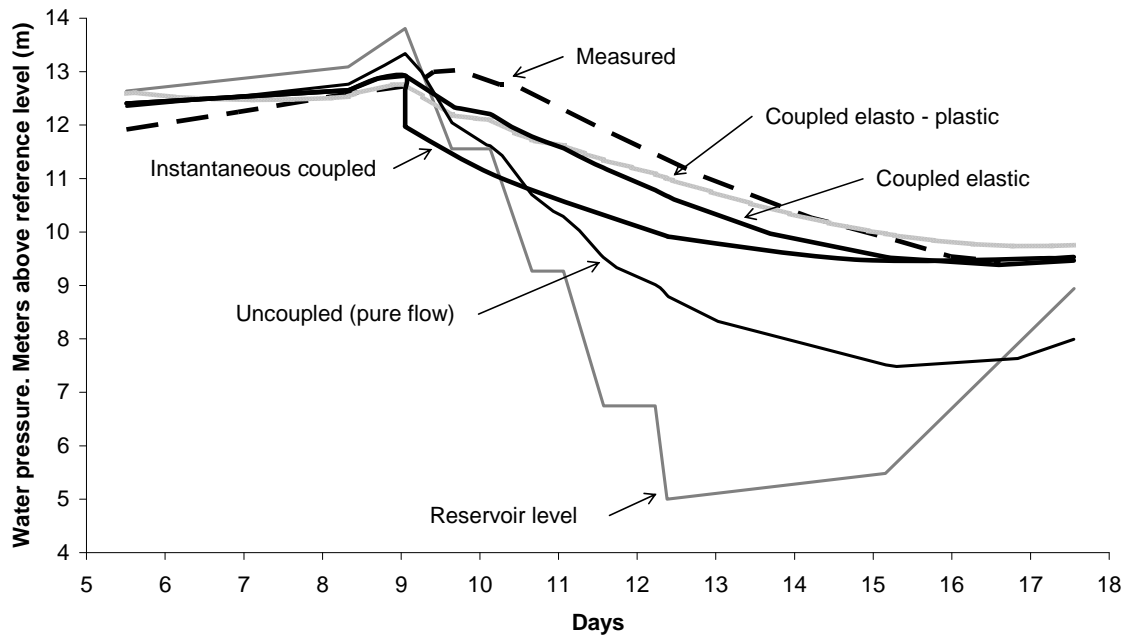


Figure 2.34 Comparison of measured pore pressures in Piezometer 2 and different calculation procedures.

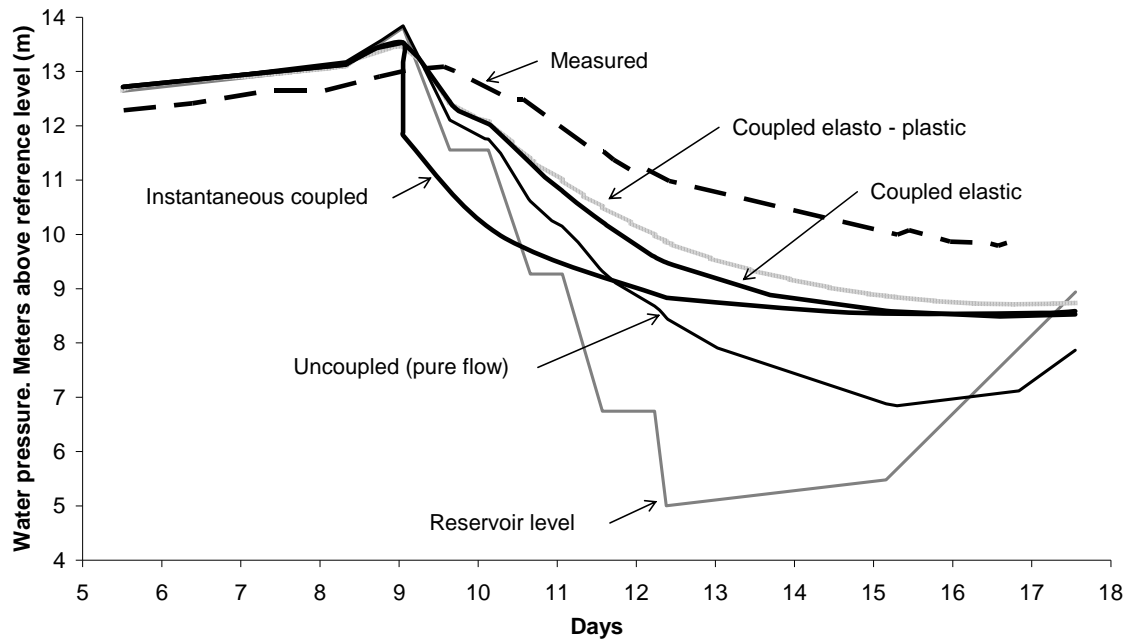


Figure 2.35 Comparison of measured pore pressures in Piezometer 4 and different calculation procedures.

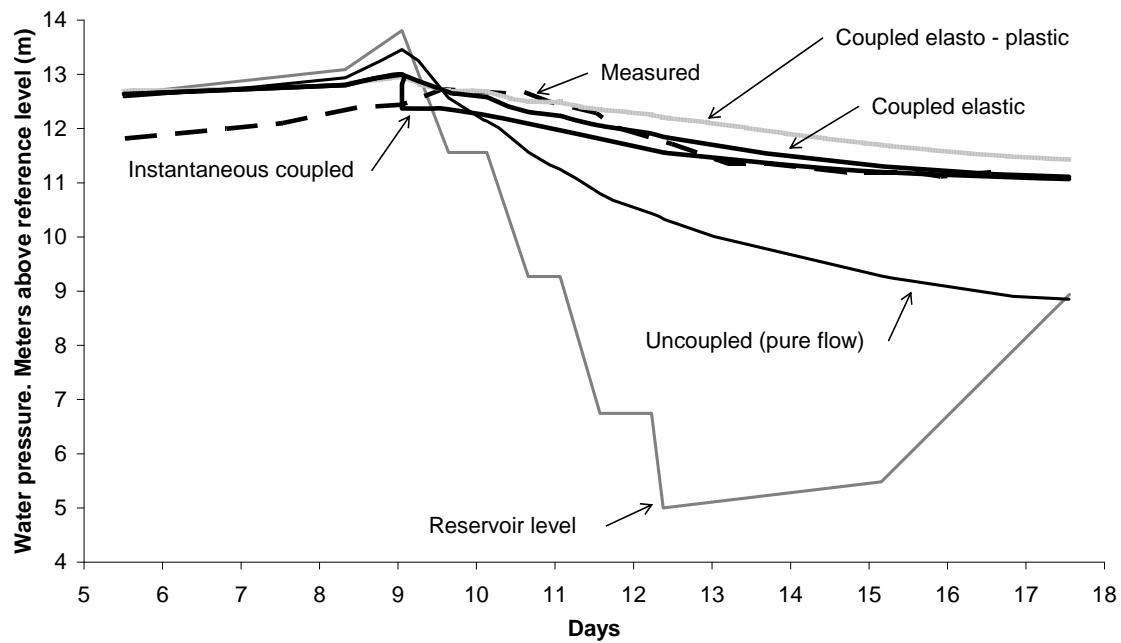
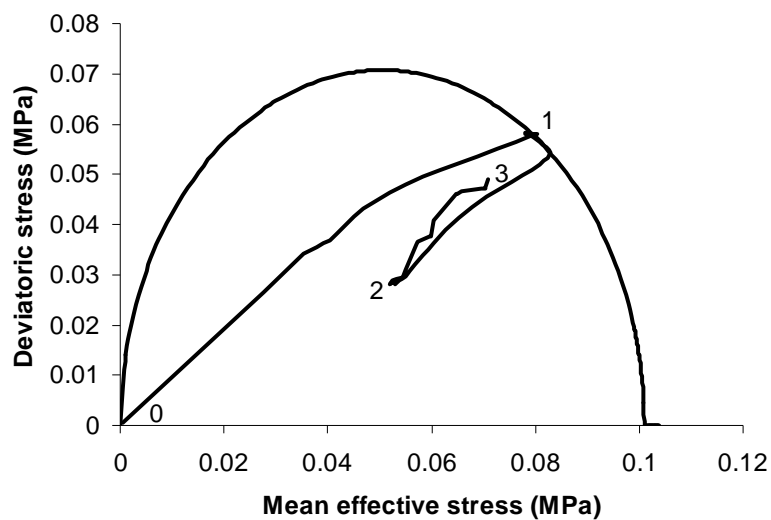


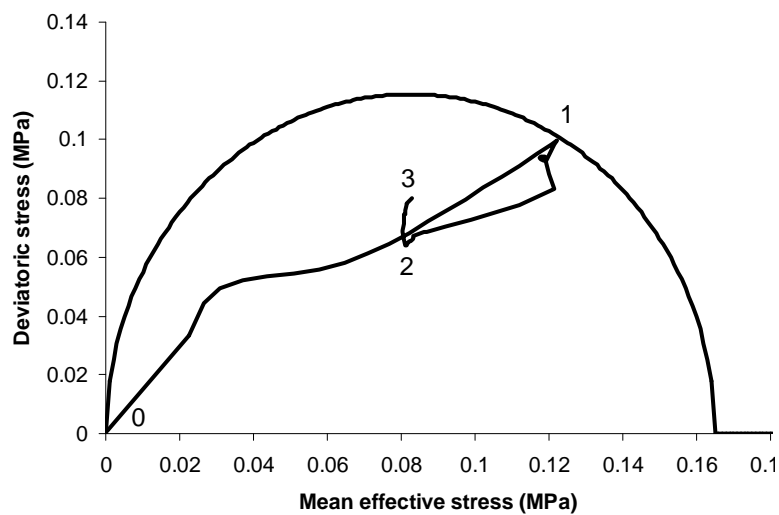
Figure 2.36 Comparison of measured pore pressures in Piezometer 5 and different calculation procedures.

There is, however, an additional effect, which leads to a different drawdown behaviour when comparing elastic and elastoplastic modelling approaches. If permeability is made dependent on void ratio, the construction of the dam will lead to lower values of permeability (distributed in a heterogeneous manner). If the dam

compacted material yields during construction, plastic volumetric compaction will add to the elastic strains. In addition, collapse phenomena upon impounding will reduce further the porosity. This effect has also been explored in the case of Shira dam. Permeability was made dependent on void ratio, e , following a Kozeny type of relationship (permeability depends on $e^3/(1+e)$). The calculated records of pore pressure evolution during drawdown are also shown in Figures 2.32 to 2.36. The reduction in permeability, if compared with the coupled elastic case, leads to a systematic increase in pore pressures. The agreement with measurements is now better in some Piezometers (1, 2 and 4).



(a)



(b)

Figure 2.37 Stress path in a (q, p') triaxial stress space of points located in the position of (a) piezometers 1 and (b) piezometer 2 during construction, impoundment and drawdown. 0-1: Construction; 1-2: Impoundment; 2-2: Drawdown. Also plotted are the yield surfaces at the end of construction.

The conclusion, for the particular embankment material of Shira dam and its overall geometry and design, is that the classical methods of analysis are far from explaining the recorded behaviour. The “instantaneous” or undrained method is conservative, but very unrealistic. A fully coupled analysis of the instantaneous drawdown results in higher pressure drops than the classical Bishop proposal. At the opposite extreme, the pure flow analysis leads to a systematic and unsafe underestimation of fill pressures during drawdown. Coupled analysis captures well the actual measurements. In the case of Shira dam, plastification during drawdown was probably nonexistent, and the simpler elastic approach provides a good approximation to recorded pore water pressures. However, the full elastoplastic simulation offers a better understanding of the phenomena taking place during construction and impounding. This is shown in the stress paths calculated, in the occurrence of yielding during construction and in the effect of permeability reduction on the drawdown response.

2.7 CONCLUSIONS

Pore water pressures in an initially submerged slope and later subjected to drawdown depend on several soil parameters and “external” conditions: soil permeability (saturated and unsaturated), soil water retention properties, mechanical soil constitutive behaviour, rate of water level lowering and boundary conditions. The Chapter stresses that a proper consideration of these aspects is only possible if a fully coupled flow – mechanical analysis, valid for saturated and unsaturated conditions is employed. A review of the literature on the subject reveals that the published procedures are plagued with numerous assumptions, which prevent often its use in real problems and make it difficult to judge the degree of conservatism -if any- introduced.

Leaving apart for the moment the issue of the transition from saturated to unsaturated conditions which takes place during drawdown, there are two fundamental mechanisms controlling the resulting pore water pressure: the change in pore pressure induced by boundary changes in stress and the new flow regime generated. Both of them require a coupled analysis for a proper interpretation and consistency of results. In particular, pure flow models are unable to consider the initial changes in pore pressure associated with stress unloading. The intensity of pore pressure changes induced by a stress modification is controlled by the soil mechanical constitutive equation. In a simplified situation, under elastic hypothesis for the soil skeleton, the pore pressure depends on the ratio of soil bulk stiffness and water compression modulus. In most situations, this ratio is small and the influence of soil effective stiffness is negligible. This implies a maximum response of the saturated material to stress changes. Without this coupling, the initial pore pressures do not change during

fast unloading. (As an illustration, pure flow models are unable to detect that all points in the porous media instantaneously feel a change in water level in a large submerged area – the “bottom of the sea” case –).

Permeability and soil stiffness controls coupled flow. The uncoupled analysis implicitly assumes a rigid soil and therefore it leads to a maximum dissipation rate. Both effects (the initial change in pore pressure and the subsequent dissipation) should be jointly considered for a better understanding of the evolution of pore pressures. In addition, the rate of change of boundary conditions is a key information to interpret the results. No simple rules can be given to estimate the pore pressures in the slope. This is even more certain if due consideration is given to the unsaturated flow regime. In this regard, some design rules for earthdam stability calculations, which provide the position of the phreatic surface in relatively “free draining” materials, have been reviewed with the help of the fully coupled, complete formulation used in this Chapter. An interesting result is that, other parameters of the problem being equal, the average height of the phreatic line increases as the air entry value of the water retention curve decreases. This is a paradoxical result at first sight, but it may be explained if one considers the amount of drained water induced by the drawdown. In addition, the position of the phreatic line does not provide enough information to calculate safety factors against slope failure if due consideration is given to the strength for positive suctions, above the zero-suction surface. Therefore, methods for drawdown analysis, which concentrate on the determination of the position of the phreatic line, using formulations for saturated flow, may lead to significant errors. The evaluation of the design chart for dams subjected to drawdown, performed in one of the sections of this paper, is a good example.

The elastoplastic analysis performed on a synthetic example (an earth and rockfill dam whose parameters correspond to a real case: Beliche dam) has provided additional information on the stress paths that develop inside the dam. Points inside the embankment, except for shallow positions, follow a K_0 – type of stress path during construction. Impounding and drawdown imply strong stress reversals. Drawdown, in particular, is characterized by a parallel increase in effective mean stress and deviatoric stress. Yield conditions may be approached although it is believed that the drawdown paths tend to remain in the elastic domain.

A well documented case history (Shira dam) was analyzed to provide further insight into the drawdown problem. The case is very interesting because the soil involved (a compacted moraine) has an intermediate permeability between impervious clays and free draining granular materials. It should be added that materials with this intermediate permeability are very common in dam engineering. Therefore, the two classical procedures to analyze drawdown effects (undrained analysis for clays and pure

flow for granular materials) will meet difficulties. In fact, these two methods proved quite unrealistic when compared with actual records of pore water pressures in different points of the dam. In particular, the pure flow (uncoupled) analysis leads to faster dissipation of pore pressures and this is an unsafe result in terms of stability calculations. The fully coupled analysis (elastic or elastoplastic) provides consistent results.

The elastoplastic analysis allows a proper consideration of the entire history of dam construction, impoundment and drawdown. Since embankment dams experience significant yielding during construction, this is an important consideration. It has been shown also that the reduction in permeability associated with material volumetric compression has a significant effect on the subsequent drawdown behaviour: it leads to higher pore water pressures being maintained inside the slope.

2.8 APPENDIX COUPLED FLOW-DEFORMATION FORMULATION FOR SATURATED/UNSATURATED CONDITIONS

This appendix summarizes the balance equations required for coupled flow-deformation for saturated and unsaturated conditions.

In what follows, it will be considered that the state variables (unknowns) are: solid displacements, \mathbf{u} (three spatial directions) and liquid pressure, P_l . Balance of momentum for the medium as a whole is reduced to the equation of stress equilibrium together with a mechanical constitutive model which relates stresses with strains. Strains are defined in terms of displacements. Small strains and small strain rates for solid deformation are assumed. Advective terms due to solid displacement are neglected once the formulation is written in terms of material derivatives (in fact, material derivatives are approximated as eulerian time derivatives). In this way, volumetric strain is properly considered.

The governing equations for non-isothermal multiphase flow of water and gas through porous deformable saline media have been presented by Olivella *et al.* (1994). A derivation is given there, and only a description of the reduced formulation for hydro-mechanical problems is presented in this appendix.

Mass balance of solid present in the medium is written as:

$$\frac{\partial}{\partial t}(\rho_s(1-\phi)) + \nabla \cdot (\mathbf{j}_s) = 0 \quad (\text{A2.1})$$

where ρ_s is the mass of solid per unit volume of solid and \mathbf{j}_s is the flux of solid. From this equation, an expression for porosity variation can be obtained if the flux of solid is

written as the velocity of the solid multiplied by volumetric fraction occupied by the solid phase and the density, i.e. $\mathbf{j}_s = \rho_s (1-\phi) \frac{d\mathbf{u}}{dt}$:

$$\frac{D_s \phi}{Dt} = \frac{(1-\phi)}{\rho_s} \frac{D_s \rho_s}{Dt} + (1-\phi) \nabla \cdot \frac{d\mathbf{u}}{dt} \quad (\text{A2.2})$$

The material derivative with respect to the solid is defined as:

$$\frac{D_s(\bullet)}{Dt} = \frac{\partial}{\partial t} + \frac{d\mathbf{u}}{dt} \cdot \nabla(\bullet) \quad (\text{A2.3})$$

Equation (A2.2) expresses the variation of porosity caused by volumetric deformation and solid density variation.

In the formulation required for the analyses in this Chapter, the water component and the liquid phase are the same. The total mass balance of water is expressed as:

$$\frac{\partial}{\partial t}(\rho_w S_w \phi) + \nabla \cdot (\mathbf{j}_w) = f^w \quad (\text{A2.4})$$

where S_w is the degree of saturation of water, ρ_w is the water density, \mathbf{j}_w is the flux of water, and f^w is an external supply of water. Water flux is a combination of a Darcy flux and an advection caused by the solid motion:

$$\frac{\partial}{\partial t}(\rho_w S_w \phi) + \nabla \cdot \left(\rho_w \mathbf{q}_w + \rho_w \phi S_w \frac{d\mathbf{u}}{dt} \right) = f^w \quad (\text{A2.5})$$

The use of the material derivative leads to:

$$\phi \frac{D_s(\rho_w S_w)}{Dt} + \rho_w S_w \frac{D_s \phi}{Dt} + \rho_w S_w \phi \nabla \cdot \left(\frac{d\mathbf{u}}{dt} \right) + \nabla \cdot (\rho_w \mathbf{q}_w) = f^w \quad (\text{A2.6})$$

The mass balance of solid is introduced in the mass balance of water to obtain, after some algebra:

$$\frac{\phi S_w}{\rho_w} \frac{D_s \rho_w}{Dt} + \phi \frac{D_s S_w}{Dt} + S_w \frac{(1-\phi)}{\rho_s} \frac{D_s \rho_s}{Dt} + S_w \nabla \cdot \left(\frac{d\mathbf{u}}{dt} \right) + \frac{1}{\rho_w} \nabla \cdot (\rho_w \mathbf{q}_w) = \frac{1}{\rho_w} f^w \quad (\text{A2.7})$$

This equation has four storage terms, related to:

Water compressibility since $\frac{1}{\rho_w} \frac{d\rho_w}{dp_w} = \frac{1}{K_w}$ is the volumetric compressibility of water

Retention curve storativity since $\frac{dS_w}{dp_w}$ is obtained from the retention curve.

Solid compressibility since $\frac{1}{\rho_s} \frac{d\rho_s}{dp} = \frac{1}{K_s}$ is the compressibility of the soil particles.

Soil skeleton compressibility since the divergence of solid velocity can be transformed into $\nabla \cdot \left(\frac{d\mathbf{u}}{dt} \right) = \frac{d}{dt} (\nabla \cdot \mathbf{u}) = \frac{d\varepsilon_v}{dt}$, and $\frac{d\varepsilon_v}{dt} = \frac{d\varepsilon_v(\boldsymbol{\sigma}', p_w)}{dt} = \frac{d\varepsilon_v}{d\boldsymbol{\sigma}} \frac{d\boldsymbol{\sigma}}{dt} + \frac{d\varepsilon_v}{dp_w} \frac{dp_w}{dt}$ is the volumetric strain rate that should be calculated with an appropriate constitutive model for the soil. The mechanical model may include effective or net stress terms (volumetric or deviatoric) or suction terms. Effective or net stress has to be considered here as the total stress minus the water pressure or the air pressure, respectively, for saturated or unsaturated conditions. The final terms are left as a function of total stress.

The relative importance of the different terms depends on the conditions of the soil. For instance, for saturated conditions the second term disappears. When the compressibility of the skeleton is large, the compressibility of the particles is negligible. The compressibility of the water may be negligible in some cases but it is not possible to neglect it in general for hard soils.

The final objective is to find the unknowns from the governing equations. Therefore, the dependent variables will have to be related to the unknowns in some way. Doing this in the last equation leads to:

$$\begin{aligned} \frac{\phi S_w}{K_w} \frac{dp_w}{dt} + \phi \frac{dS_w}{dp_w} \frac{dp_w}{dt} + S_w \left(\frac{\partial \varepsilon_v}{\partial \boldsymbol{\sigma}} \frac{d\boldsymbol{\sigma}}{dt} + \frac{\partial \varepsilon_v}{\partial p_w} \frac{dp_w}{dt} \right) + \frac{1}{\rho_w} \nabla \cdot (\rho_w \mathbf{q}_w) &= 0 \\ \frac{\phi S_w}{K_w} \frac{dp_w}{dt} + \phi \frac{dS_w}{dp_w} \frac{dp_w}{dt} + S_w \frac{\partial \varepsilon_v}{\partial \boldsymbol{\sigma}} \frac{d\boldsymbol{\sigma}}{dt} + S_w \frac{\partial \varepsilon_v}{\partial p_w} \frac{dp_w}{dt} &= -\frac{1}{\rho_w} \nabla \cdot (\rho_w \mathbf{q}_w) \end{aligned} \quad (\text{A2.8})$$

where the compressibility of the solid particles has been neglected and the source/sink term is assumed to be zero. The material derivatives have been approximated as eulerian.

This equation allows the calculation of the pressure development for a soil subjected to changes in total stress in the following way:

$$dp_w = \frac{-S_w \frac{\partial \varepsilon_v}{\partial \boldsymbol{\sigma}} d\boldsymbol{\sigma} - \frac{dt}{\rho_w} \nabla \cdot (\rho_w \mathbf{q}_w)}{\frac{\phi S_w}{K_w} + \phi \frac{dS_w}{dp_w} + S_w \frac{\partial \varepsilon_v}{\partial p_w}} \quad (\text{A2.9})$$

Deformation is assumed negative in compression from these equations, and stress is also negative in compression. This implies that $d\boldsymbol{\sigma}$ is negative in compression (loading) and produces positive pressure increments. Note that the general stress tensor is maintained because volumetric deformations can be induced by any stress variation (not only isotropic). For instance, dilatancy is a volumetric expansion induced by shear.

In Equation (A2.9), the volumetric deformation derivatives $\frac{\partial \varepsilon_v}{\partial \boldsymbol{\sigma}}$ and $\frac{\partial \varepsilon_v}{\partial p_w}$ should be calculated with an appropriate constitutive model. These are volumetric deformation terms and can be obtained from a model for unsaturated soils such as the elastoplastic model BBM (Alonso *et al*, 1990). A general equation, including the effect of effective or net stresses and the effect of suction, is written as:

$$\begin{aligned}
 d\boldsymbol{\sigma}' &= \mathbf{D}d\boldsymbol{\varepsilon} + \mathbf{h}ds \\
 d\boldsymbol{\varepsilon} &= \mathbf{D}^{-1}d\boldsymbol{\sigma}' - \mathbf{D}^{-1}\mathbf{h}ds \\
 d\varepsilon_v &= \mathbf{m}'d\boldsymbol{\varepsilon} = \mathbf{m}'\mathbf{D}^{-1}d\boldsymbol{\sigma}' - \mathbf{m}'\mathbf{D}^{-1}\mathbf{h}ds \\
 \mathbf{m}' &= [1 \quad 1 \quad 1 \quad 0 \quad 0 \quad 0]
 \end{aligned} \tag{A2.10}$$

Where suction can be defined as $s = \max(p_a - p_w, 0)$ and effective or net stress as $\boldsymbol{\sigma}' = \boldsymbol{\sigma} + \max(p_a, p_w)$. This is valid for saturated and unsaturated conditions, and considers stresses in compression as negative quantities. The model parameters are included in \mathbf{D} which is the stiffness tensor (6x6) or constitutive matrix for changes in net or effective stress and \mathbf{h} which is the constitutive vector for changes in suction. Both are nonlinear functions.

Note that the derivatives of volumetric deformation needed in Equation (A2.9) can be obtained in the following way $\frac{\partial \varepsilon_v}{\partial \boldsymbol{\sigma}} = \frac{\partial \varepsilon_v}{\partial \boldsymbol{\sigma}'} \frac{\partial \boldsymbol{\sigma}'}{\partial \boldsymbol{\sigma}}$ and $\frac{\partial \varepsilon_v}{\partial p_w} = \frac{\partial \varepsilon_v}{\partial \boldsymbol{\sigma}'} \frac{\partial \boldsymbol{\sigma}'}{\partial p_w} + \frac{\partial \varepsilon_v}{\partial s} \frac{\partial s}{\partial p_w}$. By comparison with Equation (A2.10), the following terms are obtained: $\frac{\partial \varepsilon_v}{\partial \boldsymbol{\sigma}'} = \mathbf{m}'\mathbf{D}^{-1}$ and $\frac{\partial \varepsilon_v}{\partial s} = -\mathbf{m}'\mathbf{D}^{-1}\mathbf{h}$.

The nonlinear elastic part of the BBM model, gives the following volumetric deformation:

$$d\varepsilon_v = \frac{\kappa}{1+e} \frac{dp'}{p'} + \frac{\kappa_s}{1+e} \frac{ds}{s+0.1} \tag{A2.11}$$

Where, e is void ratio, κ and κ_s are material parameters, p' is the mean net or effective stress which is defined as $p' = (\sigma_x + \sigma_y + \sigma_z)/3 + \max(p_a, p_w)$, and s is suction.

CHAPTER 3

Rapid Landslides. Thermo-Hydro-Mechanical Approach

In this chapter an analysis of rapid landslides using a thermo-hydro-mechanical approach is developed. The problem analyzed involves sliding on a well-formed failure surface in which the sliding mass remains practically unaltered and move as a block. Thermo-hydro-mechanical coupling effects in the shear zone are invoked to develop a dynamic analysis of rapid landslides. The governing equations are written and they will be integrated conveniently in following chapters for the analysis of specific landslides. But before, an introductory section is presented to discuss earlier works published on the subject and to highlight some relevant aspects of direct implication for the analysis described later. Firstly, some aspects of heating effects on saturated soils are exemplified by means of some experimental results performed in the laboratory and in the field. They show a fundamental aspect: heating under undrained conditions leads to a significant increase in pore pressure. The drained response is also briefly presented on the basis of published papers. A simple mathematical explanation of such effects is then given. In the remaining of the introductory section some relevant aspects for the analysis of landslides and its potential acceleration, namely the relationship between strength and relative shear displacement and shearing rate, are discussed.

3.1 INTRODUCTION

Many field observations indicate that large-scale translational landslides may move at different velocities over long periods of time. A simple consideration of equilibrium equations indicates that changes in boundary conditions, such as fluctuations in water levels or changes in the stress field due to construction or erosion, will induce the acceleration or deceleration of a landslide due to the lack of equilibrium between resistant and destabilizing actions applied on the landslide body.

Whatever causes the triggering, if a slide loses the equilibrium, it will move to a new position until equilibrium is reached again. Except for the case of an idealized planar landslide, the new position involves a new distribution of weight and forces. In practice, it is common to find failure surfaces with a steep inclination in the upper part that becomes flatter at the toe of the slide. Consider, for instance, the circular or “open L” shape of a failure surface. For these kind of landslide cross-sections, the movement of slope leads to a new position that contributes to the stabilization of the slide (assuming that the rest of properties and boundary conditions remain constant) and therefore, to the deceleration of the slide. However, some case records indicate that very high velocities may develop in relatively short sliding distances. The case of Vaiont, whose failure surface had an “open L” shape and reached around 100 km/h in 400 m approximately, is a reference case for fast sliding, which cannot be explained, unless the sliding resistance essentially disappears.

Several reasons have been invoked in earlier works to justify the drop of effective shearing strength required to explain the high acceleration of rapid landslides. A feasible explanation concerns the loss of shearing strength induced in brittle materials from a maximum or peak value to a residual one as the relative displacement increases. The drop of the strength involves a reduction of the resistance forces and the slide tends to accelerates. This effect can be directly associated with first-time slides and to the phenomenon of progressive failure. In pre-existing slide surfaces, resulting from ancient landslides or seismic events, the critical displacement associated with the peak value of strength has likely been exceeded in previous periods and, hence, a lower value of strength close or equal to the residual one is expected to be available along the sliding surface. In these cases, the loss of the strength with displacement cannot be arguably brought in to justify the acceleration of reactivated slides.

This discussion assumes that once the residual value of strength is reached, the available strength remains essentially constant as the slide moves. However, according to some experimental data, the rate of displacement may have a relevant effect on the residual strength. Once a landslide starts to move and residual conditions are reached, if the strength increases with the velocity, the slide will decelerate. Then the slide velocity decreases as the resisting forces increase and it comes eventually to rest when

the equilibrium is re-established. On the contrary, if the rate of displacement has the opposite effect, the strength drops below the available residual value at rest (or slow moving conditions) and the slide accelerates.

Another explanation given refers to the pore fluid pressure generated within the slip zone due to the movement of the slide. The idea, followed by several authors with some differences among them, considers the frictional work developed at sliding surface. The dissipation of this work into heat involves temperature increments that may induce the build up of pore water pressure. Heat-induced pore water pressure implies a reduction of effective stress and then, the drop of the frictional strength. Details on earlier works published on this subject will be presented later.

The three main reasons mentioned here for the acceleration of landslides (heating effects and loss of shearing strength by increasing relative displacement and shearing rate) are developed in more detail in the following sections. Heating effects will be highlighted in the work developed because it provides a consistent explanation for the rapid loss of strength necessary to accelerate slides. Accordingly, an extended review of the analysis of rapid landslides considering these effects will be presented. The thickness of shear bands, a relevant parameter in a thermo-hydro-mechanical analysis of landslides, is also discussed and a few early bibliographical references are mentioned.

3.1.1 Previous works on rapid landslide considering thermal effects

The idea of considering thermal effects in the analysis of rapid landslides was apparently presented initially by Habib (1967) who suggested that heat due to sliding friction can transform pore water into vapour, creating a gas cushion that lubricates the sliding surface. Then the unstable mass slides without friction. An equilibrium state between liquid and vapour masses takes place. In fact, this mechanism does not allow the evaporation of liquid water because the additional heat needed for evaporation cannot be generated without introducing the effect of effective stress (which is practically zero due to the excess pore water pressure generated). This idea was followed by Uriel Romero and Molina (1977), Goguel (1978) and Nonveiller (1987).

However, even if evaporation does not take place, heat generation by frictional work may also cause enough pore water pressure inside the shear band to induce the reduction of shearing strength and then the acceleration of the motion (Anderson, 1980; Voight and Faust, 1982; Davis and Smith, 1990).

A similar mechanism is analysed by the geophysics community to explain the strength in faults as a result of earthquake slip (Lachenbruck, 1980; Lee and Delaney, 1986; Andrews, 2002; Rice, 2006; Sulem *et al.*, 2007).

More recently, Vardoulakis (2000, 2002) presented an interesting contribution in this subject based on similar ideas. The case of Vaoint Landslide interpreted as a

rotational landslide was analysed. The author focused on the thermo-poro-mechanical behaviour of the clayey soil involved in the shearing surface to explain the process of pore water pressure generation by heating. Shear strength softening as displacement increases and strain rate effects were also considered based on the experimental data published by Tika and Hutchinson (1999).

The analysis presented in Vardoulakis (2002) can be summarized as follows. Once a landslide is triggered, the shear strength on the shear band reduces as a function of accumulated displacement and the velocity reached by the landslide. The actual value of the mobilised frictional strength determines the acceleration of the sliding mass as well as the rate of heat production and, as a result, the temperature evolution. If temperature remains lower than a critical value, a thermo-elastic expansion of soil skeleton takes place and it is compensated by the expansion of soil-water mixture. Under this hypothesis, a null value of the pore-pressure-temperature coefficient is obtained and hence, no excess pore water pressures due to generated heating are calculated. When temperature reaches a critical value, thermoplastic collapse (contraction) of the clay inside the shear band takes place causing excess pore pressures that feed the acceleration of the landslide. The critical collapse temperature and the pore-pressure-temperature coefficient are function of the overconsolidated ratio of the soil inside the shear band. The value OCR varies during the landslide movement since the pore water pressure depends on the generated heat.

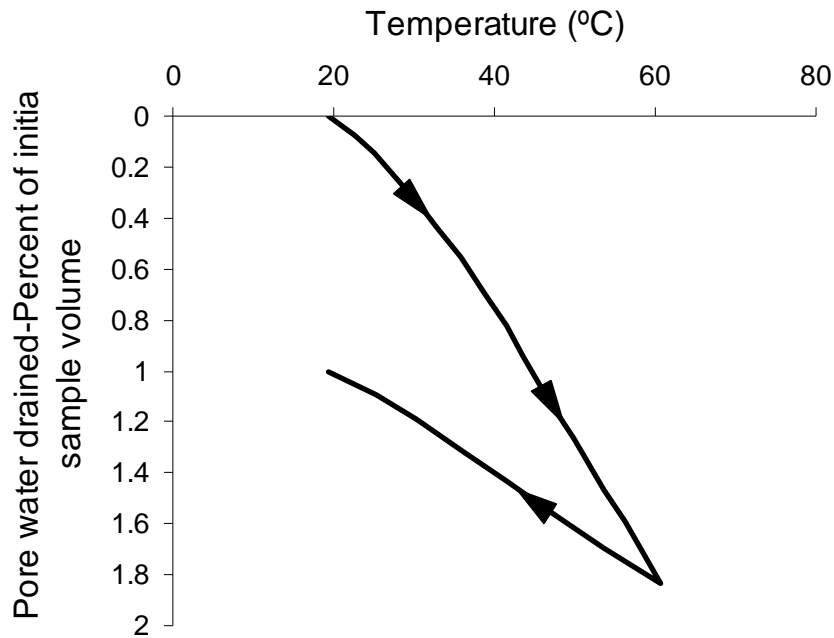
3.1.2 Heating effects in saturated porous media

Laboratory testing

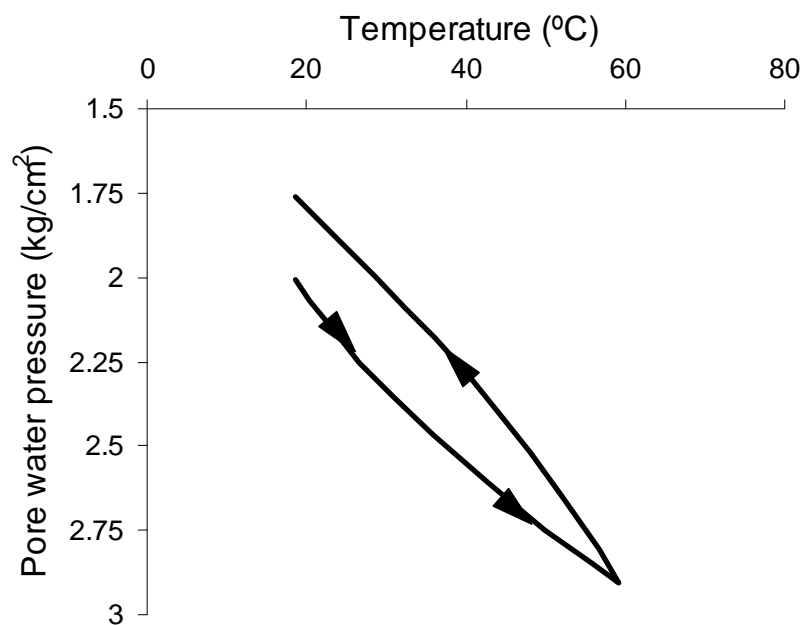
The effect of temperature on the behaviour of soils and rocks has been analysed by several authors (Campanella and Mitchell, 1963; Henkel and Sowa, 1968; Paaswell, 1967; Baldi *et al.* 1988; Huenckel and Baldi, 1990; Towhata *et al.*, 1993a,b; Tanakata *et al.*, 1997; Romero, 1999; Graham *et al.*, 2001; Sultan *et al.*, 2002; Cekerevac and Laloui, 2004; Ghabezloo and Sulem, 2008; among others).

The direct effect on volume changes and pore water pressure can be observed in early experimental tests shown in Figure 3.1 for a high porosity soil (Campanella and Mitchell, 1968). A saturated specimen of illite was subjected to a temperature increment from 20°C to 60°C followed by cooling to 20° in a triaxial test. Figure 3.1a shows the percentage of original pore water volume drained from the sample during a temperature cycle under constant all round effective stress ($\sigma'_3 = 200$ kPa) (temperature changes were imposed in increments and, after each increment, the sample was allowed to drain freely until equilibrium). In the second test (Fig. 3.1b), the same material was subjected to the same temperature cycle but in this case under undrained conditions. The variation of measured pore water pressures is shown in terms of temperature. It

may be seen that a very large pore water pressure is developed as a result of heating when the drainage is restricted.



(a)



(b)

Figure 3.1 Saturated illite under a cycle of temperature: (a) effect on sample volume under drainage conditions (cell pressure = 4 kg/cm^2 and constant all round effective stress = 3 kg/cm^2); (b) effect on the pore water pressure generated under undrained conditions (constant cell pressure = 3 kg/cm^2) (Campanella and Mitchell, 1968).

In practice, undrained and drained conditions will be mainly determined by the permeability of the soil and the rate of temperature changes. In order to examine, in a simple way, the effect of permeability on the soil response against changes of temperature, simple laboratory tests were performed.

A piece of saturated clayey rock was heated in a microwave oven (Fig. 3.2). In the experiment performed, a thermocouple temperature sensor was inserted into a specimen of Opalinus clay, which had been maintained in a humid chamber to ensure saturation. Opalinus clay is a low permeability soft clayey rock of marine origin. Clay minerals (illite, illite-smectite mixed layers, chlorite and kaolinite) dominate its mineralogical composition (40 to 80%). Quartz, calcite, siderite, pyrite, feldspar, and organic carbon are also present. Natural porosity varies between 4 and 12% (Bossart *et al.*, 2002). Pore water has a concentration of 20 g/l of sodium chloride.

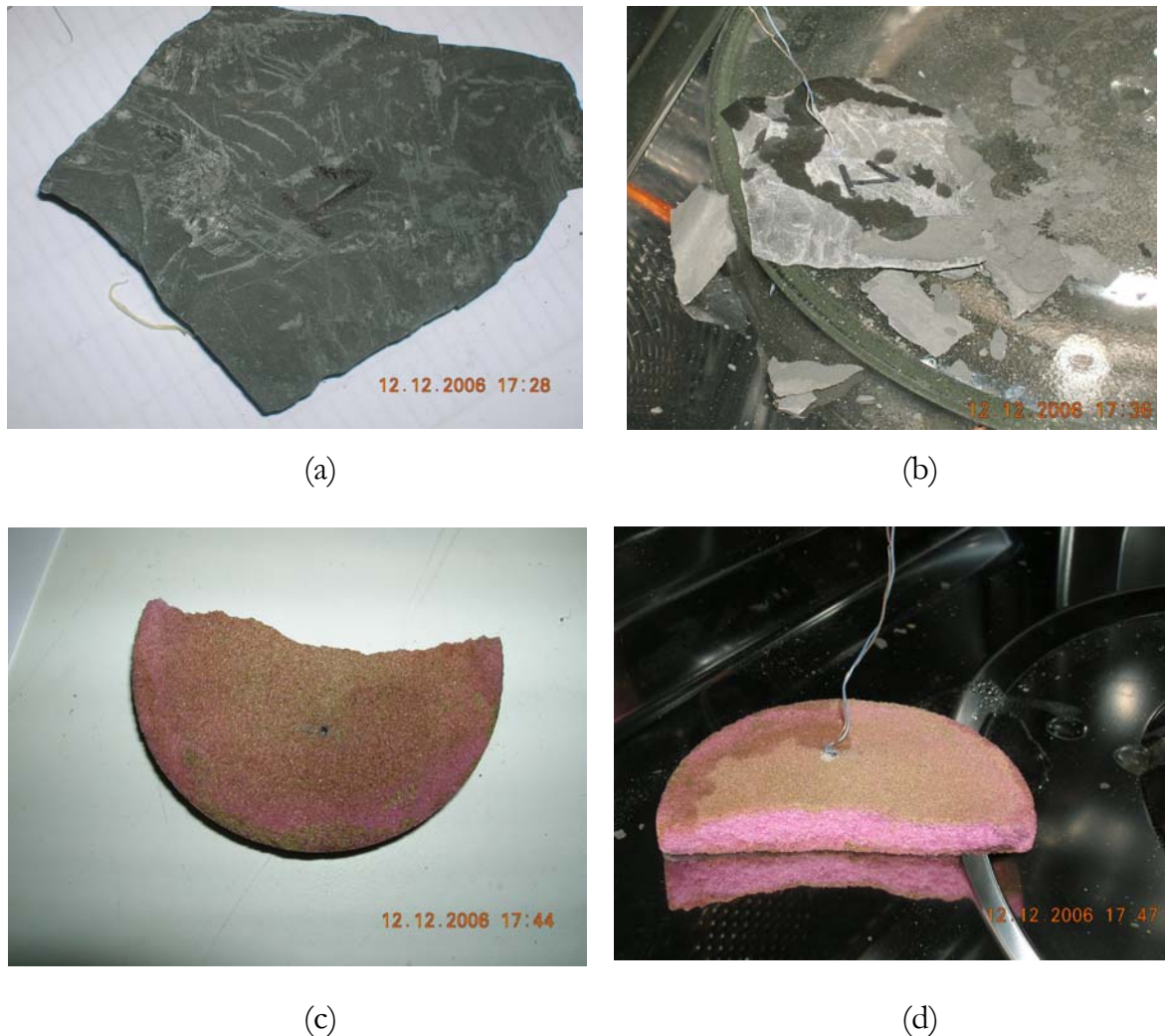


Figure 3.2 Heating experiment: (a) saturated fragment of Opalinus clay before heating; (b) the fragment, highly fissured and partially broken after heating in a microwave (cables indicate the position of the inserted thermocouple); (c) saturated porous stone before heating; (d) porous stone after heating.

Permeability coefficients (Darcy) varying between 0.8×10^{-13} m/s and 7.3×10^{-13} m/s, Young's modulus ranging between 1000 and 7000 MPa, and uniaxial compressive strength varying between 9 and 18 MPa have been reported for this clay shale by several authors (Thury and Bossart, 1999; Bock, 2001; Muñoz, 2007) on the basis of "in situ" and laboratory tests.

Figure 3.2a shows the piece of rock before heating. A thermal pulse having a nominal power of 1400 watts was applied during 40 s. The recorded temperature is shown in Figure 3.3. The specimen broke, accompanied by a clearly audible cracking noise, shortly before the end of the application of the heating pulse. At that time, the temperature reached values in excess of 170°C (Fig. 3.3). The shale specimen cracked in an explosive manner and was reduced to small fragments.

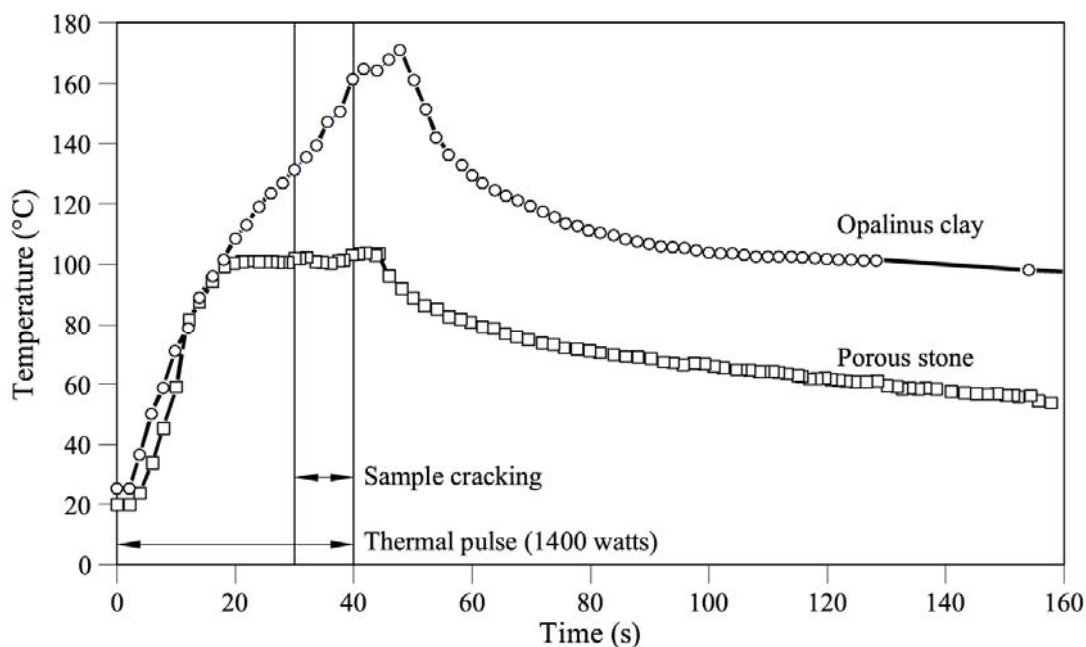


Figure 3.3 Recorded temperature during the two experiments performed in the microwave oven. A thermal pulse with a nominal intensity of 1400 watts was applied during 40 s.

A second experiment, with a totally different material, a discarded highly pervious porous stone (Fig. 3.2c), was also run. The measured temperature is shown in Figure 3.3. No cracking noise was heard during heating and the specimen remained intact after heating (Fig. 3.2d). Some water was also seen to escape from the stone. Unlike the previous experiment, the temperature record in this case showed an interesting behaviour: when the temperature measured by the thermocouple sensor reached 100°C, it remained constant at this temperature during the application of the power pulse. The water behaved as is to be expected in a free volume of water at atmospheric pressure: when the vaporization (boiling) temperature is reached, water evaporates in

the pores and the boiling temperature remains constant, at 100°C, because the heat input is “spent” in vaporizing the remaining liquid water.

It can be observed that the pore water in the shale specimen increased its temperature well beyond 100°C (it reached a peak value of 170°C (!) with no symptoms of decreasing during the power input phase). Pore water in the claystone is adsorbed in a significant proportion by clay minerals and this prevents its vaporization. The phase diagram of water provides additional information on the conditions leading to the vaporization of water (Fig. 3.5). At increasing pressure, the temperature for vaporization also increases.

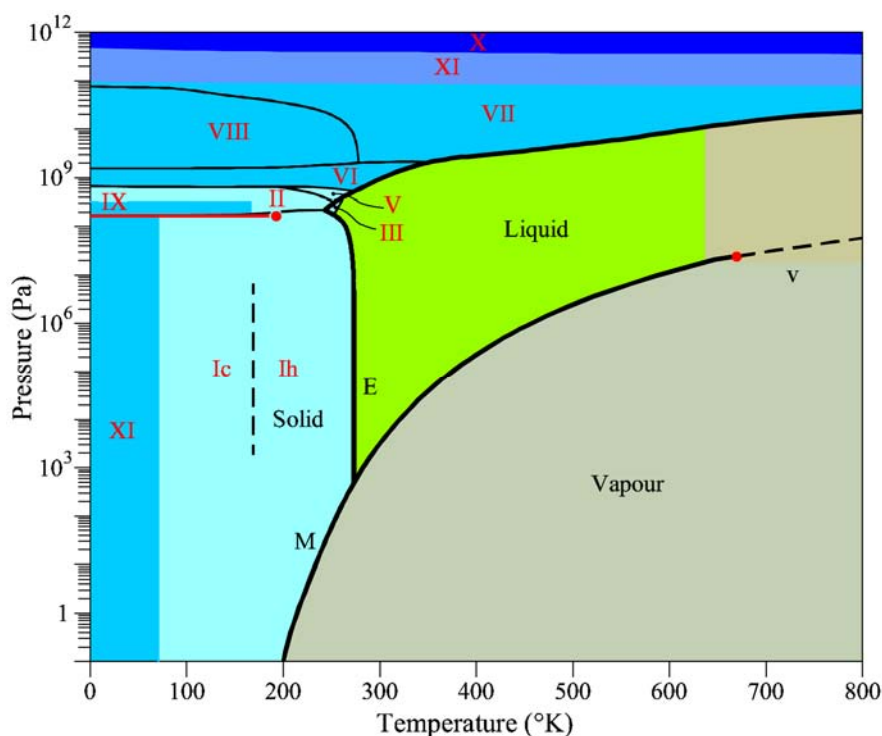


Figure 3.5 Phase diagram of water. Roman numerals indicate different types of ice. M, E and V stand for the average atmospheric conditions at the surface of Mars, Earth, and Venus, respectively (from London Southbank University website).

A simple qualitative explanation of thermal effects observed in these laboratory tests can be given with the help of Figure 3.6. It shows a saturated pore. The rock or soil skeleton around the pore is represented by a thick spherical elastic shell. Holes in radial directions connect the inner pore water with neighbouring pores. In this representation, the skeleton stiffness is controlled by the thickness and the modulus of the shell material. The number and diameter of radial holes define the material’s permeability. As a result of heating, pore water pressure tends to increase as far as solid particles and water expand and the skeleton restricts such expansion. In parallel with the development of water pressure, a dissipation process will start as water begins to flow through radial holes. Therefore, for a given rate of increase of temperature, the

attained pore water pressure will be the result of two competing mechanisms: the rate of increase of volume, directly related to the rate of increase of temperature, and the rate of dissipation governed by the permeability of the porous material (and also by the rock stiffness, in a process similar to the more familiar consolidation phenomenon).

For a given rate of temperature increase, the lower the soil or rock permeability and the stiffer the soil or rock, the higher the pore water pressure developed. Stiff clays and, particularly, clayey rocks are therefore prone to develop significant temperature-induced pore water pressures.

Note that the simple model of Figure 3.4 predicts that the pore pressure induced by the application of an external load decreases as soil or rock skeleton stiffness increases. In classical one-dimensional soil consolidation theory, the implicit assumption is that the soil skeleton has very low stiffness compared with the stiffness of water, and this implies that the external load is fully resisted by pore water: the skeleton spheres in Figure 3.4 are made of a very soft material.

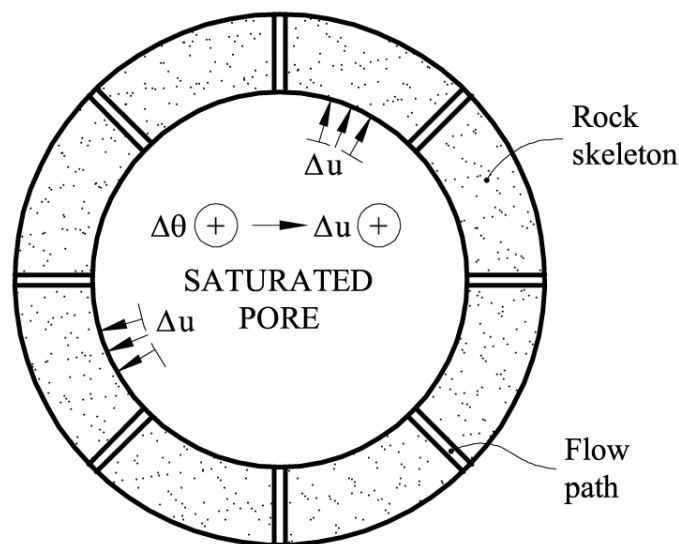


Figure 3.6 A saturated pore develops a positive pressure when temperature increases. The pore water pressure was not measured in the simple experiment described but, interestingly, a small amount of liquid water – presumably escaped from the specimen – was also observed on the floor of the oven after the broken rock fragments were removed.

Consider now a more accurate explanation. When the temperature of a saturated porous material increases, the solid particles, as well as the water in pores, dilates. Probably, local equilibrium of temperature is achieved soon and therefore the temperatures of water and solid skeleton will be essentially equal.

The volume of pore water and solid particles will increase in direct proportion to their thermal dilation coefficients, β_w and β_s , respectively. The associated volumetric strains, for a common change in temperature, $d\theta$, can be written as

$$d\varepsilon_{vw}^T = -\frac{dV_w}{V_w} = -\beta_w d\theta \quad (3.1)$$

$$d\varepsilon_{vs}^T = -\frac{dV_s}{V_s} = -\beta_s d\theta \quad (3.2)$$

where V_w and V_s are the volumes occupied by water and solid particles, respectively. Upper index T indicates that changes in temperature are the cause of the strains. β_w is substantially higher than β_s . Typical values for β_w and β_s are $3.4 \times 10^{-4} (\text{°C})^{-1}$ and $3.0 \times 10^{-5} (\text{°C})^{-1}$. Water dilates almost one order of magnitude more than solid particles. The thermal dilation of water and solid will result in an internal volumetric expansion. Compression strains are considered positive.

In the preceding explanation it was assumed that the soil or rock skeleton does not deform as a result of temperature changes. However, changes in temperature may also induce changes in the soil skeleton associated to (a) restructuration of the particles; (b) changes in interparticle forces which requires some reorientation or relative movement of soil grains in order to allow effective stress equilibrium; and (c) physicochemical clay-water interactions for the case of clayey soils which are explained by changes in thickness of the double layer (Campanella and Mitchell, 1968). All these effects on the rearrangement of the skeleton structure can be introduced by means of a thermal coefficient of the porous media, β_{pm} . Then, the total volumetric strain of the porous media ('skeleton') due to changes in temperature can be expressed as:

$$d\varepsilon_{vpm}^T = -\frac{dV_{pm}}{V_{pm}} = -\beta_{pm} d\theta \quad (3.3)$$

where V_{pm} is the total volume of the porous media, which is, under saturated conditions, equal to the sum of solid and water volume. A positive sign of coefficient β_{pm} indicates that an increase in temperature causes an increase in volume soil structure. In practice, this coefficient may reach positive, null or negative values depending on the soil, overconsolidated ratio, range of temperature applied, stress level, and other factors. In the case of clayey soils, when temperature is increased, highly overconsolidated soils initially exhibit expansion, followed by a contraction at higher temperature, whereas a normally consolidated or lightly overconsolidated soil only exhibits contraction. More details on this and some experimental observations are given later.

If water can be drained during heating and no pore water pressure builds up, the internal volumetric expansion due to thermal dilation of soil particles and water (Eqs. (3.1) and (3.2)) minus the total volume changes of the porous media (Eq. (3.3)) should be equal to the drained volume of water over the initial volume of porous media. This condition can be written for a unit of volume of porous media as follows:

$$n d\varepsilon_{vw}^T + (1-n) d\varepsilon_{vs}^T - d\varepsilon_{vpm}^T = V_{drainage} \quad (3.4)$$

where n is the porosity.

If heating is imposed under undrained conditions, the total change in volume due to temperature increments, previously calculated in Equation (3.4), can not be drained and an excess pore water pressures will be generated. Changes in pore water pressure (u_w) involve changes in effective stress that will induce volume changes in solid particles, pore water and porous media. If compressibility of solid particles is neglected and total stress is assumed constant (which means that changes in effective stress are equal to pore water pressure variations), the following equality can be written for undrained conditions:

$$n d\varepsilon_{vw}^T + (1-n) d\varepsilon_{vs}^T - d\varepsilon_{vpm}^T = -n d\varepsilon_{vw}^{u_w} - d\varepsilon_{vpm}^{u_w} \quad (3.5)$$

where volumetric strains of water ($d\varepsilon_{vw}^{u_w}$) and porous media ($d\varepsilon_{vpm}^{u_w}$) due to changes in pore water pressure (indicated by the upper index u_w) can be calculated by

$$d\varepsilon_{vw}^{u_w} = \alpha_w du_w \quad (3.6)$$

$$d\varepsilon_{vpm}^{u_w} = m_v du_w \quad (3.7)$$

Parameters α_w and m_v are the compressibility coefficients of water and porous media, respectively.

If Equations (3.1), (3.3), (3.6) and (3.7) are introduced in Equation (3.5), pore water pressure induced by a temperature change under undrained conditions can be calculated as

$$du_w = \frac{n\beta_w + (1-n)\beta_s - \beta_{pm}}{n\alpha_w + m_v} d\theta \quad (3.8)$$

Equation (3.8) supports the discussion made above based on Figure 3.6. In particular, Equation (3.8) reveals that the excess pore water pressure generated due to a temperature increase will be controlled by to the soil stiffness. In the simple laboratory test described before on Oppalinus clay (Fig. 3.2a), which can be considered in practice undrained due to the low permeability and the rapid thermal pulse, high values of excess pore water pressure were generated due to the low value of compressibility of this rock. In the absence of total external stress, as it was the case, tensile effective stresses developed and they may be able to overcome the tensile strength of the soil/rock and lead to a failure in tension, as observed in the photograph in Figure 3.2b.

Hueckel and Pellegrini (1991) also reported experimental results showing the failure of samples of low porosity (low permeability) heated from 70 to 90°C under undrained conditions under a constant deviatoric stress. The observed failure is

associated with a pore pressure build up. An increase in pore pressure leads to an effective stress drop under constant total stress conditions until failure is eventually reached.

On the other hand, Equation (3.8) indicates that if the soil expands against changes in temperature (β_{pm} positive), the expansion of solid grains and water will be partially compensated and a lower excess pore pressure will be generated. Otherwise, if the soil exhibits a thermal contraction (β_{pm} negative), the resulting excess pore pressure will be higher.

The more general case in which excess pore pressure are dissipated toward the boundaries will be discussed when describing below the balance equations.

A field heating experiment

The effect of heating rocks have been analysed in detail the last decades in the search of suitable deep geological disposals to store high level nuclear waste. A typical design is to locate the heat-emitting nuclear canisters in excavated galleries of massive and impervious rock, such as Opalinus clay used in the laboratory test discussed previously. A ring of impervious bentonite is placed around the canister to improve isolation. One of the issues in this design is to investigate the long-term performance of natural rock, exposed to an increase in temperature as a result of the heat generated by the nuclear waste. The large-scale Heating Experiment (HE), performed in the Monneri underground research laboratory (Switzerland), addresses this aspect of nuclear waste disposal research. The experiment is described in detail in EUR (2006) and in Muñoz (2007).

The scheme given in Figure 3.7a summarizes the concept of the experiment. A cylindrical heater – which simulates the waste – is located in a centred position in a vertical borehole (30 cm of diameter) excavated in Opalinus clay from the floor of a tunnel. A ring of compacted bentonite blocks was placed around the heater. Piezometers and temperature sensors were located at different radial distances and depths below the floor of the niche where the experiment was located ($z = 0$). The temperature response of sensors located at increasing radial distances is shown in Figure 3.7b. Maximum temperature at the bentonite-borehole wall contact ($r = 0.05\text{m}$) was limited to 100°C .

Pore pressure sensors were installed at points A1 and A2 (Fig. 3.7a), located at a radial distance of 0.65 m from the axis of the borehole, at two different elevations ($z = 5\text{ m}$ and $z = 6.5\text{ m}$). As temperature increased (at a rate of $0.25^\circ\text{C}/\text{day}$) until it reached a value of 40°C in sensor A1, pore water pressures also increased at measured rates of $0.012\text{ MPa}/\text{day}$ and $0.007\text{ MPa}/\text{day}$ in the two sensors, until they reached maximum values of 1.1 and 0.65 MPa respectively. Note that a substantial pressure peak

developed before pore pressure began to decrease, when the rate of temperature increase slowed down. The low permeability of Opalinus clay explains the continuous accumulation of pore pressure due to the relatively slow rate of increase of temperature. When the (permeability controlled) dissipation rate of excess water pressure dominated the process, the pore water pressure began to drop, at an essentially constant temperature.

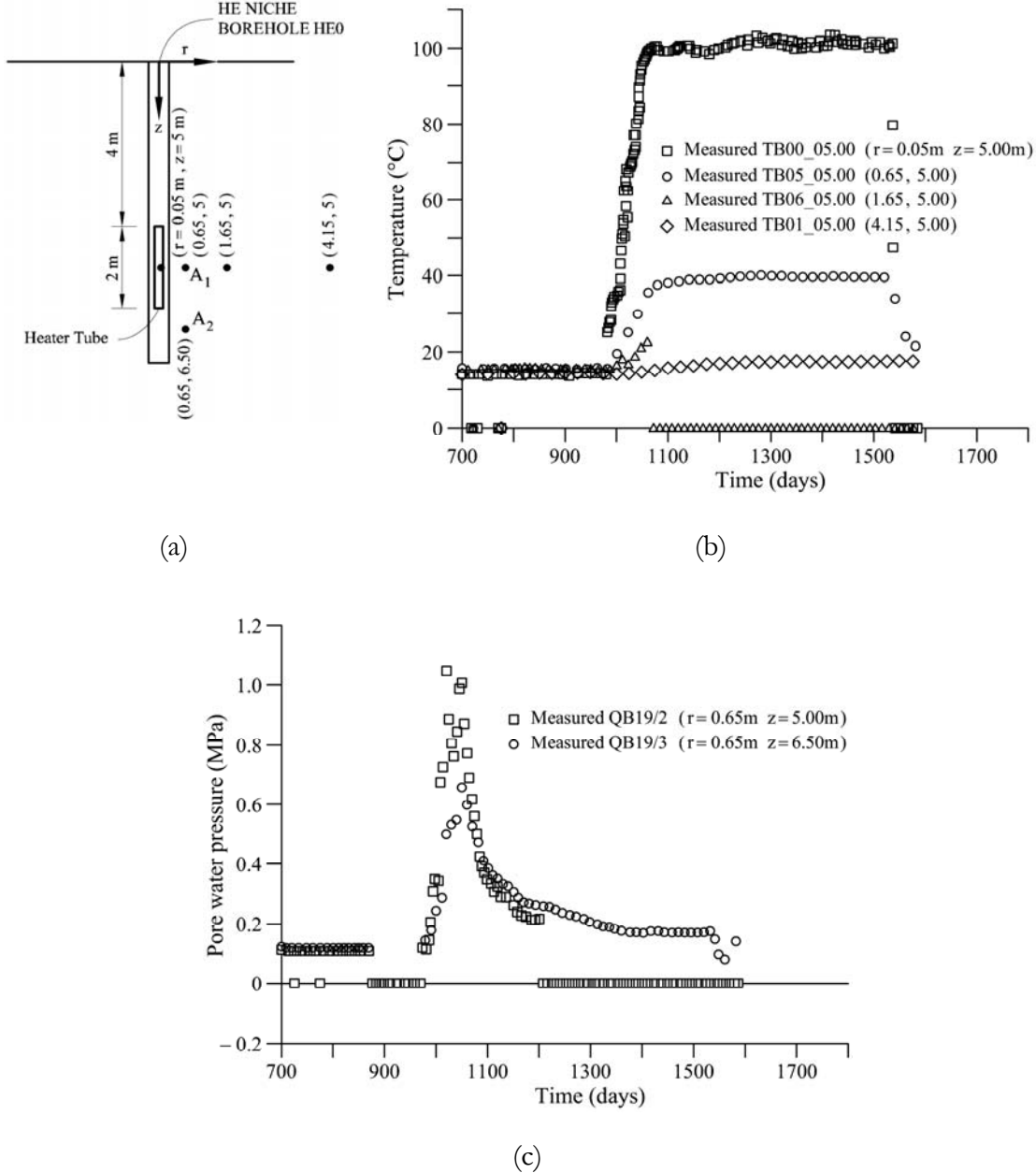


Figure 3.7 Field heating experiment of Opalinus clay: (a) schematic representation of the borehole, heater and instrumented points; (b) recorded temperature; (c) recorded pore water pressure. Heating HE Experiment, Monterri, Switzerland (Muñoz, 2007).

The maximum excess water pressure recorded in this experiment (0.9 MPa) is relatively large in absolute terms. Such water pressure is equivalent to the weight per unit area of a column of rock with a height of 40 m (if the rock had a bulk specific weight of 22.5 kN/m³). The base of such a column of Opalinus clay, if heated in the location of Piezometer QB19/3 in Figure 3.7c, will reach a zero vertical effective stress and, therefore, it will not be able to develop any frictional shear strength.

The same interpretation presented for the laboratory experimental data can be now applied to interpret the *insitu* measurements on temperature and pore water pressure presented here.

3.1.3 Additional thermo-mechanical features

Some relevant features of the mechanical response of soils combining effects of stress and temperature are briefly described here.

Effect on compressibility

There is some early experimental indication that the compressibility of soils is independent of temperature for a limited range of temperatures tested (20-100°C) (Campanella and Mitchell, 1968; Plum and Esrig, 1969).

Elastoplastic thermal strains

When a soil or rock is heated, all the constituents (solid particles and water) dilate. Even considering such thermal dilations reversible, the soil may exhibit a complex behaviour, often contractive and irreversible.

Figure 3.8 shows the total volumetric strain and drained water volume measured in a slow heating test up to 100°C on intact natural samples of Boom clay (Delage *et al.*, 2000). Boom clay is a stiff clay with a plasticity around 50%, natural porosity of about 40% and water content that varies between 24 and 30%. Samples were saturated before heating. The slow heating ensured a constant isotropic effective stress of 4 MPa. Four tests were carried out to check the repeatability of results.

It can be observed (Fig. 3.8) that no significant volumetric strains are recorded at temperatures lower than 60-70°C. Referring to the simple constitutive formulation presented in the previous section, this lack of strains during heating implies a value of parameter β_{pm} equal to 0. Beyond this value, the slopes of curves increase significantly showing a sample contraction. On the other hand, curves of drained water indicate that pore water was expelled when total volumetric strains were practically null at temperatures between 40 to 70°C depending on the test. In that range of temperatures tested, no porosity changes were measured. This fact can be interpreted considering

the difference between the water and solid thermal dilation coefficients. Solid particles may not dilate enough to induce structural changes in the soil skeleton and then porosity remains constant. Water, however, which has a higher thermal expansion capacity, tends to dilated significantly and then it is expelled.

At higher temperatures, drained water volume increases significantly to compensate not only the volume increment of solid particles and water, but also the thermal collapse or contraction of clayey soil. Several reasons for thermal collapse of a clayey porous medium have been discussed in Young *et al.* (1962), Plum and Esrig 1969, Morin and Silva (1984), Towhata *et al.* (1993), Paaswell (1967), Habibagahi (1977), Robinet *et al.* (1996) and Sudem *et al.* (2007). For instance, the thermal dilation may produce a decrease in the strength and modify the distance between clay particles. Then a change in equilibrium between Van der Waals attractive forces and electrostatic repulsive forces takes place which results in a new closer distribution of clay particles.

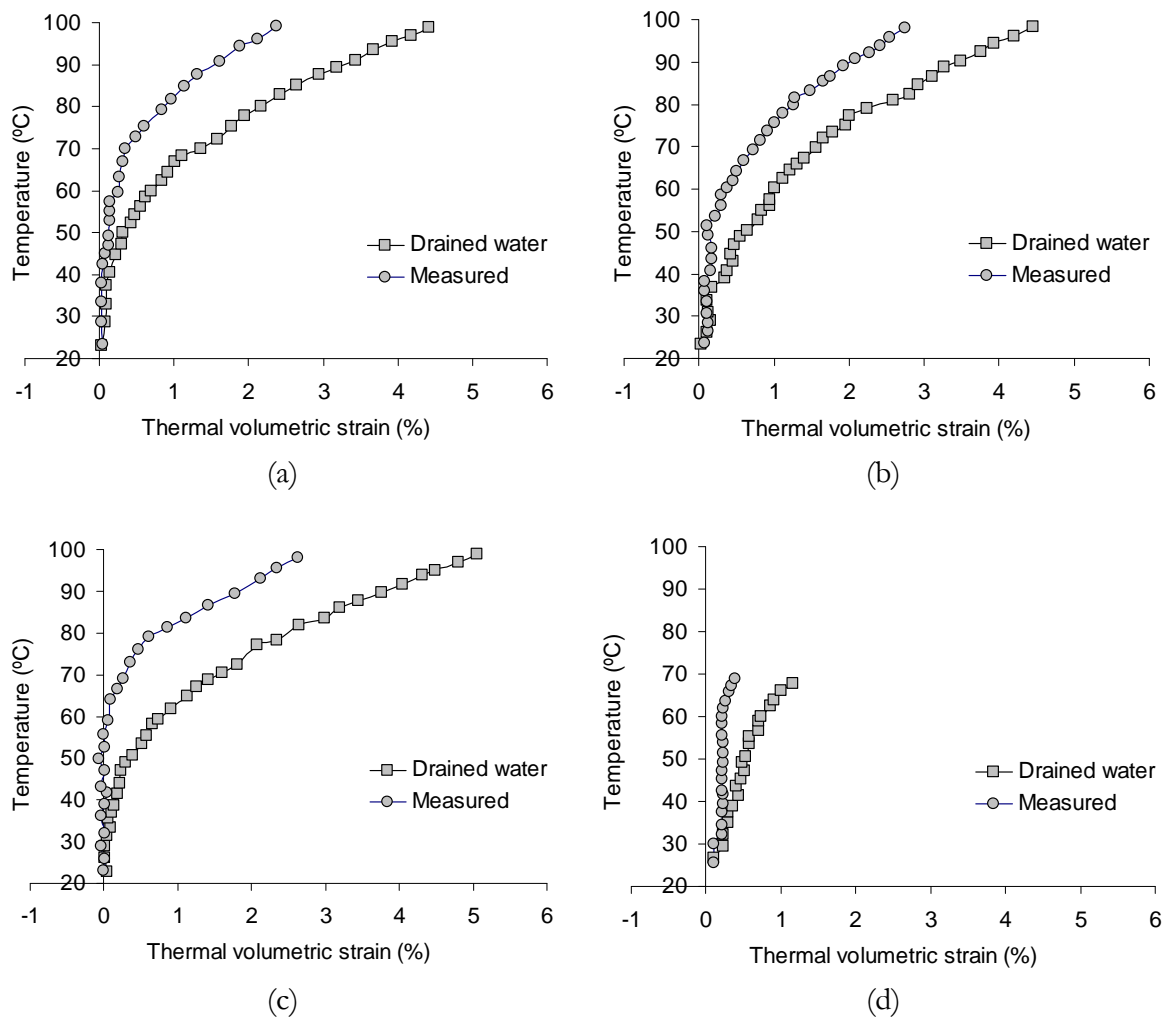


Figure 3.8 Thermal volumetric strain and drained water on Boom Clay: (a) Test 1; (b) Test 2; (c) Test 3; (d) Test 4 (Delage *et al.*, 2000).

Experimental data indicate that the drained behaviour of soil under heating is highly dependent on the stress level measured in terms of the overconsolidation ratio (OCR).

The effect of OCR under different confining stresses on the thermal behaviour of Boom clay is illustrated in Figure 3.9 (Delage *et al.*, 2004). Temperature variations from 22 to 100 °C and subsequent cooling to 22°C were applied. Normally consolidated samples showed contraction from the beginning, a result which is independent of the two mean effective stresses applied. As the OCR increases, thermal contraction appears at higher temperatures values (around 80°C). Below this temperature, linear elastic expansion is observed (the slopes of volumetric strain curves in heating and cooling are parallel).

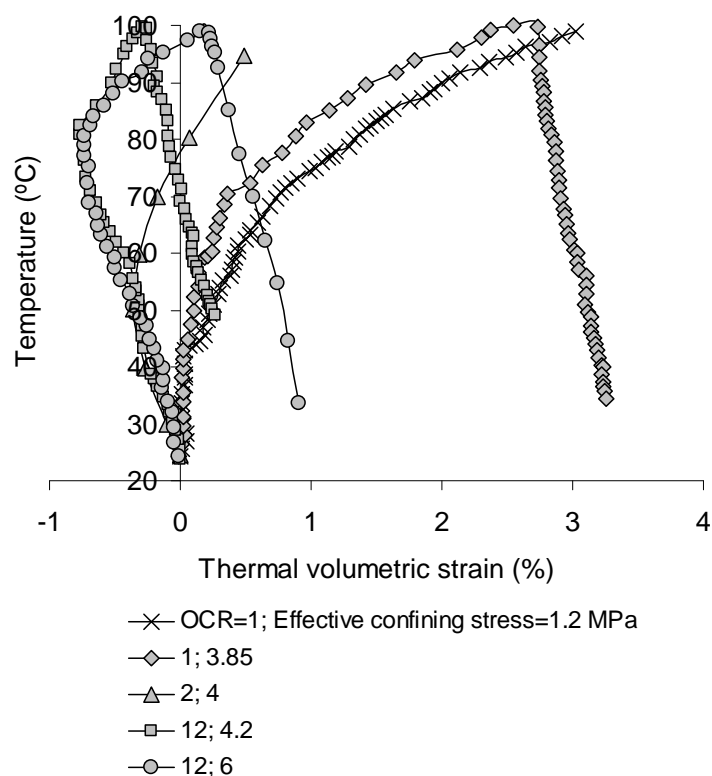


Figure 3.9 Volume changes under heating and cooling at different OCR on Boom clay (Delage *et al.*, 2004)

Other published data (Demars and Charles, 1982; Plum and Esrig, 1969; Baldi *et al.*, 1988; Towhata *et al.*, 1993; Cekerevac and Laloui, 2004) on clayey soils show similar behaviour to Boom clay.

Figure 3.9 show that irreversible contractive strains are accumulated after a whole temperature cycle specially at low OCR. Soils densify during thermal loading, at constant effective stress. This result can be interpreted as an increment in the overconsolidation ratio and, in terms of elastoplastic framework, an increment in

preconsolidated effective stress. Similar results were also observed by Towhata *et al.* (1993) and Plum and Esrig (1969).

Data on low porosity indurated claystones is scarcer. Similar trends should be expected but the intensity of temperature induced deformations would reduce substantially.

Changes in preconsolidation pressure with temperature

Loading samples previously heated under a loading smaller than the preconsolidation pressure allowed the observation of a decrease in preconsolidation pressure with the increase in temperature (Sultan, 1997; Delage *et al.*, 2004).

3.1.4 Residual shearing behaviour. Shearing rate effects

Another important aspect necessary for a comprehensible understanding of landslides acceleration is the effect of shearing on the available frictional strength.

It is well known the dependence of frictional strength with relative shear displacements at low shearing rate. Stiff and overconsolidated clays, exhibit a peak strength associated with low values of displacement. As the magnitude of shear displacement increases, under drained conditions, strength may reduce until a minimum value called residual strength. This loss of strength is mainly related with the gradual realignment of platy particles into a direction parallel to the direction of shearing. Peak strength is mainly controlled by soil structure whereas strength during sliding shear is directly related to inter-particle friction, which seems to be related to the type of clay mineral. The concept and role of residual strength, as well as the properties and effects of discontinuities, was discussed in Skempton (1964, 1966), Skempton *et al.* (1967), Skempton and Hutchinson (1969) and Chandler and Skempton (1974).

The shear strength reduction along slip-surfaces coming from landslides and tectonic shear zones has been directly evaluated by several authors (Skempton *et al.*, 1967; Alonso and Gens, 2006; Wen *et al.*, 2007; Jian *et al.*, 2009). The authors examined the shearing behaviour of samples taken from the slip surfaces and, in some cases, results were compared with tests on specimens of “intact” clay taken several centimetres away from the shear zone where particle re-orientation can not be expected. As an example, samples taken in the site of a large landslide in brown London clay (LL=83%, PI=51%, CF=55-57%) exhibited a drop of cohesion from 160 to 3 kPa and of frictional angle from 20 to 12° when intact and natural shearing samples were compared (Skempton and Petley, 1967).

During the last six decades, the drained residual strength has been extensively studied at laboratory scale and it has been correlated with soil properties as:

mineralogy, grain size and shape (i.e. clay content and the granular void ratio defined by Lupini *et al.* (1981) as the ratio between the volume of platy particles plus water over the volume of rotund particles), index properties, and normal stress. A review of laboratory works and interesting contributions on this subject was presented by Lupini *et al.* (1981). These authors identified two main modes of shearing related with different values of residual strength depending on the quantity of platy particles (Fig. 3.10):

Turbulent Mode in soils with a high proportion of rotund particles or with platy particles of high interparticle friction. In this kind of soils preferred platy particle orientation does not occur and the residual friction is high (although they may show brittleness because of stress history);

Sliding Mode in soils with high proportion of platy, low-friction particles. In this case, particles orientate and a polished continuous surface may be formed with a low residual friction angle associated.

A third *Transitional Mode* was also identified involving both turbulent and sliding shearing.

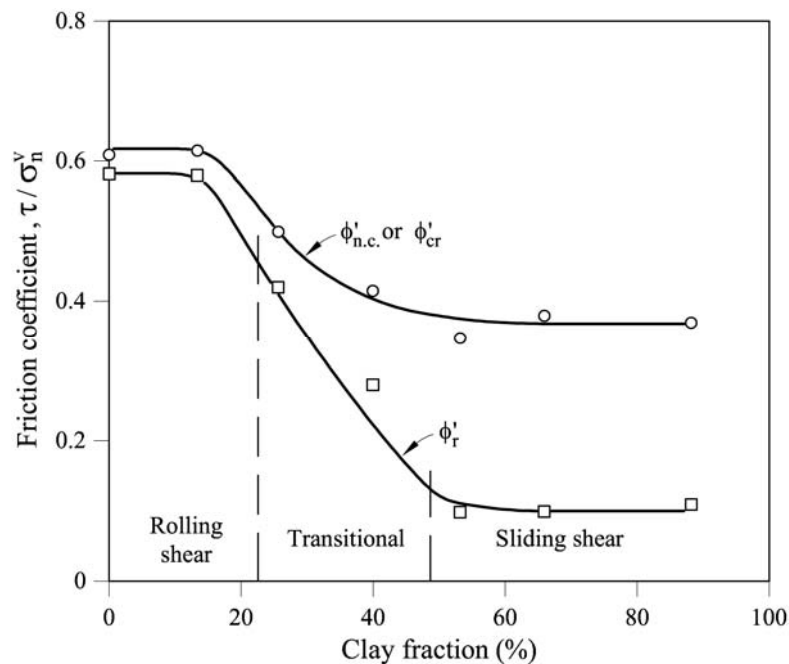


Figure 3.10 Effect of clay fraction on the normally consolidated (or critical state) friction angle and on the residual friction angle. Ring shear tests on sand-bentonite mixtures (after Lupini *et al.*, 1981 and Skempton, 1985).

Vaughan *et al.* (1978) indicated that a useful practical dividing line was provided by plasticity index, PI, for a range of typical British clays (Fig. 3.11). Clays having PI less than 25% undergo turbulent shear at large strains so that peak and residual angles of

shearing resistance, ϕ'_p and ϕ'_r , are similar. Clays having PI greater than 30% undergo sliding shear so that residual angles of shearing resistance are much lower than peak angles. And finally, for clays having PI between 25% and 30% behaviour at large strains was found to be transitional. The use of plasticity index is of restricted applicability and the attained conclusions can not be totally generalized.

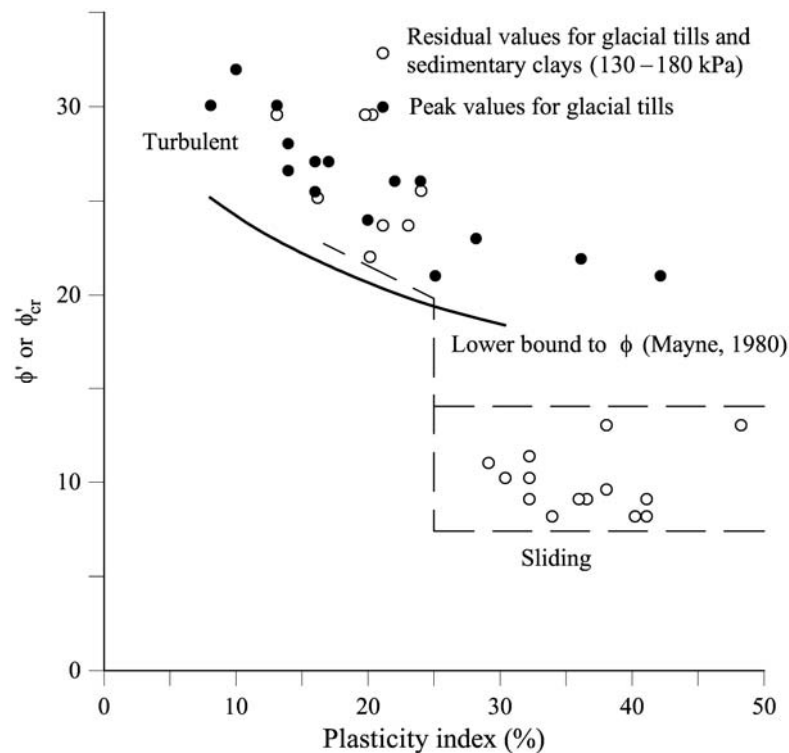


Figure 3.11 Peak friction angles and residual friction angles as a function of plasticity index for typical UK clays (based on Vaughan *et al.*, 1978)

Shearing softening of soils and rocks has two direct practical implications in the stability problems of landslides. First, the expected available resistance of pre-existing shear zones caused by old landslides or tectonic forces will be close or equal to the residual strength. In fact, available strength in pre-existing shearing planes may be lower than the expected residual strength obtained in the laboratory due to dependence on the effective normal stress. Increments in normal effective stress involve a non-linear reduction of shearing strength (Picarelli, 1990). Shear zones may be formed during geological periods under loads higher than the current one due to tectonic origin or further erosion. The lower frictional angle previously reached probably remains in the reactivation of landslides at current and lower effective normal stress.

The second practical implication of the shear strength loss with relative displacement is the phenomenon of progressive failure. Progressive failure was identified as a mechanism leading to instability of first-time slides in overconsolidated clays by Skempton, (1964), Terzaghi and Peck (1967), Bjerrum (1967), Bishop (1967)

and Bishop (1971). A review of the subject has been presented by Jardine *et al.* (2004). Progressive failure mechanism will not be discussed further here because the cases analysed in subsequent chapters are in fact reactivations of ancient landslides.

All the investigations on the strength of soils mentioned in this section concern to drained strength and its minimum value reached at slow rates of relative shearing displacement. However, the knowledge of the rate of displacement on the shearing strength is necessary if dynamic terms are included in the analysis of landslides. This is the case if the run-out of landslide or the effect of an earthquake are examined. Skempton *et al.* (1989), Bacegirdle *et al.* (1991) and Vardoulakis (2002) considered rate effects to analyse reactivated landslides

Increasing the rate of displacement may involve an undrained shearing response of the soil. Significant excess pore water pressure (positive or negative) can be generated depending on the dilatant or contractive soil behaviour. Overconsolidated clays tend to dilate. At slow rate of shearing water can flow into the zone. If shearing is fast, water migration to the shear zone can not be developed and higher peak strengths are mobilised. This effect was demonstrated by Atkinson and Richardson (1987) testing reconstituted London clay. In the case of contractive response, pore water pressure will be generated and lower frictional strength will be achieved.

However, for the purpose of the work presented here on the acceleration of reactivated ancient landslides, it is interesting to focus on observed rate-dependent phenomena of shearing strength once residual conditions have been reached rather than its effect on peak strength. Figure 3.12 presented by Tika *et al.* (1996) summarizes such effect. Fast shearing is applied after reaching residual conditions at slow rate. Four phases could be differentiated:

- (a) There is an initial threshold strength at a negligibly small displacement considerably higher than the slow drained residual strength. The threshold strength increases with increasing rate of displacement.
- (b) A second stage shows an increase in strength on the shear surface with fast displacement up to a maximum value, the fast peak strength, which is generally accepted to be higher than the residual one.

Fast peak strength is again function of the rate of displacement. Tika *et al.* (1996) concluded that a higher value of fast peak strength with respect to the threshold was observed mainly in materials showing sliding shear mode. This increment was associated with the volume changes (dilation) taking place initially within the shear zone due to disorientation of the particles aligned during the previous slow shearing because of the higher velocity of shearing.

- (c) The strength, if further fast displacement is applied, drops to a minimum value called fast residual strength. Different behaviours were observed at this stage if the magnitude of the fast residual strength was compared with the slow residual value (Fig. 3.12). If rapid residual strength is higher, the response is called positive; negative if it is lower; and neutral if residual strength does not varies with rate of shearing.

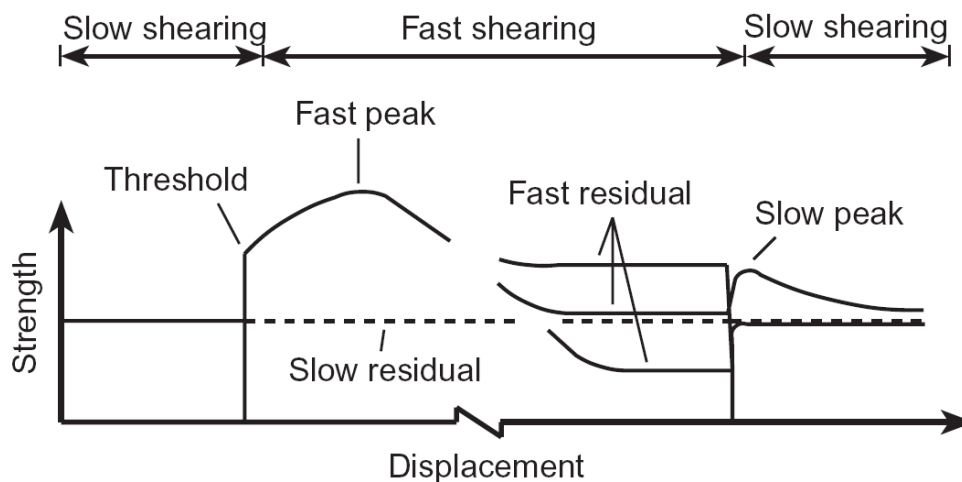


Figure 3.12 Observed rate-dependent phenomena for residual strength (Tika *et al.*, 1996).

The causes that determine the effect of the rate of displacement on the residual strength are not clear. Several reasons have been discussed in different cases: liquefaction (Terzaghi, 1956; Seed, 1968; Casagrande, 1975; Hutchinson, 1986); microstructural changes interpreted as thixotropic phenomena (Seed and Chan, 1957; Mitchell, 1960; Osipov *et al.*, 1984); mechanical fluidification (Howard, 1973; Hsu, 1975; Koerner, 1977); and also the implication of frictional heating generation analysed in this Thesis.

Tika *et al.* (1996) started at the shearing phenomena described before in order to interpret fast shearing response. Soils with turbulent shear mode maintained a value of residual strength independently of the rate of displacement, although in some of them the response was dependent on the level of normal stress. Soils with transitional shear mode showed fast residual strength lower than the slow one (negative effect). And finally, soils with sliding shear mode showed either negative or positive effects. The negative effect in particular was observed in soils with intermediate clay fraction ($CF = 3-55\%$) and low to high plasticity ($IP = 10-37\%$). No information on the compressibility or permeability of the tested materials is given in the paper.

It is important to take into account the effect of the applied velocity in the laboratory test. The velocity applied in most of fast ring shear tests published reaches a

maximum value of 6 m/min. It has been observed in some of the test reported by Tika *et al.* (1996) that a loss in strength at fast residual condition, with respect to the ‘slow’ one takes place at rates of displacement exceeding a critical value.

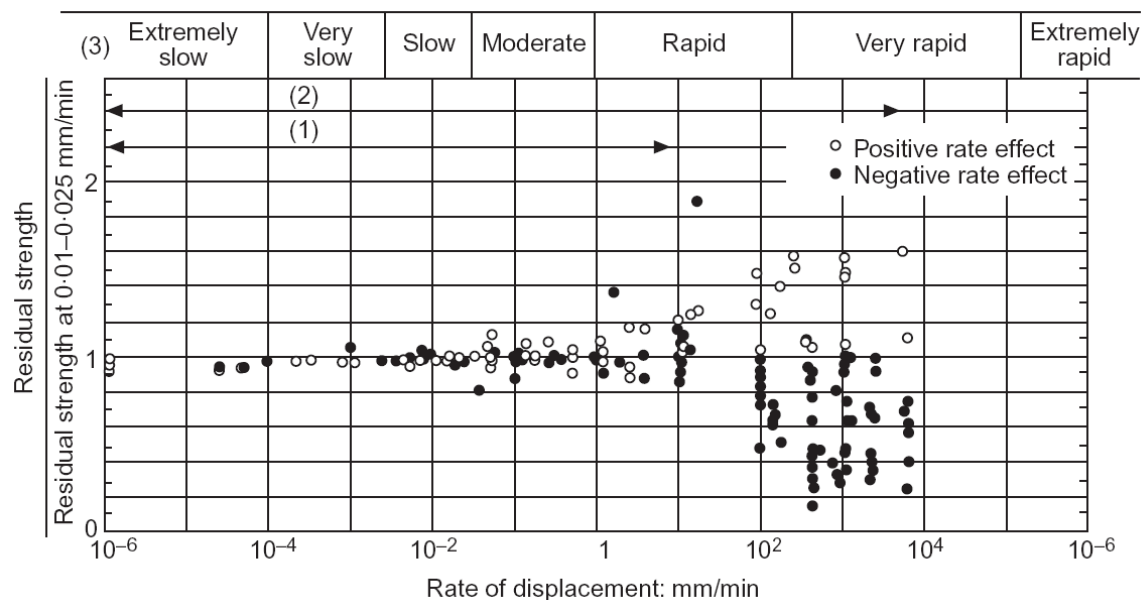


Figure 3.13 Variation of residual strength of cohesive soils with rate of displacement (Tika *et al.*, 1996).

This aspect and other experimental observations mentioned by Tika *et al.* (1996) during fast shearing tests could be appropriately interpreted considering the effect of frictional heating generation. The idea, mentioned previously, is that friction at the shear zone may induce excess pore pressures which can lead to a reduction of the residual shear strength with respect to the shear strength measured at slow rate of displacement. Figure 3.13 shows the ratio of residual strength measured at different rate of displacements over the drained residual strength reached at slow rate of displacement (between 0.01 to 0.025 mm/min). Different kind of materials (sandstone, siltstone, clayey siltstone, claystone, residual soils, clays) were tested by different authors (Lemos, 1986; Tika, 1989; Lupini, 1981). From these results, it can be concluded that for rates of displacement lower than 1 mm/min the variation of residual strength remains within the range of 10%. For rates of displacements greater than 1 mm/min (rapid to extremely rapid movement) the variation of residual strength becomes significant. In most cases, high rates of displacement involved a negative effect. In particular, positive rate effects were only observed in tests carried out on London clay ($w_L = 57-75\%$; $PI = 36-51\%$; $CF = 36-57\%$) and Kaolin ($w_L = 66-72\%$; $PI = 33-36\%$; $CF = 66-74\%$) presented by Lupini (1981) and Tika (1989) (both authors tested both materials). The fact that a critical value of rate of displacement should be exceeded to induce a reduction of the available shear strength can be explained as

follows considering the effect of frictional heat. Relatively low values of rate of displacement applied during relatively short time probably are not enough to generate the heat generation required to induce a significant increment of pore water pressure and therefore, a significant reduction of the available shear strength.

Table 3.1 Pore water pressure and temperature measurements during ring shear test at different rates of displacement (Tika *et al.*, 1996).

	Clayey siltstone (PI=21%,CF=8%) (Lemos, 1986)		Clayey siltstone (PI=24%,CF=25%) (Tika, 1989)			Claystone (PI=26%,CF=37%) (Tika, 1989)	
Porosity, n (%)	33		33.5			36.5	
Compressibility coefficient, m_v (kPa^{-1})	1.8		2.5	2.1	1.6	2.5	1.8
Rate (mm/min)	800	6200	380	370	370	400	160
Normal stress, σ_n (kPa)	492	512	135	195	385	232	500
Slow Drained Residual Strength over Normal Effective Stress, τ_{res}/σ'_n	0.274		0.383	0.326	0.262	0.189	0.185
Residual Strength at indicated rate of displacement over Total Normal Stress, τ/σ_n	0.143		0.140	0.165	0.247	0.082	0.083
Measured Maximum Increment of Temperature, $\Delta\theta$ ($^{\circ}\text{C}$)	2.50	2.40	0.71	0.84	2.42	0.59	0.64
Measured Maximum Increment of Pore Water Pressure, Δu_w (kPa)	-	-	-	25	-	-	75

Tika *et al.* (1996) also observed the response of soils with negative effect when slow shearing was applied after a fast stage. Initially, when the rate of displacement is reduced, the mobilized strength was similar to the value of fast residual strength reached at high velocity and, in a time period similar to the consolidation time of the soils (measured independently from settlement observations), the strength was

increasing until reaching the higher slow residual value of the soil. This fact seems to indicate that the strength variation is a consequence of the generated and accumulated excess pore pressure at the sliding zone. The slow residual strength is recovered when the shearing rate is reduced and heat-induced pore pressure generation gives up - because heating is proportional to the rate of displacement- and excess pore pressure dissipation takes place.

During fast stages, dissipation also takes place. However depending on different factors (permeability, compressibility, friction angles and shear velocity) heat induced pore pressure can be enough to reduce the effective shear stress even taking into account dissipation. Tika *et al.* (1996) observed that in a test in which a prolonged fast shearing was applied, the low strength persisted. This fact was used for the authors as argument against the argument that pore water pressure causes the reduction of shearing strength at high rate of displacement. However, considering again thermal effects, a lower strength may remain during long time of rapid shearing if the excess pore pressure generated by frictional heating is higher than its reduction by dissipation.

Lemos (1986), Tika (1989), and Tika and Hutchinson (1999) measured directly pore water pressure and temperature during fast shearing. Soil shearing was imposed against an instrumented rough glass interface (more details are given in Tika *et al.*, 1996). They observed that the behaviour of the tested materials when sheared against rough glass interfaces was similar to that observed in the soil-on-soil tests. Obtained results in terms of pore water pressure and temperatures measured are given in Table 3.1.

Table 3.2 Properties and mineralogy of samples from Vaiont landslide (Tika and Hutchinson, 1999).

	LL (%)	PI (%)	% 2 μm	Minerology		
				Clay minerals	Calcite	Quartz
Sample 1	49	19	27	50 %: 25 % smectite 25 % illite-smectite <5 % koalinite	45 %	<5 %
Sample 2	50	22	30	50 %: 50% illite-smectite <5% koalinite	40 %	10 %

Special consideration is now made to the shearing tests carried out on samples from the strata where the sliding surface of Vaiont landslide was located. Tests were reported by Tika and Hutchinson (1999). Properties and minorology of samples are indicated in Table 3.2. Samples were initially sheared at a drained rate of 0.0145 mm/min and residual conditions were reached. After this stage alternately fast and

slow shearing rates were applied. The influence of normal stress and shearing rate on the residual strength and rate effects was also assessed applying 250, 500 and 980 kPa. Figure 3.14 shows the stress ratio-displacement curve obtained during the slow shearing for a reconstituted samples tested at $\sigma'_n = 500$ kPa. A peak shear strength around 26° is exhibited. It reduces to a minimum residual value equal to 10° approximately. This low value can be explained by the mineralogy of the soil (Table 3.2). In the range of normal stress applied, its effect on the residual strength (Fig. 3.15) does not seem to indicate a clear tendency.

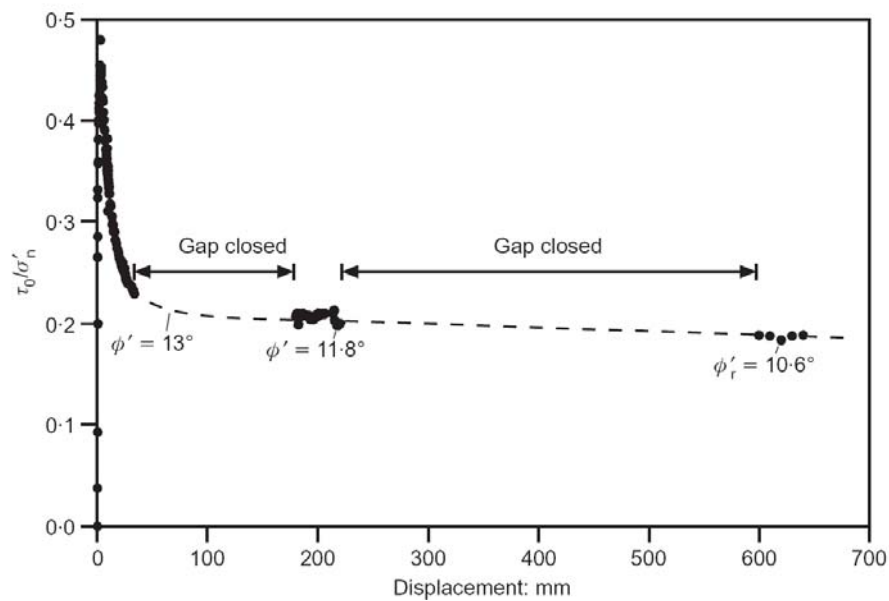


Figure 3.14 Slow shearing behaviour of a reconstituted sample from Vaiont landslide (Tika and Hutchinson, 1999).

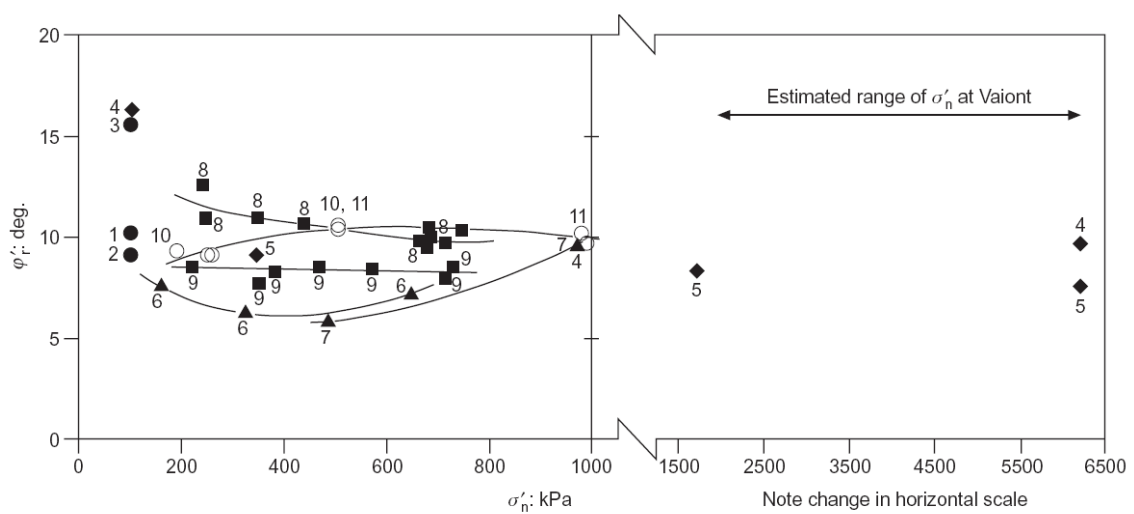


Figure 3.15 Effect of normal effective stress on slow residual strength in samples from Vaiont landslide (Tika and Hutchinson, 1999).

The influence of rate of displacement on the stress ratio at fast shearing rate over the stress ratio measured at drained (slow) residual shearing is shown in Figure 3.16. Samples exhibited a drop of strength below the slow residual value. A minimum fast strength equal to $\tau/\sigma_n = 0.081$, equivalent to $\phi' = 4.6^\circ$ was measured at 100 mm/min of shearing rate. Temperature was not measured during those tests.

It is felt that additional testing programs examining the effect of shearing rate on residual strength, which include also pore pressure and temperature measurements are needed to settle this important issue.

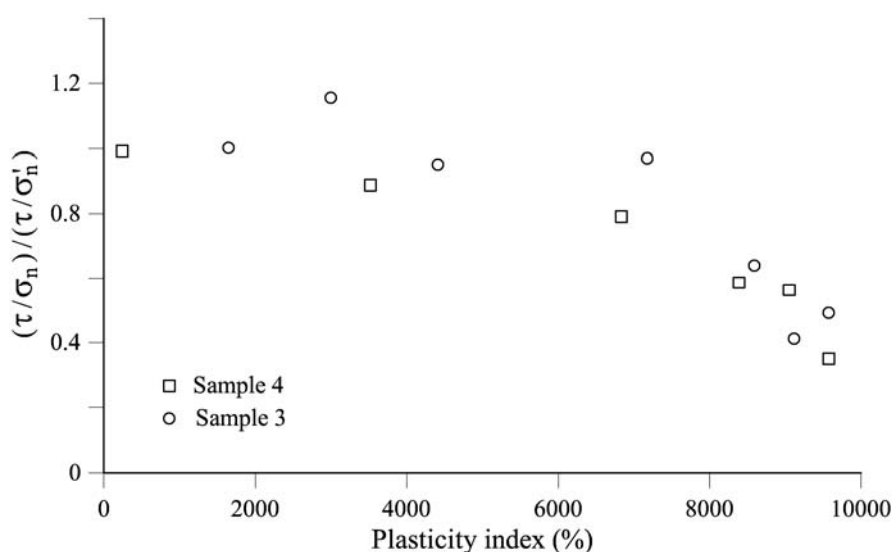


Figure 3.16 Effect of rate of displacement on shearing strength (Tika and Hutchinson, 1999).

3.1.5 Thickness of shear bands

A common observation in translational and rotational slides is that deformations are confined to a shear zone of very small thickness. In practice, shear zone is characterized by the complex set of minor shears and slip surfaces generated during the sliding. In some cases a well-defined unique shearing surface may be identified. In this worth, the implicit assumption is that a single shear band defines the slide. The thickness of the shear band, a relevant property in the analysis presented in this Thesis on rapid landslides, is difficult to estimate (Oda and Kazama, 1989). Direct observations of sliding surfaces in clayey materials indicate that their thickness is very small, typically in the range of a few millimetres. One example is given in Figure 3.17, which shows a portion of the sliding surface of Cortes landslide (Alonso *et al.*, 1993). The sliding surface was identified, when it was exposed after a large excavation, because of its greenish-gray colour, in contrast with the brown tonalities of the marl layer, two meters thick, where it was embedded. Massive limestone strata, which

essentially slid as a rigid body, covered the marl layer. The thickness of the striated layer ranged between 3 and 5 mm.



(a)



(b)

Figure 3.17 (a) Sliding surface of Cortes landslide showing motion grooves; (b) A view of the sliding surface in cross section. The upper layer of gray clay, overlying the brownish lower marl, was identified as the sliding surface.

Several authors also worked on this subject (Morgenstern and Tchalenko, 1967; Roscoe, 1970; Vardoulakis, 1980; Bridgwater, 1980; Scarpelli and Wood, 1982; Desrues 1984; Mühlhaus and Vardoulakis, 1987; Desrues *et al.* 1996; Oda and Kazama, 1998;

Didoignon *et al.*, 2001; Wood, 2002) observing shear bands of granular and fine soils by means different laboratory techniques (X-ray photographs, tomographic methods, scanning electro microscope (SEM), transmission electomicroscope (TEM)). Morgenstern and Tchalenko (1967) in their study on shear zones from slips in natural clays at microstructural scale concluded that shear zones are normally several millimetres thick. They analysed directly samples taken from the sliding surface involved in natural landslides subjected to different degrees of movement.

An important conclusion of basic research is that shear band thickness is related to a characteristic grain size. Depending on the grain size, several linear relationships between the mean particle size ($d_{50\%}$) and shear band thickness have been proposed. In sands, thickness of the shear bands is around 6 to 7 times $d_{50\%}$. In clayey soils, shear zones, where the displacement is distributed among many slip surfaces, range between 0.5 and 5 cm wide, although major concentration of relative displacement seems to be concentrated along a principal slip “surface” of 10 to 50 microns wide (Skempton *et al.*, 1967). Vardoulakis (2002) proposes a value $e \approx 200d_{50\%}$. Rice (2006) presents a comprehensive review of the thickness of the slip zone measured in active faults.

3.2 PROBLEM APPROACH AND GOVERNING EQUATIONS

For the purpose of analysing landslides including thermo-hydro-mechanical effects in the shear zone, consider in the sketch of Figure 3.18a a representative cross section of a landslide and in Figure 3.18b a thick clay layer where the sliding surface is located. The shear band proper will be located within the clay layer (Fig. 3.18c). Its thickness is many orders of magnitude smaller than the horizontal and vertical dimensions of the slide. Governing equations for the analysis of rapid landslides are here developed referring to this representation.

3.2.1 Shear strains and heat generation in the shear band

Consider a detail of a shear band of indefinite length (L) and thickness ($2e$) (Fig. 3.19). Since $L \gg e$, the excess pore pressure, $u_m(z,t)$, temperature, $\theta(z,t)$, and velocity, $v(z,t)$ are assumed to be exclusively a function of the position normal to the band direction (z) and time (t) (Fig. 3.18b,d). A common temperature is considered for solid particles and pore fluid. This is a result of the assumption of local thermal equilibrium between both species (solid and water).

If the slide moves as a rigid body with a velocity v_{max} , shear straining, which will be concentrated on the shear band, will induce an average shearing strain rate of

$$\dot{\gamma} = \frac{v_{max}}{2e} \quad (3.9)$$

where $2e$ is the thickness of the shear band. A linear distribution of velocity has been assumed.

Therefore, during the sliding motion all the straining work will be concentrated inside the band. The volumetric deformation of the clay material which constitutes the band will be very small compared with the extremely large shear deformations induced by sliding on a thin clay band. Therefore, the rate of mechanical work input per unit volume of band material will be essentially given by

$$\dot{W} = \tau_f \dot{\gamma} = \frac{\tau_f v_{\max}}{2e} \quad (3.10)$$

where τ_f is the shear strength offered by the shear band. This work done inside the shear band, neglecting elastic strains, will be dissipated entirely into heat, following the first principle of thermodynamics. As a consequence, the heat rate generated per unit volume, H is:

$$H = \dot{W}_{band} = \frac{\tau v_{\max}}{2e} \quad (3.11)$$

(units of Eq. (3.11) in a SI system are Watt/m³ or Joule/s m³). All dissipation in the fluid has been neglected.

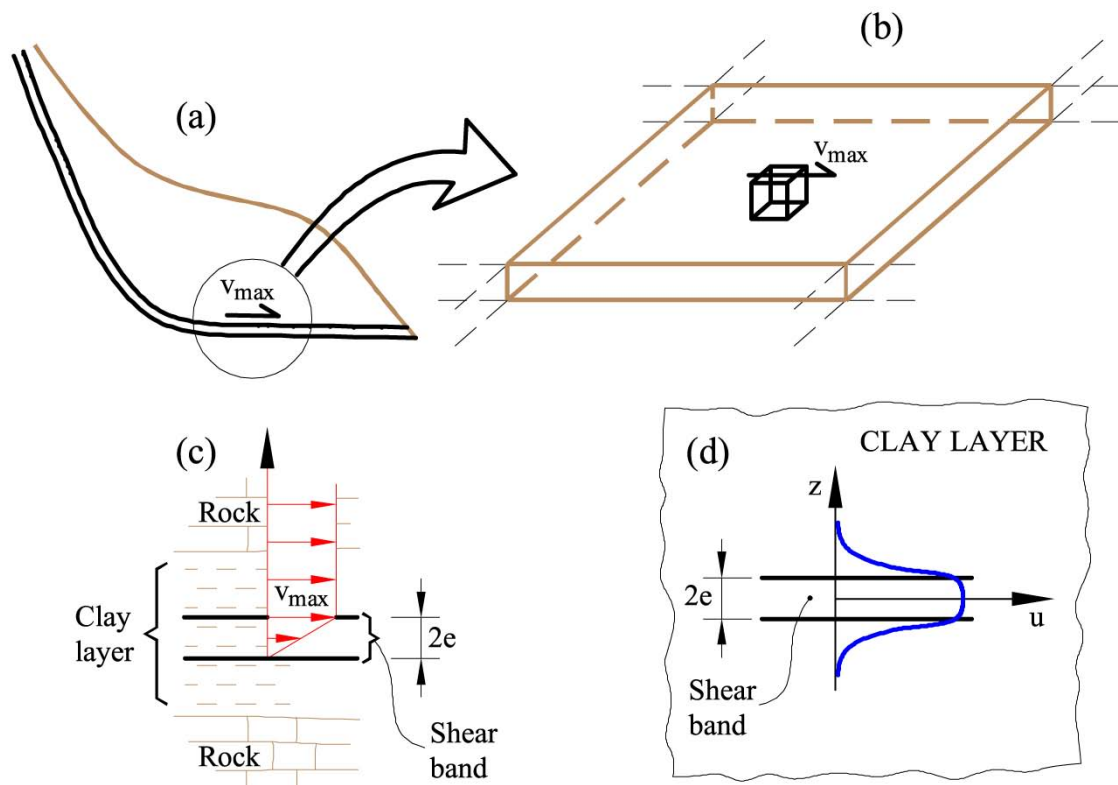


Figure 3.18 Translational landslide: a) "in situ" conditions; b) representative element of the sliding surface; c) shear band; d) local axis in the shear band.

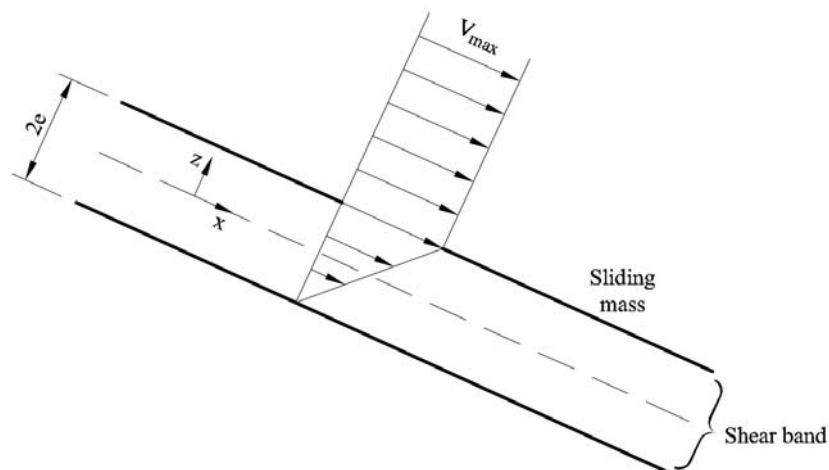


Figure 3.19 Geometry of the planar shear band.

Therefore, the band will increase its temperature during the motion and, in view of the tests discussed before, a pore water pressure in excess of the initially existing one, will develop. Note that the work of volumetric deformations is neglected compared with the shear work.

The excess pore pressure is essentially caused by the thermal dilation of the water. Therefore, despite its potential large effect in modifying effective stresses, the absolute amount of the increment of water volume in the band will be very small. Its dissipation will take place in the immediate vicinity of the band. In other words, the band and its “zone of influence” will have a small thickness (Fig. 3.18d), similar to the thickness of the band itself.

It then becomes reasonable to assume that, for the purposes of investigating the behaviour of pore pressures in the band and its vicinity, the band is essentially a planar feature located within an infinite domain. The lateral extent of this band is very large compared with its thickness and, in addition, points within the band are similar to each other. Water and energy transfer out of the band will take place in a direction normal to the band. The problem of the interaction of the band and its surroundings becomes a one dimensional problem in which the spatial coordinate (z) is directed normal to the band plane (Fig. 3.18d).

3.2.2 Balance equations inside and outside the shear band

Consider a point in a shear band (in general of argillaceous material) of thickness $2e$ surrounded by the rock substratum. The z -axis follows the direction of the gradient of water pressure and temperature generated within the band (Fig. 3.18d).

In many landslides, the shear band will be embedded in a clay layer whose thickness will be several orders of magnitude larger than the band dimensions. The shear band will typically exhibit the same characteristics of the thicker clay layer in which it is embedded. In other words, the band only marks the boundaries of the strain localization phenomena in an otherwise thicker layer. However, heat will be generated exclusively within the localization band. Therefore, in order to formulate the balance equations, it is convenient to distinguish two different materials: the narrow band itself and the remaining layer where the band has developed (Fig. 3.18). In the equations presented later superscripts “b” and “r” refer to the band and to the rest of the layer (“rock” for identification purposes).

Three balance equations should be satisfied in and around the band: the conservation of heat and the conservation of solid and fluid mass “flowing” in and outside the band. In physical terms, the problem to be solved is described as follows: the heat generated inside the band results in an increase of temperature, which is controlled by the heat dissipation taking place concurrently. The resulting temperature increase in the saturated porous band creates an excess pore water pressure. Water flow will immediately develop through the band and into the surrounding “rock”. The actual pore pressures in the band are again the result of two competing phenomena: heat induced pressure generation and flow induced pressure dissipation.

Heat balance equation

If θ is the excess temperature over the initial constant value, the balance of heat in a unit volume of the shear band is written (see Olivella *et al.*,1996) as follows:

$$H = \frac{D}{Dt}(\rho c_m \theta) + \text{div}[-\Gamma^b \mathbf{grad}(\theta)] + \text{div}\left(\rho_w c_w \theta (\mathbf{q} + n^b \frac{\partial \mathbf{u}}{\partial t})\right) + \text{div}\left((1-n^b) \rho_s c_s \theta \frac{\partial \mathbf{u}}{\partial t}\right) \quad (3.12)$$

(a) (b) (c) (d)

where $\frac{D}{Dt}$ is the material derivative with respect to the time (t). The term (3.12a) provides the rate of heat storage and ρc_m is the average product of density and heat capacity of the water-solid mixture. Term (3.12b) accounts for the heat conduction (Γ^b is the conduction coefficient). Terms (3.12c) and (3.12d) provide the advective heat transport components. In fact, the stored heat in water (w) and solid (s) is transported because of the motion of water and solid. Solid velocity ($\frac{\partial \mathbf{u}}{\partial t}$) is expressed as the time derivative of the displacement (\mathbf{u}). The velocity of water through a cross section of unit area will be given by $n^b \left(\frac{\partial \mathbf{u}}{\partial t} + \mathbf{q}^* \right)$, where n^b is the porosity in the band. The term

$n^b \mathbf{q}^* = \mathbf{q}$ is the Darcy flow rate of a fluid filtrating through a porous medium. c_w and c_s are the heat capacities of water and solid, and ρ_w and ρ_s , the corresponding densities.

The assumption made now is that terms (3.12b), (3.12c) and (3.12d) provide a negligible contribution to change the band temperature during the (fast) sliding motion. Terms (3.12c) and (3.12d) will be small because fluid and solid (skeleton) velocities will be small, especially in clay-based materials, where fast sliding is relevant. The rationale to eliminate term (3.12b) is that conduction phenomena require some time to effectively dissipate heat. It will be shown that the time-duration of dangerous sliding is only a few seconds, a small time interval for heat conduction to be relevant. This hypothesis has been checked numerically in the cases developed later.

Thus, Equation (3.12) becomes:

$$\frac{\partial}{\partial t}(\rho c_m \theta) = \rho c_m \frac{\partial \theta}{\partial t} = H \quad (3.13)$$

where the average heat storage capacity ρc_m is assumed to be constant.

Mass balance equations

Only the final conservation equations are given here. A detailed derivation may be found in Olivella *et al.* (1996). The conservation of mass in local form is written:

$$\frac{Dn^b}{Dt} = \frac{(1-n^b)}{\rho_s} \frac{D\rho_s}{Dt} + (1-n^b) \operatorname{div} \left(\frac{\partial \mathbf{u}}{\partial t} \right) \quad (3.14)$$

The conservation of water mass is given by

$$n^b \frac{D\rho_w}{Dt} + \rho_w \frac{Dn^b}{Dt} + n^b \rho_w \operatorname{div} \left(\frac{\partial \mathbf{u}}{\partial t} \right) + \operatorname{div}(\rho_w \mathbf{q}) = 0 \quad (3.15)$$

Substitution of $\frac{Dn^b}{Dt}$ from (3.14) into the water mass balance Equation (3.15) leads to:

$$\frac{n^b}{\rho_w} \frac{D\rho_w}{Dt} + \frac{(1-n^b)}{\rho_s} \frac{D\rho_s}{Dt} + \operatorname{div} \left(\frac{\partial \mathbf{u}}{\partial t} \right) + \frac{1}{\rho_w} \operatorname{div}(\rho_w \mathbf{q}) = 0 \quad (3.16)$$

which provides the mass conservation condition for water and solid.

In order to proceed, constitutive equations should now be considered. Water will be characterized by a constant compressibility coefficient, α_w , and a constant thermal expansion coefficient, β_w . Therefore, the volumetric deformation of the water, ε_w is written,

$$d\varepsilon_{vw} = \frac{dV_w}{V_w} = \frac{d\rho_w}{\rho_w} = \alpha_w dp_w - \beta_w d\theta_w \quad (3.17)$$

(compression strains are taken as positive). If equation (3.17) is integrated, the change in density from a reference state (0), to the current value of pressure and temperature (p_w, θ) is given by,

$$\rho_w = \rho_w^0 \exp\left[\alpha_w (p_w - p_w^0) - \beta_w (\theta - \theta^0)\right] \quad (3.18)$$

Differentiation of Equation (3.18) leads to

$$\frac{D\rho_w}{Dt} = \beta_w \rho_w \frac{D\theta}{Dt} + \alpha_w \rho_w \frac{Dp_w}{Dt} \quad (3.19)$$

Solid grains will be assumed to be incompressible against stress changes but not against temperature (θ) changes. Therefore, in an analogous manner,

$$\rho_s = \rho_s^0 \exp\left[-\beta_s (\theta - \theta_0)\right] \quad (3.20)$$

where ρ_s^0 is the density of solid particles at the reference temperature, θ_0 .

Derivation of Equation (3.20) leads to

$$\frac{D\rho_s}{Dt} = -\beta_s \rho_s \frac{D\theta}{Dt} \quad (3.21)$$

If Equations (3.19) and (3.21) are substituted in Equation (3.16), the following expression is obtained for the mass conservation of solid and water:

$$\left[n^b \beta_w + (1 - n^b) \beta_s\right] \frac{D\theta}{Dt} + n^b \alpha_w \frac{Dp_w}{Dt} + \text{div}\left(\frac{\partial \mathbf{u}}{\partial t}\right) + \frac{1}{\rho_w} \text{div}(\rho_w \mathbf{q}) = 0 \quad (3.22)$$

The first term is a ‘‘source’’ term due to the thermal expansion of liquid and solid; the second term describes the volume changes of water associated with changes in water pressure; the third term represents the volume change of the skeleton; and the fourth and final term provides the volume changes associated with the flow of water.

Pore pressure has two components: the hydrostatic pore pressure which depends on the position of water table and the excess pore pressure induced by heat (u_w). The position of the water table probably does not change within the short interval of the slide and then the time derivative of p_w will depend only on the excess pore pressure:

$$\frac{Dp_w}{Dt} = \frac{Du_w}{Dt} \quad (3.23)$$

Accepting that compressive volumetric deformations are positive, the term

$$\operatorname{div}\left(\frac{\partial \mathbf{u}}{\partial t}\right) = -\frac{\partial \varepsilon_{vol}}{\partial t} \quad (3.24)$$

provides the total volumetric deformation rate of the solid skeleton.

The mass balance equations derived above will be applied to the shear band where one-dimensional conditions can be assumed, as explained before. Therefore, the volumetric strain due to changes in effective stress can be estimated from the one-dimensional compressibility coefficient, m_v^b , and the increment of (normal to the band) effective stress. Volumetric strain may also take place due to changes in temperature. Taking into account both effects, Equation (3.25) can be written:

$$\operatorname{div}(\mathbf{v}) = -\frac{\partial \varepsilon_{vol}}{\partial t} = -m_v^b \left(\frac{\partial \sigma_n}{\partial t} - \frac{\partial p_w}{\partial t} \right) + \beta_{pm} \frac{\partial \theta}{\partial t} = -m_v^b \left(\frac{\partial \sigma_n}{\partial t} - \frac{\partial u_w}{\partial t} \right) + \beta_{pm} \frac{\partial \theta}{\partial t} \quad (3.25)$$

where σ_n is the total stress acting in a direction normal to the shear band. This stress will not change during the motion because the slide geometry remains unaffected. Again, time variation of hydrostatic pressure can be neglected with respect to changes of excess pore pressures. Therefore p_w can be replaced by u_w in Equation (3.25). The last term of Equation (3.25) includes the deformation of porous media due to temperature changes at constant effective stress. The term is especially significant in normally consolidated clays and to a lesser extent in overconsolidated clays. Potentially fast landslides in practice are found in old geological formations and the involved clay layers are indurated, heavily over-consolidated, low porosity materials

The final term in Equation (3.22) refers to the flow through pores due to the gradient of head (Darcy's law). A generalized Darcy's law for a compressible fluid describes the relative flow velocity \mathbf{q} in terms of gradients of pore water pressure and the gradient of elevation as follows:

$$\mathbf{q} = -\frac{k^b}{\rho_w g} \left[\mathbf{grad}(p_w) + \rho_w g \mathbf{grad}(z_g) \right] \approx -\frac{k^b}{\gamma_w} \frac{\partial u_w}{\partial z} \quad (3.26)$$

where k^b is the hydraulic conductivity, which will be assumed to be constant, and z_g is the vertical coordinate. Since the analysis is one-dimensional in a direction normal to the shear band (z direction), the gradient is simply the derivative with respect to z . The flow due to gradients of hydrostatic pressure and gradients of level (z_g term) can be neglected with respect to changes of pore water pressure. In addition, the spatial variation of the hydrostatic pore water pressure can be neglected during the slide and p_w can be replaced by u_w . Therefore, Darcy's flux depends only on the excess pore pressure.

Introducing Equations (3.23), (3.25) and (3.26) into Equation (3.22) the water and solid mass balance equation results in,

$$-\left[n^b\beta_w + (1-n^b)\beta_s\right]\frac{D\theta}{Dt} + n^b\alpha_w\frac{Du_w}{Dt} + m_v^b\left(\frac{\partial\sigma_n}{\partial t} - \frac{\partial u_w}{\partial t}\right) - \frac{1}{\rho_w}\frac{\partial}{\partial z}\left(\rho_w\frac{k^b}{\rho_w g}\frac{\partial u_w}{\partial z}\right) + \beta_{pm}\frac{\partial\theta}{\partial t} = 0 \quad (3.27)$$

A further simplification has been introduced. Under the assumption of small strain rate, material derivatives are approximated as eularian derivatives and Equation (3.27) becomes

$$\left[\beta_{pm} - n^b\beta_w - (1-n^b)\beta_s\right]\frac{\partial\theta}{\partial t} + (n^b\alpha_w + m_v^b)\frac{\partial u_w}{\partial t} - m_v^b\frac{\partial\sigma_n}{\partial t} - \frac{k^b}{\gamma_w}\frac{\partial^2 u_w}{\partial z^2} = 0 \quad (3.28)$$

valid for the shear band, $z \in [-\ell, \ell]$. In Equation (3.28) the water specific weight $\gamma_w = \rho_w g$ is introduced.

Equation (3.28) synthesizes the mass balance equations of solid (grains) and water. It is a parabolic second order differential equation with two unknowns: the temperature and the excess pore water pressure.

If the heat balance Equation (3.13) is substituted in (3.28),

$$\left[\beta_{pm} - n^b\beta_w - (1-n^b)\beta_s\right]\frac{H}{\rho c_m} + (n^b\alpha_w + m_v^b)\frac{\partial u_w}{\partial t} - \frac{k^b}{\gamma_w}\frac{\partial^2 u_w}{\partial z^2} = 0 \quad (3.29)$$

A similar expression may be written for the rock, outside the shear band. But, since no heat is being generated outside the band,

$$(n^r\alpha_w + m_v^r)\frac{\partial u_w}{\partial t} - \frac{k^r}{\gamma_w}\frac{\partial^2 u_w}{\partial z^2} = 0 \quad (3.30)$$

Equations (3.29) and (3.30) summarize the heat, solid and liquid balance equations inside and outside the shear band.

Dynamic equilibrium equation

In general terms, the approach developed before, following principles of energy and mass balance is completed by the momentum balance equation that will describe the acceleration of the landslide. A system of differential equations will be then obtained in terms of the problem variables: excess pore water pressure, temperature and displacement of the slide. The solution is given in Chapter 4 and Chapter 6 under different hypotheses for different kinematics of the slide motion.

CHAPTER 4

Fast Planar Slide. A Closed-Form Thermo-Hydro-Mechanical Solution

Heat-induced excess pore pressures on the failure surface of a planar slide have been calculated by solving mass and heat balance equations on the shear zone developed in Chapter 3. The set of differential equations obtained and the equation of motion for a planar slide have been integrated and solved in closed form for the case of incompressible fluid and incompressible soil skeleton. The solution describes the accelerated motion of the slide. The analytical solution has been compared with the numerical one when soil and water stiffness terms are not disregarded. A case study, based on a well-known translational slide (Cortes slide, Spain) has been solved. Numerical and analytical solutions are compared. Results of a sensitivity analysis indicate that the permeability of the shear band is a key parameter to control the onset of a rapid motion. For a band permeability above a threshold value, in the vicinity of 10^{-9} m/s, fast accelerated motions are very unlikely.

4.1 INTRODUCTION

If a planar slide loses the conditions for strict equilibrium an accelerated motion will start. A simple dynamic calculation involving the dynamics of rigid block sliding on an inclined base shows that, if the equilibrium is barely lost (say the driving force exceeds the resisting force by a small amount), the increase of slide velocity develops at a relatively slow pace. Some case records indicate, however, that very high velocities

may develop in relatively short sliding distances. The case of Vaiont is a reference for fast sliding (Hendon and Patton, 1985; Nonveiller, 1987), which cannot be explained, unless the sliding resistance essentially disappears. Vaiont was not a planar slide. In fact, the failure surface had an “open L” shape, which makes even more difficult to explain why it reached such a high sliding velocity (100 km/hr) in no more than 10-15 seconds. In Vaiont, equilibrium conditions were close to the critical ones for a long time (as the recorded slide motion in the last few months indicate; Nonveiller, 1987). In practice, relatively small changes in pore water pressures acting on the sliding surface lead probably to the acceleration of the slide motion.

The governing equations developed in Chapter 3 are now considered together with the motion equation for the particular case of a planar landslide. One of the aims of the analysis is finding practical criteria to decide when a planar slide may become a catastrophic event, due to its high velocity.

It turned out that, under reasonable assumptions, a closed form solution could be found for the sliding velocity. Then, other derived quantities of interest in the band (pore water pressure, temperature, available strength) could be easily calculated. The derived solution was then used to perform a sensitivity analysis, with the purpose of isolating the most relevant factors governing the triggering of a fast sliding motion.

In addition to this purpose of the work developed, analytical solutions are very useful to perform validation exercises for numerical methods. In this regard, the solution found corresponds to a highly coupled thermo-hydro-mechanical problem which involves the pore water pressure generation and dissipation in a shear band being heated by the frictional work induced by the sliding motion.

4.2 THE MOTION EQUATION FOR A PLANAR LANDSLIDE

Consider a unit length of shear band (Fig. 4.1) and the element of solid rock (total vertical weight, W) resting on it. The element of solid rock is displacing at a velocity, v^{max} , parallel to the slope (inclination: α). The available shear strength to resist the motion will be calculated at the midplane ($z=0$) of the shear band where maximum excess pore pressures ($u_w^{max}(t) = u_w(z=0, t)$) will develop. This shear strength, which will change in time because the pore water, u_w^{max} , will also change with time, is given by:

$$\tau_f(t) = \sigma'_n \tan \phi' = (\sigma_n - p_w(t)) \tan \phi' \quad (4.1)$$

where σ_n, σ'_n are the total and effective normal stresses on the band; p_w is the water pressure at the midband position ($p_w = p_{wh} + u_w^{max}$); p_{wh} is the hydrostatic pressure acting on the band before the initiation of the motion, and ϕ' is the effective friction angle of the shear band.

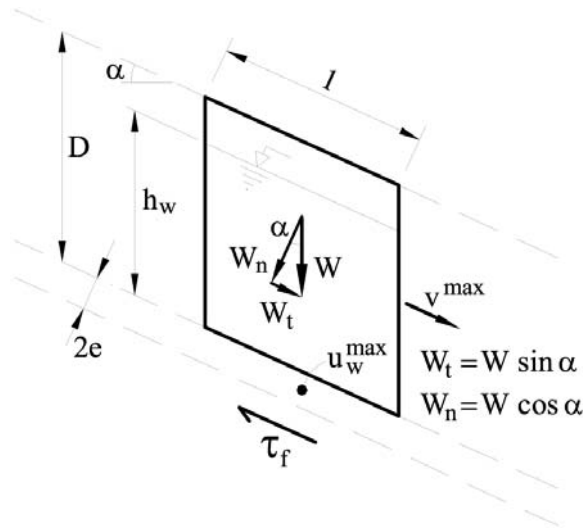


Figure 4.1 Element of rigid block sliding at velocity v on the shear band

Newton's second law, applied to the motion of the rock slice of weight, W , is now written as:

$$W \sin \alpha - \tau_f = \frac{W}{g} \frac{dv^{\max}}{dt} = M \frac{dv^{\max}}{dt} \quad (4.2)$$

where M is the mass of the reference moving block. M can be computed if the depth of the sliding surface (D in Fig. 4.1) and the average rock density, ρ_r , is known. Note that Equation 4.2 is valid for constant mass. The equilibrium pore water pressure, p_{wh} , can be estimated if the height of the phreatic surface, h_w , above the shear band is known.

4.3 NUMERICAL SOLUTION

Summarizing the results obtained in Chapter 3 and in the previous section, the set of equations governing the motion of an infinite planar slide are:

- a) Equilibrium conditions and Mohr-Coulomb strength law

$$\tau_f(t) = [W \cos \beta - P_{wh} - u_w^{\max}(t)] \tan \varphi' \quad (4.3a)$$

- b) Heat generation in the shear band

$$H(t) = \tau_f(t) \frac{v^{\max}(t)}{2e} \text{ for } z \in [-e, e] \quad (4.3b)$$

- c) Mass balance (water and solid) and heat balance in the shear band

$$\begin{aligned}
& -\left[(1-n^b)\beta_s + \beta_w n^b\right] \frac{H(t)}{\rho c_m} + (m_v^b + n^b \alpha_w) \frac{\partial u_w(z,t)}{\partial t} = \\
& = \frac{k^b}{\gamma_w} \frac{\partial^2 u_w(z,t)}{\partial z^2} \text{ for } z \in [e, e]
\end{aligned} \tag{4.3c}$$

d) Mass balance (water and solid) in the sliding mass (outside the band)

$$\begin{aligned}
& \left[m_v^r + n^r \alpha_w\right] \frac{\partial u_w(z,t)}{\partial t} = \frac{k^r}{\gamma_w} \frac{\partial^2 u_w(z,t)}{\partial z^2} \\
& \text{for } z \in (-\infty, -e] \cup [e, \infty)
\end{aligned} \tag{4.3d}$$

e) Dynamic equilibrium

$$\frac{dv^{\max}(t)}{dt} = \frac{1}{M} \left[W \sin \beta - \tau_f(t) \right] \tag{4.3e}$$

In this particular case, a planar landslide, the total stress acting on the shear band is constant. No deformations associated with temperature changes are considered here ($\beta_{pm} = 0$). They are mainly significant in normally consolidated clays. Potentially fast landslides in practice are found in old geological formations and the involved clay layers are, in general, indurated, heavily over-consolidated, low porosity materials.

This system of equations can be immediately reduced to three equations if the strength (τ_f) and heat rate (H) expressions are replaced in Equations (4.3c,e). A single equation for the dependent variable u_w could eventually be found. To solve these equations it is also necessary to define the appropriate initial and boundary conditions. A natural initial condition for the dynamic problem is a situation in which static equilibrium has been slightly exceeded. It would imply the initiation of motion. In such situation, the initial slide velocity and excess pore pressure would be zero and no heat would have been generated. Therefore,

$$u_w(z, t_0) = 0; v(z, t_0) = 0 \text{ and } \theta(t_0) = \theta_{ref} \tag{4.4a,b,c}$$

where θ_{ref} is the initial temperature at the beginning of the slide motion.

It was mentioned before that frictional heat is generated at a constant rate within the shear band, between $z = -e$ and $z = e$. No heat is generated, at any time, outside of the shear band. Therefore the excess pore pressure produced by heat is constant in the shear band and zero in the rest of the domain. However, the unbalance of water pressures between points inside and outside of the shear band induces its dissipation. It will be also accepted that the two boundaries of the shear band have identical material properties. Since the gradient of hydrostatic pressure may be neglected in the band, given its small thickness, it follows that the axis $z = 0$ is a symmetry axis.

Therefore, the solution of the problem will be sought for $z \geq 0$ and symmetry conditions will be forced at $z = 0$. This condition implies a zero flow through $z = 0$:

$$\mathbf{q}|_{z=0} = -\frac{k^b}{\gamma_w} \frac{\partial u_w}{\partial z} = 0 \quad \Rightarrow \quad \frac{\partial u_w}{\partial z} \Big|_{z=0} = 0 \quad (4.5)$$

At the other boundary, $z = e$, continuity of excess pore pressure and flow rate has to be satisfied on both sides of the border:

$$u_w|_{z=e^-} = u_w|_{z=e^+} \quad (4.6a)$$

$$\mathbf{q}|_{z=e^-} = \mathbf{q}|_{z=e^+} \quad \Rightarrow \quad k^b \frac{\partial u_w}{\partial z} \Big|_{z=e^-} = k^r \frac{\partial u_w}{\partial z} \Big|_{z=e^+} \quad (4.6b)$$

Changes in water pressure outside the band will extend to relatively small distances because the volume of water expelled by the band is very small. Small changes in porosity within a limited distance outside the band will be able to absorb the transient flow of water. Therefore, no effect on the calculated pore pressures outside the band will be noticed if a zero excess pore water pressure is specified at an infinite distance:

$$u_w|_{z=\infty} = 0 \quad (4.7)$$

A forward finite difference procedure was used to solve the system of Equations (4.3) with the boundary and initial conditions of Equations (4.4)-(4.7). Time derivatives were approximated by a forward Euler scheme. First and second spatial derivatives were approximated by central difference expressions. The calculation procedure is indicated in Appendix 4.1.

Once the numerical approximations of the derivatives are substituted into the system Equations (4.3c,d,e) (Appendix 4.1 for details) the following discrete set of equations is obtained:

$$\begin{aligned} u_w(z_i, t + \Delta t) &= u_w(z_i, t) + c_v \frac{\Delta t}{\Delta z^2} \\ & \left[u_w(z_{i+1}, t) - 2u_w(z_i, t) + u_w(z_{i-1}, t) \right] + \\ & + c_H \Delta t H(t) \quad \text{for } i = n_1, n_e \end{aligned} \quad (4.8a)$$

$$\begin{aligned} u_w(z_i, t + \Delta t) &= u_w(z_i, t) + c_v^r \frac{\Delta t}{\Delta z^2} \\ & \left[u_w(z_{i+1}, t) - 2u_w(z_i, t) + u_w(z_{i-1}, t) \right] \\ & \text{for } i = n_e, n_L \end{aligned} \quad (4.8b)$$

$$v^{\max}(t + \Delta t) = v^{\max}(t) + \frac{\Delta t}{M} [W \sin \beta - \tau_f(t)] \quad (4.8c)$$

where the one-dimensional spatial domain of integration ($z \geq 0$) has been discretized in n_L elements. n_1 corresponds to $z=0$ and n_e to $z=e$, the outside limit of the shear band. In Equations (4.8),

$$c_v = \frac{k^b}{(m_v^b + n^b \alpha_w) \gamma_w}$$

is the consolidation coefficient of the shear band material;

$$c_v^r = \frac{k^r}{(m_v^r + n^r \alpha_w) \gamma_w}$$

is the consolidation coefficient of the material outside of the shear band; and

$$c_H = \frac{(1 - n^b) \beta_s + \beta_w n}{(m_v^b + n^b \alpha_w) \rho c_m}$$

is a parameter which integrates the dilation coefficients of water and solid, the compressibility of soil skeleton and water and the mean specific heat of the soil.

A forward marching procedure has been devised to calculate the independent variables (excess pore water pressure and velocity) for points in the shear band and outside it.

The numerical solution of the problem starts at the boundaries where the values of the variables are known at any time. The set of discretized equations provides, step by step, all the unknowns at any time and position of the domain of integration. Initial excess pore pressure at any point was assumed to be zero and the initial temperature was assumed to be 10 °C.

The Forward Euler Method of integration may be numerically unstable if the Δt is larger than a stability limit which is a function of material parameters and Δz . Convergence of explicit integration schemes of standard parabolic equations (such as the consolidation equation) is achieved if the time and spatial increments satisfy the condition: $\frac{c_v \Delta t}{\Delta z^2} \leq 0.5$.

This condition applies to the homogeneous part of the parabolic equation (Coussy, 2004) and it may be thought that the field Equation (4.3c) leads to a similar relationship. Unfortunately, the “independent” term (proportional to the heat input $H(t)$) in Equation (4.3c) is a function of the pore pressure, through Equations

(4.3a,b,e). Nevertheless, the preceding condition has been accepted as a reference in the calculations presented below. In general, care has been taken to check that the calculated pore pressures did not change for time steps below a certain value used in calculations.

The calculated velocity will increase as long as the sliding mass is unbalanced (driving forces exceed resisting ones). This is the case even if the excess pore pressure at initial time is zero, because a positive increment of velocity will be calculated. Then, the positive value of generated heat, due to the velocity reached at the first time step, will result in an increment of temperature and excess pore pressure in the shear band. At the following time step, this positive excess pore pressure will reduce the effective frictional strength and will accelerate the slide mass. The slide will start to move in an accelerated motion. The numerical solution will be used subsequently, as a reference calculation, to discuss the analytical solution and the effect of some simplifying hypothesis introduced.

4.4 ANALYTICAL SOLUTION

Clay layers which include the sliding surface, in practical situations, are often indurated materials of relatively high stiffness. Therefore, the storage term associated with changes in pore pressure in Equations (4.3c,d) is small compared with the thermal dilation effects. Water compressibility, (α_w in Eq. 4.8c) is also a small quantity, probably smaller than the soil compressibility, m_v . The assumption made is that the term $m_v + n\alpha_w \approx 0$ (this is achieved if water and porous media are assumed to be incompressible). Then the system of Equations 4.3, becomes,

$$\tau_f(t) = [W \cos \beta - P_{wh} - u_w^{\max}(t)] \tan \varphi' \quad (4.9a)$$

$$H(t) = \tau_f(t) \frac{v^{\max}(t)}{2e} \text{ for } z \in [-e, e] \quad (4.9b)$$

$$\frac{\partial^2 u_w(z, t)}{\partial z^2} = \frac{[(1-n^b)\beta_s + \beta_w n^b] \gamma_w}{k^b \rho c_m} H(t) \text{ for } z \in [-e, e] \quad (4.9c)$$

$$\frac{\partial^2 u_w(z, t)}{\partial z^2} = 0 \text{ for } z \in (-\infty, -e] \cup [e, \infty) \quad (4.9d)$$

$$\frac{dv^{\max}(t)}{dt} = \frac{1}{M} [W \sin \beta - \tau_f(t)] \quad (4.9e)$$

The differential equations (4.9c) and (4.9d) can be integrated as follows:

$$u_w(z,t) = -\frac{\left[(1-n^b)\beta_s + \beta_w n^b\right]\gamma_w}{2k^b \rho c_m} H(t) z^2 + K_1 z + K_2 \quad \text{for } z \in [-e, e] \quad (4.10)$$

$$u_w(z,t) = C_1 z + C_2 \quad \text{for } z \in (-\infty, -e] \cup [e, \infty) \quad (4.11)$$

where K_1, K_2, C_1 and C_2 are integration constants that will be found applying the following set of boundary conditions:

(a) Symmetry conditions:

$$q\Big|_{z=0} = -\frac{k^b}{\gamma_w} \frac{\partial u_w}{\partial z}\Big|_{z=0} = 0 \Rightarrow K_1 = 0 \quad (4.12a)$$

(b) Continuity of flow rate at $z=e$:

$$\mathbf{q}\Big|_{z=e^-} = \mathbf{q}\Big|_{z=e^+} \Rightarrow k^b \frac{\partial u_w}{\partial z}\Big|_{z=e^-} = k^r \frac{\partial u_w}{\partial z}\Big|_{z=e^+} \quad (4.12b)$$

Then constant C_1 can be obtained:

$$C_1 = -\frac{\left[(1-n^b)\beta_s + \beta_w n^b\right]\gamma_w}{k^r \rho c_m} H(t) e \quad (4.12c)$$

(c) Hydraulic boundary conditions outside the shear band. Changes in water pressure outside the shear band take place in relatively small distances. This is a consequence of the small volume of water released by the band itself when heated. This comment will be reviewed later when discussing the results of the numerical calculations. It will be assumed that at a certain distance from the shear band ($z \geq Y$) pore water pressure will not be affected by the processes taking place in the shear band. This condition can be considered by enforcing that, at $z = Y$:

$$u_w(Y,t) = C_1 Y + C_2 = 0$$

Therefore,

$$C_2 = \frac{\left[(1-n^b)\beta_s + \beta_w n^b\right]\gamma_w}{k^r \rho c_m} H(t) e Y \quad (4.12d)$$

(d) Continuity of excess pore water pressure at $z = e$:

$$u_w(e^-, t) = u_w(e^+, t)$$

In view of previous results, K_2 can be expressed as:

$$K_2 = \frac{[(1-n^b)\beta_s + \beta_w n^b] \gamma_w}{\rho c_m} H(t) \left(\frac{e^2}{2k^b} - \frac{1}{k^r} (e^2 - eY) \right) \quad (4.12e)$$

Once the integration constants given by Equations (4.12) are substituted into Equations (4.10) and (4.11), the analytical expressions of excess pore water pressure inside and outside the shear band are given by:

$$u_w(z, t) = \frac{[(1-n^b)\beta_s + \beta_w n^b] \gamma_w}{k^b \rho c_m} H(t) \left(\frac{z^2 - e^2}{2} - \frac{k^b}{k^r} (e^2 - eY) \right) \text{ for } z \in [-e, e] \quad (4.13a)$$

$$u_w(z, t) = \frac{[(1-n)\beta_s + \beta_w n] \gamma_w}{k^r \rho c_m} H(t) e(z - Y) \text{ for } z \in [-Y, -e] \cup [e, Y] \quad (4.13b)$$

The band shearing resistance will be controlled by the maximum pore pressure developed, which will occur at the mid plane ($z = 0$). The excess pore water pressure at $z=0$ is equal to:

$$u_w^{\max}(t) = u_w(0, t) = \frac{[(1-n)\beta_s + \beta_w n] \gamma_w}{k^b \rho c_m} H(t) \left(-\frac{e^2}{2} - \frac{k^b}{k^r} (e^2 - eY) \right) \quad (4.14)$$

Consider now Equations (4.9). Modified expressions for the heat (Eq. (4.9b)) and for the motion equation (4.9e) can be obtained by substituting in them the equation for the shear strength (4.9a):

$$H(t) = (W \cos \beta - P_{wh} - u_w^{\max}(t)) \tan \varphi' \frac{v^{\max}(t)}{2e} \quad (4.15)$$

$$\frac{dv^{\max}(t)}{dt} = \frac{W \sin \beta}{M} - \frac{W \cos \beta - P_{wh}}{M} \tan \varphi' + \frac{\tan \varphi'}{M} u_w^{\max}(t) \quad (4.16)$$

Finally, if Equation (4.15) is substituted into Equation (4.14) and the result is introduced into Equation (4.16), the following ordinary differential equation for the slide velocity is obtained:

$$\frac{dv^{\max}(t)}{dt} = \frac{b + av^{\max}(t)}{1 + cv^{\max}(t)} \quad (4.17)$$

where:

$$a = -\frac{[(1-n)\beta_s + \beta_w n] \gamma_w}{k^b \rho c_m} \left(-\frac{e^2}{2} - \frac{k^b}{k^r} (e^2 - eY) \right) \frac{W \sin \beta \tan \varphi'}{2eM}$$

$$b = \frac{W \sin \beta}{M} - (W \cos \beta - P_{wh}) \frac{\tan \varphi'}{M}$$

$$c = -\frac{[(1-n)\beta_s + \beta_w n] \gamma_w}{k^b \rho c_m} \left(-\frac{e^2}{2} - \frac{k^b}{k_r} (e^2 - eY) \right) \frac{\tan \phi'}{2e}$$

are constants.

Equation (4.17) can be solved, integrating by the method of separated variables between $(t = t_0; v^{\max} = v_0^{\max})$ and (t, v)

$$\int_{v_0^{\max}}^{v^{\max}} \frac{1 + cv^{\max}(t)}{b + av^{\max}(t)} dv^{\max}(t) = \int_{t_0}^t dt \quad (4.18)$$

It provides the following explicit relationship between time and sliding velocity:

$$t = \frac{a - cb}{a^2} \ln \left(\frac{av^{\max} + b}{av_0^{\max} + b} \right) + \frac{c}{a} (v^{\max} - v_0^{\max}) \quad (4.19)$$

where v_0^{\max} is the maximum velocity at initial time (t_0) . The maximum velocity at any time can be obtained implicitly as a root of Equation (4.19).

4.5 SUMMARY OF ASSUMPTIONS

Several assumptions have been made in the preceding derivations. These assumptions are summarized as follows:

- Velocity of the shear band varies linearly across the band thickness.
- Heat conduction and heat convection are neglected.
- Average heat storage capacity of the soil in the band (ρc) is assumed to be constant.
- One-dimensional conditions are assumed to relate volumetric strain rate and stress rate.
- Water flow due to gradients of elevation are neglected with respect to the changes of excess pore water pressure.
- Solid particles are assumed incompressible against stress changes.
- The porous material inside and outside the shear band and the water are assumed to be incompressible $(m_v + n\alpha_w \approx 0)$.

The last assumption has only been imposed in the derivation of the analytical solution leading to the velocity of a planar slide, defined by Equation (4.19).

4.6 SOLVED CASE

In this section, the two solutions presented above for a planar slide (analytical and numerical) are compared. In one case (numerical) the band and surrounding rock will

be considered deformable. In addition, water will be modelled as a compressible fluid. This case, described by the set of Equations (4.3a-c) will be solved by a finite difference numerical procedure. In the second solution (analytical) the shear band and the surrounding rock are assumed to be rigid and the set of equations describing the case is given by Equations (4.9a-e). The solution for this case was given in the previous section.

The case analyzed has been inspired in the large translational slide of Cortes (Fig. 4.2). This slide was described in detail in Alonso *et al.* (1993) and it has the advantage that most of the required parameters are available. An old large translational landslide was detected on the left bank of a reservoir built in the Júcar River (in the province of Valencia, Spain). It was reactivated by a quarry excavation that provided granular material for the dam construction. A problem of concern was the possibility that the sliding mass, whose volume was estimated in $5 \cdot 10^6 \text{ m}^3$, could accelerate and invade the reservoir producing a dangerous wave. Cortes landslide was stabilized by a weight-transfer procedure (designed by conventional limit-equilibrium procedures) and the risk of a fast motion was eliminated. However, it has remained as an interesting case which had similarities with the Vaiont case although the scale of the slide was substantially smaller. Table 4.1 includes all the relevant physical constants of the problem and the geotechnical properties are given in Table 4.2. The sliding surface was precisely located in a marl layer which didn't dip uniformly. Three wedges can be distinguished. In the upper part, 150 m long, the marl layer dips 25° , in an intermediate zone (the longest one, about 250 meters long) the layer dips at a nearly uniform angle of 16° and, finally, the lower wedge, only 25 meters long, has a horizontal base. In the analysis presented here, this slide geometry is simplified as a planar slide having a constant slope of 16° representative of the central and the longest part of the actual slide.

Excavation of the upper wedge allowed the observation of the failure surface. The sliding surface was located in a continuous clay layer no more than 3-5 mm thick. Its friction angle (17°) was obtained in the laboratory by testing the actual sliding surface in the shear box. This value coincided with the friction derived from back-analysis. According to the assumption made in the analysis of Cortes landslide an average pore-water head of 2 m has been imposed in the sliding surface. Under these conditions a planar slide 15.3 m thick, having the same slope as the central long stretch of Cortes (16°) is in strict equilibrium.

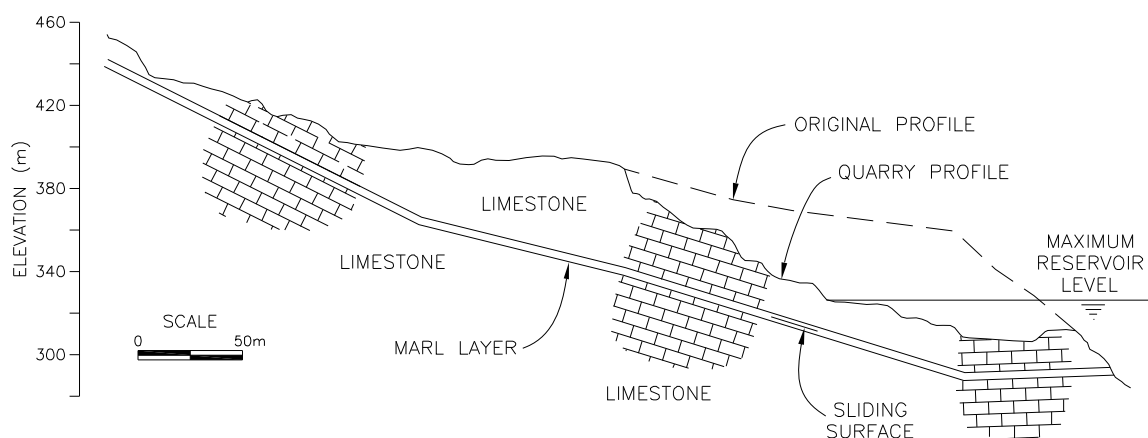


Figure 4.2 Representative cross section of Cortes slide Alonso *et al.* (1993).

Table 4.1 Physical properties

Parameter	Symbol	Value	Unit
Water density	ρ_w	1000	kg/m ³
Solid density	ρ_s	2700	kg/m ³
Coefficient of compressibility of water	α_w	$5 \cdot 10^{-10}$	1/Pa
Water thermal expansion coefficient	β_w	$3.42 \cdot 10^{-4}$	1/°C
Solid thermal expansion coefficient	β_s	$3 \cdot 10^{-5}$	1/°C
Water specific heat	c_w	$4.186 \cdot 10^3$ 1.0	J/kg·°C cal/ kg·°C
Solid specific heat	c_s	$8.372 \cdot 10^2$ 0.20	J/kg·°C cal/ kg·°C

The thickness of the shear band has been assumed to be 5 mm. However, a sensitivity analysis changing this value will be presented later. No distinction between the properties of the shear band and the surrounding material has been made. The material is characterized by a porosity of 0.25, by a low permeability ($k = k^b = k^r = 10^{-17} \text{ m}^2$) and by a low coefficient of the one dimensional compressibility parameter ($m_v = m_v^b = m_v^r = 3.71 \times 10^{-9} \text{ Pa}^{-1}$). These parameters have been chosen according with the properties and experimental results presented in Alonso *et al.* (1993).

The slide will be made unstable by imposing a small increase (10 cm of water column) of the position of the water table. The response of the slide calculated analytically as well as numerically, is shown in Figures 4.3 and 4.9. The temperature and the displacement obtained with the assumption of incompressible band material and incompressible water was calculated by means of a simple numerical integration due to the implicit closed form expression for the velocity.

Table 4.2 Geotechnical properties

Parameter	Symbol	Value	Unit
Porosity	n	0.25	-
Density of sliding mass	ρ_r	2350	kg/m ³
Effective frictional angle	ϕ'	17	°
Permeability	k	10 ⁻¹⁰	m/s
Compressibility coefficient	m_v	3.71 · 10 ⁻⁹	1/Pa
Thickness of the shear band	$2e$	2.5	mm
Thickness of the slide	D	15.3	m
Slope of the planar slide	α	16	°
Height of phreatic level	h_w	2	m

The development of pore water pressures in the band is shown in Figure 4.3, which shows the isochrones for a few discrete time instants. Water pressures dissipate towards the boundaries and the maximum is computed at the band centre. Excess pore pressures extend a few millimetres into the surrounding rock in the numerical solution. In the analytical case developed the dissipation boundary is maintained at the edge of the band ($Y = e$). The effect of changing the parameter Y is presented later. It will be concluded that the assumed hypothesis ($Y = e$) leads to the most accurate results compared with the numerical solution. Pore pressures develop faster in the analytical solution because it does not take into account the storage term associated with band and water stiffness.

In the numerical solution, during the first 5 seconds, the generated heat does not have any relevant effect. The excess pore pressure remains negligible because the frictional work generated is very small and the heat released is not enough to increase sufficiently the pore pressure. Note also that, in the case of the analytical solution, the initial slow response of the slide lasts only one second. Eventually, as time increases, pore pressure build-up is capable of reducing the resisting shear strength. Then the

driving force increases, the slide accelerates, the work input and the temperature in the shear band increase and additional pore pressures are generated. This phenomenon is illustrated in the remaining plots. It was found that the two approaches lead to very similar values of the excess water pressure inside the band.

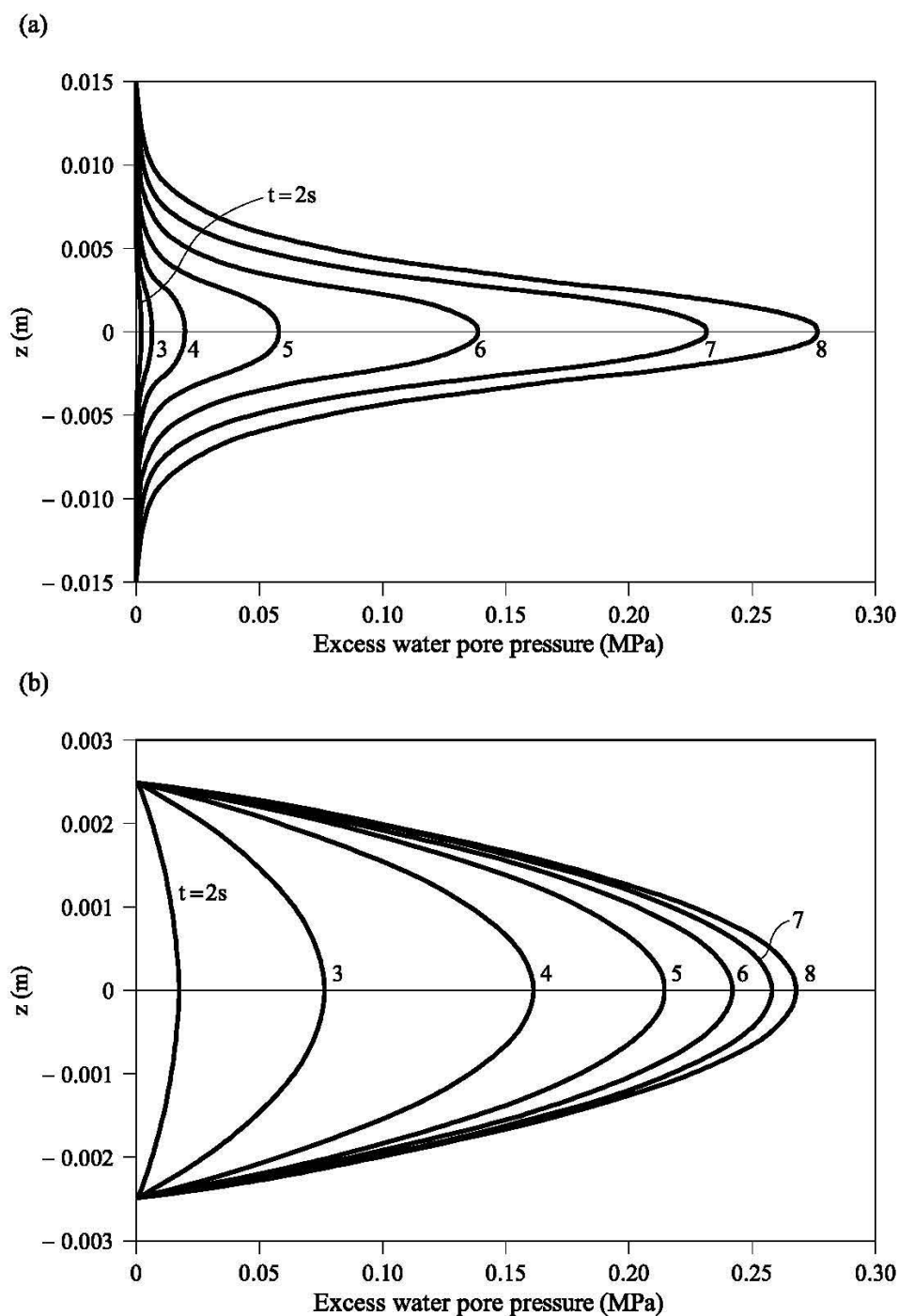


Figure 4.3 Calculated excess pore water pressures in the shear band: (a) deformable band (numerical solution); (b) rigid band (analytical solution).

A consequence of the almost equal excess pore pressures calculated with the two approaches in the centre of the band is that the development of slide velocity in time is very similar for the two cases as Figure 4.4 indicates. The analytical solution predicts a shorter time to reach a given velocity (a few seconds) but this is of no relevance in practice. Excess pore water pressures develop also with a similar pattern (Fig. 4.5). They reach a maximum value (0.30 MPa) within a few seconds. Later, they remain constant. As the pore water pressures rise, the effective normal stress against the band decreases and the frictional strength decreases to very low values (Fig. 4.6). Then the frictional work decreases also and the combined effect of pore pressure dissipation and reduced heat generation leads to a constant value of excess pore water pressure. Note that the small value of the calculated strength and the increasing sliding velocity provides some positive heat input which is capable of maintaining an increase in temperature and a generation of excess pore pressures which is compensated by the dissipation towards the band boundaries.

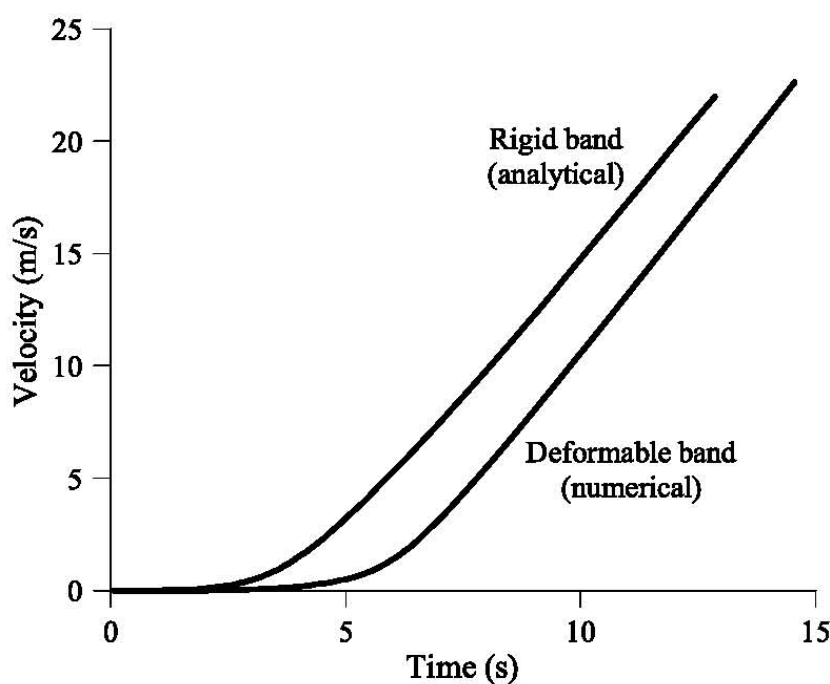


Figure 4.4 Calculated slide velocities.

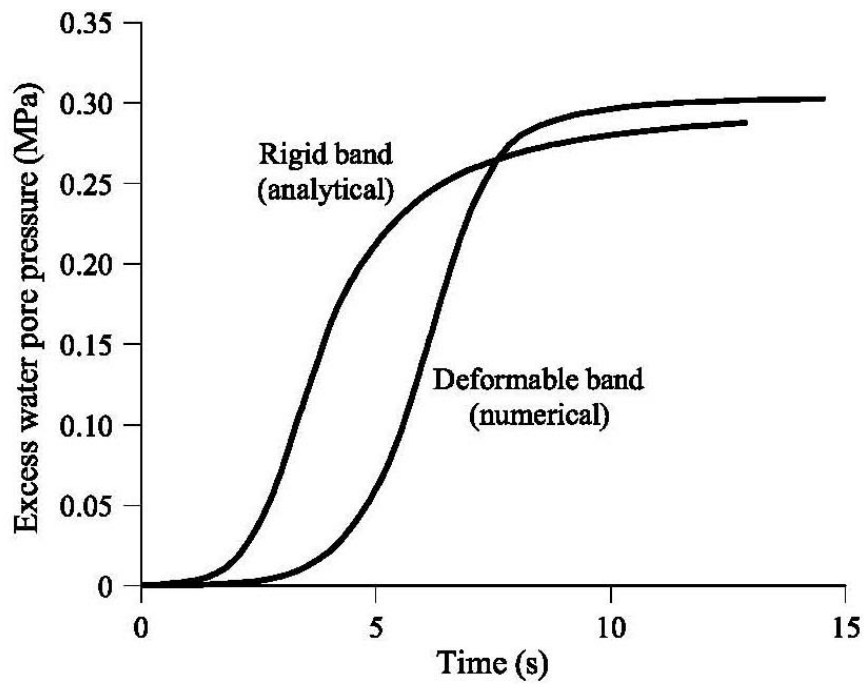


Figure 4.5 Calculated pore water pressures.

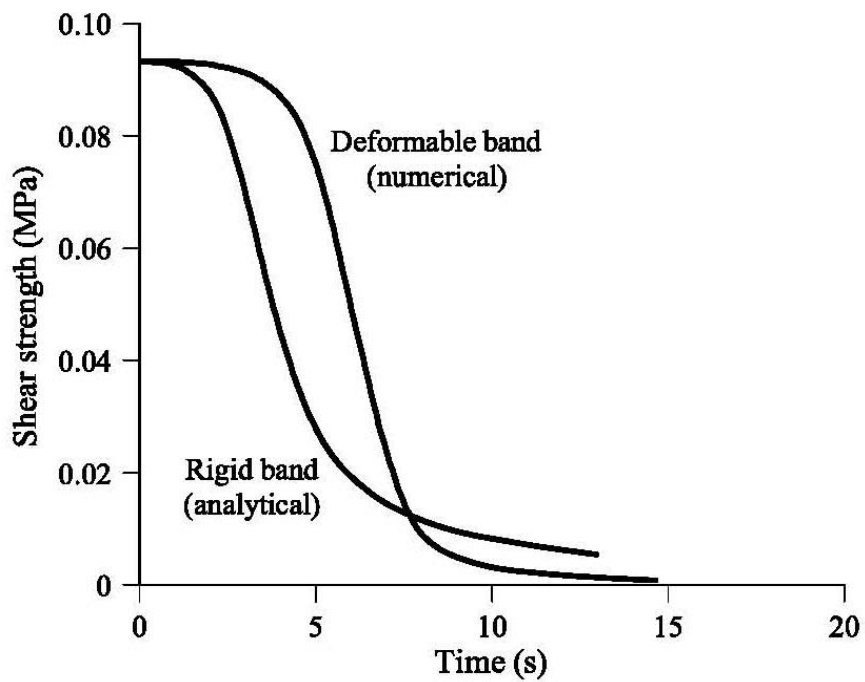


Figure 4.6 Calculated shear strength in the middle plane of the band.

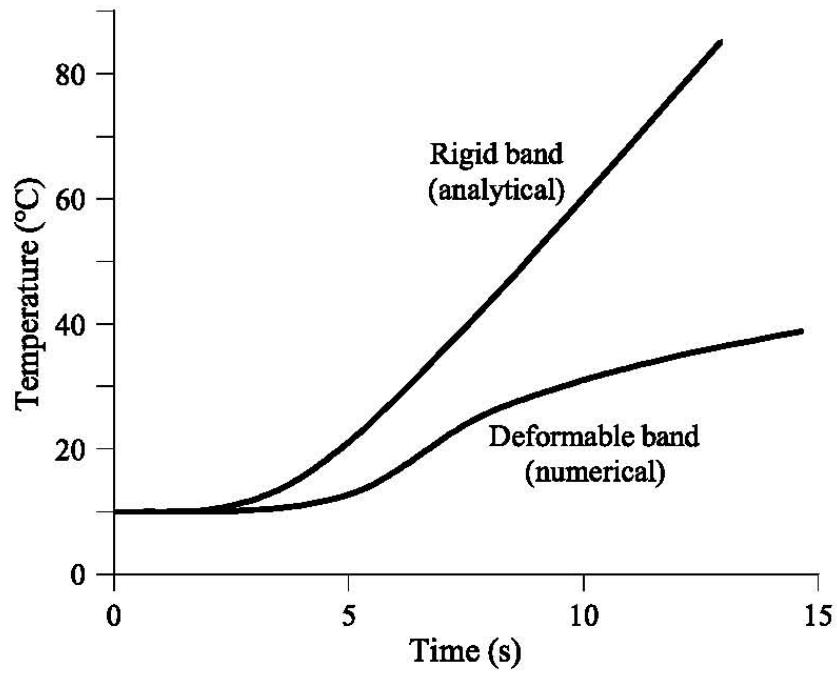


Figure 4.7 Calculated band temperature.

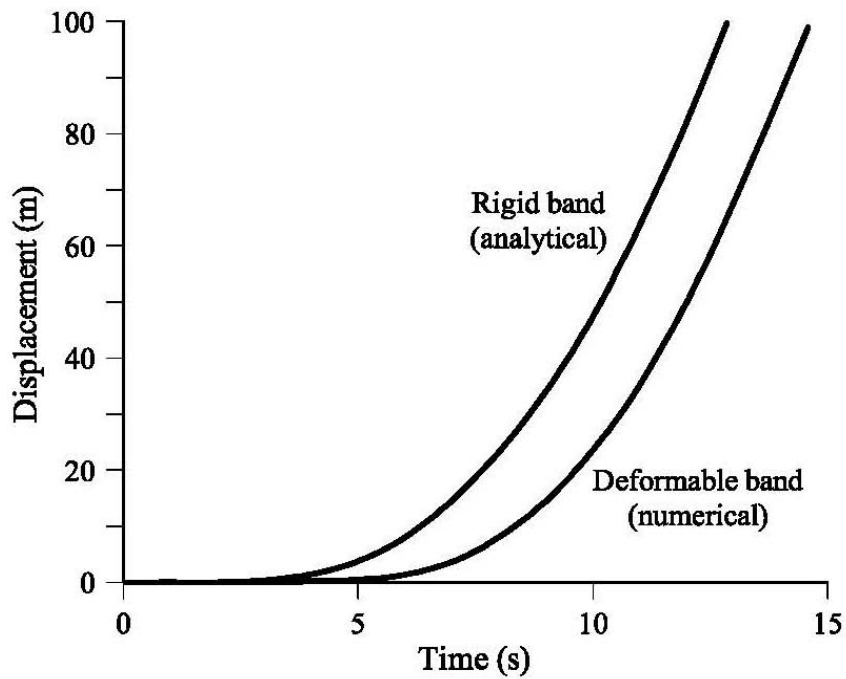


Figure 4.8 Calculated displacement records.

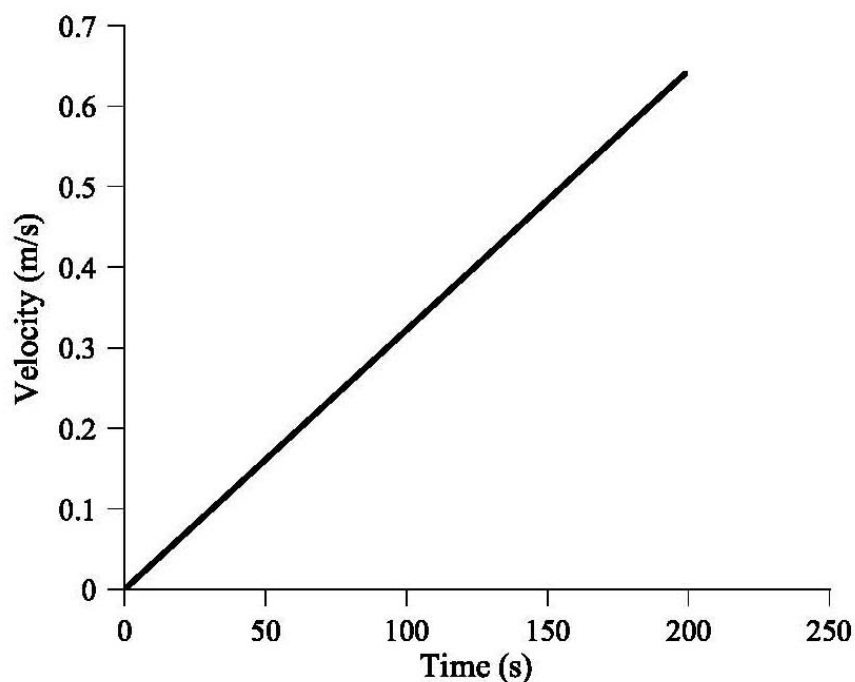


Figure 4.9 Calculated velocity and displacement of the unstable slide with no consideration of thermal effects.

In the example solved the temperature in the band increases a few degrees during the first few seconds of accelerated motion (Fig. 4.7). Again, the analytical solution leads to a faster increase in temperature. The displacement history of the slide is quite similar in the two cases (Fig. 4.8). The first 100 m of displacement is reached in a few seconds (16 s in the numerical solution; 12 s in the analytical case). These are minor differences in practice. In fact, if the dynamics of the slide are simply a consequence of the purely accelerated motion of the unstable wedge, with no consideration of thermal effects, an extremely slow motion is computed for the first few seconds of the slide (Fig. 4.9). In fact, higher permeability values of the shear band material lead to negligible heating effects and the results are practically equal to those calculated with a conventional analysis without heating.

The heat conduction term of the heat balance was neglected in the formulation presented above and in the calculations presented. In order to check this hypothesis, additional numerical work was performed, taking into account the heat dissipation term. The effect of this term in the results was not relevant for the common values of the conduction coefficient for rocks and the results obtained were undistinguishable from the numerical results reported here.

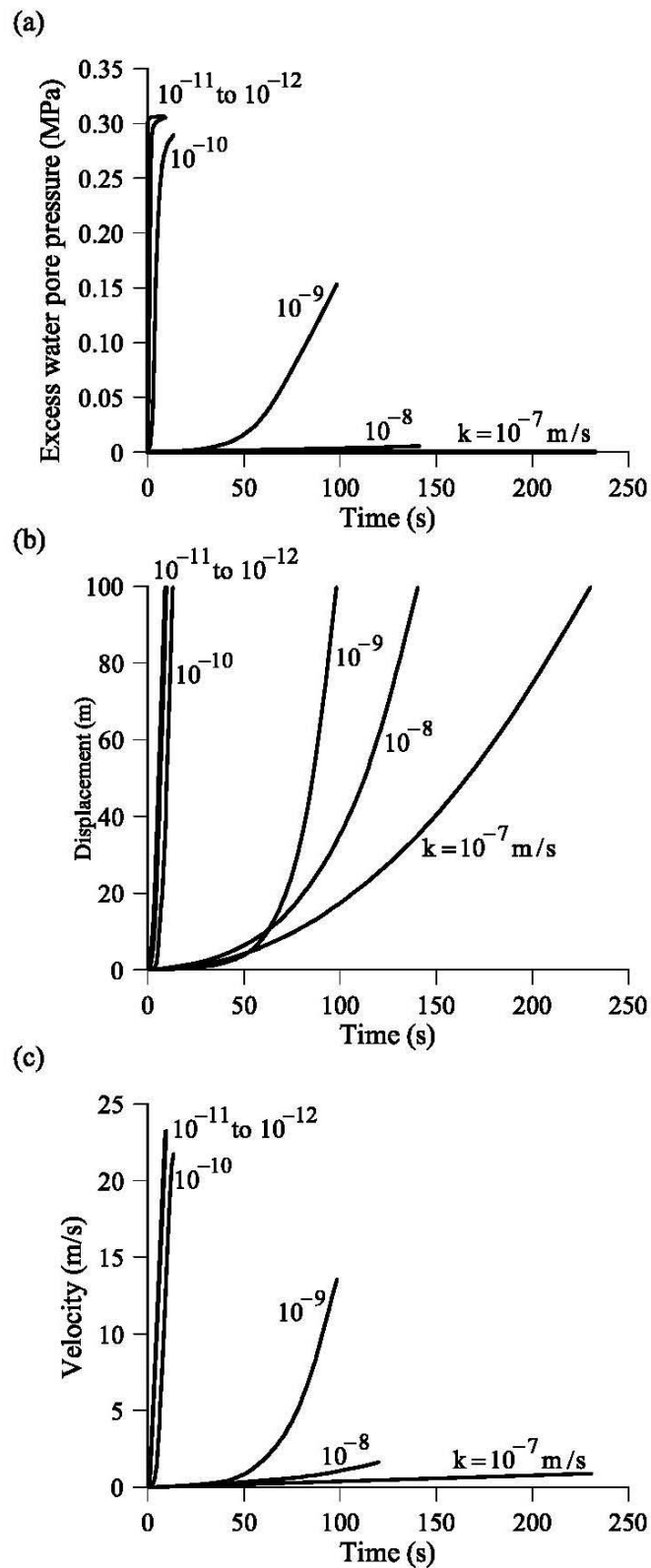


Figure 4.10 Effect of band permeability on (a) velocity; (b) excess pore water pressure; (c) displacement history. All of them calculated for a maximum displacement of 100 m. Analytical solution.

4.7 SENSITIVITY ANALYSIS

4.7.1 Effect of permeability and shear band thickness

The effect of band permeability on slide velocity and pore pressure generation of the band, during the interval necessary for the slide to reach a displacement of 100 m is illustrated in Figure 4.10. Increasing the permeability leads to a slower response of the pore pressure build-up and a delayed acceleration of the slide. All the cases presented in Figure 4.10 correspond to a common band thickness of 5 mm and they were calculated though the analytical solution. Figure 4.10 suggests that beyond a critical permeability the pore water pressure dissipation within the band is enough to prevent any accelerated motion of the slide.

But, in order to reach a general conclusion it is necessary to combine two parameters: band thickness and band permeability. The thickness of shear bands has been reported by several authors (Morgenstern, 1987; Roscoe, 1970; Vardoulakis, 1980; Scarpelli and Wood, 1982; Desrues, 1984; Vardoulakis, 2002). An important conclusion of basic research is that shear band thickness is related to a characteristic grain size (see Section 3.1.5).

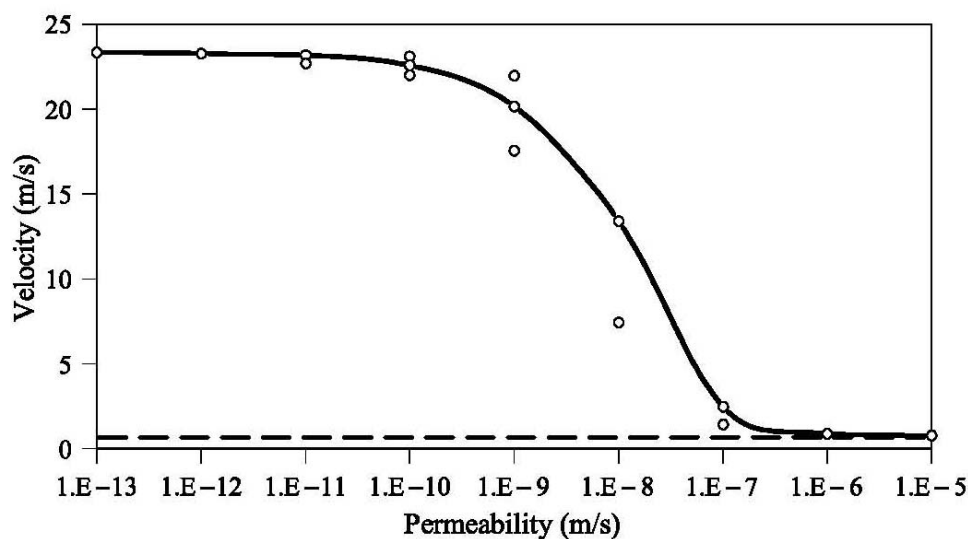
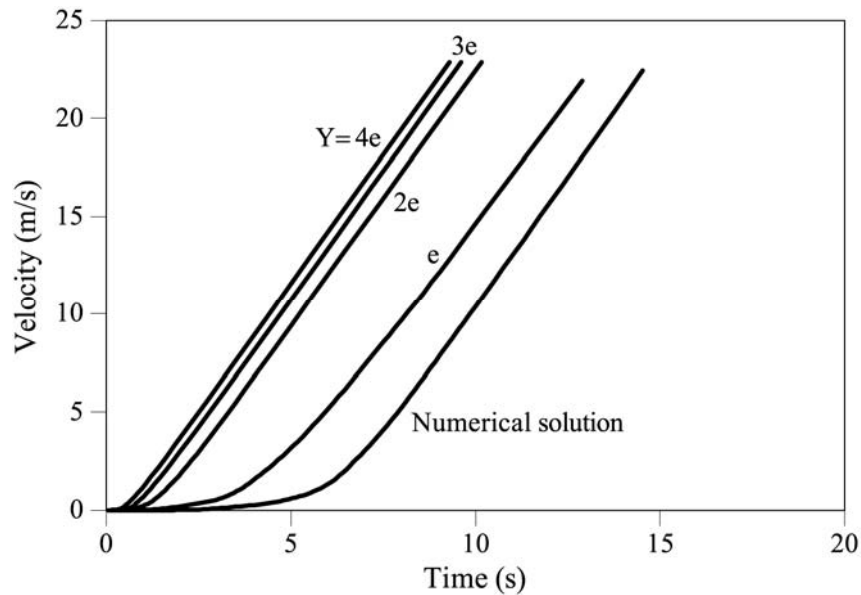


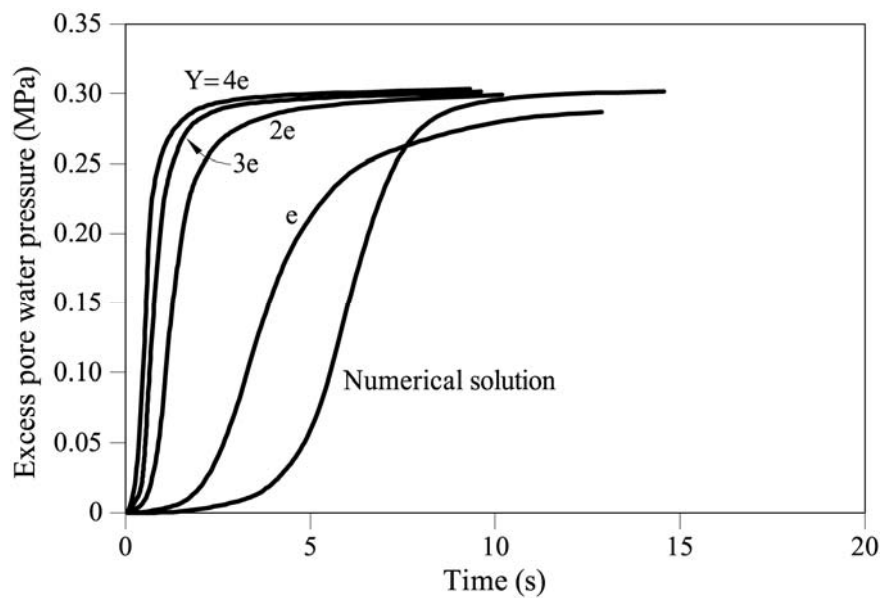
Figure 4.11 Calculated maximum slide velocity in 100m displacement.

On the other hand, permeability is also roughly related to the grain size distribution. Therefore, band thickness and band permeability are related even if this relationship is a first approximation. It could be expected that in low permeability materials shearing bands should be narrow. If permeability increases, band thickness should also increase. In the sensitivity analysis performed band thicknesses and values of permeability were varied in a wide range (10^{-13} to 10^{-6} m/s for the band permeability and 0.5 to 50 mm for the band thickness). The resulting combinations are collected in

Table 4.3. In view of the preceding considerations, only a wide band, centred in the diagonal of the band thickness-permeability matrix is really significant. This band has been marked in Table 4.3. The cases included in the band probably cover all situations likely to be found in practice. The previous planar sliding case has been analyzed for all the combinations indicated in the table. In all cases the analytical solution was used.



(a)



(b)

Figure 4.12 Effect of changing parameter Y on the (a) maximum slide velocity and (b) excess pore pressure (in the middle of the shear band).

The results, in terms of the calculated maximum velocity for 100 m displacement are shown in Figure 4.11. They show that permeability has a dominant effect. In fact, it appears that a threshold range of band permeability separates two regions: the high velocity region, characterized by values of permeability lower than 10^{-10} m/s and a stable region for values of permeability in excess of 10^{-7} m/s. This result does not depend on the band thickness. This conclusion is strictly valid for the simplified conditions of the analysis performed but it points out that a simple practical procedure to decide the danger of an active planar slide is to determine the permeability of the clay in which the sliding surface has developed and to compare it with the permeability values suggested previously for the “fast” and “stable” regions.

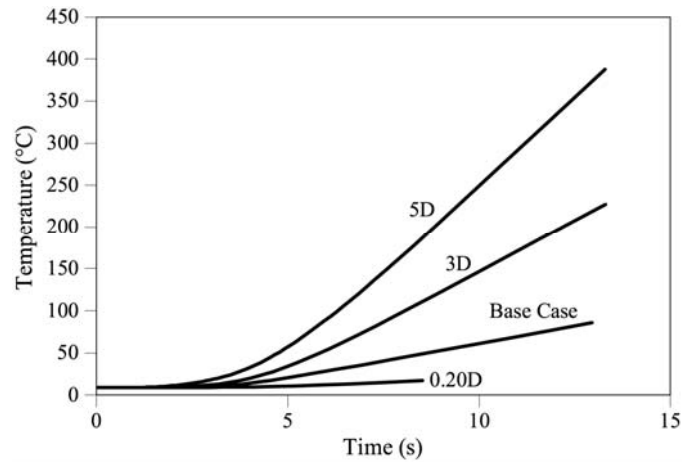
Table 4.3 Effect of band permeability and thickness

MAXIMUM VELOCITY REACHED IN 100 METERS OF DISPLACEMENT									
Thickness (mm)	Permeability (m^2)								
	10^{-20}	10^{-19}	10^{-18}	10^{-17}	10^{-16}	10^{-15}	10^{-14}	10^{-13}	10^{-12}
0.25	23.3	23.2	21.9	13.4	2.4	0.9	0.8	0.8	0.8
0.5	23.3	23.2	22.6	17.5	4.2	1.1	0.8	0.8	0.8
2.5	23.3	23.3	23.1	21.9	13.4	2.42	0.9	0.8	0.8
5	23.3	23.3	23.2	22.5	17.5	4.17	1.1	0.8	0.8
10	23.3	23.3	23.2	22.9	20.2	7.4	1.4	0.9	0.8
25	23.3	23.3	23.2	23.1	21.9	13.41	2.4	0.9	0.8

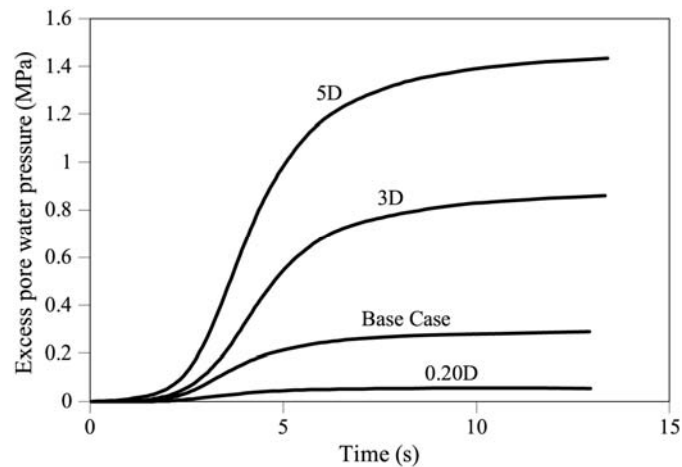
4.7.2 Effect of the position of dissipation boundary (parameter Y) in the analytical solution

Solving the system of Equation (4.9) involves defining a priori the region outside the shear band in which excess of pore pressure are developed ($-Y < z < Y$). A linear variation of the excess pore pressure is specified in this zone (Eq. (4.9d)). If the compressibility of the water and the porous media are considered (working with the numerical solution, Eq. 4.3), the region affected by the heat induced pore pressure is part of the solution. It depends on the water storage capacity of the porous media and the permeability. In the solved case (analytical solution) presented above no excess pore pressure is allowed outside of the band ($Y=0$). In order to show the effect of changing the value of Y , slide velocity and maximum excess pore pressure are plotted in time for Y values ranging from $Y=e$ to $Y=4e$ in Figure 4.12. These values are inspired by the results of the numerical solution (Fig. 4.5a). The remaining parameters have not been modified with respect to the solved case. Pore pressure develops faster if larger values of Y are considered because a higher excess pore pressure is imposed at the edge of the shear band. If the results are compared with the numerical solution, also plotted in the figure, limiting strictly the excess pore pressures inside of the band

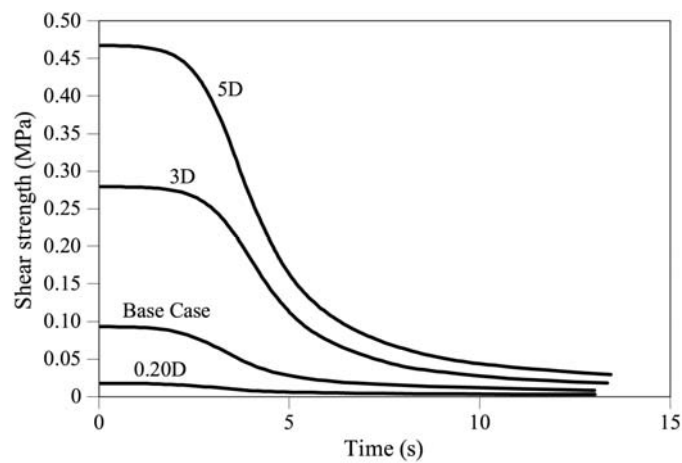
($Y = e$) leads to the most accurate analytical solution, which has been used in the analysis of Cortes landslide presented in this Chapter.



(a)



(b)



(c)

Figure 4.13 Effect of slide thickness on the (a) temperature; (b) excess pore pressure; (c) shear strength on the mid-band. Analytical solution. Base case is characterized by $D = 15.3$ m.

4.7.3 Effect of depth of sliding surface

The reference case corresponds to $D = 15.3$ m. Changing the thickness of the slide implies that normal stresses on the failure plane will change also. Therefore, the heat generated during sliding will also change. It is therefore expected that temperature, pore pressure, and mobilized strength will be controlled by the thickness of the slide. This is shown in Figure 4.13. It is easily checked that these variables depend linearly on the slide thickness, for any instant of the slide motion.

However, the motion of the slide is essentially unaffected. The reason is that driving and resisting forces are scaled by the same amount when the slide thickness changes. The practical conclusion is that the risk, measured in terms of attained velocity, is independent of the thickness (size) of the slide. Deep slides, however, are capable of generating high temperatures (Fig. 4.13a) which may modify some of the basic assumptions made in the formulation of the problem, namely, the constitutive behaviour of the shear band material, the possibility of clay melting for very high temperatures or the generation of water vapour on the sliding plane. These phenomena are of concern for significantly deep landslides (Fig. 4.13).

4.8 CONCLUSIONS

A likely reason for the very high velocities reached in some occasions by translational slides is the generation of pore water pressures in the basal shear band as a result of the frictional heat input induced by the sliding motion. A well-known case in this regard is the catastrophic Vaiont slide. Finding the velocity of the slide requires the solution of a highly coupled problem which involves thermal, mechanical and flow phenomena. In the case of planar slides resting on a narrow shear band (the sliding surface itself), the set of balance equations may be solved in closed form under certain simplifying assumptions. The solution presented in the chapter does not consider heat conduction phenomena and heat advection in the shear band and its vicinity. It also neglects the fluid storage term associated with the skeleton deformability and the water compressibility. However, these effects are of minor significance compared to the main phenomena: heat accumulation in the shear band, pore pressure generation due to temperature increase and permeability controlled dissipation of excess pore water pressures within the shear band. It has been found that the assumption of full dissipation of excess pore pressures at the shear band edge (made in the derivation of the analytical solution) leads to a solution remarkably close to the numerical solution of the complete problem. The analytical solution found may prove useful to validate numerical procedures and it may be used as a fundamental basic solution for other sliding geometries not considered here. In addition, a comparison of calculations based on the analytical solution with numerical approximation, when soil and water compressibility are included, reveals that the closed form solution is accurate enough for practical purposes.

A sensitivity analysis carried out to investigate the effects of band permeability and thickness has shown that the band permeability is the key parameter to judge on the risk of having a very fast slide. A threshold permeability around the values $k = 10^{-9} - 10^{-7}$ m/s ($k_0 = 10^{-16} - 10^{-14}$ m²) separates two regions. For values of permeability smaller than the threshold an accelerated fast motion may develop. For higher permeability values, the slide motion becomes fully drained and the risk of high slide accelerations disappears.

It was also found that changes in temperature, excess pore water pressures and available shear strength in the shear band depend linearly on the slide thickness. However, the development of velocity and run out distances are not affected by the depth of the failure surface.

APPENDIX 4.1 FINITE DIFFERENCE APPROXIMATION OF SYSTEM OF EQUATIONS (4.3)

A forward finite difference procedure was developed to solve the system of Equations (4.3) together with the initial and boundary conditions given in Equations (4.4)–(4.7). Consider in Figure A4.1 the domain of integration. The one-dimensional spatial domain is subdivided into n small elements of thickness Δz . The z_i coordinate of any point is defined by an index i such that $z_i = i\Delta z$. The following indices define singular points: $i = n_0$ corresponds to $z = 0$; $i = n_e$ to $z = e$. The far boundary is located at a distance $z = L$, where $i = n_L$. The horizontal axis in Figure A4.1 corresponds to time. The system of equations will be solved for each time interval Δt .

Time derivatives at any time t , for $z = z_i$ can be approximated by (Forward Euler Method):

$$\left. \frac{\partial f}{\partial t} \right|_{z_i} \approx \frac{f(z_i, t + \Delta t) - f(z_i, t)}{\Delta t} \quad (\text{A4.1})$$

where $f(z, t)$ is a general function of position (z) and time (t).

The first and second derivative with respect to z will be approximated by a central difference

$$\left. \frac{\partial f}{\partial z} \right|_t \approx \frac{f(z_{i+1}, t) - f(z_{i-1}, t)}{\Delta z} \quad (\text{A4.2a})$$

$$\left. \frac{\partial^2 f}{\partial z^2} \right|_t \approx \frac{f(z_{i+1}, t) - 2f(z_i, t) + f(z_{i-1}, t)}{(\Delta z)^2} \quad (\text{A4.2b})$$

Once the numerical approximations of the derivatives (Eqs. (A4.1) and (A4.2)) are substituted into the system of Equations (4.3c,d,e), the following discrete set of equations is obtained:

$$u_w(z_i, t + \Delta t) = u_w(z_i, t) + c_v \frac{\Delta t}{\Delta z^2} [u_w(z_{i+1}, t) - 2u_w(z_i, t) + u_w(z_{i-1}, t)] + c_H \Delta t H(t) \quad \text{for } i = n_1, n_e \quad (\text{A4.3a})$$

$$u_w(z_i, t + \Delta t) = u_w(z_i, t) + c_v^r \frac{\Delta t}{\Delta z^2} [u_w(z_{i+1}, t) - 2u_w(z_i, t) + u_w(z_{i-1}, t)] \quad \text{for } i = n_e, n_L \quad (\text{A4.3b})$$

$$v_{\max}(t + \Delta t) = v_{\max}(t) + \frac{\Delta t}{M} [W \sin(\beta) - \tau_f(t)] \quad (\text{A4.3c})$$

In these equations,

$$c_v = \frac{k}{(m_v + n\alpha_w)\gamma_w} \quad (\text{A4.4})$$

is the consolidation coefficient of the shear band material;

$$c_v^r = \frac{k_r}{(m_v^r + n\alpha_w)\gamma_w} \quad (\text{A4.5})$$

is the consolidation coefficient of the material outside the shear band; and

$$c_H = \frac{(1-n)\beta_s + \beta_w n}{(m_v + n\alpha_w)\rho c_m} \quad (\text{A4.6})$$

is a parameter that integrates the dilation coefficients of water and solid, the compressibility of soil skeleton and water and the mean specific heat of the soil.

Equations (A4.3a,b) are explicit mathematical expressions for the excess of pore pressure in a point z_i , at a given time $(t + \Delta t)$, if the old values (at the previous time, t) in three points: point z_i and the points just above and below (z_{i-1} and z_{i+1}), are known. This calculating procedure is graphically illustrated in Figure A5.1. Equation (A5.3) provides the new value of the maximum velocity as a function of the old values (previous step) of maximum velocity and excess of pore pressure at $z = 0$. Heat (H) and effective frictional strength (τ_f) are given by Equations (4.3a,b) at the previous time t . It appears, therefore, that a forward marching procedure has been devised to

calculate the independent variables (excess pore water pressure and velocity). The procedure requires that initial and boundary values are defined.

Initial and boundary conditions must also be expressed in a numerical way. The symmetry condition at $z = 0$ (Eq. (4.5)), valid at any time, can be approximated by extending the domain with an additional interval from $z = 0$ to $z = z_{-1} = -\Delta z$. Then, if the excess pore pressure at $z = z_{-1}$, $u_w(z_{-1}, t)$ is forced to be

$$u_w(z_{-1}, t) = u_w(z_1, t) \quad (\text{A4.7})$$

at any time, the condition

$$\left. \frac{\partial u_w}{\partial z} \right|_t = 0 \text{ in } z = 0$$

is automatically satisfied in view of Equation (A4.7).

The general expression (A4.3a) for $z = 0$ can now be written

$$u_w(z_0, t + \Delta t) = u_w(z_0, t) + c_v \frac{\Delta t}{\Delta z^2} [2u_w(z_1, t) - 2u_w(z_0, t)] + \Delta t c_H H(t). \quad (\text{A4.8})$$

The numerical expression of the boundary condition at the edge of the shear band ($z = e$) (Eq. (4.6)), is obtained by means of a forward finite difference as follows:

$$k \frac{u_w(z_{n_e}, t) - u_w(z_{n_{e-1}}, t)}{\Delta z} = k_r \frac{u_w(z_{n_{e+1}}, t) - u_w(z_{n_e}, t)}{\Delta z} \quad (\text{A4.9})$$

This equality allows the calculation of excess pore water in $z = e$ at any time as a function of the values of excess pore water in the points just above and below (at the same time):

$$u_w(z_{n_e}, t) = \frac{k_r u_w(z_{n_{e+1}}, t) + k u_w(z_{n_{e-1}}, t)}{k_r + k} \quad (\text{A4.10})$$

The numerical expression of boundary condition at the upper limit of the discretization (Eq. (4.7)), where the excess of pore pressure must be zero, is simply

$$u_w(z_{n_L}, t) = 0 \quad (\text{A4.11})$$

Regarding the initial conditions (Eqs. (4.4)), the numerical equivalents are given by

$$u_w(z_i, t_0) = 0 \text{ for } i \in [1, n_L] \quad (\text{A4.12})$$

$$v(z_i, t_0) = 0 \text{ for } i \in [1, n_L] \quad (\text{A4.13})$$

$$\theta(t_0) = \theta_{ref} \text{ for } i \in [1, n_L] \quad (\text{A4.14})$$

At the initial time (t_0), all values are known. The excess pore water pressure in the next time increment can be calculated by means of Equations (A4.3a,b) in $[n_0, n_e)$ and $(n_e, n_L]$, respectively. Note that n_e is not included in those intervals. However, the continuity condition, expressed in Equation (A4.10), provides the new value of excess pore pressure at $z = e$.

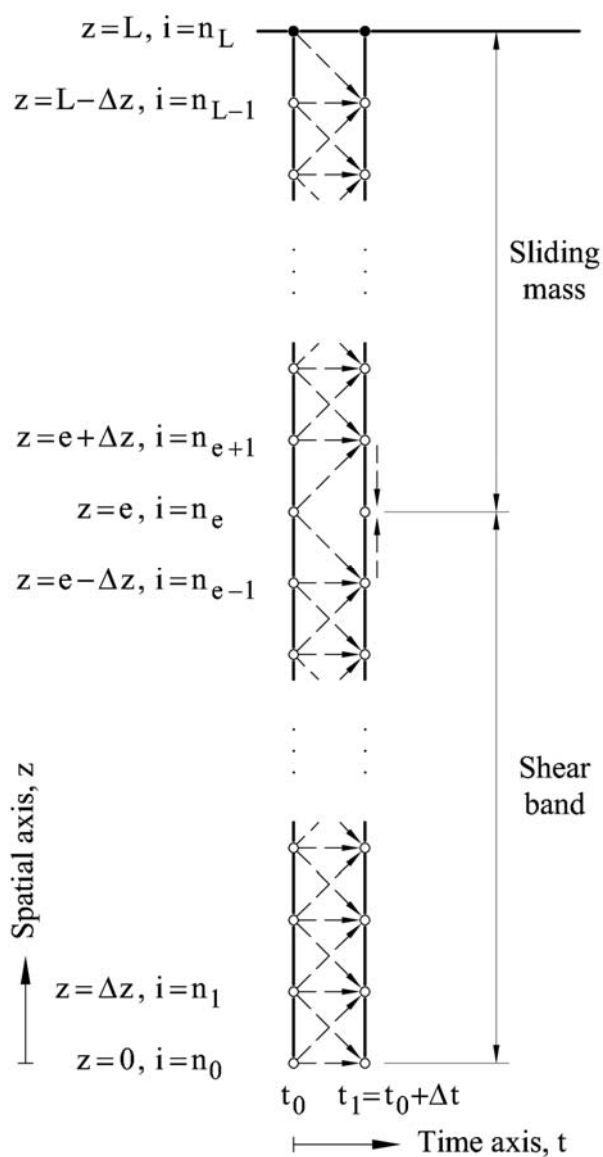


Figure A4.1 Dynamics of a planar infinite slope. Domain of integration.

The value of the maximum velocity at the first time step is obtained by means of Equation (A4.3c) (with $v_{\max}(t_0) = 0$). Once velocity and excess of pore pressure are known at the new time step, the new value of heat and effective frictional strength can be calculated through Equations (A4.3a,b). Also, the temperature in the shear band can be obtained, at each time step, by means of Equation (3.13), writing it in a numerical form as follows:

$$\theta(t + \Delta t) = \theta(t) + \Delta t \frac{H(t)}{\rho c_m} \quad (\text{A4.15})$$

Summarizing, the numerical solution of the problem starts at the boundaries where the values of the variables are known at any time. The set of discretized equations provides, step by step, all the unknowns at any time and position of the domain of integration. Since initial conditions of excess pore pressure at any point, as well as the initial temperature are zero, the value of pore water pressure at the first time step ($t = \Delta t$) will be zero.

These approximations lead to a Forward Euler Method of integration which may be numerically unstable if Δt is larger than the stability limit, which is a function of material parameters and Δz . If the solution becomes unstable, the calculated values of the unknown function display an oscillatory behaviour in time that prevents convergence. Convergence of explicit integration schemes of standard parabolic equations (such as the consolidation equation) is achieved if the time and spatial increments satisfy the condition:

$$\frac{c_v \Delta t}{\Delta z^2} \leq 0.5 \quad (\text{A4.16})$$

This condition applies to the homogeneous part of the parabolic equation (Nakamura, 1990) and it may be thought that our field Equation (4.3c) leads to a similar relationship. Unfortunately, the “independent” term (proportional to heat input $H(t)$) in Equation (4.3c) is a function of pore pressure, through Equations (4.3a,b,e). Nevertheless, the preceding condition has been accepted as a reference in the calculations presented below. In general, care has been taken to check that the calculated pore pressures did not change for time steps below a certain value used in calculations.

The calculated velocity will increase as long as the sliding mass is unbalanced (driving forces exceed resisting ones). This is the case, even if the excess pore pressure at initial time is zero, because a positive increment of velocity will be calculated. Then, the positive value of generated heat, due to the velocity reached at the first time step, will result in an increment of temperature and excess pore pressure in the shear band. At the following time step, this positive excess pore pressure will reduce the effective

frictional strength and will accelerate the slide mass. The slide will start to move in an accelerated motion.

The numerical procedure described above has been programmed in Fortran 90. The program is included in Appendix 6.1 to show all the details of the computational procedure and to allow the reader to perform its own calculations.

CHAPTER 5

Static Equilibrium and Run-Out Analysis of Vaiont Landslide

Vaiont slide has been represented by a model of two interacting evolutive wedges. Mass conservation during the motion implies that the upper wedge transfers mass to the lower one through an internal shearing plane. The model respects available in situ observations. It was formulated in dynamics terms. Outcomes of the analysis are the determination of safety factors of the valley before dam impoundment, and the calculation of run-out distance once the motion starts. The approach gives a simple explanation to the stability of the slide, previous to failure. Rock strength degradation of the mobilized mass as motion develops has also been included. This degradation, even if it is intense, was unable to explain the very high estimated landslide velocities. This aspect is faced in the next chapter.

5.1 INTRODUCTION

Vaiont landslide (Italy) has attracted world wide attention into the causes and processes involved in the failure. Interest in Vaiont has never decreased within the technical community despite the 45 yrs elapsed since the accident. Papers analyzing the failure have been published at a maintained rate in Journals and Conferences. The landslide is one of the largest (in terms of volume of mobilized mass) in historic times. As stated by Hendron and Patton (1987):

“It is likely that more information has been published and more analyses have been made of the Vaiont data than for any other slide in the world”.

This Chapter and the next one are an additional contribution to this long list. Only the essentials of the landslide are reported here to justify the models developed. Vaiont has been described in many papers. A significant subset is given in the references of this Chapter.

One of the main reasons which explain the interest in Vaiont landslide is the difficulty to explain the extremely high velocity of the moving mass. The implication of this lack of understanding is that the risk associated with other landslide occurrences of similar nature (natural slides affected in its toe by increasing water levels, a common situation in dam engineering) cannot be properly evaluated.

This Chapter presents a review of Vaiont slide. It focuses on the kinematics of the slide. Two representative sections have been analysed by formulating a dynamic equilibrium highlighting the importance of the internal strength of the mobilized rock. The approach gives a simple explanation to the stability of the slide, previous to failure, even if it is accepted that the main failure surface remains at residual strength conditions. Some authors (Mencl, 1966, Lo *et al.*, 1972, Sitar *et al.*, 2005; Sitar and MacLaughlin, 1997) have also suggested that the strength offered by the rock mass could explain the stability of the slide before the impounding of the reservoir. This idea is also favoured in this work and it will be used in the model developed to analyze the slide. The analysis for the rapid sliding is developed in the next Chapter.

In the first part of this Chapter the main features of the slide and of the events which happened previously to the failure are presented. This information is fundamental for the assumptions adopted in the subsequent analysis presented in this Chapter and the next one.

5.2 FUNDAMENTAL INFORMATION ON VAIONT

Between 1957 to 1967 a double curvature arch dam, 276 m high, was built to store water of the Vaiont River in the Italian alps, approximately 80 km north of the city of Venice. The dam was built in a narrow canyon cut by the river in massive Jurassic limestone. At the end of 1960, once the dam was built and the reservoir partially impounded, a long continuous peripheral crack, 1 m wide and 2.5 km in length, marked the contour of a huge mass, creeping towards the reservoir in the Northern direction (Fig. 5.1). In the following three years the downward motion of the slide was monitored by means of surface markers. Some data provided by them is also plotted in Figure 5.2. In addition, water pressures in perforated pipes, located in four boreholes (location shown in Fig. 5.2), were monitored starting in July 1961. However, all the investigation efforts provided limited information on some key aspects of the landslide

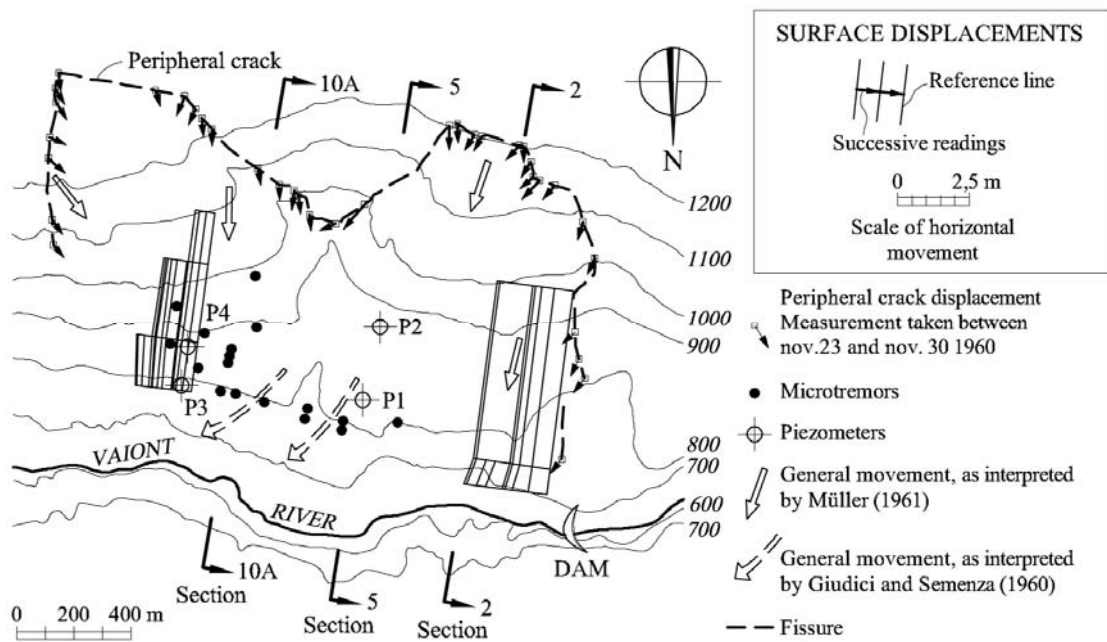


Figure 5.1 Map of Vaiont sliding area. Note the position of the arch dam on the lower right hand corner of the figure (Simplified from Belloni and Stefani (1987) with additional information from several authors).

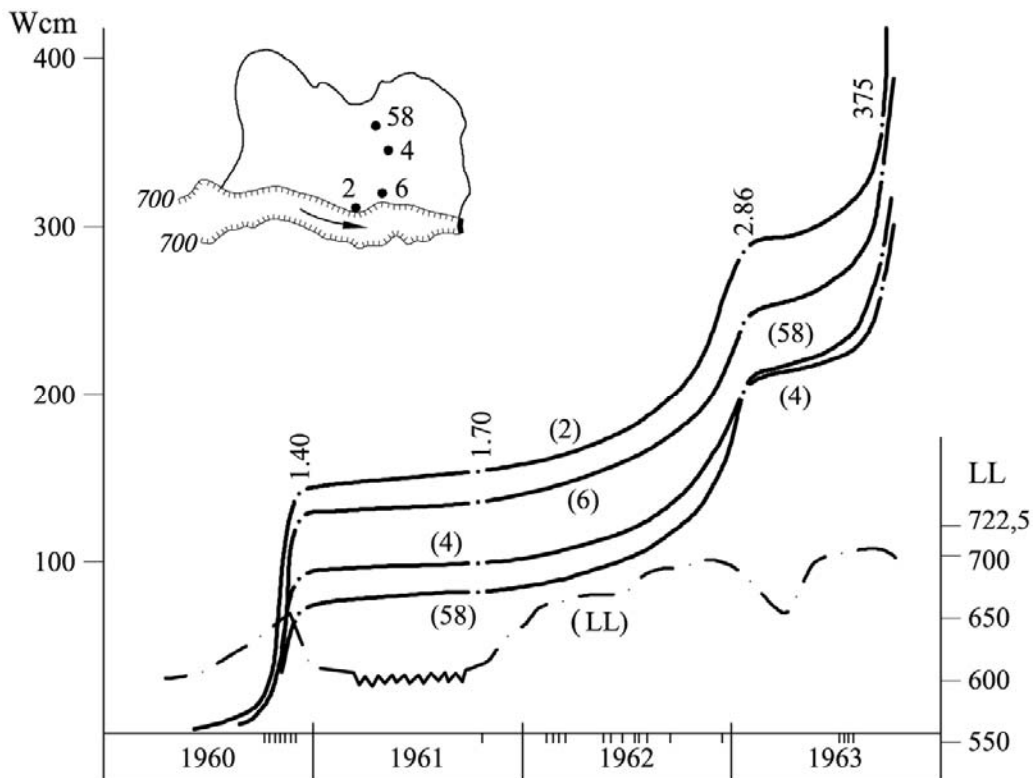


Figure 5.2 Accumulated displacements of surface markers in the period 1960-1963 and its correlation with reservoir elevation. Seismic events are marked in the time scale (After Nonveiller, 1987).

such as the position and shape of the sliding surface and the pore water pressures acting on it. The measured rate of displacements of surface markers could be roughly correlated with the water level of the reservoir (Fig. 5.3). After two cycles of reservoir elevation, which partially filled and emptied the reservoir in the period 1960-1962, the water level reached a maximum (absolute) elevation of 710 m, at the end of September 1963. At that time, the accumulated displacements of surface markers had reached values in excess of 2.50–3 m (Fig. 5.3). The figure shows a good correlation between the increase in water level in the reservoir and the acceleration of landslide displacements. Surface velocities of 20–30 cm per day were registered in the days preceding the final rapid motion which took place on October 9, 1963. An estimated total volume of rock of $280 \cdot 10^6 \text{ m}^3$ became unstable, accelerated, and invaded the reservoir at an estimated speed of 30 m/s (around 110 km/hour). The displaced mass generated a gigantic wave, 270 m high, which flew over the dam (which stood without breaking) and destroyed several villages downstream, causing more than 2000 casualties.

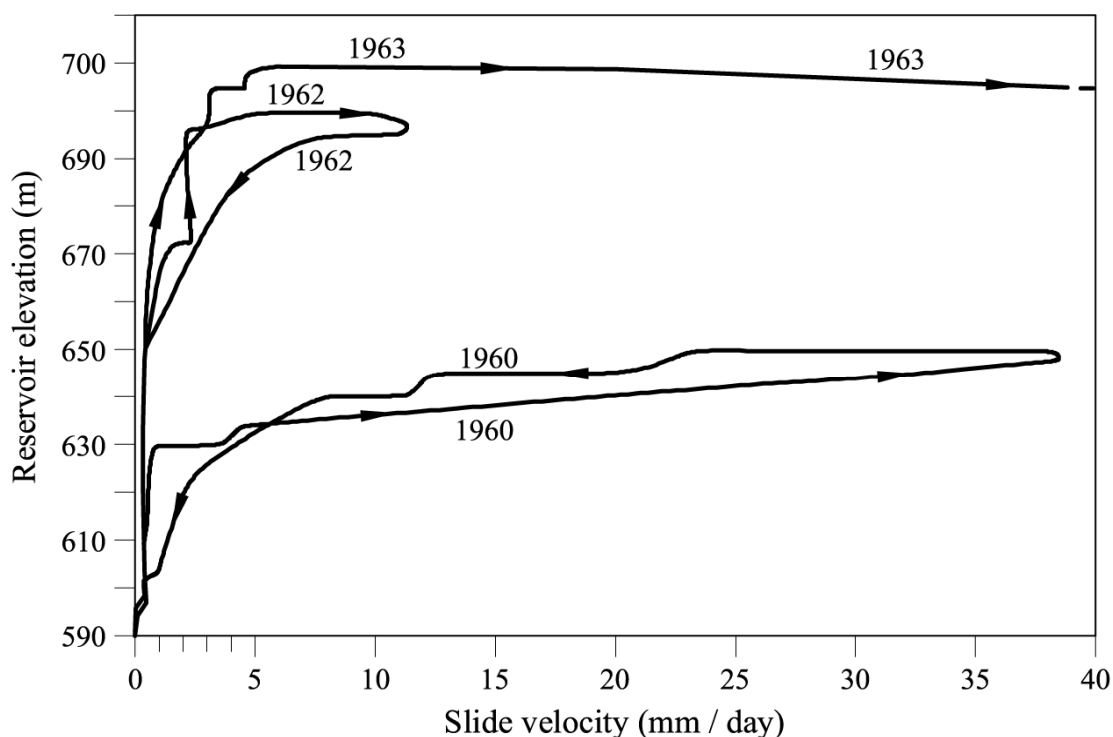


Figure 5.3 Relationship between water level in the reservoir and sliding velocity (Hendron and Patton, 1985).

5.2.1 Geological setting

The Vaiont river, which flows from East to West, cuts a large syncline structure which folds Jurassic and Cretaceous strata (Fig. 5.4). The syncline created the “open chair” shape of the Jurassic strata of the left margin of the river, which can also be seen in the figure. The axis of the syncline plunges a few degrees towards the East (normal

to the plane of the figure). The syncline shape eventually defined the geometry of the failure surface, which is always important information to understand the subsequent behaviour of the slide. E. Semenza, an engineering geologist son of the dam designer, made important contributions to understand the geology of the site. In his book “La Storia del Vaiont raccontata del geologo che ha scoperto la frana (“The story of Vaiont told by the geologist who has discovered the slide”, Semenza, 2001), he includes a tentative reconstruction of the past history of the slide in a series of representative cross-sections which are reproduced in Figure 5.5.

This reconstruction conveys a clear message from a geomechanical point of view: the failure surface, which was probably initiated several tens of thousands of years ago, has been subjected to an ever increasing story of accumulated relative displacements. The second important point is that the rock mass affected by the 1963 landslide had suffered a history of cracking and “damage” during recent geological times. The sliding surface is located in strata of the upper Malm period (upper Jurassic). Clays and marls were found in these layers (see below the description of the failure surface). Above the sliding surface finely stratified layers of marl and limestone from the Malm period were identified. Below the sliding surface, the Jurassic limestone banks of the Dogger period remained unaffected. In the upper part, limestone strata from the lower Cretaceous crowned the moving mass. In general, the folded layers of limestone and marl were strongly fractured (drilling water was often lost in the exploratory borings performed in 1960).

Two representative cross-sections of the slide, located upstream of the dam position at distances of 400 m and 600 m, respectively, are reproduced in Figure 5.6 (Sections 2 and 5; Hendron and Patton, 1985). The two cross-sections will later be used to analyze the stability conditions of the landslide.

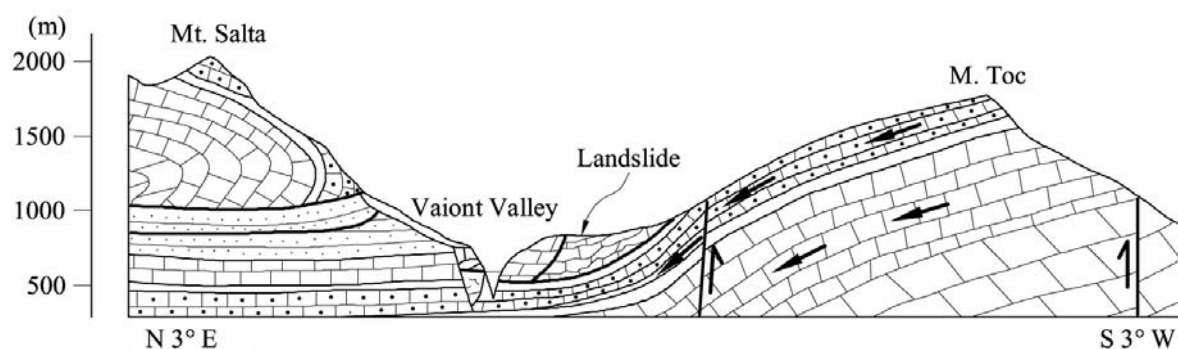


Figure 5.4 A North (Monte Toc) South (Monte Salta) section showing the general layout of the syncline, the Vaiont gorge and the position of the ancient landslide (vertical scale = horizontal scale) (after Semenza and Ghirotti, 2000).

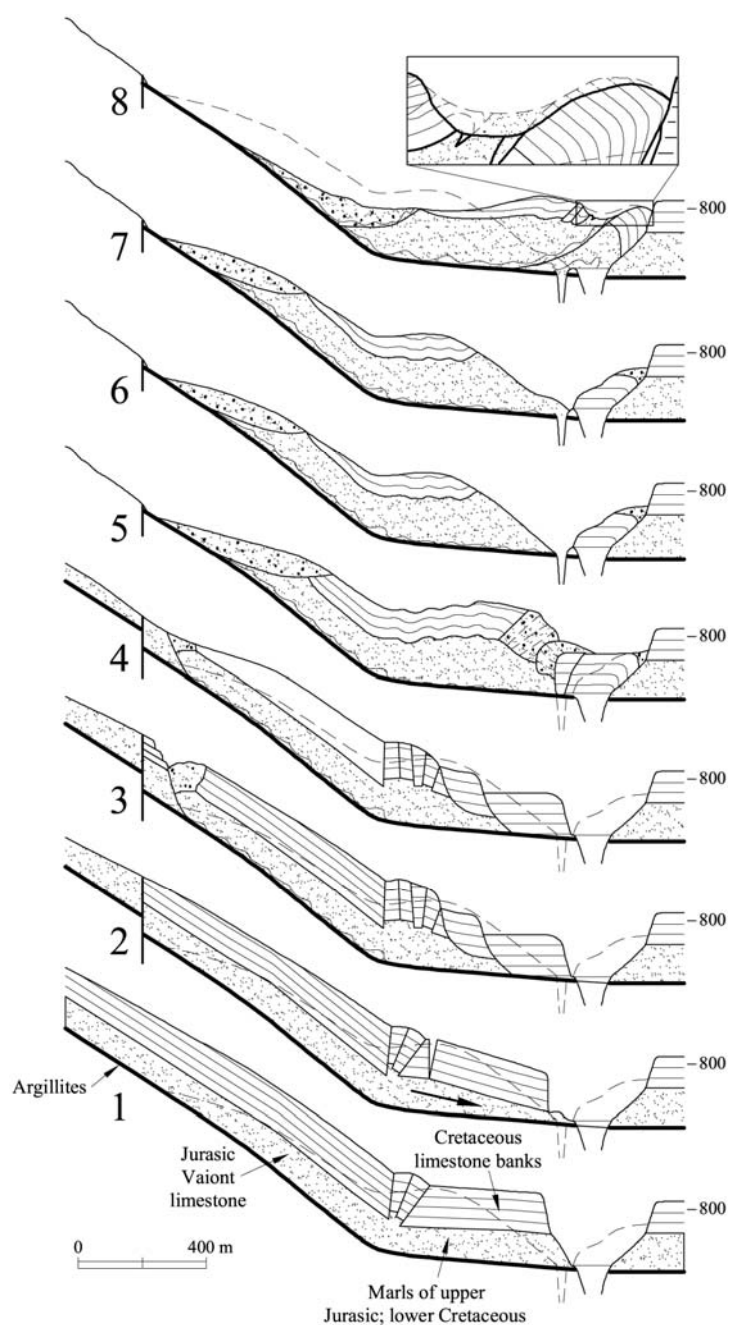


Figure 5.5 Tentative reconstruction of the paleo-slide of Vaiont. 1: Situation before the first motion (end of last glaciation?); 2: First motion of the slope; 3: Process of progressive sliding (undulated continuous line) and rotational slides at the toe; 4: Successive erosion phenomena on the upper parts; 5: Ancient landslide and intense fracturing of strata. The valley is invaded by the gigantic slide. 6: The slide before November 4, 1960, after thousands of years of erosion. The river has cut a new, narrow gorge. 7: The profile after a “small” landslide on November 4, 1960; 8: The final shape of the cross-section after the slide of October 8, 1963 (present situation). The inset shows an eroded part of the slide surface by the rapidly moving waters displaced by the slide. (Simplified from Semenza, 2001).

5.2.2 The sliding surface

In their comprehensive report of 1985, Hendron and Patton (1985) describe the detailed investigation performed to identify the nature of the sliding surface. The conclusion is that thin (a few centimeters thick) continuous layers of high plasticity clay were consistently found in the position of the failure surface. Samples from these clay layers were tested by different laboratories and the results are described in Hendron and Patton (1985).

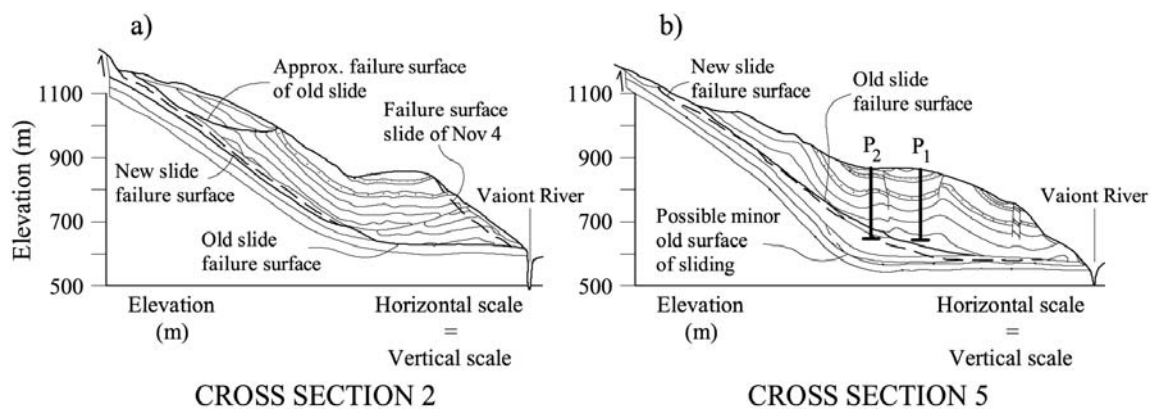


Figure 5.6 Two representative cross-sections of the landslide: (a) Section 2; (b) Section 5. See location in Figure 5.5. (After Hendron and Patton, 1985). The position and length of piezometers P1 and P2 is shown on cross-section 5.

The clays were found highly plastic a result explained by their significant Ca-montmorillonite content. Liquid limits well in excess of 50% were often found. More recently Tika and Hutchinson (1999) reported the values $w_L = 50\%$ and $PI = 22\%$ (Table 3.2).

Direct shear tests on remoulded specimens have also been reported by Hendron and Patton (1985). In some cases stress reversals were applied in order to find residual conditions. In fact, the past history of the landslide indicates that the residual friction angle was the relevant strength parameter along the failure surface. Measured average values of residual friction angle ranged between 8° and 10° . These values are consistent with existing correlations between residual friction angles and clay plasticity (Lupini *et al.* 1981) (Fig. 3.11). Tika and Hutchinson (1999) used the ring shear apparatus to find also the residual strength (Fig. 3.14). This test, conducted on remoulded specimens, approximates better the large relative shear displacements experienced in nature by the actual sliding surface. They also measured a residual friction angle of 10° for a relative shear displacement in excess of 200 mm. Tika and Hutchinson (1999) also examined the effect of shearing rate (Fig. 3.15). They found a further reduction in residual friction which reached low values (5°) for shearing rates around 0.1 m/s, a velocity which is still far lower than the estimated sliding velocities of the real failure. This aspect is not directly considered in the dynamic equilibrium calculation developed here.

As discussed in Chapter 3, the measured reduction in the available frictional strength with rate of displacement may be a consequence of thermo-hydro-mechanical coupling phenomena taking place due to heat generation by frictional work at the shear zone, which will be included in the analysis developed in the next Chapter.

Hendron and Patton (1985) estimated that some factors (areas of the sliding surface without clay, some localized shearing across strata, irregularities in the geometry of the sliding surface) could increase the average residual friction angle operating in the field and they estimate that $\phi'_{res} = 12^\circ$ is a good approximation for static conditions.

5.2.3 Monitoring data before the slide

The main purpose behind the limited instrumentation available was to relate the level of the reservoir with the measured vertical and horizontal displacements of a number of topographic marks distributed on the slide surface. Data on horizontal displacements, plotted as a function of position and time in several profiles following the South-North direction in Figure 5.1, indicate that surface points in different cross-sections had essentially the same displacement rates an information which suggest that the slide was moving as a rigid body. The direction of the slide is also indicated in the figure by several arrows. Some of them (small arrows along the peripheral crack) indicate that the moving mass was actually detaching from the stable rock, implying no frictional resistance. This is clearly the case of the western side of the slide. In the eastern side the lower part of the peripheral crack does not seem to have been fully developed at the time of the survey. Some authors (Hendron and Patton, 1985; Hungr *et al.*, 1989) have developed three-dimentional block models which include this lateral contribution.

Seismic (volumetric p-wave) velocities were measured in central parts of the slide in December 1959 and again in December 1960. A drop in velocity from $v_p = 5-6$ km/s in 1959 to $v_p = 2.5-3$ km/s was recorded. This information may be interpreted as an indication of the progressive weakening of the rock mass due to the distortion induced by the creeping motion of the slide. The velocities initially recorded at the end of 1959 are very high and they correspond to a rock of good quality, Barton (2007). This is perhaps surprising in view of the prehistoric landslide motions described above. The strong drop in seismic velocity in just one year, which is a tiny fraction of time within the complex life of the landslide, seems exaggerated but it is pointing towards significant shear distortions within the rock mass, motivated by the first impoundment of the reservoir which implied a water level rise of 200 m. The associated increase in pore water pressures on the sliding surface is very large and it is unlikely that rainfall events in the past could have produced such a strong drop in effective stress, especially in the lower part of the slide.

It should be emphasized that these p-wave velocities are much higher than the velocities measured in soils, even if they are dense and compact. In other words, the strength which may be associated with the shearing of the rock mass above the sliding surface is orders of magnitude larger than the strength available at the clay-dominated thin layers at the base of the slide, being sheared along sedimentation planes of very high continuity.

5.2.4 Water pressures and rainfall

The position of piezometers (they were open perforated pipes) was indicated, in plan view, in Figure 5.1 and in cross-section in Figure 5.6. A perforated pipe only provides information on the average water pressures crossed by the tube. Note too that the pipes, except Piezometer 2, did not reach the position of the sliding surface. Therefore, they did not provide direct information on the water pressures actually existing in the vicinity of the sliding surface, which is fundamental information to perform a drained stability analysis of the landslide.

In general, the water level recorded by the piezometers follow closely the changing level of the reservoir. The exception was Piezometer 2, at least during the initial part of the recording period. The initial readings in this piezometer indicated water pressures significantly above (90 m of water column) the reservoir surface. This information has been interpreted as an indication of additional factors, other than the level in the reservoir, which may control the water pressure at the sliding surface. Since the cretaceous limestone, affected by karstic phenomena, is a rather pervious mass, rainfall water infiltrating at high elevations may result in artesian pore pressures against the impervious Malmö formations located at the base of the landslide. However, no further and direct evidence of this possibility was recorded. On the other hand, the simultaneous variation of piezometer and reservoir levels is a good indication of the high permeability of the rock mass above the sliding surface.

When water level in the reservoir is plotted against the recorded slide velocity (Fig. 5.3), an interesting result is obtained. Increasing water level leads to an increase in sliding velocity. The relationship is highly nonlinear and it tends towards an asymptotic limit which is an indication of failure. The problem with Figure 5.3 is that this relationship is not unique, a result which is not expected if the slide motion is thought to be governed by the effective normal stresses acting on the sliding surface, which, in turn, is controlled by the reservoir level. In fact, the second reservoir filling led to a second asymptotic value for the water level in the reservoir.

This result was probably one important reason behind the decision to increase the water level for the third time in search of a higher (but safe) level in the reservoir which would allow the normal operation of the dam. The idea behind this decision, apparently put forward by Müller (1987), is that the rock reacts in a different way when it is wetted for the first time, compared with its reaction when it has already been wet

before. There is no fundamental mechanical basis for this proposition, however. The fact is that during the third attempt to raise the water level, displacement velocities increased continuously and the final attempts to reduce the velocity of the slide by lowering the level of the reservoir (Fig. 5.3) did not work.

An explanation for the apparent inconsistency of results in Figure 5.3 could be found if reservoir water level and rainfall are combined in the spirit that the prevailing water pressures on the sliding surface, irrespective of their origin, should control the stability. Hendron and Patton (1985) found a reasonably good explanation if rainfall, averaged over the preceding 30 days, and water level are jointly considered to explain the landslide velocity. The actual failure occurred for a 30-day precipitation of 240 mm when the reservoir was at elevation 700 m. Leonards (1987) analyzed further the rainfall records and the history of reservoir elevation and could not find a satisfactory explanation, free of inconsistencies, for the relationship between velocities of the slide, reservoir elevation and previous rainfall. The pore pressure regime prevailing at the sliding surface remains rather uncertain in the Vaiont landslide.

5.3 AN EVOLUTIVE TWO-WEDGE STABILITY MODEL

The two representative cross-sections 2 and 5 in Figure 5.6 have been represented in Figure 5.7 in a simplified version, which is, however, close to the original drawings. The two plots highlight that the failure surface could be described by two planes: a lower horizontal plane daylighting at the river canyon wall and an inclined planar surface. A rock wedge whose thickness decreases upwards rests on the inclined plane. The rock mass reaches its maximum thickness, 270 m, in the central lower part of the slide above the horizontal sliding plane.

A good proportion of reported stability analyses of Vaiont, especially in the years following the failure, have concentrated in the determination of the friction angle necessary for stability (Jaeger, 1965a,b; Nonveiller, 1967; Mencl, 1966; Skempton, 1966; Kenney, 1967). Classic procedures for stability analysis in soil mechanics using limit equilibrium methods were used. The preceding account of the relevant information on Vaiont, namely the data presented by Hendron and Patton (1985) indicates, however, that the friction angle at the failure surface could hardly be larger than 12°.

Two main reasons support this statement: the fact that Vaiont was a case of landslide reactivation (which implies large previous shearing displacements at the sliding surface and hence a clear situation of residual strength conditions) and the small residual friction angles (8°-10°) measured in the highly plastic clays (Caumontmorillonite rich) found in the clays associated with the sliding surface.

Therefore a relevant question is: Are the representative cross-sections in Figure 5.7 stable, given the value of the basal friction angle and the estimated conditions of pore water pressure, when the reservoir reached elevations in the range 650 to 700 m?

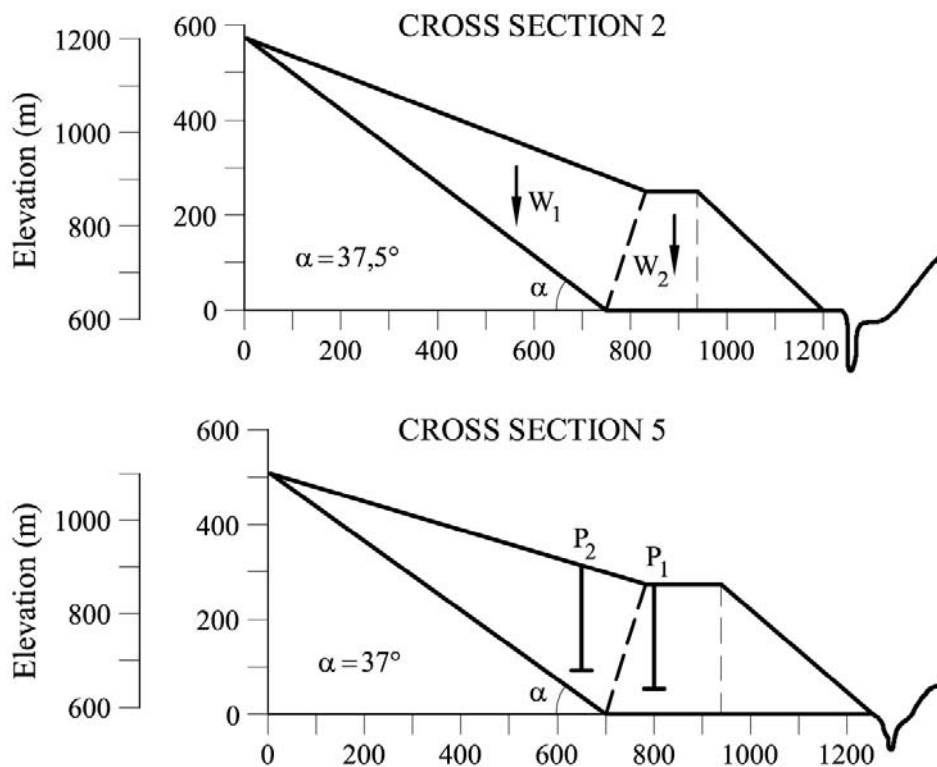


Figure 5.7 Cross-sections 2 and 5 of Vaiont landslide. Initial geometry.

The cross-sections plotted in Figure 5.6 suggest that the slide may be defined as two interacting wedges: an upper one (Wedge 1) sliding on a plane having a dip of 36° - 37° and a lower one (Wedge 2) sliding on a horizontal plane. Since a (common) friction angle of 12° is acting at the basal sliding surfaces, the upper wedge is intrinsically unstable and will push the lower resisting wedge. The weights of the two wedges and the distribution of pore water pressures prevailing on the sliding plane will, as a first approximation, dictate the stability conditions. However, the interaction between the two wedges plays also a relevant role to explain the stability, as discussed below.

It is worth at this point to examine the kinematics of the slide. If the motion starts, one may imagine the slide as a train sliding downwards, an image which is brought to justify that the absolute velocity in the upper and lower parts of the slide are essentially the same. Surveying data plotted in Figure 5.1 supports this simple hypothesis. The difference in velocity (or displacement) when comparing the upper and lower parts of the slide lies obviously in the direction of these vectors: they will be parallel to the underlying failure surface. A conflict arises, however, at the kink or junction between the two sliding planes. It is hard to imagine that voids will develop in the layered sequence of marl and limestone at 270 m depth. The alternative is the bending and shearing of strata. In fact, a single shearing plane may be invoked to accommodate the sudden change direction of velocity at the kink. This is indicated in Figure 5.8a, where sliding velocity vectors v_1 (in the direction of the upper inclined surface) and v_2 (horizontal, parallel to the basal plane) are plotted with a common origin. This velocity

diagram represents the conditions at the kink (point A), where the rock approaches A with velocity v_1 and leaves it with velocity v_2 . The relative motion of the two wedges (vector v_{12}) is directed in the direction of the bisector of the angle between the upper and lower sliding surfaces. Therefore, the change in the direction of the velocities of the two wedges may be accommodated by a relative shear in the direction of the bisector plane plotted in Figure 5.8.

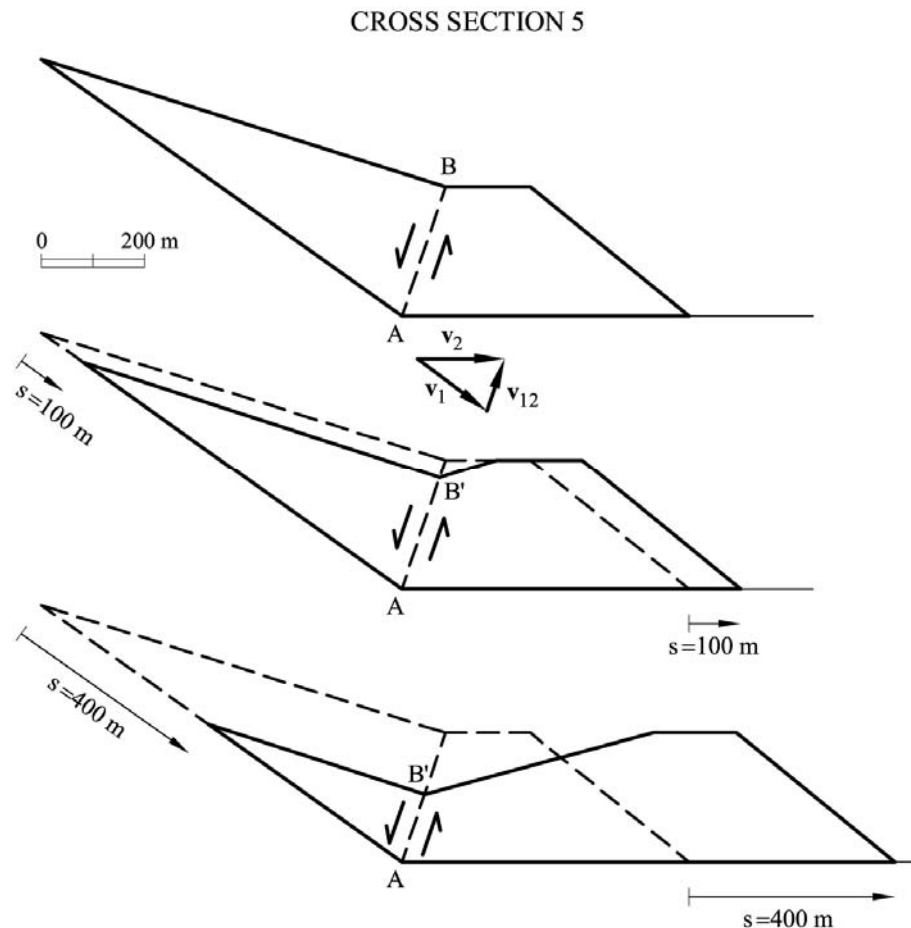


Figure 5.8 Kinematics of sliding. Section 5.

The motion of the slide implies that mass from the upper wedge is transferred to the lower block, increasing its volume. Therefore, the weight of the upper unstable wedge decreases and, at the same time, the weight of the lower block, resting on a sub-horizontal surface, increases. The net result is an improvement of stability. In this process the sliding resistance along the common plane separating the two wedges has to be overcome. If it is accepted, because of the preceding discussion, that the common plane of intense shear bounding the two wedges is the bisector plane, the evolution of the geometry of the sliding mass may be approximated by the successive cross-sections shown in Figure 5.8 for total slide displacements $s = 0$ m, $s = 100$ m and $s = 400$ m. Figure 5.8 is a graphical expression of the condition of mass conservation

during the landslide motion. It will be used later to perform a dynamic analysis of the failure.

5.3.1 Internal shearing

Shearing across the common plane AB between the upper and lower wedges (Fig. 5.8) has a direction approximately perpendicular to the sedimentation planes of the marl and limestone layers of the Malmö period overlying the failure surface. The shear resistance offered by plane AB is difficult to estimate because of the intricate geometry involved at several scales and the limited continuity of joints. Following Hoek (2007), the strength of rock masses may be approximated if some basic characteristics are determined (rock matrix unconfined strength; degree of jointing and state of the surfaces, lithology, etc). Figure 5.9 shows the strength envelope in a Mohr stress plane for a rock mass which may approximate the Malmö layers above the sliding surface of Vaiont. Details of the defined rock mass are given in the caption of Figure 5.9. It may correspond to the Vaiont slide mass, which was described as follows by Müller (1987), after the failure:

“The part of the stratigraphic column exposed in the slide mass consists of beds of partially crystalline limestones, limestones with hard siliceous inclusions, marly limestones and marls. Many beds are strongly folded and show indications of slope tectonics. Its geological structure but also its geological sequence has remained essentially unchanged. The entire rock mass remained intact and the sediment facies is nearly unchanged. Apart from some newly formed faults, the only other effects of the slide were the opening of existing joints and the development of new joints, resulting in an overall volume increase of 4-6% and an associated reduction of the mechanical coherence of the rock mass”

The strength envelope is nonlinear but a Mohr-Coulomb approximation is also shown in Figure 5.9 for a range of normal stresses centered at $\sigma'_n = 2$ MPa, a stress which may represent average conditions on the bisector plane AB (Fig. 5.8). The Mohr-Coulomb strength parameters ($c' = 0.787$ MPa; $\phi' = 38.5^\circ$) define the linear M-C approximation.

The relevant point is that the shear plane AB may offer a substantial resistance to be sheared and this resistance has probably a significant role in stability. Shearing across a rock mass is typically associated with the release of energy. In fact, in the years preceding the failure, when three attempts to fill the reservoir were made, seismic events were recorded on the slide surface. Their location has been plotted in Figure 5.1. They approximately span, in plan view, the position of the shear plane AB plotted in Figure 5.8. Nonveiller (1987), quoting a report on these shocks mentions that *“...the shocks generated in the zone of the slide signify dilation of the material in a zone of sagging of the rock.”*

These events had an increasing frequency in periods of slide acceleration, when the reservoir level increased. This is shown in Figure 5.2, where seismic events have been plotted as small marks in the time axis (lower part of the figure).

It was also reported that the rock experienced a global degradation, reflected in a substantial drop of p-wave velocities, as a result of the slide motion during the period December 1959-December 1960. All this evidence supports the conclusion that a rock mass around the position of the ideal shear plane AB was subjected to intense shearing during the cycles of filling and emptying the reservoir in the years previous to the failure.

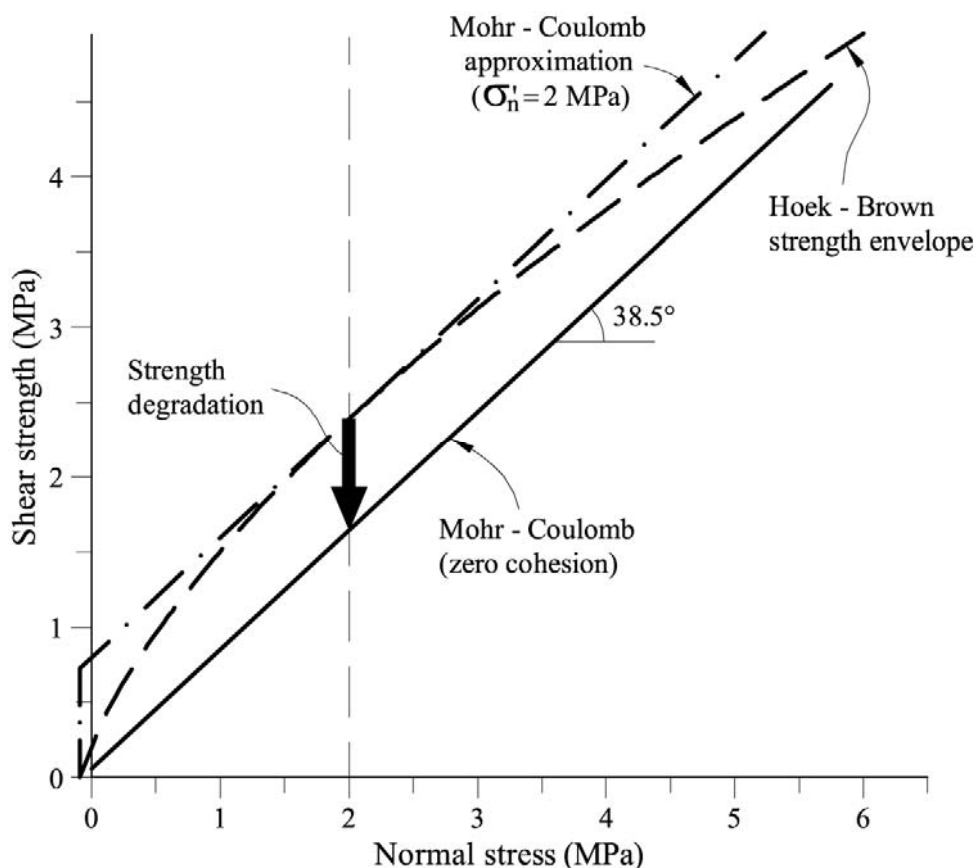


Figure 5.9 Strength envelope of a rock mass described as: Strength of intact material: 50 MPa (limestone-claystone); Hoek Geological Strength Index (GSI = 50) (very blocky, interlocked, partially disturbed, with multifaceted angular blocks formed by four or more joint sets), Hoek m_i parameter $m_i = 9$ (marls, soft limestones); degradation parameter $D = 0.5$ (in a scale 0 to 1). (According to Hoek-Brown classification of rock masses). Also shown is the Mohr-Coulomb approximation for a normal stress of 2 MPa ($c' = 0.787$ MPa, $\phi' = 38.5^\circ$) and an arrow showing the degradation of cohesive intercept at constant ϕ' value

A loss of strength (reduction of mechanical coherence in Müller words) was certainly a consequence of this straining. Typically cohesion is first lost but friction tends to remain without much change. This drop of cohesion as a result of straining

along plane AB has also been shown in Figure 5.9. In the model described below, the apparent cohesion in the shear plane AB will be reduced as the slide moves forward. Going back again to Figure 5.8, as slide displacement increases, “new” planes of rock cross the shearing position AB, which remains fixed at the position of the bisector plane, which is independent of the slide motion. The consequence is that the shear strength along this plane will not decrease in a sudden and intense manner. Certainly the motion of the slide will have some weakening effect, which is difficult to quantify.

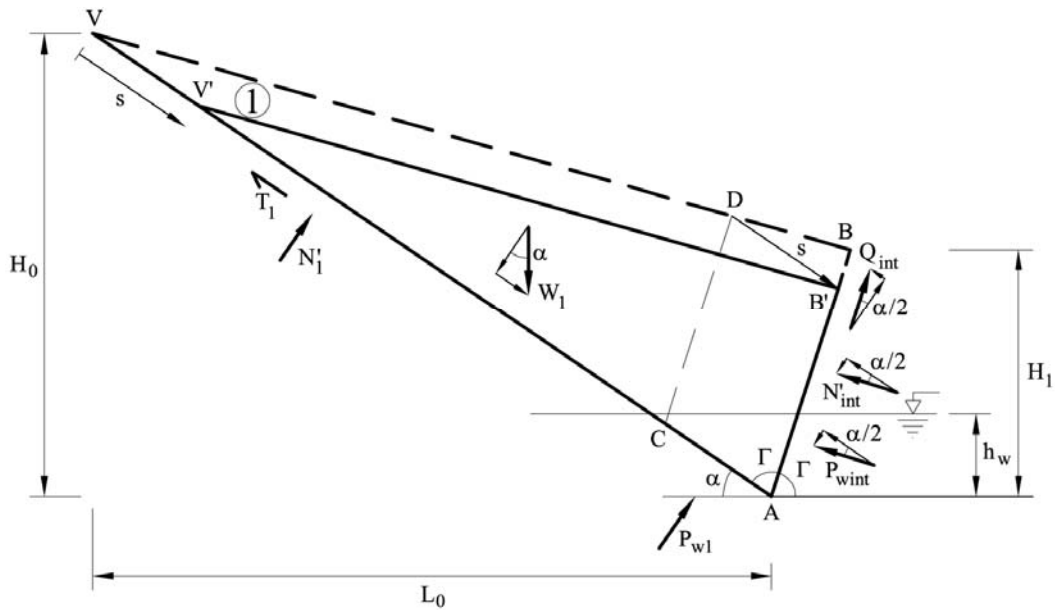


Figure 5.10 Geometry and forces on upper Wedge 1.

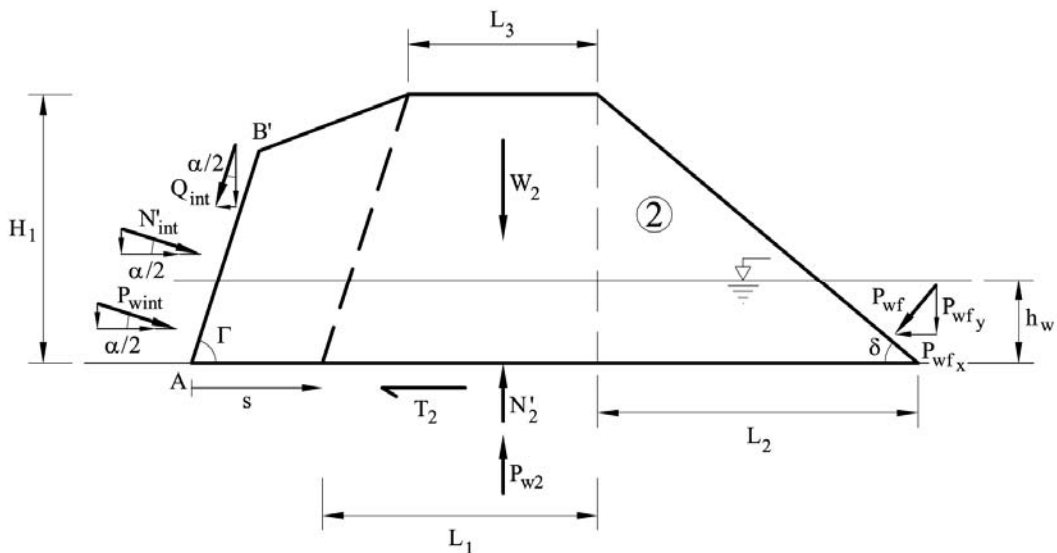


Figure 5.11 Geometry and forces on lower Wedge 2.

5.3.2 Motion equations

A model based on the interaction of two wedges will now be developed. The main assumptions are: The upper and lower wedges change their geometry during sliding, as shown in Figure 5.8. The upper wedge loses volume, which is added to the lower one. During this process the common plane AB reduces in length. Shearing across AB (or, more generally, AB') is described by a Mohr-Coulomb strength criterion ($\tau = c'_r + \sigma' \tan \phi'_r$). In addition, the cohesive intercept, c'_r , is made dependent on the slide displacement, s . This is a simplified procedure to introduce strength degradation of the rock mass during the slide motion. The friction angle is maintained constant. The lower sliding surface is assumed to be in residual conditions with strength parameters ($c'_b = 0$; $\phi'_b = 12^\circ$). Pore water pressures are given by a horizontal phreatic level.

Equilibrium conditions are formulated in dynamic terms. In this way it will be possible to analyze the effect of strength degradation of the shearing plane AB' on slide motion. Static conditions of equilibrium are a particular case of the dynamic case. Only inertia terms are considered. No viscous effects are introduced.

Equilibrium conditions will be written for the upper and lower wedge and a common interaction force across plane AB will be enforced.

Upper Wedge 1 Consider the wedge geometry and external forces in Figure 5.10. Equilibrium parallel to the motion (displacement s ; velocity $v = ds/dt$) reads:

$$W_1 \sin \alpha - T_1 - N'_{\text{int}} \cos(\alpha/2) - Q_{\text{int}} \sin(\alpha/2) - P_{\text{wint}} \cos(\alpha/2) = \frac{d(M_1 v)}{dt} \quad (5.1)$$

where M_1 is the mass of Wedge 1, ($W_1 = M_1 g$; g : gravity acceleration). The time derivative of the right-hand side of Equation (5.1) can be developed as

$$\frac{d(M_1 v)}{dt} = M_1 \frac{dv}{dt} + \frac{dM_1}{dt} v \quad (5.2)$$

Equilibrium in normal direction to the basal sliding plane leads to:

$$W_1 \cos \alpha - N'_1 + N'_{\text{int}} \sin(\alpha/2) - Q_{\text{int}} \cos(\alpha/2) - P_{\text{wl}} + P_{\text{wint}} \sin(\alpha/2) = 0 \quad (5.3)$$

where the interaction effective forces Q_{int} and N'_{int} are related through

$$Q_{\text{int}} = c'_r AB' + N'_{\text{int}} \tan \phi'_r \quad (5.4)$$

In addition, the shear resistance on the base of the wedge is given by

$$T_1 = N'_1 \tan \phi'_b \quad (5.5)$$

The motion Equation (5.1), in view of (5.3)-(5.5) becomes:

$$W_1 s_1 - N'_{\text{int}} s_2 + c'_r AB' s_3 - P_{\text{wint}} s_4 + P_{\text{w1}} \tan \phi'_b = \frac{d(M_1 v)}{dt} \quad (5.6)$$

where s_i are trigonometric constants, given by:

$$s_1 = \sin \alpha - \tan \phi'_b \cos \alpha \quad (5.7a)$$

$$s_2 = \tan \phi'_b \sin(\alpha/2) - \cos(\alpha/2) \tan \phi'_r \tan \phi'_b + \cos(\alpha/2) + \sin(\alpha/2) \tan \phi'_r \quad (5.7b)$$

$$s_3 = \tan \phi'_b \cos(\alpha/2) - \sin(\alpha/2) \quad (5.7c)$$

$$s_4 = \tan \phi'_b \sin(\alpha/2) + \cos(\alpha/2) \quad (5.7d)$$

For static equilibrium ($\frac{d(M_1 v)}{dt} = 0$), Equation (5.6) provides the normal interaction force between the two wedges:

$$N'_{\text{int}} = \frac{1}{s_2} (W_1 s_1 + c'_r AB' s_3 - P_{\text{wint}} s_4 + P_{\text{w1}} \tan \phi'_b) \quad (5.8)$$

When the wedge slides a distance s along the basal plane, the length of the shear plane reduces from AB to AB' (Figure 5.8). Since triangles AVB and $AV'B'$ are similar, it is easy to find:

$$AB' = \frac{L_0 / \cos \alpha - s}{L_0 / \cos \alpha} \frac{H_1}{\cos(\alpha/2)} \quad (5.9)$$

where H_1 is the thickness of the lower wedge over the sliding plane. The volume of Wedge 1 can be expressed as a function of the initial geometric parameters and the displacement s as

$$V_{\text{Wedge 1}} = \frac{1}{2} \left(\frac{L_0}{\cos \alpha} - s \right)^2 \frac{H_1}{L_0} \cos \alpha \quad (5.10)$$

The mass and weight of the wedge can be now easily calculated by multiplying the volume of Equation 5.10 by the density (δ_r) and unit weight (γ_r) of the rock, respectively.

Time variation of mass can be obtained as follow:

$$\frac{dM_1}{dt} = \delta_r \frac{dV_{\text{Wedge 1}}}{dt} = -\delta_r \left(\frac{L_0}{\cos \alpha} - s \right) \frac{H_1}{L_0} \cos \alpha \frac{ds}{dt} \quad (5.11)$$

where the time variation of the displacement ($\frac{ds}{dt}$) is equal to the velocity.

Lower Wedge 2 The wedge geometry and external forces are given in Figure 5.11. The wedge is shown displaced forward a distance s .

Equilibrium parallel to the direction of motion at a velocity $v = ds/dt$ reads:

$$N'_{\text{int}} \cos(\alpha/2) - Q_{\text{int}} \sin(\alpha/2) - T_2 = \frac{d(M_2 v)}{dt} \quad (5.12)$$

where M_2 is the mass of Wedge 2 ($W_2 = M_2 g$; g : gravity acceleration). Note that the horizontal components of the water pressure forces P_{wint} and P_{wf} are equal and opposite in sign. The terms on the right-hand side of the Equation (5.12) can be developed following Equation (5.2). Since the total mass of the slide is constant, the time variation of M_2 will be equal to the time variation of M_1 indicated in Equation (5.2) but with an opposite sign.

Under limiting conditions, the base resistance is given by

$$T_2 = N'_2 \tan \phi'_b \quad (5.13)$$

and taking Equation (5.4) into account,

$$N'_{\text{int}} \cos(\alpha/2) - N'_2 \tan \phi'_b - (c'_r AB' + N'_{\text{int}} \tan \phi'_r) \sin(\alpha/2) = \frac{d(M_2 v)}{dt} \quad (5.14)$$

Equilibrium in normal direction to the horizontal sliding plane gives:

$$W_2 - N'_2 + N'_{\text{int}} \sin(\alpha/2) + (c'_r AB' + N'_{\text{int}} \tan \phi'_r) \cos(\alpha/2) + P_{\text{wint}} \sin(\alpha/2) + P_{\text{wfy}} - P_{\text{w}_2} = 0 \quad (5.15)$$

where P_{wfy} is the vertical component of the water pressure force acting on the slope surface. Equation (5.15) provides an expression for N'_2 which is then introduced in Equation (5.14). The following expression is then found for the equation of motion in the direction of sliding:

$$N'_{\text{int}} s_5 - c'_r AB' s_6 - P_{\text{wint}} s_7 + (P_{\text{w}_2} - P_{\text{wfy}} - W_2) \tan \phi'_b = \frac{d(M_2 v)}{dt} \quad (5.16)$$

where s_i are trigonometric constants, given by:

$$s_5 = \cos(\alpha/2) - \tan \phi'_b \sin(\alpha/2) - \cos(\alpha/2) \tan \phi'_r \tan \phi'_b - \sin(\alpha/2) \tan \phi'_r \quad (5.17a)$$

$$s_6 = \tan \phi'_b \cos(\alpha/2) + \sin(\alpha/2) \quad (5.17b)$$

$$s_7 = \tan \phi'_b \sin(\alpha/2) \quad (5.17c)$$

The effective interaction force between the two wedges is now found from Equation (5.16):

$$N'_{\text{int}} = \left(\frac{1}{s_5} \right) \left(c'_r AB' s_6 + P_{\text{wint}} s_7 + (P_{\text{w}_2} - P_{\text{wfy}} - W_2) \tan \phi'_b + \frac{d(M_2 v)}{dt} \right) \quad (5.18)$$

A single motion equation may now be found if N'_{int} , given by (5.18), is replaced in the motion equation for the upper wedge (5.6). Rearranging terms, the following equation of motion is derived:

$$W_1 t_1 + (W_2 - P_{w2} + P_{wfy}) t_2 + c'_r AB' t_3 - P_{\text{wint}} t_4 + P_{w1} t_5 = s_5 \frac{d(M_1 v)}{dt} + s_2 \frac{d(M_2 v)}{dt} \quad (5.19)$$

where

$$t_1 = s_1 s_5 \quad (5.20a)$$

$$t_2 = \tan \phi'_b s_2 \quad (5.20b)$$

$$t_3 = s_3 s_5 - s_2 s_6 \quad (5.20c)$$

$$t_4 = s_4 s_5 + s_7 s_2 \quad (5.20d)$$

$$t_5 = \tan \phi'_b s_5 \quad (5.20e)$$

5.4 STATIC EQUILIBRIUM AT FAILURE AND SAFETY FACTORS

Under strict static equilibrium conditions, ($\frac{dv}{dt} = 0$ and masses of each wedge remain constant), Equation (5.19) provides the value of the apparent effective cohesion along the shearing plane AB in terms of the friction angle on AB, ϕ'_r , the wedge weights, the pore pressure forces on their boundaries and the geometrical factors:

$$c'_r = \frac{-W_1 t_1 - (W_2 - P_{w2} + P_{wfy}) t_2 + P_{\text{wint}} t_4 - P_{w1} t_5}{AB' t_3} \quad (5.21)$$

The resultants of water pressure forces entering the above equations are easily found as follows:

$$P_{wfy} = \frac{h_w^2 \gamma_w}{2 \tan \delta} \quad (5.22a)$$

$$P_{w2} = (L_1 + L_2 + s) h_w \gamma_w \quad (5.22b)$$

$$P_{w1} = \frac{h_w^2 \gamma_w}{2 \sin \alpha} \quad (5.22c)$$

$$P_{\text{wint}} = \frac{h_w^2 \gamma_w}{2 \cos(\alpha/2)} \quad (5.22d)$$

Initial ($s = 0$) wedge volumes, in view of Figures 5.10 and 5.11, are given by

$$V_{10} = \frac{L_0 H_1}{2 \cos \alpha} \quad (5.23a)$$

$$V_{20} = \frac{L_1 + L_2 + L_3}{2} H_1 \quad (5.23b)$$

which allow the calculation of wedge weights.

Cross-sections 2 and 5 (Fig. 5.6) are characterized by the geometrical parameters given in Table 5.1. The upper wedges of Sections 2 and 5 have a similar volume. However, the lower wedge of Section 2 has a significantly lower volume than Section 5. Therefore, Section 5 is more stable than Section 2, for a common set of strength parameters. Conditions for static equilibrium of these two sections will be first examined with the help of the set of relationships derived in the previous section. Since it has been argued that the residual friction at the basal sliding surface is a parameter known with sufficient certainty, the condition of stability may be used only to determine the strength parameters on the shear plane AB. In fact, only combinations of the pair (c'_r ; ϕ'_r) may be found since only one condition is available: the condition of static equilibrium at the initiation of failure (Eq. (5.21)).

Table 5.1. Geometrical parameters of cross-sections 2 and 5

	H_0 (m)	H_1 (m)	L_0 (m)	L_1 (m)	L_2 (m)	α (°)	δ (°)	V_1 (m ³ /m)	V_2 (m ³ /m)
Section 2	580	245	750	190	260	37.7	43.3	116142	68149
Section 5	510	260	700	240	320	36	39.1	112590	93000

This is a nonlinear equation relating c'_r and ϕ'_r , which has been plotted in Figure 5.12 for Sections 2 and 5, assuming ϕ'_b equal to 12° and a rock specific weight of 23.5 kN/m³.

Forces P_w (Eq. (5.22)), which provides the effect of water pressures on both wedges, should correspond to failure conditions. Both water pressure influences, those associated with the preceding rainfall (which was shown to have a non-negligible effect) and those induced by the reservoir water level, will be lumped into a water level height above the lower horizontal sliding surface, h_w . Data given by Hendron and Patton (1985) provides the estimation of the equivalent value of h_w , i.e.: the reservoir water level, in the absence of rain in the preceding 30-day period, which explains the failure. This height correspond to the elevation 710 m approximately and therefore, in Section 5 it implies a value $h_w = 120$ m. This reservoir elevation corresponds, in Section 2, to water height of $h_w = 90$ m (the failure surface daylights at a higher elevation at

Section 2; see Fig. 5.4). The $(c'_r; \phi'_r)$ values plotted in Figure 5.12 correspond to these two water elevations over the lower horizontal sliding plane.

Section 2 is “more demanding” in terms of required rock strength simply because of the relative weight of upper and lower wedges. This situation is reflected in the higher strength values required for equilibrium calculated for Section 2 (Fig. 5.12). It is interesting to check that the $(c'_r; \phi'_r)$ combinations in Figure 5.12 are in fairly good agreement with the strength expected in the rock sheared across bedding planes, discussed before. Since the variability of ϕ'_r values is small compared with the expected variation of cohesive intercepts (c'_r), a band of expected $(c'_r; \phi'_r)$ pairs, centred around $\phi'_r = 38^\circ$ - 40° has been plotted in Figure 5.12 as a reasonable estimation of the rock strength along the shear plane AB.

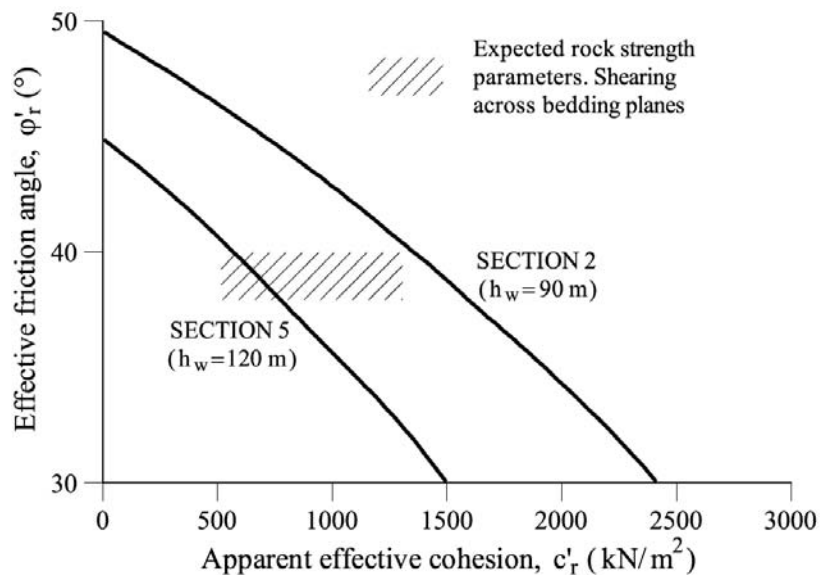


Figure 5.12 Strength parameters across shearing plane AB for equilibrium. Sections 2 and 5. Basal friction: $\phi'_b = 12^\circ$.

If Section 5 is taken as a representative cross-section of the slide, the following combinations lead to strict equilibrium of Vaiont slide: $(c'_r = 768.35 \text{ kPa}; \phi'_r = 38^\circ)$; $(c'_r = 561.3 \text{ kPa}; \phi'_r = 40^\circ)$.

The model of two interacting wedges developed before includes two failure surfaces: the “basal” surface which bounds the landslide and an internal shear surface (AB) which makes it kinematically possible. The nature of both surfaces is quite different: the former is located in a high plasticity clay in residual conditions whereas the internal shear surface crosses sedimentary planes, distorts a competent rock and exhibits a significant strength (however, it is quite possible that shear displacements will decrease to some extent the shear strength of this shear plane). For a particular situation of the slide (for instance, under natural conditions before dam construction)

the two shearing surfaces will most probably not mobilize their shear strength in equal proportions. Likewise, if a change in external conditions takes place (reservoir impoundment, or rainfall) the available strength will not be mobilized at the same time among the two surfaces because the shear stiffness of the shearing surfaces and, indeed, of the whole rock mass will also play a significant role.

Since the problem is complicated, let us accept, to initiate the discussion, that two different safety factors, F_b and F_r , are appropriate for the two surfaces. Then, the mobilized strength parameters will be defined as follows:

$$\tan \phi'_{b_{mob}} = \frac{\tan \phi'_b}{F_b}; \quad \tan \phi'_{r_{mob}} = \frac{\tan \phi'_r}{F_r}; \quad c'_{r_{mob}} = \frac{c'_r}{F_r} \quad (5.24a,b,c)$$

A relevant issue is to ask for the safety factor, F_r , of the Vaiont slide at the beginning of impoundment (i.e.: $h_w=0$) in the hypothesis that the mobilized stress at the basal sliding surface remained at the residual value, $\phi'_b=12^\circ$, (i.e.: $F_b=1$). It is also of interest to know how would F_r change, still under $F_b=1$, if the slide moves forward following the mechanism described in Figure 5.8.

Alternatively, one may wish to maintain the classic approach and to find a unique and global safety factor, F , for the two situations mentioned, ($F = F_b = F_r$). The two possibilities will be examined here.

The first problem is to decide which are the actual strength parameters on the shearing surfaces defined. If Section 5 is accepted as representative of sliding conditions, it was found that $\phi'_b = 12^\circ$, $c'_r = 768.35$ kPa and $\phi'_r = 38^\circ$ are a reasonable approximation to the actual strength prevailing on shearing surfaces. For conditions other than those leading to failure (for instance no water pressure acting on the slide) the preceding equilibrium conditions are still valid provided the strength parameters are substituted by the mobilized values. Then, since the mobilized parameters are expressed in terms of the (true) strength parameters through the definition of safety factors (Eq. 5.24), the equilibrium equations derived before provide a relationship which should be satisfied by the safety factor(s). The equilibrium equation will now be a function of F_b and F_r and therefore only one safety factor may be determined - either F if it is accepted that $F = F_b = F_r$, or F_r if F_b is fixed, for instance at $F_b = 1$, or any other alternative -.

If the mobilized strength parameters (Eq. 5.24) are substituted into the equilibrium Equation 5.21, the following expression is obtained:

$$\frac{c'_r}{F_r} = \frac{-W_1 t_1(F_r, F_b) - (W_2 - P_{w2} + P_{wfy}) t_2(F_r, F_b) + P_{wint} t_4(F_r, F_b) - P_{w1} t_5(F_r, F_b)}{AB' t_3(F_r, F_b)} \quad (5.25)$$

where the dependence of the t_i and s_i expressions on the safety factors has been explicitly indicated. If Equation 5.25 is developed it turns out to be a second order algebraic equation for F_r , which may be solved, if F_b is assumed to be known.

Safety factors F_r of Section 5 of Vaiont slide were obtained for:

- Water pressure conditions prior to failure. As discussed before, pore water pressure effects are integrated into the variable h_w , the reservoir level over the lower horizontal sliding plane.
- The changing geometry, as the slide moves forward and the water level maintains the maximum elevation, $h_w=120$ m. This is a purely static analysis performed on different geometries of the slide as it moves forward. The dynamics of the motion will be introduced in the next section and it will be discussed in more detail in Chapter 6.

The effect of h_w on safety factor F_r , when $F_b = 1$, is plotted in Figure 5.13. The calculated value for $h_w=0$ ($F_r=1.2$) is not particularly high and it indicates that the mobilized strength in the rock mass before any impounding was quite substantial in order to maintain the slope in equilibrium.

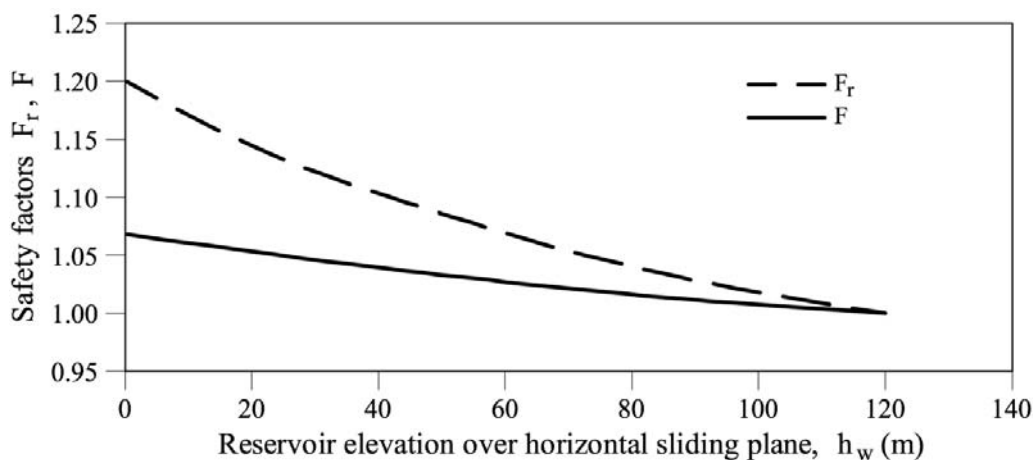


Figure 5.13 Section 5. Evolution of safety factors, F_r (if $F_b = 1$; see text) and global safety factor, F , when water level increases in the reservoir.

The analysis of the changing geometry, sketched in Figure 5.8, leads to the safety factors F_r plotted in Figure 5.14. The increase of F_r , again for $F_b = 1$, becomes more pronounced as the slide displacement increases. The high values calculated for $s = 150$ m ($F_r = 5$), indicate that the mobilized resistance across the shear plane AB is no longer necessary to maintain equilibrium. In fact, beyond $s = 179$ m, the residual friction angle at the main sliding surface is able to maintain the slope in equilibrium without any contribution from the sheared rock mass across the shear plane AB.

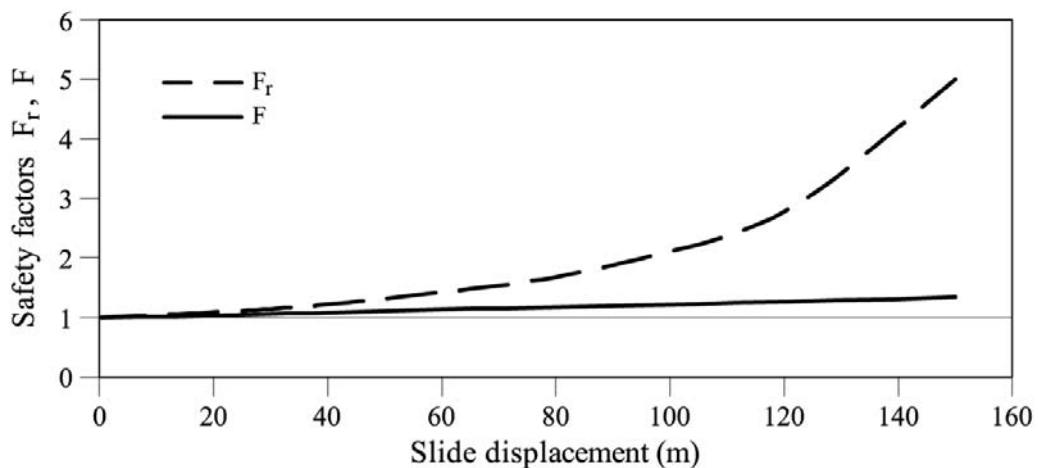


Figure 5.14 Section 5; $h_w = 120$ m. Evolution of safety factors, F_r (if $F_b=1$; see text) and global safety factor, F , with slide displacement.

Let us consider now the determination of a unique global safety factor F . The condition $F = F_b = F_r$ has to be introduced in Equation 5.25. The equilibrium Equation 5.25 now becomes a fourth order polynomial for the unknown F . Calculated global safety factors have been plotted also in Figures 5.13 and 5.14. Computed values of F are now significantly lower than the previously reported values of F_r .

The global safety factors calculated for changing water levels within a very large range (0 to 120 m of water column) (Fig. 5.13) look particularly low (F decreases from $F = 1.07$ for $h_w = 0$ m to $F = 1$ for $h_w = 120$ m). This is a consequence of the very large size of the landslide but it also points out that the presence of the reservoir implied a relatively minor change in the safety of the slope, always within the perspective of risk associated with the classical definition of a global safety factor. Moreover, this result is also an indirect indication that in very large landslides, feasible remedial measures are expected to lead to relatively low increments of safety factor.

Figure 5.14 shows that the motion of the slide results in geometries with increasing global safety factor. Given the preceding comments, changes are far from being negligible. In fact, displacements of 40, 100 and 150 m imply F values of 1.08, 1.22 and 1.36 respectively.

5.5 LANDSLIDE RUNOUT

Equilibrium conditions, when inertia terms are included, result in the motion Equation (5.19). This equation has the following form:

$$a = \frac{dv}{dt} = f(s) = f\left(\int_0^t v dt\right) \quad (5.26)$$

At any given time of the motion, slide acceleration ($a = \frac{dv}{dt}$) is a function of slide displacement, s . Function f includes also information on geometry, specific weights, water pressures and strength parameters. Finding a closed form solution for $v(t)$ is a hard task but the structure of Equation (5.26) allows to develop a simple explicit numerical algorithm of integration. In view of the nature of the problem and the simplicity of the underlying mechanical model it is probably not justified in this case to look for more sophisticated integration procedures.

It was argued, when developing the model of two interacting wedges, that the effective rock cohesive intercept, c'_r , would be degraded during shear along the plane AB. Since relative shear displacements along AB are controlled by displacement s , a simple degradation model is to make c'_r dependent on s . For instance,

$$c'_r = c'_{r0} \exp(-\Gamma s) \quad (27)$$

where Γ is a constant (units: length⁻¹) which controls the rate of rock degradation and c'_{r0} is the initial cohesion intercept ($c'_{r0} = 768.35$ kPa for cross-section 5, if $\phi'_r = 38^\circ$, accepting $\phi'_b = 12^\circ$). Expression (5.27) was also included in the motion equation in order to explore the effect of loss of shear strength on the dynamics of the motion. It is not reasonable, however, to expect a strong degradation of cohesion along AB' and the reason is that the rock mass "crosses" the plane AB' during the motion and therefore new –more or less undisturbed- rock is continuously sheared across AB.

Consider the following scenario: in a situation of strict equilibrium (reservoir elevation at $h_w = 120$ m in cross-section 5) the water level is increased by a small amount (say $h_w = 121$ m) and it is maintained constant thereafter. It is desired to find the motion of the slide until a new situation of equilibrium is reached. Since the slide improves its static stability conditions as s increases it should be expected that after some displacement, the slide will come to rest.

The solution to this problem (which is the solution of Equation (5.19) plotted as a relationship between the run out (s) and the velocity on the moving mass (v) is shown in Figure 5.15 for no degradation of the rock strength ($\Gamma = 0$). The result shows that the slide stops after a displacement of 0.35 m and reaches a maximum velocity of 1.2 cm/s. If the water level is increased to $h_w = 124$ m and to $h_w = 130$ m, maximum displacements and velocities increase as shown also in Figure 5.15 but the calculated values are very far from the actual behaviour of the landslide, which reached velocities estimated in 30 m/s, more than two orders of magnitude higher than the maximum values found in this calculation.

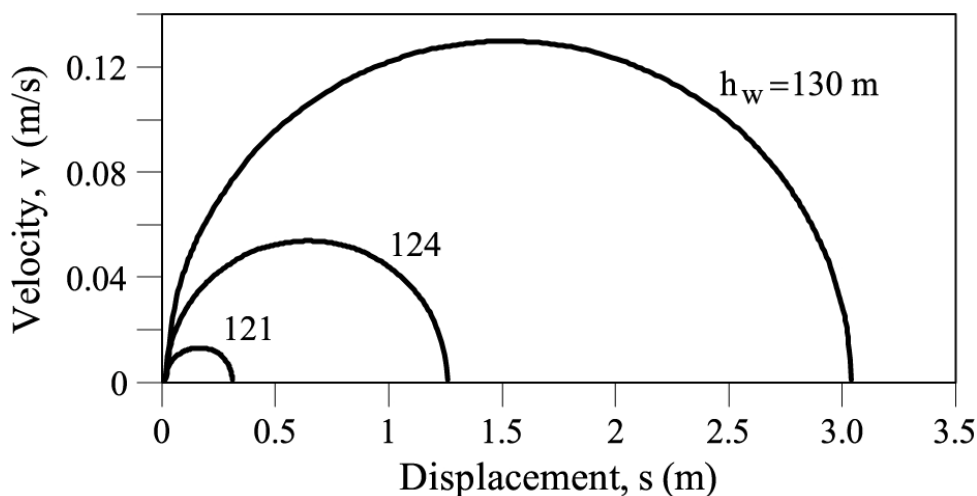


Figure 5.15 Cross-section 5. Calculated run outs and slide velocities for $h_w = 121$ m, 124 m and 130 m. No rock strength degradation ($\Gamma = 0$).

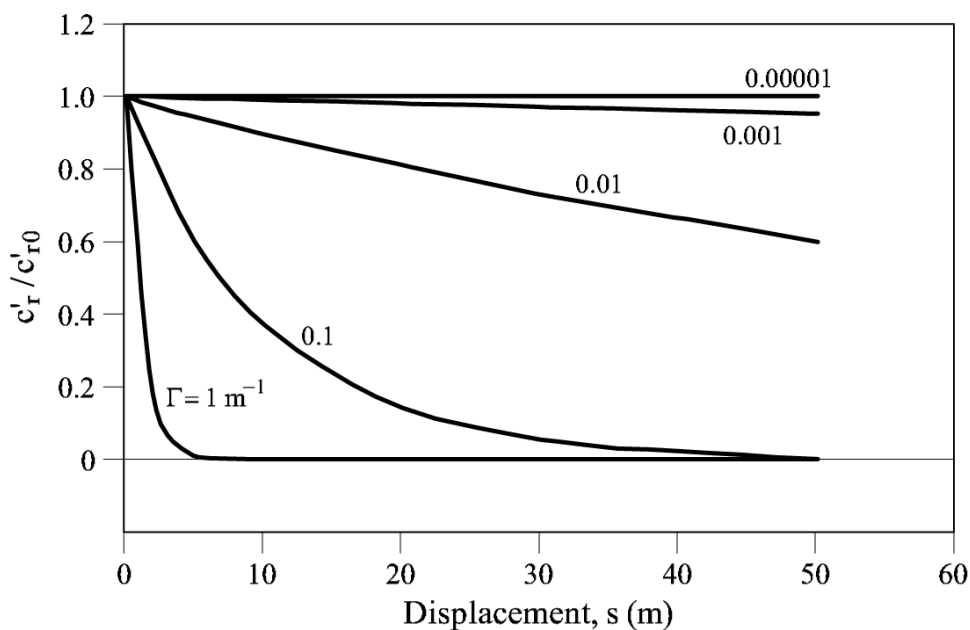


Figure 5.16 Assumed loss of effective cohesive strength parameter across shearing plane AB with slide displacement, for several values of parameter Γ .

The situation changes if some rock strength degradation is introduced into the analysis. Figure 5.16 is a plot of Equation (5.27) for a few values of the degradation parameter Γ . It will be used as a reference for the results of run-out calculations. Now the scenario is to start the slide motion by increasing the water level (to $h_w = 121$ m) and to accept a certain degradation of the rock during the motion. The calculated response of the slide, again in terms of velocity versus displacement, is shown in Figures 5.17 and 5.18. A moderate degradation of the effective strength parameter of the rock ($\Gamma = 0.01$, Fig. 5.17) has a limited effect on the maximum sliding velocity and

on the travelled distance. However, if the degradation of rock effective cohesion is more rapid ($\Gamma = 0.1$ and $\Gamma = 1$; Fig. 5.18), the slide is able to travel long distances (60–80 m) although the maximum velocity does not increase beyond 3 m/s (10.8 km/h) even if a very rapid and complete destruction of the rock effective cohesion is imposed (for $\Gamma = 1$, see Fig. 5.18). Under the more realistic assumption of moderate rock degradation, $\Gamma \leq 1$, the maximum slide velocity is quite small. In all the cases analyzed, the mechanism leading to stop the landslide motion is the change in geometry of the slide as it moves downwards.

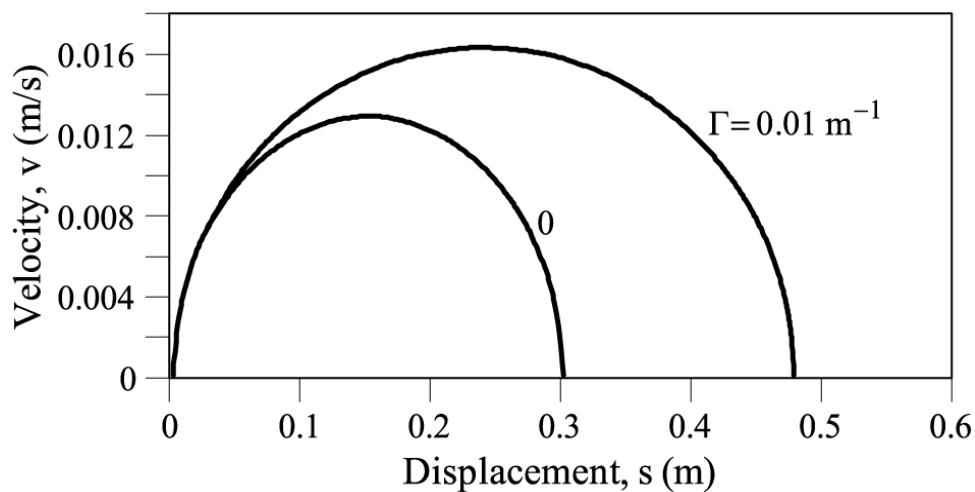


Figure 5.17 Cross-section 5. Calculated run outs and slide velocities for $h_w = 121$ m. Effect of rock strength degradation ($\Gamma = 0$ and $\Gamma = 0.01$).

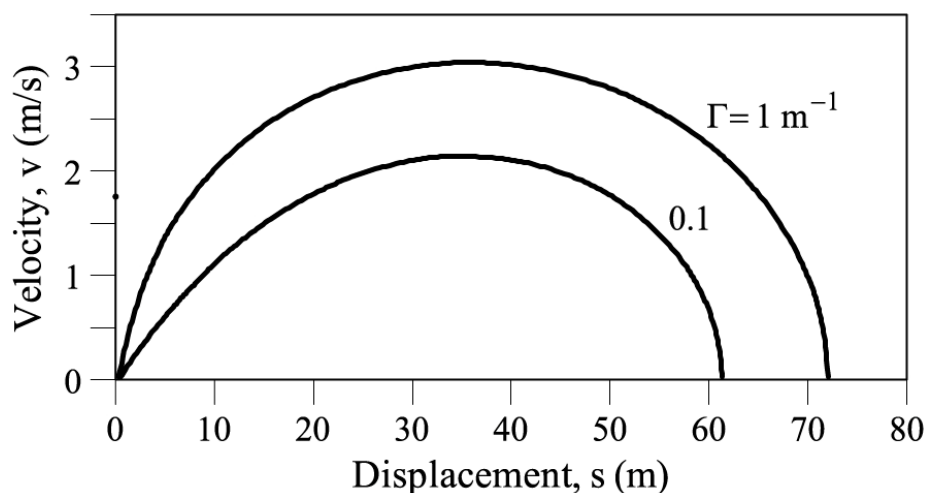


Figure 5.18 Cross-section 5. Calculated run outs and slide velocities for $h_w = 121$ m. Effect of rock strength degradation ($\Gamma = 0.1$ and $\Gamma = 1$).

The dynamic analysis developed here maintains unanswered the key question of the extremely high velocities reached by the slide. However, it indicates that a loss of

internal rock strength, associated to the slide motion itself, is a potential mechanism to accelerate the slide.

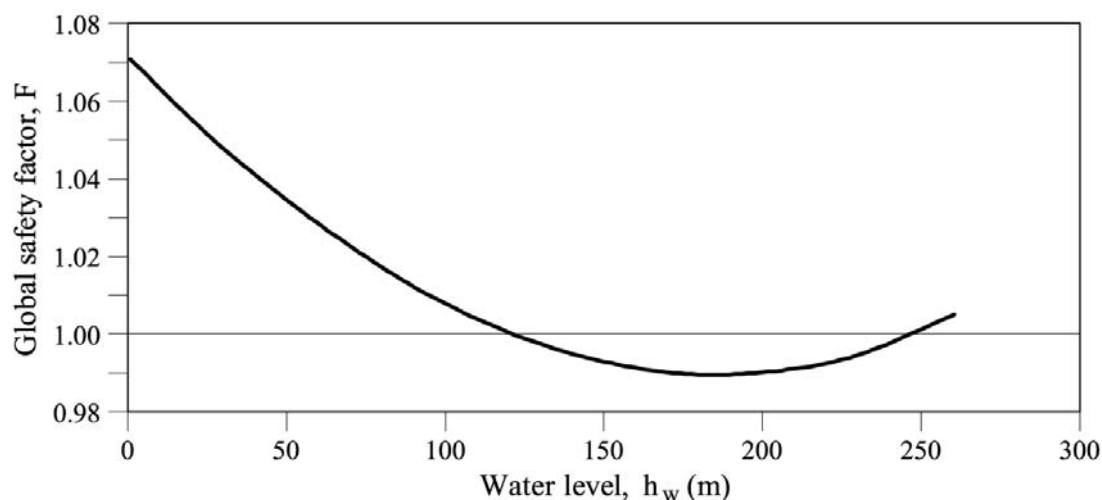


Figure 5.19 Variation of global safety factor with height of water above horizontal basal plane. Two-wedge model. Section 5 of Vaiont.

5.6 DISCUSSION

The investigations on the past history of the landslide by Semenza (2001), synthesized in Figure 5.5, and the work of Hendron and Patton (1987) highlight two fundamental aspects: Vaiont was a case of a slide reactivation and the sliding surface was located in fairly continuous layers of high plasticity clay. Taken together, the implication is that the basal sliding surface could not offer, against a new reactivation of the slide (essentially induced by an increase in pore water pressures in the lower massive passive wedge of the slide), an effective friction angle larger than 10° - 12° . A good proportion of published back-analyses of Vaiont, which use conventional methods of limit equilibrium in order to find the actual friction angle prevailing at the sliding surface at the time of failure, lead to an inconsistent situation. In fact, published back-analysis leads to friction angles in the range 18° - 28° (Kenney, 1967; Hendron and Patton, 1985). Vaiont exhibits a safety factor significantly lower than one if a friction angle of 10° - 12° (and zero effective cohesion) is used in any of the currently available methods of slices.

In order to address this inconsistency, Hendron and Patton (1987) argue that the side friction on the Eastern edge of the slide provided the necessary resisting force to ensure equilibrium (however, some limited information on the direction of displacements on this border -plotted in Figure 5.1-, tends to indicate that the moving mass was detaching from the stable rock massif). The alternative explanation developed here is that the kinematics of the motion, even in a two-dimensional cross-section, requires the relative shearing between the two large rock wedges defining the slide. Leonards (1987) also pointed out that the motion of the slide required such a

rock shearing between the upper and the lower sliding blocks. The estimated shearing strength parameters across the common plane are in a reasonable accordance with the expected mass strength of cretaceous marls and limestones of Vaiont.

The acceleration of the motion during the catastrophic failure escapes the capabilities of the models presented here. A loss of strength is expected when rock masses are sheared, due to its inherent brittleness and the complex development of strains within the moving mass. The end result is a loss of the cohesive components of strength. Such a loss, when imposed on the strength available on the interacting shearing plane between the upper and lower wedges, results in an acceleration of the slide, which is, however, unable to explain the high velocities reached by the landslide, even if a rapid and complete loss of rock cohesion is imposed. If the mechanism of side friction proposed by Hendron and Patton (1985) is accepted as additional resisting phenomena, the need for a convincing mechanism for strength loss is even more pronounced.

5.7 CONCLUSIONS

Some fundamental aspects of Vaiont slide are invoked to propose a consistent, yet simple, kinematic model for the slide. They are:

- The basal sliding surface was most probably in residual conditions. This is explained by the known geologic history of the left bank of Vaiont River. Vaiont was a case of reactivation of an ancient slide which experienced several large scale motions in the past.
- Residual shear tests on Målm clays found on the sliding surface indicate that the basal operative friction angle was close to 12° .
- The geometry of the cross-section of the slide requires that during the sliding motion shearing of rock strata normal to bedding planes take place. The strength of this rock mass has been estimated on the basis of available descriptions. Other field data, namely the recorded seismic events, support also a progressive shearing of rock strata in the years previous to the slide.
- The rock overlying the failure surface was essentially pervious. Water pressures were essentially controlled by reservoir elevation although there are evidences which suggest also a contribution of the previous rainfall regime.

A simple evolutive two-wedge model was developed to accommodate these observations. Mass is being transferred from an upper unstable wedge to a lower stable one during the motion. A common shearing plane bounds the two wedges.

Dynamic equilibrium equations are formulated. They incorporate the conditions of mass conservation. Internal shearing is approximated by a Mohr-Coulomb failure

criterion. The partial motion equations combine into a unique motion equation for the entire landslide which can be integrated.

In a first series of analyses, static conditions were investigated. Safety factors have been defined and found for conditions of the slide previous to reservoir water elevation. A low global safety factor (equal to 1.07) was calculated for an empty reservoir. It was also found, as expected, that the increasing slide displacement, once the motion was started, leads to an increase in safety factor (the weight transfer from the upper to the lower wedge explains this result).

In an attempt to explain the increasing velocity of the slide, the possibility of internal rock strength degradation was introduced. Under this scenario the strength of the internal shearing plane is made dependent on the slide displacement. Only cohesion intercepts are degraded. It was found that if no degradation of the rock strength is considered, an initial unbalance of forces (say by increasing in one meter the reservoir elevation over the situation for strict equilibrium) leads to small displacements (30 cm) and very small maximum velocities (1.2 cm/s) before reaching a new equilibrium state. These figures change as degradation is assumed to increase. However, a full loss of cohesive strength of the rock leads to maximum velocities not exceeding 3 m/s (against the estimated value of 30 m/s). Full degradation of strength is very unlikely, however, because the internal shearing, as the slide displaces, is affecting “new” rock masses in their downhill motion. It is concluded that the internal rock strength degradation is a contributing factor to the acceleration of the slide but it fails to explain the high velocity reached by the slide. This is the subject of the companion paper in which thermal effects are introduced without changing the kinematical description of the motion.

CHAPTER 6

Thermo-Hydro-Mechanical and Dynamic Analysis of Vaiont Landslide

Thermally induced excess pore pressures developed in Chapter 3 have been included into the two wedge evolutive model of Vaiont landslide presented in Chapter 5. The problem requires the solution of a system of four coupled balance equations for the shear bands and the surrounding rock as well as the joint equation of motion of the entire slide. The model predicts the high velocity observed and is consistent with other data (slide geometry, residual strength, conditions on the sliding surface). The interpretation of a sensitivity and scale analysis suggests that there exists a threshold permeability band, in the range 10^{-8} to 10^{-10} m/s, which separates potentially fast motions from slow motions (a result also attained in planar landslide analysis presented in Chapter 4).

6.1 INTRODUCTION

In Chapter 5, an attempt was made to determine the run-out of Vaiont landslide taking, as a reference model, an evolutive two-wedge representation of cross Section 5 (Fig. 5.7). Starting at a condition of near equilibrium at $t = 0$, it was assumed that the strength of the plane separating the two wedges could degrade as shearing displacements developed along this plane during the motion. It was found that, even in the extreme case of a fast and complete loss of cohesion acting on this plane (an unlikely event), the slide maximum velocity did not exceed 3 m/s. In order to explain

the estimated high velocities of the slide (30 m/s), a consistent mechanism or physical process, leading to a total loss of basal shear strength, has to be found.

The favourite explanation of a number of published contributions on the subject is associated with the development of frictional heat at the sliding surface developed in Chapter 3.

6.2 DYNAMICS OF VAIONT SLIDING GEOMETRY

The analysis of the infinite slide presented in Chapter 4 is useful to understand the thermo-hydraulic process that takes place in a shear band and its effect of the overall slide motion. However, the geometry of the Vaiont slide introduces significant changes which will be presented here. The slide is now divided in two wedges (1 and 2), following the analysis presented in Chapter 5.

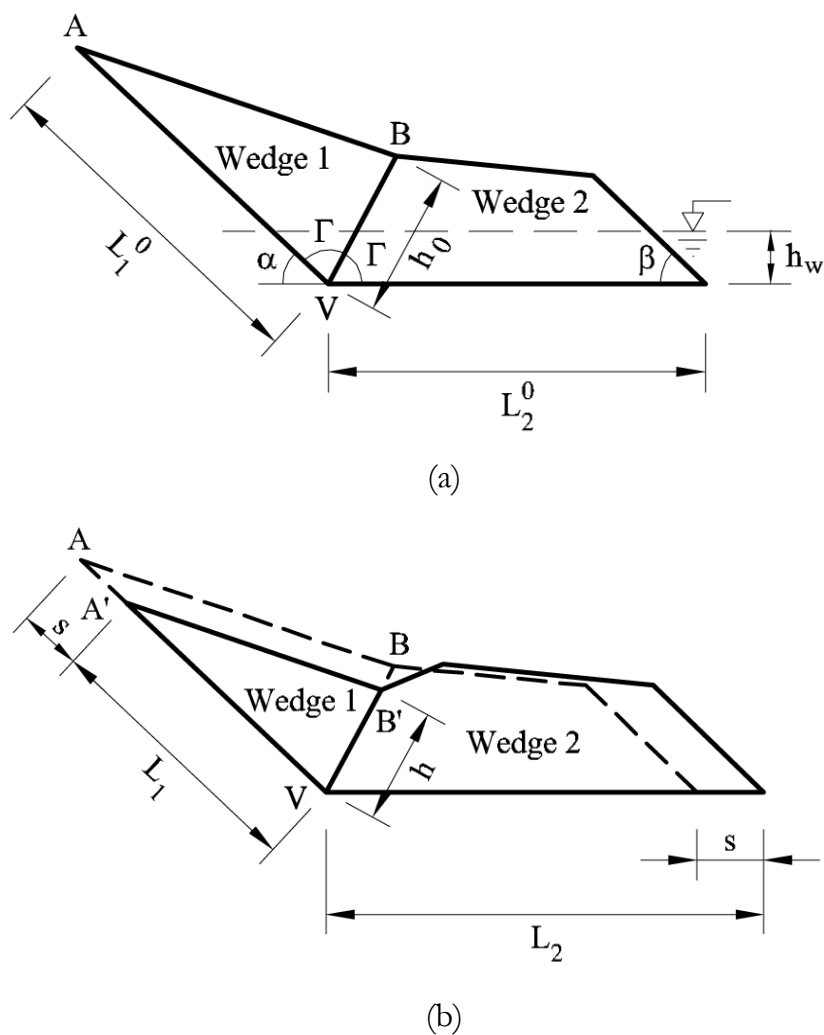


Figure 6.1 Cross-section 5 of Vaiont: (a) Initial geometry (b) Geometry after a displacement s .

The analysis follows the calculation procedure developed in Chapter 3: mass and energy balance have to be written for the shear bands limiting the two wedges and the overall dynamic equilibrium of the two wedges has to be satisfied.

Consider in Figure 6.1 the geometry of Vaiont (also used in Chapter 5) The lower wedge (Wedge 2), resting on a horizontal plane, supports (passively) the unstable upper wedge (Wedge 1) which slides on an inclined plane.

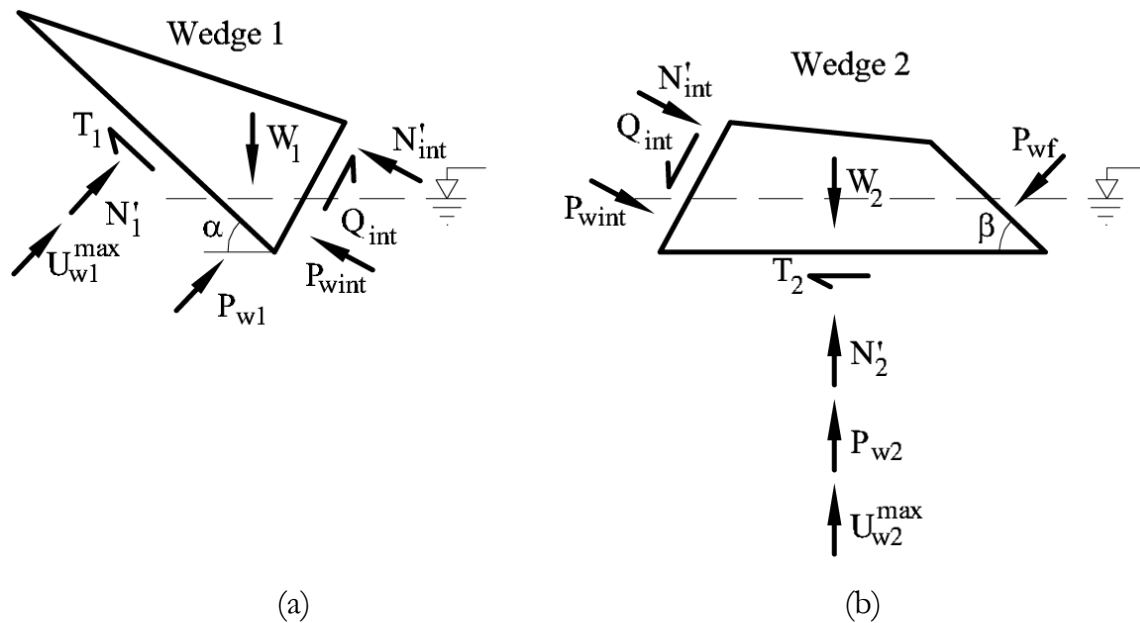


Figure 6.2 Geometry and forces on wedges: (a) Wedge 1; (b) Wedge 2.

6.2.1 Balance equations

Mass and energy balance of the lower shear band and equilibrium conditions for the entire moving mass will be written separately for each wedge. Forcing the slide to move as a single unit, the governing equations of the movement of the landslide will be obtained.

The effective interaction forces across the common plane (AB'; see Figs. 6.1 and 6.2) between the two wedges have two components, N' and Q_{int} , normal and tangential to the plane. Forces due to hydrostatic pore water pressures P_{w1} , P_{w2} , P_{wint} and P_{wf} will be controlled by the reservoir water level which will be assumed to be constant during the landslide.

Since the shear resistant forces of each wedge (T_1 and T_2) are different (although a unique frictional angle is accepted, normal resultant forces on the basal planes, N'_1 and N'_2 , need not to be equal), the work input into the bounding shear bands of the two wedges will be different. Therefore, two different values for the shear band

temperature (θ_1 and θ_2) and for the excess pore water pressures (u_{w1} and u_{w2}) will be developed in the two wedges. Specific balance equations should be written for each one of the two wedges. To avoid confusions, each part of the shear band will be denoted by Shear Band 1 or 2 according to the wedge involved. The same thickness and material properties will be assumed for the two bands.

Consider first the one-dimensional balance equations already developed for a planar band and its vicinity. They will now be directly applied to Wedge 1. The z_1 -direction corresponds to the normal direction of the Shear Band 1. The generated heat (H_1) in the Shear Band 1 is expressed as

$$H_1(t) = \tau_{f1}(t) \frac{v_{\max}(t)}{2e} \text{ for } z_1 \in [-e, e] \quad (6.1)$$

The frictional strength (τ_{f1}) will be derived from equilibrium conditions as done previously for the infinite slide.

Neglecting conduction and diffusion of heat, heat balance in the Shear Band 1 reads

$$H_1(t) = \rho c_m \frac{\partial \theta_1(t)}{\partial t} \text{ for } z_1 \in [-e, e] \quad (6.2)$$

Following the procedure developed in Chapter 3, mass balances inside and outside of the Shear Band 1 are, (see Eqs. 3.29 and 3.30)

$$\begin{aligned} -[(1-n)\beta_s + \beta_w n] \frac{H_1(t)}{\rho c_m} + [m_v + n\alpha_w] \frac{\partial u_{w1}(z_1, t)}{\partial t} - m_v \frac{\partial \sigma_{v1}(t)}{\partial t} = \\ = \frac{k}{\gamma_w} \frac{\partial^2 u_{w1}(z_1, t)}{\partial z_1^2} \text{ for } z_1 \in [-e, e] \end{aligned} \quad (6.3a)$$

$$\begin{aligned} [m_{vr} + n_r \alpha_w] \frac{\partial u_{w1}(z_1, t)}{\partial t} - m_v \frac{\partial \sigma_{v1}(t)}{\partial t} = \\ = \frac{k_r}{\gamma_w} \frac{\partial^2 u_{w1}(z_1, t)}{\partial z_1^2} \text{ for } z_1 \in (-\infty, -e] \cup [e, \infty) \end{aligned} \quad (6.3b)$$

No deformation associated with temperature changes are considered for the over-consolidated clayey layer where the slide surface were located ($\beta_{pm} = 0$). In fact no data about the thermal drained behaviour of this material is available. However, in view of the hard nature of this Cretacic layer, heat effects on the soil skeleton are expected to be small.

Regarding Wedge 2, the generated heat can be expressed as

$$H_2(t) = \tau_{f2}(t) \frac{v_{\max}(t)}{2e} \text{ for } z_2 \in [-e, e] \quad (6.4)$$

valid in the normal direction (z_2) to the Shear Band 2. The heat balance will be given by

$$H_2(t) = \rho c_m \frac{\partial \theta_2(t)}{\partial t} \text{ for } z_2 \in [-e, e] \quad (6.5)$$

Likewise, mass balance inside and outside of the Shear Band 2 is written as

$$\begin{aligned} -[(1-n)\beta_s + \beta_w n] \frac{H_2(t)}{\rho c_m} + [m_v + n\alpha_w] \frac{\partial u_{w2}(z_2, t)}{\partial t} - m_v \frac{\partial \sigma_{v2}(t)}{\partial t} = \\ = \frac{k}{\gamma_w} \frac{\partial^2 u_{w2}(z_2, t)}{\partial z_2^2} \text{ for } z \in [-e, e] \end{aligned} \quad (6.6a)$$

$$\begin{aligned} [m_{vr} + n_r \alpha_w] \frac{\partial u_{w2}(z_2, t)}{\partial t} - m_v \frac{\partial \sigma_{v2}(t)}{\partial t} = \\ = \frac{k_r}{\gamma_w} \frac{\partial^2 u_{w2}(z_2, t)}{\partial z_2^2} \text{ for } z_2 \in (-\infty, -e] \cup [e, \infty) \end{aligned} \quad (6.6b)$$

These expressions complete the balance equations for the two shear bands.

6.2.2 Dynamic equilibrium of the two wedges

Dynamic equilibrium equations were derived in Chapter 5. They will be written for each wedge. For directions parallel and normal to the basal sliding plane the equations for Wedge 1 are (see Fig. 6.2):

$$W_1(t) \sin(\alpha) - T_1(t) - N'_{\text{int}}(t) \cos\left(\frac{\alpha}{2}\right) - Q_{\text{int}}(t) \sin\left(\frac{\alpha}{2}\right) - P_{\text{wint}} \cos\left(\frac{\alpha}{2}\right) = \frac{d(M_1(t) v_{\text{max}}(t))}{dt} \quad (6.7a)$$

$$\begin{aligned} W_1(t) \cos(\alpha) - N'_1(t) + N'_{\text{int}}(t) \sin\left(\frac{\alpha}{2}\right) - Q_{\text{int}}(t) \cos\left(\frac{\alpha}{2}\right) + \\ P_{\text{wint}} \sin\left(\frac{\alpha}{2}\right) - P_{w1} - u_{w1}^{\text{max}}(t) L_1(t) = 0 \end{aligned} \quad (6.7b)$$

The right-hand term of Equation (6.7a) can be developed as:

$$\frac{d(M_1(t) v_{\text{max}}(t))}{dt} = M_1(t) \frac{dv_{\text{max}}(t)}{dt} + v_{\text{max}}(t) \frac{dM_1(t)}{dt} \quad (6.8)$$

and the time variation of mass of the wedge can be expressed as a function of the time variation of the displacement (ds/dt), which is equal to the velocity (v):

$$\frac{dM_1}{dt} = \delta_r \frac{V_{\text{Wedge 1}}}{dt} = -\delta_r \left(\frac{L_0}{\cos \alpha} - s \right) \frac{H_1}{L_0} \cos \alpha \frac{ds}{dt} \quad (6.9)$$

The shear resistance force on the base of the Wedge 1 (T_1) is expressed, following Mohr–Coulomb strength criterion, as:

$$T_1(t) = N'_1(t) \tan \phi'_b \quad (6.10)$$

The mobilized shear force on the common plane between wedges is given by:

$$Q_{\text{int}}(t) = c'_r h(t) + N'_{\text{int}}(t) \tan \phi'_r \quad (6.11)$$

where ϕ'_b is the effective residual friction angle of the sliding surface, c'_r is the effective cohesion of the rock, and ϕ'_r the effective friction angle of the rock. The values of these strength parameters are indicated in Table 1. These values have been justified in Chapter 5.

Table 6.1 Strength parameters of the sliding rock mass.

Parameter	Symbol	Value	Unit
Cohesion	c'_r	762.24	MPa
Friction angle	ϕ'_r	38	°

The water pressure force due to the presence of a water table of height h_w acting against Wedge 1 is:

$$P_{w1} = \frac{h_w^2 \gamma_w}{2 \sin \alpha} \quad (6.12)$$

The water pressure force acting against the right boundary of Wedge 1 (Fig. 6.2b) is calculated as:

$$P_{w\text{int}} = \frac{h_w^2 \gamma_w}{2 \cos \alpha} \quad (6.13)$$

and the value of P_{w2} is given by:

$$P_{w2}(t) = L_2(t) h_w \gamma_w \quad (6.14)$$

Dynamic equilibrium expressions for Wedge 2 (parallel and normal to the slide direction, respectively) are

$$N'_{\text{int}}(t) \cos\left(\frac{\alpha}{2}\right) - Q_{\text{int}}(t) \sin\left(\frac{\alpha}{2}\right) - T_2(t) = \frac{d(M_2(t) v_{\text{max}}(t))}{dt} \quad (6.15a)$$

$$\begin{aligned}
W_2(t) - N'_2(t) + N'_{\text{int}}(t) \sin\left(\frac{\alpha}{2}\right) + Q_{\text{int}}(t) \cos\left(\frac{\alpha}{2}\right) + \\
P_{\text{wint}} \sin\left(\frac{\alpha}{2}\right) + P_{\text{w}f} \cos\beta - P_{w_2}(t) - u_{w_2}^{\text{max}}(t) L_2(t) = 0
\end{aligned} \tag{6.15b}$$

The shear resistance on the base of Wedge 2 (T_2) is given by

$$T_2(t) = N'_2(t) \tan \phi'_b \tag{6.16}$$

Note that these equations depend on the displacement, s , travelled by the wedges.

If Equations (6.7) to (6.16) are properly combined, a single motion equation for the total slide mass is obtained as follows:

$$\begin{aligned}
t_{W_1} W_1(t) + t_{W_2} W_2(t) + t_{P_{\text{wint}}} P_{\text{wint}} + t_{P_{\text{w}f}} P_{\text{w}f} + t_{P_{w_1}} P_{w_1} + \\
t_{P_{w_2}} P_{w_2}(t) + t_{u_{w_1}} u_{w_1}^{\text{max}}(t) L_1(t) + t_{u_{w_2}} u_{w_2}^{\text{max}}(t) L_2(t) + \\
t_{c_r} c_r h(t) + t_{dM_1, dt} \frac{dM_1}{dt} v_{\text{max}}(t) + t_{dM_2, dt} \frac{dM_2}{dt} v_{\text{max}}(t) = \\
= (t_{M_1} M_1(t) + t_{M_2} M_2(t)) \frac{dv_{\text{max}}(t)}{dt}
\end{aligned} \tag{6.17}$$

where the t_i coefficients depend on the section geometry and on the cohesive and frictional parameters of the materials involved as indicated in the Appendix 6.2.

The shear strength acting on the basal sliding surface of the two wedges is found as the ratio of the total resistance forces T_1 or T_2 and the current base lengths L_1 or L_2 . They are given by:

$$\begin{aligned}
T_1(t) = \left[r_{W_1} W_1(t) + r_{W_2} W_2(t) + r_{P_{\text{wint}}} P_{\text{wint}} + r_{P_{\text{w}f}} P_{\text{w}f} + r_{P_{w_1}} P_{w_1} + \right. \\
r_{P_{w_2}} P_{w_2}(t) + r_{u_{w_1}} u_{w_1}^{\text{max}}(t) L_1(t) + r_{u_{w_2}} u_{w_2}^{\text{max}}(t) L_2(t) + r_{c_r} c_r h(t) + \\
\left. r_{dM_1, dt} \frac{dM_1}{dt} v_{\text{max}}(t) + r_{dM_2, dt} \frac{dM_2}{dt} v_{\text{max}}(t) \right] / \left[r_{M_1} M_1(t) + r_{M_2} M_2(t) \right]
\end{aligned} \tag{6.18a}$$

$$\begin{aligned}
T_2(t) = \left[s_{W_1} W_1(t) + s_{W_2} W_2(t) + s_{P_{\text{wint}}} P_{\text{wint}} + s_{P_{\text{w}f}} P_{\text{w}f} + s_{P_{w_1}} P_{w_1} + \right. \\
s_{P_{w_2}} P_{w_2}(t) + s_{u_{w_1}} u_{w_1}^{\text{max}}(t) L_1(t) + s_{u_{w_2}} u_{w_2}^{\text{max}}(t) L_2(t) + s_{c_r} c_r h(t) + \\
\left. s_{dM_1, dt} \frac{dM_1}{dt} v_{\text{max}}(t) + s_{dM_2, dt} \frac{dM_2}{dt} v_{\text{max}}(t) \right] / \left[s_{M_1} M_1(t) + s_{M_2} M_2(t) \right]
\end{aligned} \tag{6.18b}$$

where coefficients “ r ” and “ s ” are function of geometry and of wedge masses. They are collected in Appendix 6.2.

Summarizing the preceding results, the system of equations to be solved includes the balance equations for the two shear bands (2+2 equations) and the equation for the dynamic equilibrium of the entire landslide (one equation):

$$\begin{aligned}
 -[(1-n)\beta_s + \beta_w n] \frac{H_1(t)}{\rho c_m} + [m_v + n\alpha_w] \frac{\partial u_{w1}(z_1, t)}{\partial t} - m_v \frac{\partial \sigma_{n1}(t)}{\partial t} = \\
 = \frac{k}{\gamma_w} \frac{\partial^2 u_{w1}(z_1, t)}{\partial z_1^2} \quad \text{for } z_1 \in [-e, e]
 \end{aligned} \tag{6.19a}$$

$$[m_v^r + n_r \alpha_w] \frac{\partial u_{w1}(z_1, t)}{\partial t} - m_v^r \frac{\partial \sigma_{n1}(t)}{\partial t} = \frac{k_r}{\gamma_w} \frac{\partial^2 u_{w1}(z_1, t)}{\partial z_1^2} \quad \text{for } z_1 \in (-\infty, -e] \cup [e, \infty) \tag{6.19b}$$

$$\begin{aligned}
 -[(1-n)\beta_s + \beta_w n] \frac{H_2(t)}{\rho c_m} + [m_v + n\alpha_w] \frac{\partial u_{w2}(z_2, t)}{\partial t} - m_v \frac{\partial \sigma_{n2}(t)}{\partial t} = \\
 = \frac{k}{\gamma_w} \frac{\partial^2 u_{w2}(z_2, t)}{\partial z_2^2} \quad \text{for } z_2 \in [-e, e]
 \end{aligned} \tag{6.19c}$$

$$\begin{aligned}
 [m_v^r + n_r \alpha_w] \frac{\partial u_{w2}(z_2, t)}{\partial t} - m_v^r \frac{\partial \sigma_{n2}(t)}{\partial t} = \\
 = \frac{k_r}{\gamma_w} \frac{\partial^2 u_{w2}(z_2, t)}{\partial z_2^2} \quad \text{for } z_2 \in (-\infty, -e] \cup [e, \infty)
 \end{aligned} \tag{6.19d}$$

$$\begin{aligned}
 t_{w_1} W_1(t) + t_{w_2} W_2(t) + t_{p_{wint}} P_{wint} + t_{p_{wf}} P_{wf} + t_{p_{w1}} P_{w1} + t_{p_{w2}} P_{w2}(t) + \\
 t_{u_{w1}} u_{w1}^{\max}(t) L_1(t) + t_{u_{w2}} u_{w2}^{\max}(t) L_2(t) + t_{c_r} c_r h(t) + \\
 t_{dM_1, dt} \frac{dM_1}{dt} v_{\max}(t) + t_{dM_2, dt} \frac{dM_2}{dt} v_{\max}(t) = (t_{M_1} M_1(t) + t_{M_2} M_2(t)) \frac{dv_{\max}(t)}{dt}
 \end{aligned} \tag{6.19e}$$

where the heat generation rates H_1 and H_2 are given by Equations (6.1) and (6.4) and shear stresses $\tau_{1f} = T_1 / L_1$ and $\tau_{2f} = T_2 / L_2$, by Equations (6.18).

To solve these equations it is also necessary to define the appropriate initial and boundary conditions. A natural initial condition for the dynamic problem is a situation in which static equilibrium has been slightly exceeded. It would imply the initiation of motion. In such a situation, the initial excess pore pressure and slide velocity would be zero and no heat would be generated. Therefore,

$$u_{w1}(z, t_0) = u_{w2}(z, t_0) = 0 \tag{6.20a}$$

$$v(z, t_0) = 0 \tag{6.20b}$$

$$\theta_1(t_0) = \theta_2(t_0) = \theta_0 \tag{6.20c}$$

where θ_0 is the reference initial temperature at the beginning of the slide motion.

It was mentioned before that frictional heat is generated at a constant rate within the shear band, between $z = -e$ and $z = e$. No heat is generated, at any time, outside of the shear band. Therefore, the heat generated excess pore pressure is constant in the shear band and zero in the remaining of the domain. However, the unbalance of water pressures between points inside and outside of the shear band induces its dissipation. It

will be also accepted that the soil outside the two boundaries of the shear band is described by a common set of material properties. Since the gradient of hydrostatic pressure may be neglected in the band, given its small thickness, it follows that the axis $z = 0$, in the middle of shear band (Fig. 3.19), is a symmetry axis.

Therefore, the solution of the problem will be sought for $z \geq 0$ and symmetry conditions will be forced at $z = 0$. This condition implies a zero flow through $z = 0$.

$$\mathbf{q}_1|_{z=0} = -\frac{k}{\gamma_w} \frac{\partial u_{w1}}{\partial z_1} = 0 \Rightarrow \left. \frac{\partial u_{w1}}{\partial z} \right|_{z_1=0} = 0 \quad (6.21a)$$

$$\mathbf{q}_2|_{z=0} = -\frac{k}{\gamma_w} \frac{\partial u_{w2}}{\partial z_2} = 0 \Rightarrow \left. \frac{\partial u_{w2}}{\partial z} \right|_{z_2=0} = 0 \quad (6.21b)$$

At the other boundary, $z = e$, continuity of excess pore pressure and flow rate has to be satisfied on both sides of the shear band-rock interface:

$$u_{w1}|_{z_1=e^-} = u_{w1}|_{z_1=e^+} \quad (6.22a)$$

$$u_{w2}|_{z_2=e^-} = u_{w2}|_{z_2=e^+} \quad (6.22b)$$

$$\mathbf{q}_1|_{z_1=e^-} = \mathbf{q}_1|_{z_1=e^+} \Rightarrow k \left. \frac{\partial u_{w1}}{\partial z_1} \right|_{z=e^-} = k_r \left. \frac{\partial u_{w1}}{\partial z_1} \right|_{z_1=e^+} \quad (6.22c)$$

$$\mathbf{q}_2|_{z_2=e^-} = \mathbf{q}_2|_{z_2=e^+} \Rightarrow k \left. \frac{\partial u_{w2}}{\partial z_2} \right|_{z_2=e^-} = k_r \left. \frac{\partial u_{w2}}{\partial z_2} \right|_{z_2=e^+} \quad (6.22d)$$

Changes in water pressure outside the band will extend to relatively small distances because the volume of water expelled by the band is very small. Small changes in porosity within a limited distance outside the band will be able to absorb the transient flow of water. Therefore, no effect on the calculated pore pressures outside the band will be noticed if a zero excess pore water pressure is specified at an infinite distance:

$$u_{w1}|_{z_1=\infty} = 0. \quad (6.23a)$$

$$u_{w2}|_{z_2=\infty} = 0. \quad (6.23b)$$

The problem, summarized in Equations (6.19) to (6.23), was solved by means of a finite difference approximation following the methodology shown in Appendix 4.1 for the case of planar landslide. Numerical procedure has been programmed in a Fortran code included in Appendix 6.1.

6.3 COMPUTED RESULTS

The system of Equations (6.19) was solved and integrated by finite differences. Once in a situation of strict equilibrium the slide was made unstable by rising 10 cm the water level in the reservoir. Figures 6.3 and 6.4 presents some results. Calculation ended when the slide reached a displacement of 400 m which is approximately the

length travelled by Vaiont landslide. The physical explanation of phenomena taking place in the shear band and the response of the slide can be summarized as follows. As soon as a wedge is unstable the dynamic equilibrium allows the calculation of some sliding velocity. This velocity and the current shear stress at the shear band provides some heat input which is introduced into the combined thermo-hydro-mechanical balance equation of the shear band and its vicinity. The set of partial differential equations is solved and a new pore pressure in the shear band is calculated. In the calculations made, the pore pressure on the band axis (which is a maximum) is used to modify again the equilibrium conditions and to calculate a new sliding velocity. Velocity and mobilized strength in the band provide a new work input (heat) and the calculation resumes.

Results for a “base case” are presented first. The constitutive parameters used in this case are given in Table 6.2. This set of parameters approximates the case of Vaiont. Note that most of the parameters are physical constants.

No precise laboratory information on the permeability of the clay sliding surface seems to be available. Hendron and Patton (1985) use the value $k = 1.6 \cdot 10^{-10}$ m/s in their analysis. Vardoulakis (2002) uses $k = 1.1 \cdot 10^{-11}$ m/s. The high plasticity values consistently measured and the presence of montmorillonite probably favors a low clay permeability. A value $k = 1.0 \cdot 10^{-11}$ m/s was selected here as a base case. Shear band permeability is one of the key parameters of the model. It is subjected to high uncertainty. A sensitivity analysis, discussed later, was performed to analyze the effect of changing clay permeability. An estimated oedometric coefficient of compressibility equal to $5 \cdot 10^{-10}$ 1/Pa has been used. Band thickness, an important parameter, was unknown. However, this point will be discussed at length later.

Calculated isochrones of excess pore water pressure in the shear band below Wedges 1 and 2 are given in Figure 6.3 for the first 10 seconds of motion, when the slide velocity was 4 m/s. The average excess pore water pressure reached, at $t = 10$ s, maximum values of 1.6 MPa and 4.8 MPa under Wedges 1 and 2 respectively. Note that the unloading associated with the loss of weight of Wedge 1 results in a small pore pressure reduction outside the shear band. This has no effect on the motion, which is controlled by the maximum pore pressures on the center of the band. At $t = 10$ s the available shear strength in the center of the shear band was already very small and the heat generated (and the associated pore pressure build-up) decreased sharply. As a result, the pore pressure dissipation towards the surrounding soil dominated the following time steps. This explanation can be followed in more detail in Figure 6.4 where global performance variables for the entire slope have been plotted against time for Wedge 1. The slide reaches a displacement of 200 m 30 s after the initiation of the motion (Fig. 6.4f). At this time the velocity is 23 m/s (close to 83 km/h). These are values consistent with field observations.

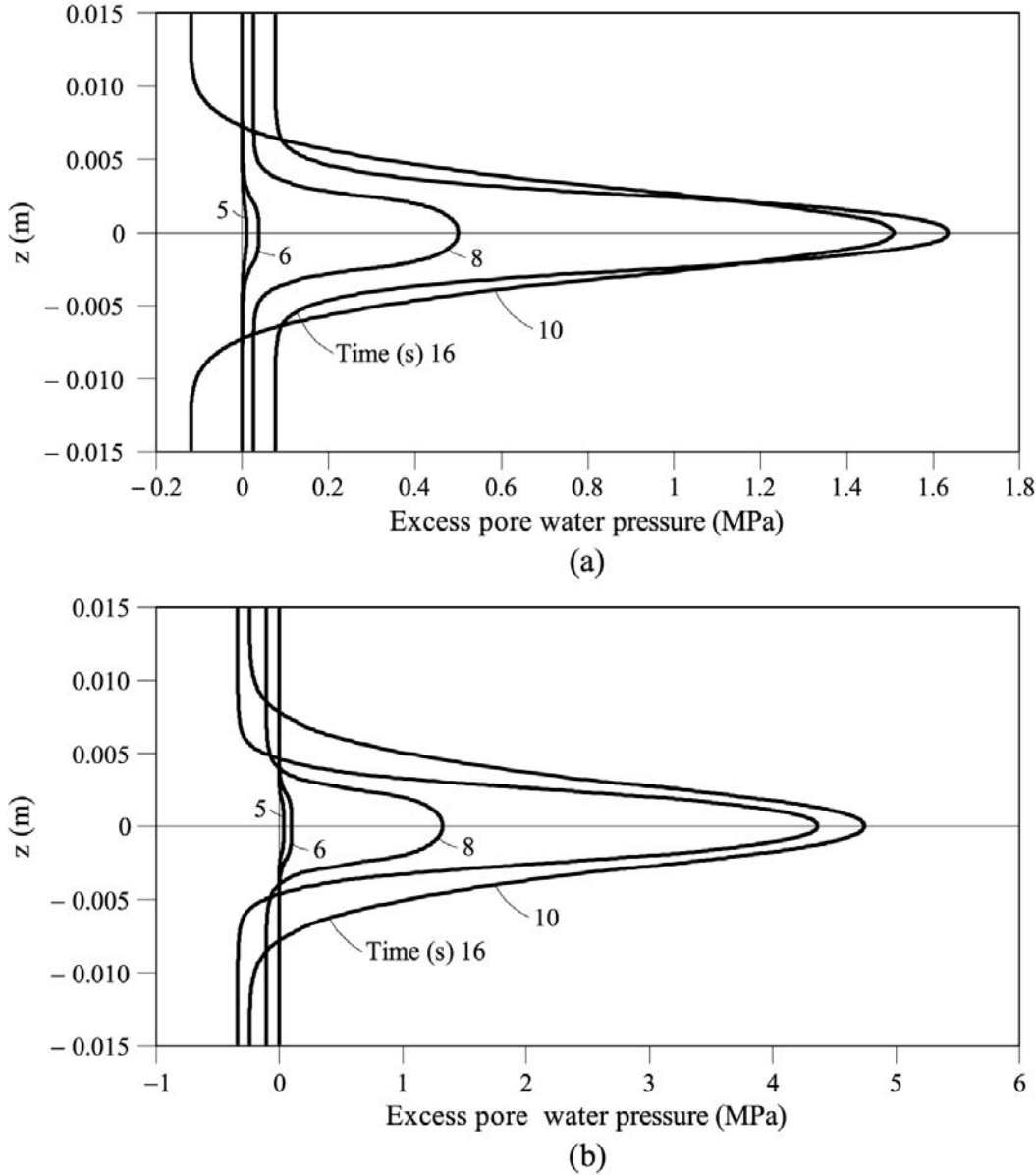


Figure 6.3 Dynamic analysis of Section 5 of Vaiont. Base case (shear band permeability, $k = 1 \cdot 10^{-11} \text{ m/s}$). Excess pore water pressure isochrones in the shear band and adjacent soil. Shear band extends from $z = 0.0025 \text{ m}$ to $z = -0.0025 \text{ m}$: (a) Under Wedge 1; (b) Under Wedge 2.

Further insight is provided by the evolution of temperature, the drop in strength and the work (or heat) input into the shear band. The maximum temperature calculated in this case is slightly higher than 100°C . The drop of shear strength is rapid from $t = 7 \text{ s}$ to $t = 12 \text{ s}$. The work performed increases fast during this period due to the rapid increase in velocity but it later decays because of the very low value of shear strength. The entire behaviour of the band and, hence, of the landslide, depends in a fully coupled manner on the mass and heat transfer phenomena in the thin shear band and its immediate vicinity.

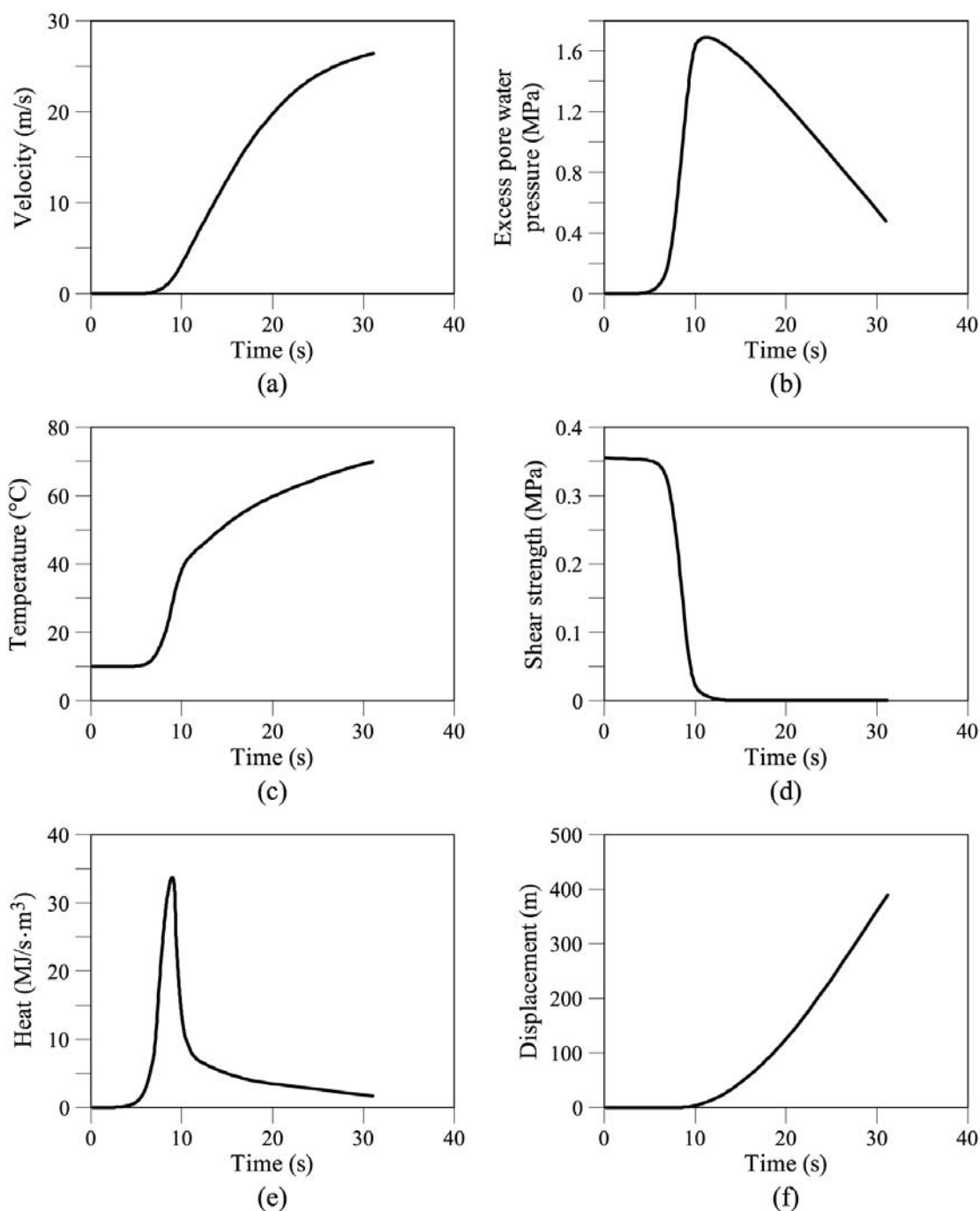


Figure 6.4 Dynamic analysis of Section 5 of Vaiont. Base case (shear band permeability, $k = 1 \cdot 10^{-11}$ m/s). Wedge 1. Evolution in time of: (a) Velocity; (b) Excess pore water pressure in the middle of the band; (c) Temperature; (d) Shear strength of shear band; (e) Heat generated in the band; (f) Slide displacement.

Changing the permeability of the shear band leads to significant changes in behaviour. It can be checked that a more impervious band leads to minor changes, when compared with the base case (Fig. 6.5 for $k = 10^{-12}$ m/s). When it is made more pervious pore water pressure dissipation becomes more significant and the effective normal stress (and the shear strength) maintains higher values. The slide also

accelerates fast and the high velocities coupled with relatively higher shear strengths lead to larger heat inputs into the band and to higher temperatures. These effects can be followed in Figure 6.5, where the case for $k = 10^{-10}$ m/s has been represented.

Table 6.2 Dynamic analysis of Vaiont Parameters for the “Base case”.

Parameter	Symbol	Value	Unit
Water			
Density	ρ_w	1000	kg/m ³
Coefficient of compressibility	α_w	$5 \cdot 10^{-10}$	1/Pa
Thermal expansion coefficient	β_w	$3.42 \cdot 10^{-4}$	1/°C
Specific heat	c_w	$4.186 \cdot 10^3$ 1.0	J/kg · °C cal/ kg · °C
Solid particles			
Density	ρ_s	2700	kg/m ³
Thermal expansion coefficient	β_s	$3 \cdot 10^{-5}$	1/°C
Specific heat	c_s	$8.372 \cdot 10^2$ 0.20	J/kg · °C cal/ kg · °C
Shear band material			
Porosity	n	0.2	-
Permeability	k	$1 \cdot 10^{-11}$	m/s
Compressibility coefficient	m_v	$1.5 \cdot 10^{-9}$	1/Pa
Friction angle (residual)	ϕ'	12	°
Sliding mass material			
Density	ρ_r	2350	kg/m ³

The discussion is necessarily more complex because shear band permeability is only one of the parameters controlling the development of pore pressures. Relevant parameters are also the band thickness and its stiffness. To some extent, permeability and band thickness provide the same information: both are related to the grain size distribution. Narrow or, alternatively, thick shear bands are expected in impervious or pervious materials, respectively. Stiffness is a different type of property and rock-like or soil-like materials may be found for the same mineralogy and grain size distribution.

An analysis of the combined effect of permeability and stiffness has been made and will be discussed immediately. But, before, we will examine a very important practical issue, namely, the effect of changing the size of the slide on its dynamic behaviour because Vaiont was an extreme case. Landslides are commonly of a much lower volume.

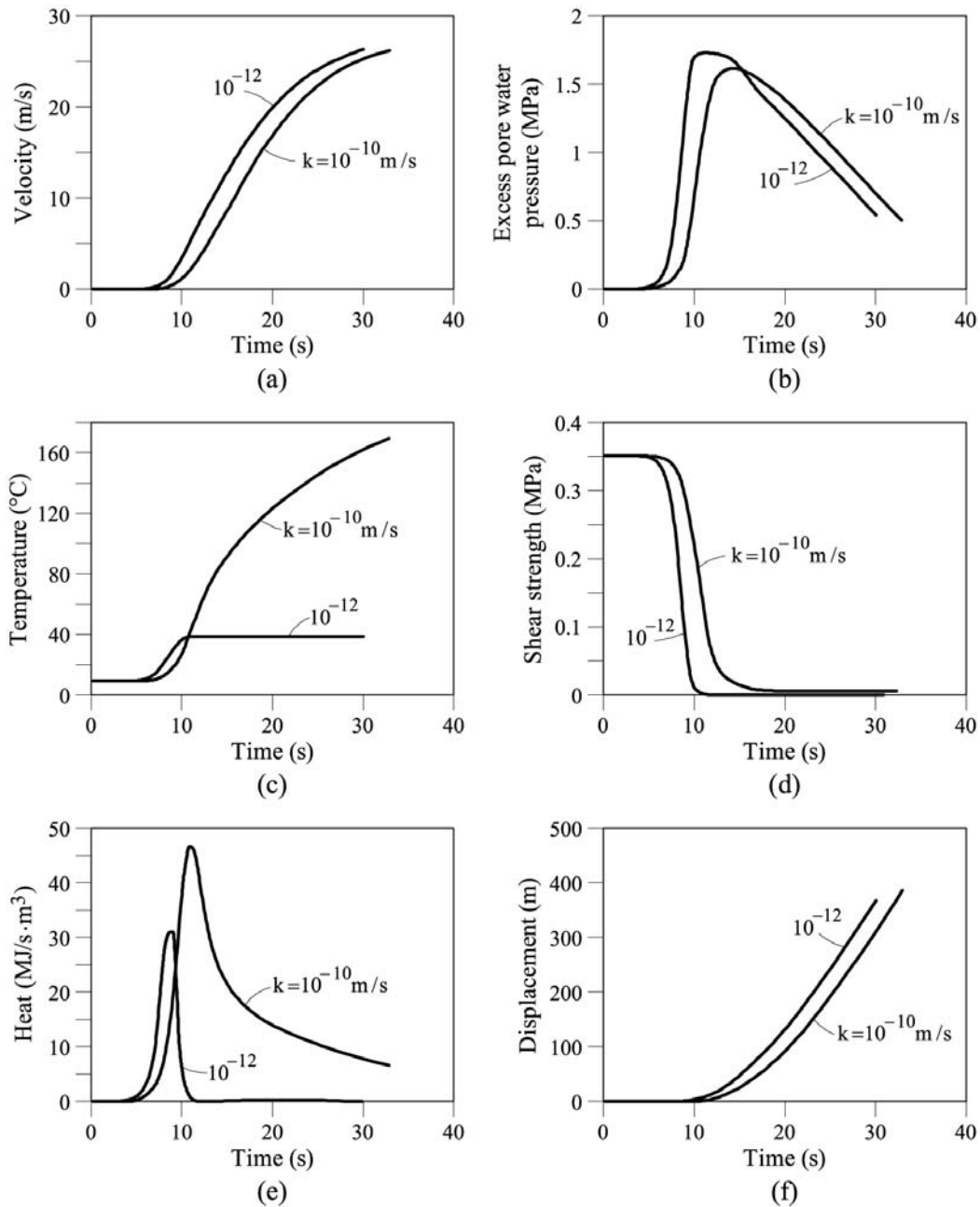


Figure 6.5 Dynamic analysis of Section 5 of Vaiont. Shear band permeability, $k = 10^{-10} \text{ m/s}$ and $k = 10^{-12} \text{ m/s}$. Wedge 1. Evolution in time of: (a) Velocity; (b) Excess pore water pressure in the middle of the band; (c) Temperature; (d) Shear strength of shear band; (e) Heat generated in the band; (f) Slide displacement.

6.4 SCALE EFFECTS

Vaiont was a very large landslide (a mobilized volume close to 300 million m³ was estimated). A slide 100 times smaller is still a very large landslide. For instance, the 5 million m³ Cortes landslide, described in Alonso *et al.* (1995) and analysed in Chapter 4, posed a significant threat to the 100 m high Cortes concrete arch dam. Its overall dimensions (length, height) were roughly 1/10 of Vaiont dimensions. Moreover, many dangerous rock and soil slides described in the literature are one order of magnitude smaller than Cortes slide. Vaiont was an extreme case, of very rare occurrence, on a world basis. Therefore, a relevant question is: Is the velocity reached by Vaiont also a common occurrence or, at least, a real possibility in smaller and much more frequent landslides?

A comprehensive answer to this question would require a lengthy analysis of the dynamic behaviour of different types of landslides. But a simple answer can be given if the main characteristics of Vaiont (a displacement type of motion involving a mass of rigid rock, sliding on a clay layer) are maintained and the geometrical dimensions are reduced without any further change in material properties or geometrical arrangement. In fact, if all the dimensions of Vaiont are reduced by a factor of 10, a landslide very similar to Cortes slide is obtained. If this slide becomes (slightly) unstable, how would it evolve if heat-induced water pressure develops at the sliding surface?

A new case has been run, modifying the scale of the Vaiont landslide. The new geometry is defined by reducing the dimensions (lengths and heights) of Wedges 1 and 2 (Fig. 6.1a) by a factor of 10. The water level was located at the same relative position and the cohesion of the central shearing plane was reduced to bring the slope to the state of strict equilibrium. The remaining properties are also given in Table 6.2. The motion was triggered by a slight increase (1 cm) of the water level in the lower wedge.

The calculated response of this slide is shown in Figure 6.6 for a base case ($k = 1 \cdot 10^{-11}$ m/s). Calculations were run in time until the slide reached a displacement of 50 m. The calculated heat input into the shear band and the maximum excess pore pressures are now one order of magnitude smaller than in the previous case. As a result, the temperature increase of the band is very moderate (4°C). The shear strength, however, is lost after a few seconds and the slide is able to reach a significant velocity. A maximum value of 8.5 m/s is obtained at the end of the calculation period. The implication is that this reduced slide may be also dangerous, if the circumstances of the analysis are fulfilled in practice.

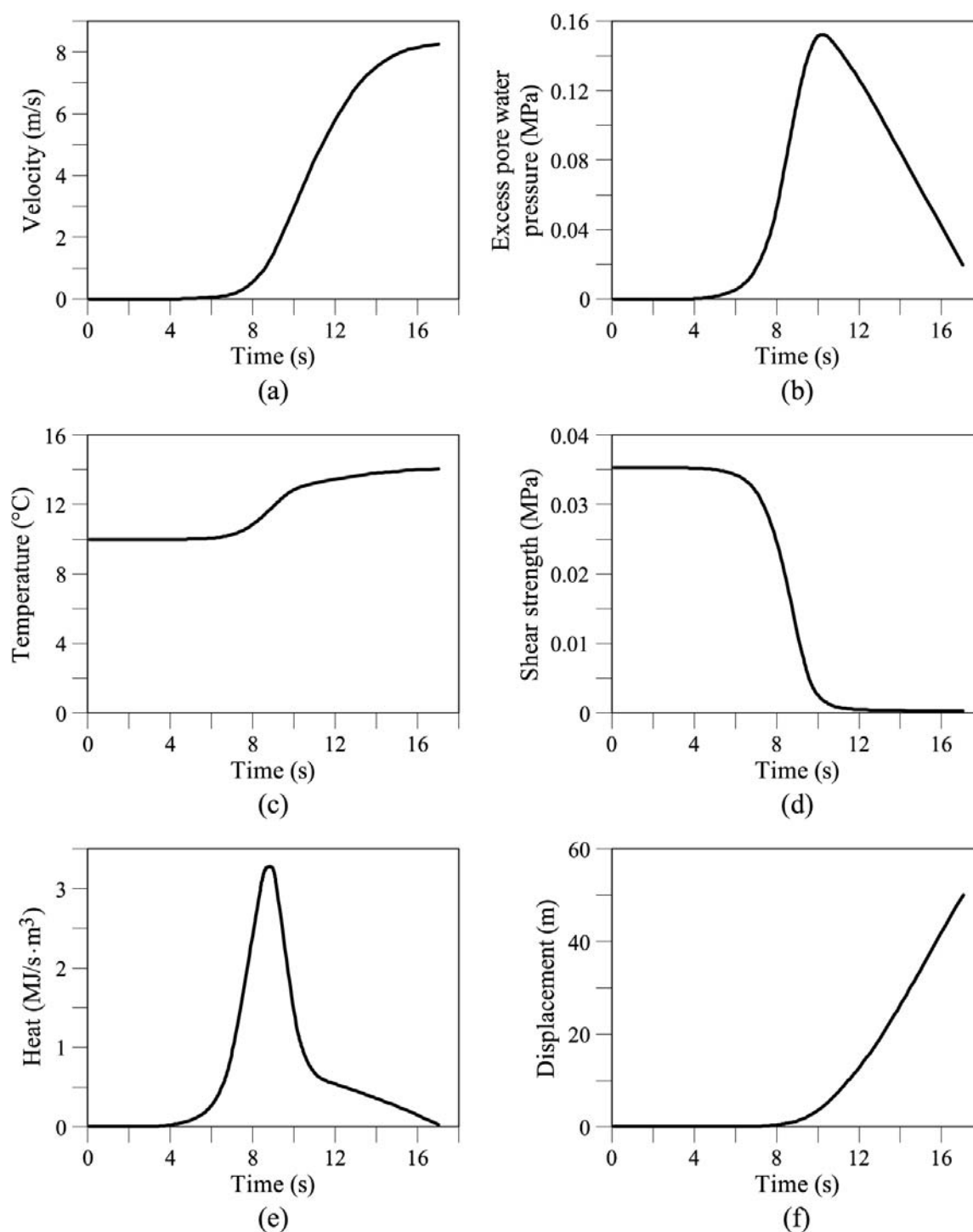


Figure 6.6 Reduced Vaiont landslide (dimensions $\times (1/10)$; volumes $\times (1/100)$). Slide response for a base case (shear band permeability, $k = 1 \cdot 10^{-11}$ m/s). Wedge 1. Evolution in time of: (a) Velocity; (b) Excess pore water pressure in the middle of the band; (c) Temperature; (d) Shear strength of shear band; (e) Heat generated in the band; (f) Slide displacement.

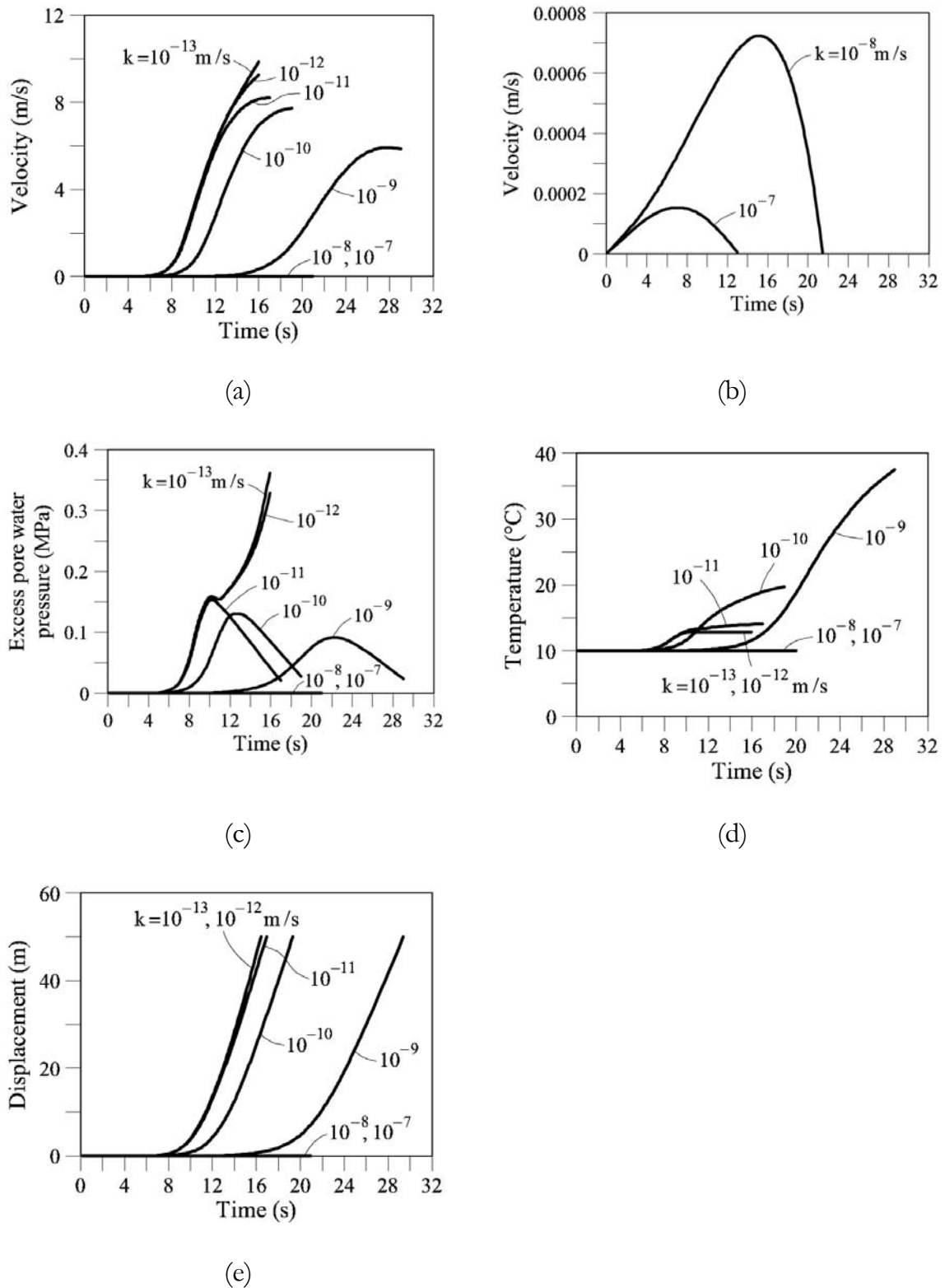


Figure 6.8. Reduced Vaiont landslide (dimensions $\times (1/10)$; volumes $\times (1/100)$). Wedge 1. (a) Effect of the permeability on the landslide velocity; (b) detail for high band permeability; (c) excess pore water pressure in the middle of the band; (d) temperature in the band; (e) slide displacement.

Band permeability seems to be a key parameter to control the response of the slide. This is shown in detail in Figure 6.7. Band values of permeability of 10^{-9} m/s and larger do not trigger any heat-induced effect. This threshold is obviously associated with the band thickness used in calculations (5 mm), but a more comprehensive analysis is given below. Since the two-wedge mechanism analyzed has a self-equilibrating mechanism, the small initial triggering effect (increasing water pressure in the shear band by 10 cm) is “absorbed” by the changing geometry and the slide comes to rest after some small displacement. If the permeability decreases below this threshold the coupled thermo-hydro-mechanical processes taking place in the band result in a progressive accumulation of pore pressures and in an accelerated slide motion. The critical permeability is the same, irrespective of the size of the slide. Temperature increase in the band, when the slide accelerates ($k < 10^{-9}$ m/s) is now quite moderate in most cases. However, for the reasons already explained, there exists some specific k values (in the vicinity of $k = 10^{-10}$ m/s) which result in a strong dissipation of energy at the band and, accordingly, in a significant temperature increase (37°C are obtained -Figure 6.7d- at the end of the calculation interval).

Summarizing, smaller slides, similar in shape to the Vaiont case, may also reach significant velocities. It appears that band permeability is a key parameter controlling slide acceleration. Below a certain threshold value (around $k = 10^{-9}$ m/s for the geometry and parameters selected for the case analyzed) the slide may reach a high velocity. It appears that this threshold k value of the sliding band is independent of the size of the slide. However, when the size of the slide decreases, the generated band excess pore pressures and temperatures reduce. In fact, it appears that for slides having the size of a “reduced Vaiont” by a factor of 10 in the scale of dimensions, maximum temperature increments in the shear band will be no more than a few degrees. It turns out that the generated temperature depends also on the thickness of the shear band. Before general conclusions are reached in this regard, it is convenient to perform a sensitivity analysis of the calculated solution when the thickness, permeability and stiffness of the band are varied between acceptable limits.

6.5 DISCUSSION

A better insight into the physics of the problem is gained if a sensitivity analysis of the main controlling factors is performed. Consider first the issue of the combined effect of band permeability and band thickness. In view of previous results, permeability values in the range 10^{-13} to 10^{-9} m/s and band thickness varying between 0.5 mm and 50 mm have been selected. Two confined stiffness moduli were selected, having in mind that in most cases the shearing surfaces in landslides are located in soft clayey rocks: $m_v = 10^{-9}$ Pa⁻¹ (a relatively stiff clayey rock) and $m_v = 10^{-8}$ Pa⁻¹ (a relatively soft clayey rock). Then, for each combination (k , $2e$, m_v) the movement of the slide with scaled geometry of Vaiont has been calculated. The calculated maximum

velocities and band temperatures, for a maximum run out of 50 m, are given in Figures 6.8 and 6.9.

Consider first the case of a stiff shearing band ($m_v = 10^{-9} \text{ Pa}^{-1}$) in Figure 6.8. The calculated velocities for varying band thickness remain in a narrow band. Velocities reach high values (8 – 9 m/s) when the permeability is low (10^{-12} to 10^{-10} m/s). For relatively large values of permeability (higher than 10^{-8} m/s) the velocity of the slide drops to zero. In these cases the initially unstable situation is soon counter-acted by the self-stabilizing mechanism of the slide (weight transfer from the upper to the lower wedge).

The transition from the “rapid regime” to the “slow” or self-stabilizing situation occurs for values of permeability in the range 10^{-9} to 10^{-8} m/s .

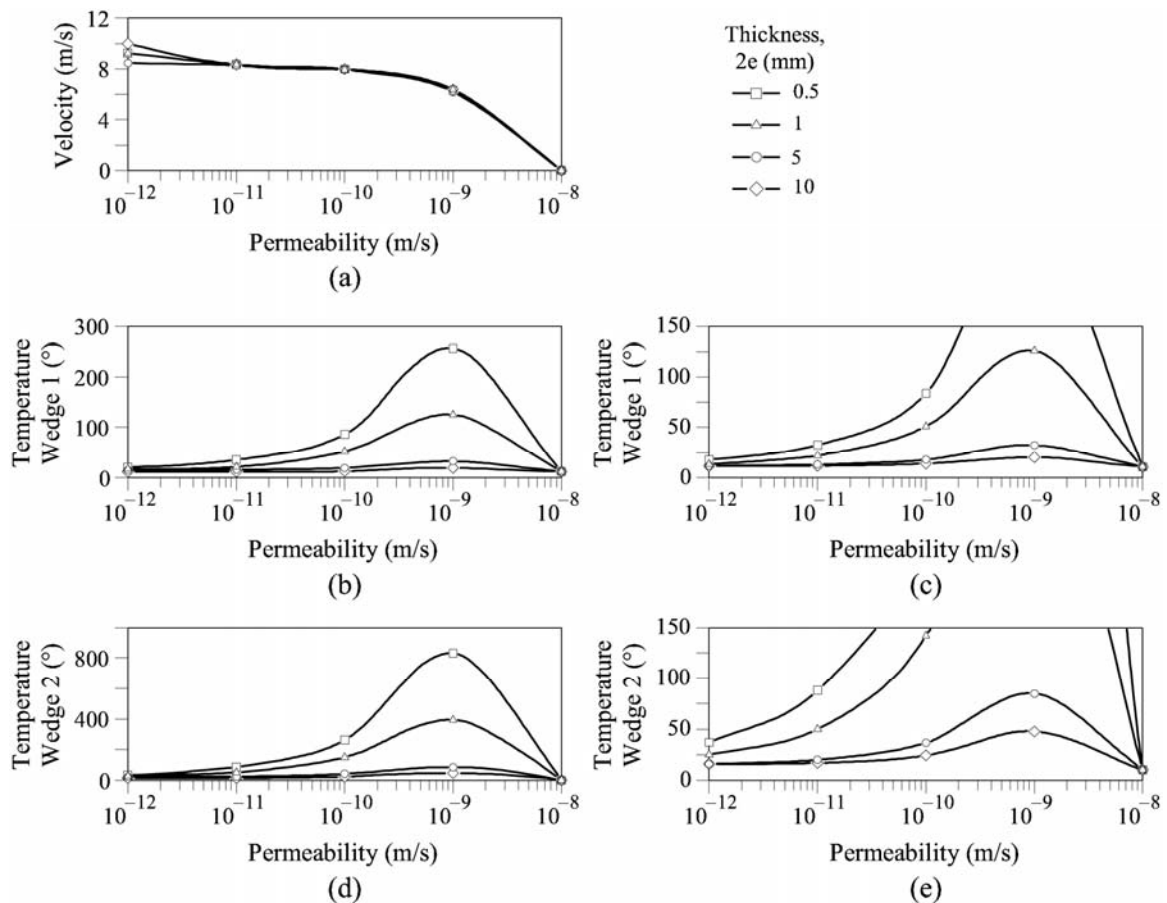


Figure 6.8 Reduced Vaiont landslide (dimensions $\times (1/10)$; volumes $\times (1/100)$). Stiff shearing band, $m_v = 10^{-9} \text{ Pa}^{-1}$. Effect of shear band permeability and thickness on (a) landslide velocity; (b) temperature for Wedge 1; (c) temperature for Wedge 1, detail; (d) temperature for Wedge 2; (e) temperature for Wedge 2, detail.

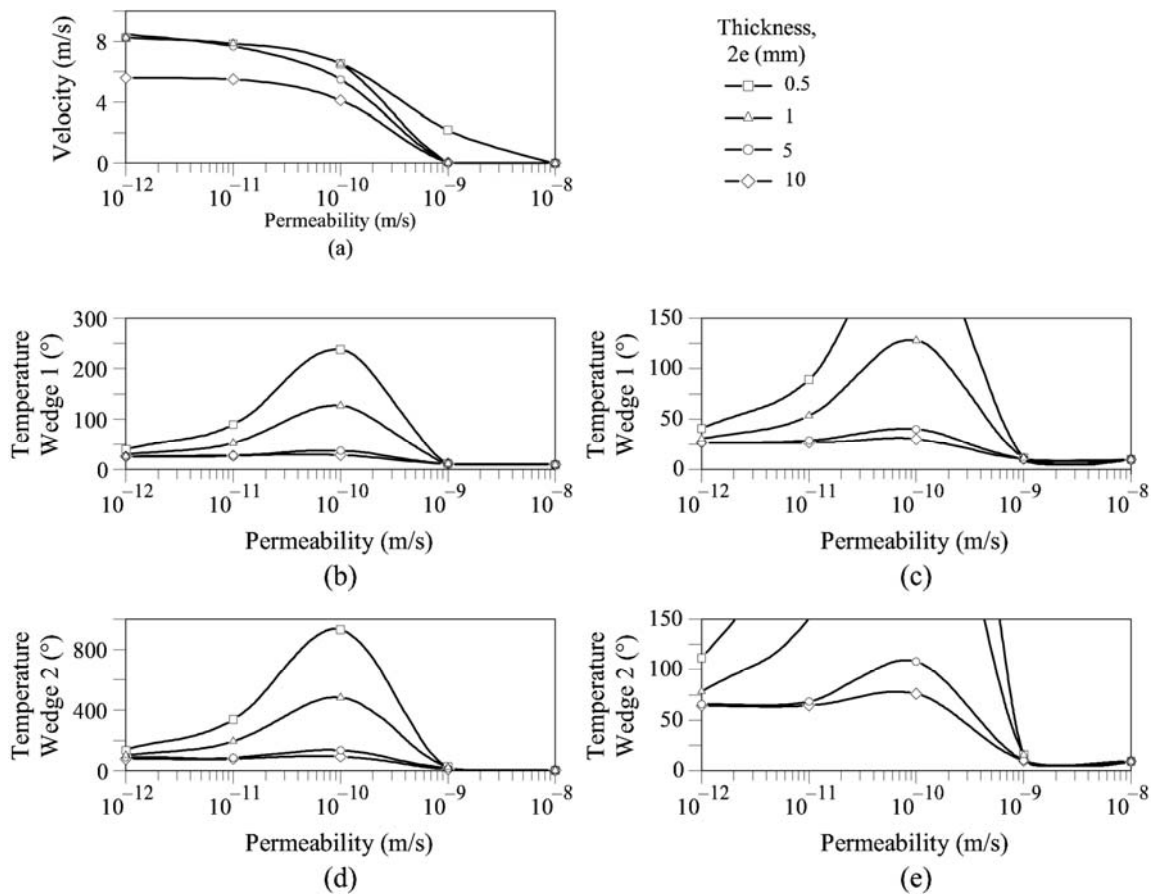


Figure 6.9 Reduced Vaiont landslide (dimensions $\times (1/10)$; volumes $\times (1/100)$). $m_v = 10^{-8} \text{ Pa}^{-1}$. Effect of shear band permeability and thickness on (a) landslide velocity; (b) temperature for Wedge 1; (c) temperature for Wedge 1, detail; (d) temperature for Wedge 2; (e) temperature for Wedge 2, detail.

Calculated temperatures for varying band permeability and band thickness are represented in Figure 6.8b,c for Wedge 1 and in Figure 6.8d,e for Wedge 2 (stiff band material in both cases). The normal effective stress in Wedge 1 against the sliding plane is significantly smaller than the value calculated for Wedge 2. Resisting shear stresses react in the same manner and the work input for Wedge 1 is smaller if compared with Wedge 2. The consequence is that temperatures in Wedge 1 remain at moderate values in the “fast” and “slow” ranges of values of permeability. Temperature increases in the intermediate “regime” leads to a significant mechanical work input into the band because the combination of non-negligible shear strength and a substantial sliding velocity.

Band thickness controls the temperature development. A maximum temperature of 259 °C for Wedge 1 is calculated for $k = 10^{-9} \text{ m/s}$ and $2e = 0.5 \text{ mm}$. Temperatures are higher in Wedge 2 for the reason given before and they reach a peak value close to 800 °C for $k = 10^{-9} \text{ m/s}$ and $2e = 0.5 \text{ mm}$. These high temperatures would require a more

precise formulation of the constitutive model of the band material and, possibly, the presence of additional physical phenomena (water vaporization) which are outside the limits of this work. But in most cases in practice the maximum temperature calculated is moderate and the analysis developed should represent reasonably well the relevant physical phenomena.

Similar qualitative results were obtained for the softer band material ($m_v = 10^{-8} \text{ Pa}^{-1}$) (Fig. 6.9). In order to explain the results, consider the balance equation for solid and water mass (Eq. 6.19), written now in the following form where the rate of pore pressure change has been isolated:

$$\frac{\partial u_w}{\partial t} = \frac{k}{\gamma_w [m_v + n\alpha_w]} \frac{\partial^2 u_w}{\partial z^2} + \frac{m_v}{[m_v + n\alpha_w]} \frac{\partial \sigma_n}{\partial t} + \frac{[(1-n)\beta_s + \beta_w n]}{[m_v + n\alpha_w]} \frac{\tau_f v_{\max}}{2e\rho c_m} \quad (6.20)$$

Use has been made also of Equations (6.1) and (6.2) which provide the relationship between temperature and rate of work input into the band. Three phenomena contribute to change pore water pressures in the band: the dissipation due to flow of water (first term), the variation of total normal external stress (second term), and the generation of pore pressures due to water and solid dilation, controlled by heat (or rate of work input) (third term). The three terms are affected by the compressibility coefficient of the band material, m_v (in the denominator). In particular, the rate of heat-induced generation of pore pressures is reduced when the compressibility of the material increases. A softer rock pore accommodates better an increase in water dilation, and leads to a lower pore pressure. The remaining terms in Equation 35 are also controlled by m_v (an increase in m_v also results in a decrease in the dissipation rate of pressures) and it is difficult to predict the final result in a particular case without actually performing the calculations. If the heat-associated term dominates, excess pore pressures, other conditions maintained, will decrease when m_v increases – softer material – and the normal effective force on the sliding surface will increase. This implies, in general terms, a higher resistance to sliding and a reduced velocity.

The plots in Figure 6.8a and 6.9a show the final velocities when the slide has displaced 50 m. It indicates that the increase in m_v leads to a systematic reduction in calculated velocities for any value of permeability. A consequence of this reduction is that the transition permeability between the fast and slow regimes now ranges between 10^{-10} and 10^{-9} m/s. Another obvious consequence is that the time to reach a given displacement should increase when m_v increases.

Consider finally the effect of m_v in the development of temperatures in the shear band (compare plots in Figs. 6.8b,c,d, and Figs. 6.9b,c,d). The plotted temperatures correspond to the end of the calculation period, when the slide in all cases has reached a displacement of 50 m. Therefore, the plot provides an accumulated quantity which is proportional (in the absence of any dissipation by conduction and advection, given the fast phenomena analyzed) to the total work input during the sliding time.

In the “fast” regime (low permeability) the pore pressure generation term for a softer soil (third term in Eq. 6.20) is smaller than the same term for a rigid material. Therefore, in order to accelerate (pore pressures should increase until effective stresses reduce to very low values), heat has to accumulate during a longer time for a softer material. The direct consequence is that the time to get the accelerated motion of the slide should increase for a softer material, a result already advanced. It turns out that the accumulated heat for the softer material (the integrated value of the slide velocity times the available shear strength) is higher than the calculated value for the stiffer material. As a result, temperatures increase in the case of softer materials. This is shown in the plots for the low range of values of permeability. When the permeability increases and enters into the “slow” regime, the comparison of the temperature calculated for the two m_r values cannot be discussed in the preceding terms because the slide stops soon after the initial instability because of the fast dissipation of excess pore pressures.

The preceding set of comments illustrates the intricate coupling among the different phenomena and the difficulty to make predictions on the basis of a simple reasoning.

6.6 CONCLUSIONS

A seemingly convincing explanation for the accelerated motion of Vaiont relies on the development of excess pore pressures generated by the temperature increase of the sliding surface. This is a consequence of the slide motion itself. A key condition to explain the phenomenon is the existence of a basal sliding plane located in a layer of low permeability high plasticity clay in residual conditions. Then, the self-feeding mechanism of pore pressure generation in the sliding surface may eventually lead to very high sliding velocities (~ 25 m/s) which are reached in a few seconds (~ 30 seconds) even if proper account is given to the self-stabilizing evolving geometry of the slide and even if progressive failure mechanisms, potentially acting on internal shearing surfaces, are not considered.

Slide geometry and strength properties of the sliding surface(s) are not enough to understand the dynamics of Vaiont. Three parameters have been found important to explain the motion: the thickness of the sliding band, its permeability and its (confined) stiffness. Permeability is the major player. This is because it includes, in an approximate manner, the information provided by the shear band thickness. In fact, shear band thickness and permeability are both related to the particle size distribution of the band material. The sensitivity analysis performed for a scaled Vaiont slide has also shown that below a certain permeability threshold (established around 10^{-8} to 10^{-10} m/s depending on the clay stiffness), the maximum pore pressure development in the shear band, which is the value controlling the shear strength, is not much affected by the band thickness, within a reasonable range of values. Above this threshold permeability

value, pore pressure dissipation is enough to de-activate the process of pore pressure build-up and, therefore, the slide does not accelerate. In other words, the threshold permeability identified marks the transition from a potentially risky slide to a safe one. Of course, this conclusion is valid for the slide geometry analyzed and it should not be extended to other sliding configuration without further analysis.

In very large landslides (the case of Vaiont), when conditions for accelerated motion exist, there are critical combinations of band permeability and band thicknesses that result in a substantial and rapid increase in shear band temperature. This is a natural outcome of the formulation and it is a consequence of the existence of small – but not negligible- shear strength in the shear band and an increasing shear strain rate as the sliding velocity increases. The permeability of the band in these cases is low enough to maintain a significant pore pressure in the band but high enough to maintain a non negligible effective normal stress. The calculated temperatures (hundreds or even thousands of °C) are enough to induce water vaporization and rock melting. These phenomena are not covered by the formulation developed, which only explains water pressure increase as a result of thermal dilation effects. The estimated sliding band parameters, in the case of Vaiont, lead to a moderate increase in temperature (< 100 °C), which is not able to vaporize the interstitial pore water of the clayey band.

When the size of the slide decreases the temperature generated in the band decreases also because the work input into the band decreases. A reduction of Vaiont dimensions by a factor of 1/10 still leads to a very large slide (a few million cubic meters), which has been analyzed. Sliding band temperatures are substantially lower in this case. For an impervious band ($k < 10^{-9}$ m/s) maximum temperature increments are moderate (a few degrees). Even in extreme cases, for critical k values of the sliding band, it is unlikely for the temperature to raise more than 100 °C. Vaporization (and certainly rock melting) is excluded in these cases. Since most slides do not reach, in practice, such a volume (a few million cubic meters), water vaporization and rock melting are extreme phenomena of rare occurrence.

The fact that temperature increase will likely remain moderate or low in most slides does not prevent, however, the development of significant velocities. The reason is that the reduced increase in pore water pressure in those cases is also matched by a reduced normal effective stress on the sliding surface. Therefore, the condition of zero effective stress may also be reached during motion. However, the smaller the slide is, the shorter the sliding path necessary to substantially change its geometry, to evolve to another type of motion, or to be affected by another geometrical restriction to its motion. These considerations, added to the reduced momentum of the slide, tend to limit the danger associated with smaller slides.

Although the two-wedge analysis described provides a reasonable explanation for the final catastrophic motion of Vaiont slide, the previous history of landslide creep-

like displacements (see Chapter 5) cannot possibly be reproduced with the model developed here. Other phenomena such as viscous strength components at the failure surface or the strength degradation of the rock mass could be invoked to approximate the measured velocities prior to failure. Additional limitations can be identified both in the model and in the available information: the geometry has been maintained two-dimensional and as simple as possible; pore water pressures prevailing at the failure surface were never measured; the effect of previous rainfall regime is essentially unknown; the actual conditions (in particular, the continuity of the high plasticity clay layer) of a significant proportion of the sliding surface remain buried by the slide and are essentially unknown, etc. Therefore, complexities and uncertainties around Vaiont are far from being resolved. However, it remains as a fascinating case and a permanent source of inspiration in the field of landslide analysis.

APPENDIX 6.1 FLOWCHART AND COMPUTER PROGRAM FOR THE DYNAMIC ANALYSIS OF THE INFINITE PLANAR AND TWO-WEDGE SLIDES

The numerical procedures described above for the dynamic analysis of the infinite slide and the two interacting wedges was programmed in Fortran 90. The complete code is included at the end of this appendix.

The program is subdivided in two main branches (Fig. A6.1) attending to the type of slide by means of two subroutines: *Infinite_planar_slide* and *Two_interacting_wedges*.

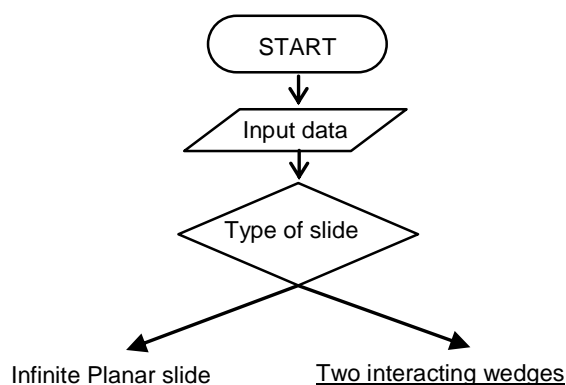


Figure A6.1 Flowchart of the main program.

The main program is structured in three parts. First, all the input parameters that can be modified by the user are defined: material parameters, reference temperature, type of the slide and its geometry, parameters for the discretization by finite differences, and control parameters. Regarding the discretization parameters, the user has to define the number of spatial steps in the shear band and in the sliding mass. As

the thickness of the shear band is previously defined, the length of spatial increment (Δz) and the position of the coordinate of the upper boundary (L) is determined by default. The time interval (Δt) is defined, by default, by limiting the value of the stability coefficient ($c_v \Delta t / \Delta z^2$) to 0.3 in order to guarantee the stability.

Second, auxiliary parameters and constants are calculated by the program. In general, this part should not be modified by the user. Finally, in the third part of the main program, a subroutine is called depending on the type of slide.

The numerical procedure starts in the subroutines. Results are calculated and stored in external files, within the same subroutines. At intervals defined by the time frequency (Dtw_time), which is specified by the user in the main program, the values of velocity, excess pore pressure in the middle of the shear band, heat, displacement, shear strength, and temperature are written in data files. Excess pore pressure profiles for $z = 0$ to $z = L$ are also stored in external files following the time frequency ($Dtw_profile$) specified. The numerical procedure goes on until the maximum displacement ($displ_max$) is reached or until the slide velocity becomes zero (the landslide stops) for the case of two interacting wedges.

The implementation of the numerical procedures in the subroutines follows the flow chart diagrams included in Figures A6.3 and A6.4.

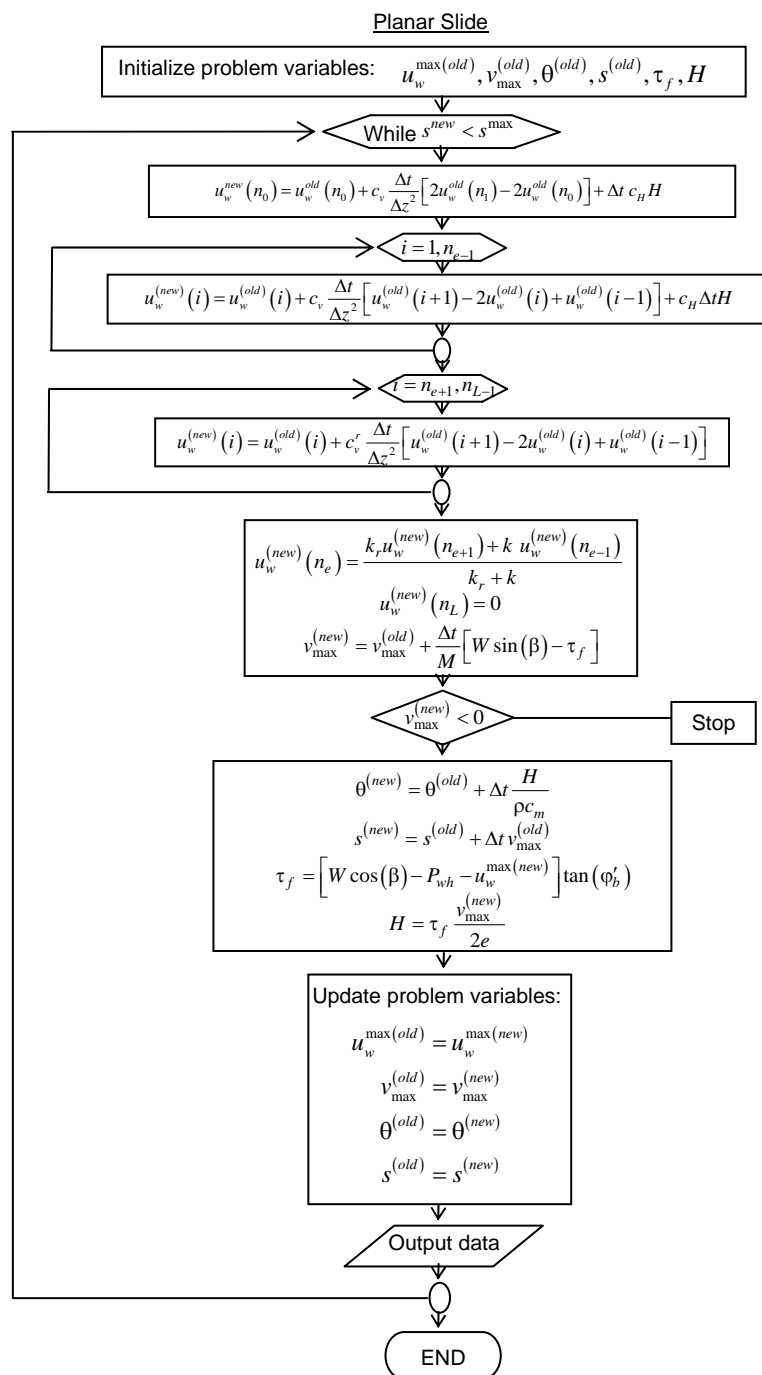


Figure A6.2 Flow chart diagram of subroutine Planar_slide.

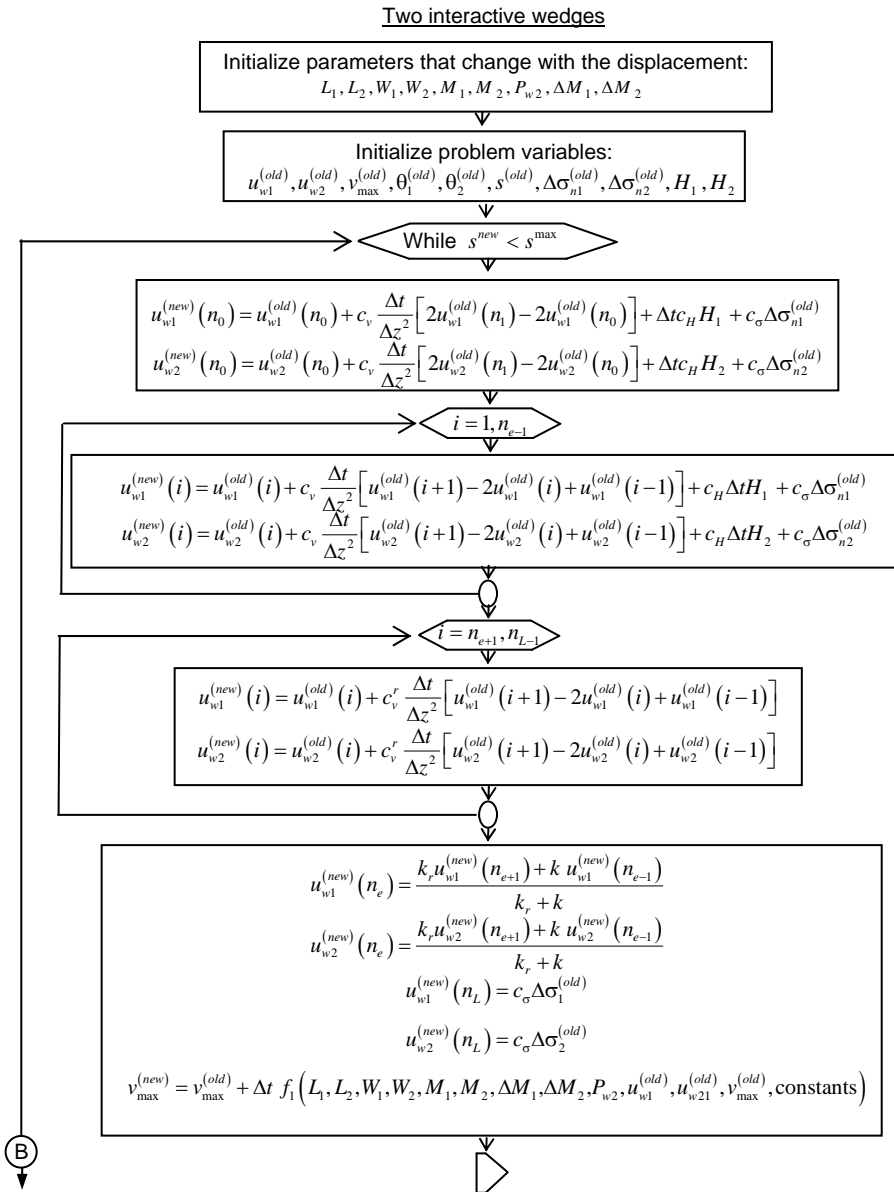


Figure A6.3 Flow chart diagram of subroutine Two_interacting_wedges.

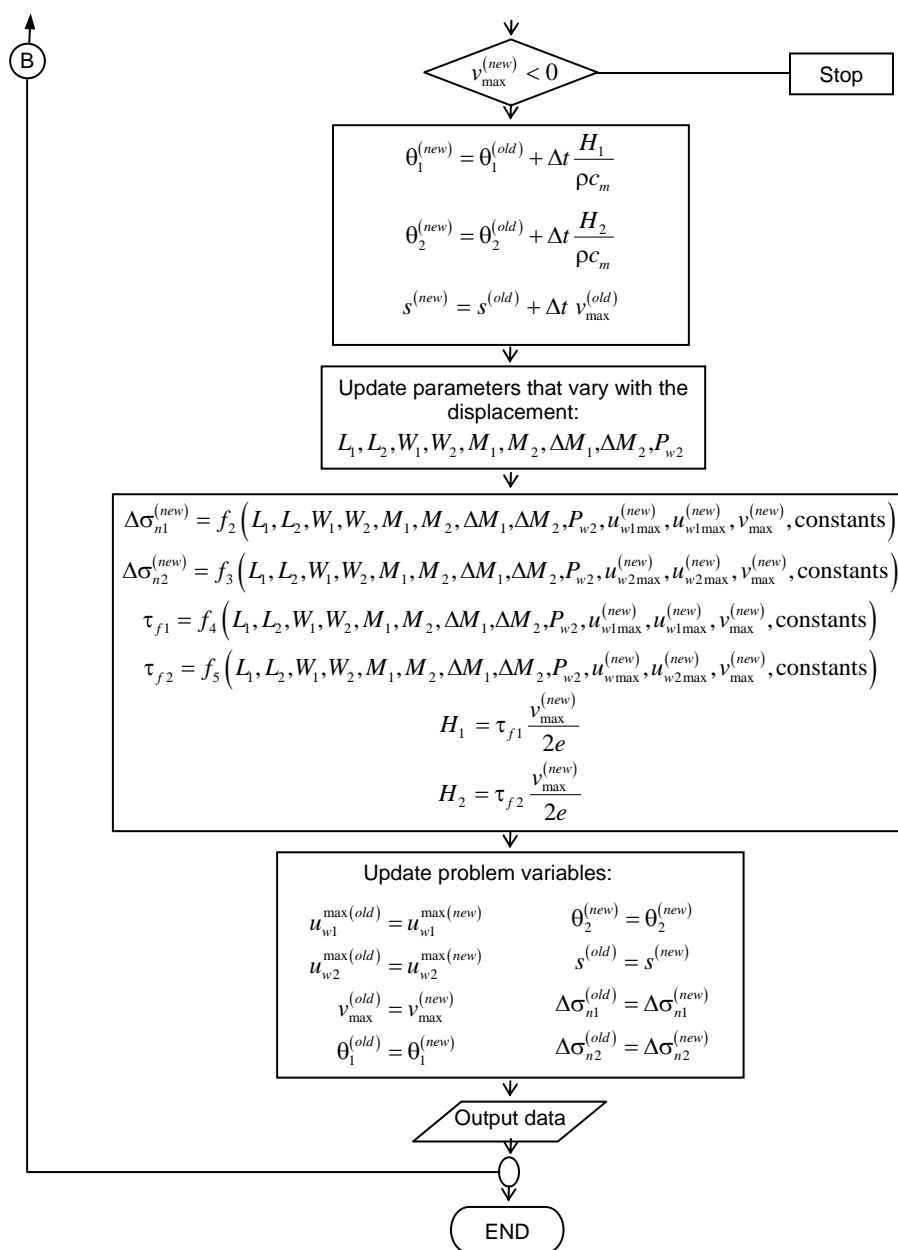


Figure A6.3 (continued) Flow chart diagram of subroutine Two_interacting_wedges.

```

!*****!
!
!                               PROGRAM                               !
!
!                               VAIONT LANDSLIDE: DYNAMIC ANALYSIS   !
!
!*****!

implicit real*8 (a-h,o-z)

!*****!
!                               PARAMETERS TO BE DEFINED BY THE USER !
!*****!
pi =3.141592654

! MATERIAL PARAMETERS
!Water parameters
delta_w = 1.e3                !kg/m3; density
gamma_w = 9800.0              !N/m3; specific weight
alpha_w = 5.e-10              !1/Pa; compressibility coefficient
beta_w = 3.4e-4               !1/°C; thermal dilation coefficient
c_w =4186.0                   !J/(kg·°C); specific heat
!Solid parameters
delta_s = 2.7e3               !kg/m3; density
beta_s = 3.0e-5              !1/°C; thermal dilation coefficient
c_s = 837.2                   !J/(kg·°C); specific heat
!Shear band parameters
zn_band = 0.2                 !porosity
zk_band = 1.e-11              !m/s; permeability
zmv_band =1.5e-9              !1/Pa;1D compressibility coefficient
fib=12.0*pi/180.              !rad; effective frictional angle in the band
!Sliding mass parameters
zn_rock = 0.2                 !porosity
delta_rock = 2350.            !kg/m3; density
gamma_rock =23500.            !N/m3: specific weight
zk_rock = 1.e-11              !m/s; permeability
zmv_rock = 1.5e-9             !1/Pa; 1D compressibility coefficient
fir = 38.*pi/180.             !rad; effective frictional angle rock-rock
coher =762.247e3              !Pa; cohesion rock-rock
cc = 0.d0                     !1/m; rock cohesion degradation rate with the
displacement (if it is equal to zero, there is no degradation

! INITIAL CONDITIONS
!Initial excess pore pressure, velocity and displacement have been !imposed equal to zero
by default
theta_ref =10.0               !°C; reference temperature

! TYPE OF SLIDE
ntype_failure = 2              !1:infinite planar slide
                                !2:two interacting wedges

! GEOMETRIC PARAMETERS AND HYDROSTATIC FORCES
e = 2.5e-3                     !m; 2e = thickness of shear band
if (ntype_failure.eq.1) then
zHeight =240.                  !m; thickness of planar landslide
zHeight_w =120.                !m; height of phreatic level
beta_slope = 9.490*pi/180.     !rad; slope angle
else if (ntype_failure.eq.2) then
zH_wedge1 = 510.0              !m; height of upper triangular Wedge 1
zH1_wedge2 = 260.0             !m; left height of lower Wedge 2
zH2_wedge2 = 260.0             !m; right height of lower Wedge 2
Base_wedge1 = 700.0            !m; horizontal length of Wedge 1
zL2_0_p1 = 240.                !m; partial base length (1) of Wedge 2
zL2_0_p2 = 320.                !m; partial base length (2) of Wedge 2
alpha = 36.07*pi/180.          !rad; angle Wedge 1
beta = atan(zH2_wedge2/zL2_0_p2) !rad; angle Wedge 2
zHeight_w = 120.1              !m; water level
endif

! CONTROL VARIABLES
displ_max = 400.0              !m; maximum displacement allowed in calculation

! DISCRETIZATION (FINITE DIFFERENCE)
nze = 500                      !num. of spatial intervals between z=0 and z=e

```

```

zL = 0.02          !m; coordinate of upper boundary
sfb = 0.3         !stability factor of the band for difference
                  !approximation

! CONTROL PARAMETERS OF OUTPUT DATA
Dtw_profile=2.    !seconds; Time between successive writings
                  !of pore pressure profiles
Dtw_time=1.      !seconds; Time between successive writings
                  !of problem variables varying in time

!*****
!                AUXILIAR PARAMETERS COMPUTED BY THE PROGRAM
!*****

!Auxiliary material parameter
gamma_s = 9.8*delta_s          !N/m3; specific weight
c_delta_band = (1.-zn_band)*delta_s*c_s+zn_band*c_w*delta_w
                  !Pa/°C;specif heat*density
cv_band = zk_band/(gamma_w*(zn_band*alpha_w + zmv_band))
                  !1/s; consolidation coef. of the band
c_delta_rock = (1.-zn_rock)*delta_s*c_s+zn_rock*c_w*delta_w
                  !Pa/°C;specific
heat*density
cv_rock = zk_rock/(gamma_w*(zmv_rock+zn_rock*alpha_w))
                  !1/s; consolidation coef. of the
                  !sliding mass

!Auxiliary geometric parameters and hydrostatic forces
if (ntype_failure.eq.1) then
  Pw = zHeight_w*gamma_w          !N; hydrostatic force on the base
  zmass=zHeight*delta_rock*cos(beta_slope) !kg/m; mass per unit of
                  !length
  weight = zHeight*gamma_rock*cos(beta_slope) !N/m;total weight
                  !of the sliding mass per unit of
length
else if (ntype_failure.eq.2) then
  zL1_0 = sqrt(zH_wedge1*zH_wedge1+Base_wedge1*Base_wedge1)
                  !m; base of wedge 1
  zL2_0 = zL2_0_p1+zL2_0_p2 !m; total base length of wedge 2
  delta = 0.5*(pi-alpha)
  shi = 0.5*alpha
  Pwint = 0.5*zHeight_w*zHeight_w*gamma_w/sin(delta)
                  !N; hydrostatic force on common shearing
                  !plane between wedges
  Pwf = 0.5*zHeight_w*zHeight_w*gamma_w/sin(beta)
                  !N; hydrostatic force on the right edge of
                  !lower wedge 2
  z1_shp10 = zH1_wedge2/cos(shi)
                  !m; length of common shearing plane between
                  !wedges
  Areal_0 = 0.5*zL1_0*z1_shp10*cos(shi)
                  !m2; initial area of wedge 1
  ddd = zH1_wedge2/tan(delta)
  Area2_0 =0.5*zH1_wedge2*ddd+
. 0.5*(zH1_wedge2+zH2_wedge2)*(zL2_0_p1-ddd)+
. 0.5*zH2_wedge2*zL2_0_p2 !m2: initial area edge 2
  Pw1_0 = 0.5*zHeight_w*zHeight_w*gamma_w/sin(alpha)
                  !N; hydrostatic force on base of wedge 1
  Pw2_0 = zHeight_w*zL2_0*gamma_w
                  !N; hydrostatic force on base of wedge 2
endif

!Constants in the balance equations for mass and heat
cv_band = zk_band/(gamma_w*(zn_band*alpha_w + zmv_band))
c_heat = -((zn_band*beta_w+(1-zn_band)*beta_s))/
. (c_delta_band*(zn_band*alpha_w + zmv_band))
c_sigma_vertical = zmv_band/(zn_band*alpha_w + zmv_band)
cv_rock = zk_rock/(gamma_w*(zn_rock*alpha_w + zmv_rock))

!Auxiliary parameter for the discretization by finite difference
Dz = e/(nze-1)          !length of spatial intervals
nz = int(zL/Dz)         !num. of spatial intervals
Dt = sfb*Dz*Dz/cv_band!seconds; time intervals

```



```

        zero = 1.e-10

! INITIATE COUNTERS
    iw_profile = 0 !Counter for writing pore pressure profiles
    iw_time = 0      !Counter for writing problem variables varying in
                    !time

! INITIALIZE PROBLEM VARIABLES
!Excess pore pressure
    do i=1,nz
        Utold(i) = 0.0
    enddo
!Velocity
    vtold = 0.0
!Temperature
    theta_told = theta_ref
!Displacement
    displ_told = 0.0
!Shear strength
    tau_failure = (weight*cos(beta_slope)-Pw)*tan(fib)
!Heat
    Heat=0.0

! CALCULATION PROCEDURE STARTS
    DO WHILE (displ_tnew.lt.displ_max)
        k=k+1
        t=k*Dt

!Excess pore pressure
        Utnew(1) = Utold(1)+sfb*(2.*Utold(2)-2.*Utold(1))-
            Dt*c_heat*Heat
        .
        do i=2,nze-1
            Utnew(i) = Utold(i)+sfb*(Utold(i+1)-2.*Utold(i)+Utold(i-1))-
                Dt*c_heat*Heat
        .
        enddo

        do j=nze+1,nz-1
            Utnew(j) = Utold(j)+sfr*(Utold(j+1)-2.*Utold(j)+Utold(j-1))
        enddo

        Utnew(nz) = 0.0

        Utnew(nze) = (zk_rock*Utnew(nze+1)+zk_band*Utnew(nze-1))/
            (zk_rock+zk_band)
        .

!Velocity
        Utnew = vtold+Dt*(weight*sin(beta_slope)-
            . tau_failure)/zmass

!Temperature
        theta_tnew = theta_told+Dt* Heat/c_delta_band

!Displacement
        displ_tnew = displ_told+Dt*vtold

!Shear strength
        tau_failure = (weight*cos(beta_slope)
            . -Pw-Utnew(1))*tan(fib)

        if (tau_failure.lt.zero)then
            write (6,*) 'tau_failure is negative'
            tau_failure = 0.0
        endif

!Heat
        Htnew = tau_failure*vtnew/(2.*e)

! UPDATE VARIABLES
!Excess pore pressure
    do m=1,nz
        Utold(m) = Utnew(m)
    enddo

```



```

! OPEN FILES TO WRITE RESULTS
  open (unit=2, file='Velocity.dat', status='unknown')
  open (unit=3, file='Excess_pore_pressure_z0.dat', status='unknown')
  open (unit=4, file='Heat.dat', status='unknown')
  open (unit=7, file='Displacement.dat', status='unknown')
  open (unit=8, file='Strength.dat', status='unknown')
  open (unit=9, file='Temperature.dat', status='unknown')

! WRITING TITLES IN RESULTS FILES
  write (2,*) ' Time(s) ', 'Velocity(m/s) '
  write (3,*) ' Time(s) ', 'U1 (MPa) ', 'U2 (MPa) '
  write (4,*) ' Time(s) ', 'Heat_Wedge1 (MJ/s.m3) ',
  . 'Heat_Wedge2 (MJ/s.m3) '
  write (7,*) ' Time(s) ', 'Displacement (m) '
  write (8,*) ' Time(s) ', 'Shear_strength_Wedge1 (MPa) ' ,
  . 'Shear_strength_Wedge2 (MPa) '
  write (9,*) ' Time(s) ', 'Temperature Wedge1(°) ' ,
  . 'Temperature Wedge2(°) '

  zero=1.e-10

! INITIALIZE COUNTERS
  iw_profile=0 !Counter for writing pore pressure profiles
  iw_time=0 !Counter for writing problem variables varying in
  !time

! INITIALIZE VALUES PARAMETERS THAT CHANGE WITH THE DISPLACEMENT
!Weights
  W1 = Area1_0*gamma_rock
  W2 = Area2_0*gamma_rock
!Mass
  zM1 = Area1_0*delta_rock
  zM2 = Area2_0*delta_rock
!Lengths
  zL1 = zL1_0
  zL2 = zL2_0
  z1_shpl = z1_shpl0
!Hydrostatic forces
  Pw1 = Pw1_0
  Pw2 = Pw2_0

! INITIALIZE PROBLEM VARIABLES
!Excess pore pressure
  do i=1,nz
    Ultold(i) = 0.0
    U2told(i) = 0.0
  enddo
!Changes of notation
  U1 = Ultold(1)
  U2 = U2told(1)
!Velocity
  vtold = 0.0
!Temperatures
  thetal_old = theta_ref
  theta2_old = theta_ref
!Displacements
  stold = 0.0
!Total vertical stress increments
  dSn1 = 0.0
  dSn2 = 0.0
!Mass increments
  dM1dt = 0.0
  dM2dt = 0.0
!Heat
  H1 = 0.0
  H2 = 0.0

! CALCULATION PROCEDURE STARTS
  DO WHILE (stnew.lt.displ_max)
    k=k+1

!Excess pore pressures
    Ultnew(1) = Ultold(1)+sfb*2.*(Ultold(2)-Ultold(1))-
    . c_heat*Dt*H1 + c_sigma_vertical*dSn1

```

```

    U2tnew(1) = U2told(1)+sfb*(2.*U2told(2)-2.*U2told(1))-
    c_heat*Dt*H2 + c_sigma_vertical*dSn2

do i=2,nze-1
    Ultnew(i) = Ultold(i)+
    sfb*(Ultold(i+1)-2.*Ultold(i)+Ultold(i-1))-
    c_heat*Dt*H1 + c_sigma_vertical*dSn1
    U2tnew(i) = U2told(i)+
    sfb*(U2told(i+1)-2.*U2told(i)+U2told(i-1))-
    c_heat*Dt*H2 + c_sigma_vertical*dSn2
enddo

do j=nze+1,nz-1
    Ultnew(j) = Ultold(j)+
    sfr*(Ultold(j+1)-2.*Ultold(j)+Ultold(j-1)) +
    c_sigma_vertical*dSn1
    U2tnew(j) = U2told(j)+
    sfr*(U2told(j+1)-2.*U2told(j)+U2told(j-1)) +
    c_sigma_vertical*dSn2
enddo
Ultnew(nz) = Ultold(nz)+c_sigma_vertical*dSn1
U2tnew(nz) = U2told(nz)+c_sigma_vertical*dSn2

Ultnew(nze) = (zk_rock*Ultnew(nze+1)+zk_band*Ultnew(nze-1))/
(zk_rock+zk_band)
U2tnew(nze) = (zk_rock*U2tnew(nze+1)+zk_band*U2tnew(nze-1))/
(zk_rock+zk_band)

!Changes of notation
U1 = Ultnew(1)
U2 = U2tnew(1)
cg = zh_cha

!Velocity
vtnew = vtold + Dt *
.((W2 *tan(fib)** 2 * sin(shi) - 0.2D1 * cos(shi) *tan(fir)*
#tan(fib)** 2 * Em1 *sin(shi) + cos(shi) *tan(fir)*tan(fib)** 2 * U
#1 * zL1 + Pw2 *tan(fib)** 2 * cos(shi) *tan(fir)- W2 *tan(fib)** 2
# * cos(shi) *tan(fir)+ U2 * zL2 *tan(fib)** 2 * cos(shi)*tan(fir)
#+ cos(shi) ** 2 * Em1 -tan(fib)* cos(shi) ** 2 *tan(fir)* Em1 + 0.
#2D1 * sin(shi) * cos(shi) * coher * cg + cos(shi) *tan(fib)* Em1 *
# sin(shi) - cos(shi) *tan(fir)* Em1 * sin(shi) -tan(fib)* cos(shi)
# *tan(fir)* dM1dt * vtold - dM2dt * vtold *tan(fib)* cos(shi) * ta
#n(fir)+ 0.2D1* sin(shi) *tan(fib)** 2 * cos(shi) * coher * cg - Pw
#2 *tan(fib)** 2 * sin(shi) - Em2 * cos(beta) *tan(fib)** 2 * cos(s
#hi) *tan(fir)+ Em2 * cos(beta) *tan(fib)** 2 * sin(shi) +tan(fib)*
# cos(shi) *tan(fir)* W1 * sin(alpha) + sin(shi) *tan(fir)*tan(fib)
#* Pw1 - sin(shi) *tan(fir)* dM1dt * vtold + sin(shi) *tan(fir)* W1
# * sin(alpha) +tan(fib)* sin(shi) * W1 * sin(alpha) + sin(shi) * t
#an(fir)*tan(fib)*U1 * zL1 + sin(shi) *tan(fib)** 2 * U1 * zL1 - U2
# * zL2 *tan(fib)** 2 * sin(shi) -tan(fib)* sin(shi) * dM1dt * vtold
#d -tan(fib)* Pw2 * sin(shi) *tan(fir)+tan(fib)* W2 * sin(shi) * ta
#n(fir)+dM2dt * vtold *tan(fib)* sin(shi) + dM2dt * vtold * sin(shi)
#) *tan(fir)+ dM2dt * vtold * cos(shi) + W2 *tan(fib)* cos(shi) - P
#w2 *tan(fib)* cos(shi) + cos(shi) * dM1dt * vtold - cos(shi) * tan
#(fib)*Pw1 -tan(fib)* U2 * zL2 * sin(shi) *tan(fir)+ sin(shi) * tan
#(fib)** 2* Pw1 +tan(fib)* Em2 * cos(beta) * sin(shi) *tan(fir)+ Em
#2 * cos(beta) *tan(fib)* cos(shi) - cos(shi) *tan(fib)* U1 * zL1 -
# U2 * zL2 *tan(fib)* cos(shi) + cos(shi) *tan(fir)*tan(fib)** 2 *
#Pw1 - cos(shi) * W1 * sin(alpha) - sin(shi) *tan(fib)** 2 * W1 * c
#os(alpha) + cos(shi) *tan(fib)* W1 * cos(alpha) - cos(shi) *tan(fi
#r)*tan(fib)** 2 * W1 * cos(alpha) - sin(shi) *tan(fir)*tan(fib)* W
#1 * cos(alpha)) / (-zM1 * cos(shi) - zM2 * cos(shi) + zM1*tan(fib)
# * sin(shi) + zM2 *tan(fib)* cos(shi) *tan(fir)+ zM1 * sin(shi) *
#tan(fir)+zM1 *tan(fib)* cos(shi) *tan(fir)- zM2 *tan(fib)* sin(shi)
#) - zM2 * sin(shi) * tan(fir)))

    if (vtnew.lt.-zero) then
        write (6,*) 'The slide stops'
        stop
    endif

!Temperature
thetal_tnew = thetal_old+Dt*H1/c_delta_band

```

```

theta2_tnew = theta2_old+Dt*H2/c_delta_band

!Displacement
stnew = stold+vtold*Dt
!Parameters that change with the displacement
zL1 = zL1_0 - stnew
zL2 = zL2_0 + stnew
zl_shpl = zL1*zl_shpl0/zL1_0
Area1= 0.5*zL1*zl_shpl*cos(shi)
zInc_Area = Area1_0 - Area1
Area2 = Area2_0 + zInc_Area
W1 = Area1*gamma_rock
W2 = Area2*gamma_rock
zM1 = Area1*delta_rock
zM2 = Area2*delta_rock
Pw2 = Pw2_0 + z_Height_w*stnew*gamma_w
coher = coher0*exp(cc*stnew)
dM1dt = -delta_roca*zL1*zl_shpl*cos(shi)*vtnew/zL1
dM2dt = -dM1dt

!Effective normal force on base of Wedge 1
zN1 = -(Pw1*zM1*tan(fib) * cos(shi) * tan(fir)+ U1*zL1*zM1*
#tan(fib) * cos(shi) * tan(fir)- 0.2D1*cos(shi)*tan(fir)*zM1 * tan
#(fib)*Em1 * sin(shi) + 0.2D1 *sin(shi) *zM1 *tan(fib) * cos(shi)
##* coher * cg + U1 * zL1 * zM1 * sin(shi) *tan(fir)+ Em1 * sin(shi)
# * zM1 * cos(shi) - cos(shi) *tan(fir)* zM1 *tan(fib)* W2 + cos(sh
#i) *tan(fir)* zM1 *tan(fib)* Pw2 - U1 * zL1 * zM1 * cos(shi) - zM2
# * coher * cg + zM1 * coher * cg - W1 * cos(alpha)*zM1 *tan(fib)
##* cos(shi) *tan(fir)+ sin(shi) * zM1 * dM2dt * vtold - sin(shi) *
#zM2 * dM1dt * vtold + sin(shi) * zM1 * tan(fib)*W2 - sin(shi) * zM
#1 * tan(fib) * Pw2 + Pw1 * zM1 *tan(fib)* sin(shi) + Pw1 * zM1*sin
#(shi) *tan(fir)- Pw1 * zM2 * sin(shi) *tan(fir)+ sin(shi) * zM2 *
#W1 * sin(alpha) - sin(shi) * zM1 *tan(fib)*U2 * zL2 + U1 * zL1 *
#zM1 * tan(fib)*sin(shi) - U1 * zL1 * zM2 * sin(shi) *tan(fir)- Pw1
# * zM1 * cos(shi) - Pw1 * zM2 * cos(shi) - W1 * cos(alpha) * zM1 *
#tan(fib) * sin(shi) - cos(shi) *tan(fir)* zM2 * W1 *sin(alpha)+ s
#in(shi) * zM1 *tan(fib)* Em2 * cos(beta) + cos(shi) *tan(fir)* zM2
# * dM1dt * vtold - 0.2D1 * cos(shi) ** 2 * coher * cg * zM1 - cos(
#shi) *tan(fir)* zM1 * dM2dt * vtold - W1 * cos(alpha) * zM1 * sin(
#shi) *tan(fir)+ Em1 * zM2 *tan(fir)- cos(shi) *tan(fir)* zM1 * tan
#(fib)*Em2 * cos(beta) + W1 * cos(alpha) * zM2 * sin(shi) *tan(fir)
#- Em1 * zM1 *tan(fir)+ cos(shi) *tan(fir)* zM1 *tan(fib)* U2 * zL2
# - U1 * zL1 * zM2 * cos(shi) + cos(shi) ** 2 * Em1 * zM1*tan(fir)
##+ W1 * cos(alpha) * zM1 * cos(shi) + W1 * cos(alpha) * zM2 * cos(s
#hi) / (-zM1 * cos(shi) - zM2 * cos(shi) + zM1 *tan(fib)*sin(shi)
# + zM2 *tan(fib) *cos(shi) *tan(fir)+ zM1 *sin(shi)*tan(fir)+ zM
#1 *tan(fib) * cos(shi) *tan(fir)- zM2 *tan(fib) *sin(shi)-zM2 * s
#in(shi) *tan(fir))

!Effective normal force on base of wedge 2
zN2 =-(-Em2 *cos(beta) *zM2 *tan(fib)* cos(shi)*tan(fir)- Em2
##* cos(beta) * zM1 * sin(shi) *tan(fir)+ Em2 * cos(beta) * zM1 * co
#s(shi) - W2 * zM2 *tan(fib)* cos(shi) *tan(fir)+ U2 * zL2 * zM2 *
#tan(fib)*cos(shi)*tan(fir)+ Em1 * sin(shi) * zM1 * cos(shi) - 0.2
#D1 * cos(shi) *tan(fir)* zM2 *tan(fib)* Em1 * sin(shi) + 0.2D1 * s
#in(shi) * zM2 *tan(fib)* cos(shi) * coher * cg - zM2 * coher * cg
##+ zM1 * coher * cg + cos(shi) *tan(fir)* zM2 *tan(fib)* Pw1 - sin(
#shi) * zM2 *tan(fib)* W1 * cos(alpha) + sin(shi) * zM2 *tan(fib)*
#Pw1 + sin(shi) * zM1 * dM2dt * vtold - sin(shi) * zM2 * dM1dt * vt
#old + Pw2 * zM1 * sin(shi) *tan(fir)- Pw2 * zM2 *tan(fib)* sin(shi)
#) - Pw2 * zM2 * sin(shi) *tan(fir)- W2 * zM1 * sin(shi) *tan(fir)+
# W2 * zM2 *tan(fib)* sin(shi) + W2 * zM2 * sin(shi) *tan(fir)+ sin
#(shi) * zM2 * W1 * sin(alpha) + sin(shi) * zM2 *tan(fib)* U1 * zL1
# + U2 * zL2 * zM1 * sin(shi) *tan(fir)- U2 * zL2 * zM2 *tan(fib)*
#sin(shi) - U2 * zL2 * zM2 * sin(shi) *tan(fir)- Pw2 * zM1 * cos(sh
#i) + W2 * zM1 * cos(shi) - Pw2 * zM2 * cos(shi) + W2 * zM2 * cos(s
#hi) + cos(shi) *tan(fir)* zM2 * W1 * sin(alpha) + Em2 * cos(beta)
##* zM2 *tan(fib)* sin(shi) + Em2 * cos(beta) * zM2 * sin(shi) * tan
#(fir)+ Em2 * cos(beta) * zM2 * cos(shi) - cos(shi) *tan(fir)*zM2 *
# dM1dt * vtold + cos(shi) *tan(fir)* zM2 *tan(fib)* U1 * zL1 + cos
#(shi) *tan(fir)* zM1 * dM2dt * vtold - 0.2D1 * cos(shi) ** 2 * tan
#(fir) * zM2 * Em1 + Em1 * zM2 *tan(fir)-cos(shi)*tan(fir)* zM2 * t
#an(fib)*W1* cos(alpha) - Em1 * zM1 *tan(fir)+ 0.2D1 * cos(shi) **
# 2 * coher * cg * zM2 - U2 * zL2 * zM1 * cos(shi) - U2 * zL2 * zM2

```

```

# * cos(shi) + Pw2 * zM2 *tan(fib)* cos(shi) *tan(fir)+ cos(shi) **
# 2 * Em1 * zM1 *tan(fir))/ (-zM1 * cos(shi) - zM2 * cos(shi) + zM1
# *tan(fib)* sin(shi) + zM2 *tan(fib)* cos(shi) *tan(fir)+ zM1 * si
#n(shi) *tan(fir)+ zM1 *tan(fib)* cos(shi) *tan(fir)- zM2 *tan(fib)
#* sin(shi) - zM2 * sin(shi) *tan(fir))

      if (zN1_tnew.lt.zero) then
        zN1_tnew = 0.0
      endif
      if (zN2_tnew.lt.zero) then
        zN2_tnew = 0.0
      endif

!Total normal forces
      zN1tot = zN1+Pw1+U1*zL1
      zN2tot = zN2+Pw2+U2*zL2

!Total vertical stresses
      Sn1_tnew = -zN1tot/zL1
      Sn2_tnew = -zN2tot/zL2

!Total vertical stress increments
      if (k.eq.1) then
        dSn1_tnew = 0.0
        dSn2_tnew = 0.0
      else
        dSn1 = Sn1_tnew-Sn1_told
        dSn2 = Sn2_tnew-Sn2_told
      endif

!Shear strength
      Taul = (zN1/zL1) * tan(fib)
      Tau2 = (zN2/zL2) * tan(fib)

!Heat
      H1 = Taul*vtnew/(2.*e)
      H2 = Tau2*vtnew/(2.*e)

! UPDATE PROBLEM VARIABLES
!Excess pore pressure
      do i=1,nze
        U1told(i) = U1tnew(i)
        U2told(i) = U2tnew(i)
      enddo
!Velocity
      vtold = vtnew
!Temperatures
      thetal_old = thetal_tnew
      theta2_old = theta2_new
!Displacement
      stold = stnew
!Total vertical stresses
      Sn1_told = Sn1_tnew
      Sn2_told = Sn2_tnew

! WRITING RESULTS AT SELECTED TIMES
      if ((k.eq.2).or.(mm.eq.k)) then
        write (6,*) k,' Profile results have been written'
        iw_profile = iw_profile+1
        mm=int(int_write_profile)*iw_profile
        t=k*Dt
        iarchivo=iw_profile+100
        write (iarchivo,*) 'Time(s) ',t
        do m=1,nze+10
          z=(m-1)*Dz
          write (iarchivo,'(2(e15.5,1x))') z, U1tnew(m)
        enddo
        do m =          nze+11,nz,10
          z = m*Dz
          write (iarchivo,'(2(e15.5,1x))') z, U1tnew(m)
        enddo
      endif
      if ((k.eq.1).or.(nn.eq.k)) then
        iw_time = iw_time+1

```

```

nn = int(int_write_time)*iw_time
t=k*Dt
write (2,'(2(e15.5,1x))') t, vtnew
write (3,'(3(e15.5,1x))') t, U1tnew(1)*1.e-6,U2tnew(1)*1.e-6
write (4,'(3(e15.5,1x))') t, H1/1.e6,H2/1.e6
write (7,'(2(e15.5,1x))') t, stold
write (8,'(3(e15.5,1x))') t, Tau1 *1.e-6,Tau2*1.e-6
write (9,'(3(e15.5,1x))') t, theta1_tnew,theta2_tnew
endif

ENDDO

close (2)
close (3)
close (4)
close (7)
close (8)
close (9)

return
end

```

APPENDIX 6.2 PARAMETERS OF THE BALANCE EQUATIONS FOR THE DYNAMIC ANALYSIS OF TWO INTERACTING WEDGES

Parameters which complete the dynamic equilibrium equation of the two wedges (Eq. 32) are:

$$\begin{aligned}
t_{W_1} &= \left(-\tan \phi'_b \tan \phi'_r - \tan^2 \phi'_b\right) \sin\left(\frac{\alpha}{2}\right) \cos \alpha + \left(\tan \phi'_r + \tan \phi'_b\right) \sin\left(\frac{\alpha}{2}\right) \sin \alpha + \\
&\left(\tan \phi'_b - \tan^2 \phi'_b \tan \phi'_r\right) \cos\left(\frac{\alpha}{2}\right) \cos \alpha + \tan \phi'_b \tan \phi'_r \cos\left(\frac{\alpha}{2}\right) \sin \alpha - \cos\left(\frac{\alpha}{2}\right) \sin \alpha \\
t_{W_2} &= \left(\tan \phi'_b - \tan^2 \phi'_b \tan \phi'_r\right) \cos\left(\frac{\alpha}{2}\right) + \left(\tan^2 \phi'_b + \tan \phi'_b \tan \phi'_r\right) \sin\left(\frac{\alpha}{2}\right) \\
t_{P_{\text{int}}} &= -2 \tan \phi'_r \sin\left(\frac{\alpha}{2}\right) \cos\left(\frac{\alpha}{2}\right) (1 + \tan^2 \phi'_b) \\
t_{P_{\text{wf}}} &= \left(\tan^2 \phi'_b + \tan \phi'_b \tan \phi'_r\right) \sin\left(\frac{\alpha}{2}\right) \cos \beta + \left(1 - \tan \phi'_b \tan \phi'_r\right) \cos\left(\frac{\alpha}{2}\right) \sin \beta + \\
&\left(\tan \phi'_b - \tan^2 \phi'_b \tan \phi'_r\right) \cos\left(\frac{\alpha}{2}\right) \cos \beta + \left(\tan \phi'_b + \tan \phi'_r\right) \sin\left(\frac{\alpha}{2}\right) \sin \beta \\
t_{P_{w1}} &= \tan^2 \phi_b \tan \phi'_r \cos\left(\frac{\alpha}{2}\right) + \tan \phi'_b \tan \phi'_r \sin\left(\frac{\alpha}{2}\right) + \tan^2 \phi'_b \sin\left(\frac{\alpha}{2}\right) - \tan \phi'_b \cos\left(\frac{\alpha}{2}\right) \\
t_{P_{w2}} &= \tan^2 \phi'_b \tan \phi'_r \cos\left(\frac{\alpha}{2}\right) - \tan \phi'_b \tan \phi'_r \sin\left(\frac{\alpha}{2}\right) - \tan^2 \phi'_b \sin\left(\frac{\alpha}{2}\right) - \tan \phi'_b \cos\left(\frac{\alpha}{2}\right) \\
t_{u_{w1}} &= \left(\tan^2 \phi'_b \tan \phi'_r - \tan \phi'_b\right) \cos\left(\frac{\alpha}{2}\right) + \left(\tan^2 \phi'_b + \tan \phi_b \tan \phi'_r\right) \sin\left(\frac{\alpha}{2}\right) \\
t_{u_{w2}} &= \left(\tan^2 \phi'_b \tan \phi'_r - \tan \phi'_b\right) \cos\left(\frac{\alpha}{2}\right) - \left(\tan^2 \phi'_b + \tan \phi'_b \tan \phi'_r\right) \sin\left(\frac{\alpha}{2}\right)
\end{aligned}$$

$$t_{c_r} = 2 \cos\left(\frac{\alpha}{2}\right) \sin\left(\frac{\alpha}{2}\right) (1 + \tan^2 \varphi'_b)$$

$$t_{dM_1 dt} = \cos\left(\frac{\alpha}{2}\right) - (\tan \varphi'_b + \tan \varphi'_r) \sin\left(\frac{\alpha}{2}\right) - \tan \varphi'_b \tan \varphi'_r \cos\left(\frac{\alpha}{2}\right)$$

$$t_{dM_2 dt} = \cos\left(\frac{\alpha}{2}\right) + (\tan \varphi'_b + \tan \varphi'_r) \sin\left(\frac{\alpha}{2}\right) - \tan \varphi'_b \tan \varphi'_r \cos\left(\frac{\alpha}{2}\right)$$

$$t_{M_1} = (\tan \varphi'_r + \tan \varphi'_b) \sin\left(\frac{\alpha}{2}\right) + (\tan \varphi'_r \tan \varphi'_b - 1) \cos\left(\frac{\alpha}{2}\right)$$

$$t_{M_2} = -(\tan \varphi'_r + \tan \varphi'_b) \sin\left(\frac{\alpha}{2}\right) + (\tan \varphi'_r \tan \varphi'_b - 1) \cos\left(\frac{\alpha}{2}\right)$$

Coefficients r and s in Equations (33a) and (33b) are given by

$$r_{W_1} = M_1 \tan \varphi'_b \cos \alpha \left(\cos\left(\frac{\alpha}{2}\right) - \tan \varphi'_r \sin\left(\frac{\alpha}{2}\right) - \tan \varphi'_b \sin\left(\frac{\alpha}{2}\right) - \tan \varphi'_b \tan \varphi'_r \cos\left(\frac{\alpha}{2}\right) \right) +$$

$$M_2 \tan \varphi'_b \left(\tan \varphi'_r \cos \alpha \sin\left(\frac{\alpha}{2}\right) + \sin\left(\frac{\alpha}{2}\right) \sin \alpha - \tan \varphi'_r \cos\left(\frac{\alpha}{2}\right) \sin \alpha + \cos \alpha \cos\left(\frac{\alpha}{2}\right) \right)$$

$$r_{W_2} = M_1 \tan^2 \varphi'_b \left(\sin\left(\frac{\alpha}{2}\right) - \tan \varphi'_r \cos\left(\frac{\alpha}{2}\right) \right)$$

$$r_{P_{\text{wint}}} = M_1 \tan \varphi'_b \sin\left(\frac{\alpha}{2}\right) \left(-\cos\left(\frac{\alpha}{2}\right) - s \tan \varphi'_r \sin\left(\frac{\alpha}{2}\right) - 2 \tan \varphi'_r \tan \varphi'_b \cos\left(\frac{\alpha}{2}\right) \right) + M_2 \tan \varphi'_r \tan \varphi'_b$$

$$r_{P_{\text{wf}}} = M_1 \tan^2 \varphi'_b \cos \beta \left(\sin\left(\frac{\alpha}{2}\right) - \tan \varphi'_r \cos\left(\frac{\alpha}{2}\right) \right)$$

$$r_{P_{w1}} = M_1 \tan \varphi'_b \left(-\cos\left(\frac{\alpha}{2}\right) + \tan \varphi'_r \sin\left(\frac{\alpha}{2}\right) + \tan \varphi'_b \sin\left(\frac{\alpha}{2}\right) + \tan \varphi'_b \tan \varphi'_r \cos\left(\frac{\alpha}{2}\right) \right) -$$

$$M_2 \tan \varphi'_b \left(\cos\left(\frac{\alpha}{2}\right) + \tan \varphi'_r \sin\left(\frac{\alpha}{2}\right) \right)$$

$$r_{P_{w2}} = M_1 \tan^2 \varphi'_b \left(\tan \varphi'_r \cos\left(\frac{\alpha}{2}\right) - \sin\left(\frac{\alpha}{2}\right) \right)$$

$$r_{u_{w1}} = M_1 \tan \varphi'_b \left(\tan \varphi'_r \sin\left(\frac{\alpha}{2}\right) + \tan \varphi'_b \sin\left(\frac{\alpha}{2}\right) - \cos\left(\frac{\alpha}{2}\right) + \tan \varphi'_b \tan \varphi'_r \cos\left(\frac{\alpha}{2}\right) \right) -$$

$$M_2 \tan \varphi'_b \left(\tan \varphi'_r \sin\left(\frac{\alpha}{2}\right) + \cos\left(\frac{\alpha}{2}\right) \right)$$

$$r_{u_{w2}} = M_1 \tan^2 \phi'_b \left(\tan \phi'_r \cos \left(\frac{\alpha}{2} \right) - \sin \left(\frac{\alpha}{2} \right) \right)$$

$$r_{c_r} = M_1 \tan \phi'_b \left(\sin^2 \left(\frac{\alpha}{2} \right) - \cos^2 \left(\frac{\alpha}{2} \right) + 2 \tan \phi'_b \sin \left(\frac{\alpha}{2} \right) \cos \left(\frac{\alpha}{2} \right) \right) - M_2 \tan \phi'_b \cos^2 \left(\frac{\alpha}{2} \right)$$

$$r_{dM_1 dt} = M_2 \tan \phi'_b \left(\tan \phi'_r \cos \left(\frac{\alpha}{2} \right) - \sin \left(\frac{\alpha}{2} \right) \right)$$

$$r_{dM_2 dt} = M_1 \tan \phi'_b \left(-\tan \phi'_r \cos \left(\frac{\alpha}{2} \right) + \sin \left(\frac{\alpha}{2} \right) \right)$$

$$r_{M_1} = \tan \phi' \cos \left(\frac{\alpha}{2} \right) - \tan \phi'_r \tan \phi' \sin \left(\frac{\alpha}{2} \right) - \tan^2 \phi'_b \sin \left(\frac{\alpha}{2} \right) - \tan^2 \phi'_b \tan \phi'_r \cos \left(\frac{\alpha}{2} \right)$$

$$r_{M_2} = -\tan^2 \phi'_b \tan \phi'_r \cos \left(\frac{\alpha}{2} \right) + \tan^2 \phi'_b \sin \left(\frac{\alpha}{2} \right) + \tan \phi'_b \cos \left(\frac{\alpha}{2} \right) + \tan \phi'_b \tan \phi'_r \sin \left(\frac{\alpha}{2} \right)$$

and

$$s_{W_1} = M_2 \left(\tan \phi'_r \tan \phi'_b \cos \left(\frac{\alpha}{2} \right) \sin \alpha + \tan \phi'_b \sin \left(\frac{\alpha}{2} \right) \sin \alpha - \tan^2 \phi'_b \sin \left(\frac{\alpha}{2} \right) \cos \alpha - \tan \phi'_r \tan^2 \phi'_b \cos \left(\frac{\alpha}{2} \right) \cos \alpha \right)$$

$$s_{W_2} = M_1 \tan \phi'_b \left(\cos \left(\frac{\alpha}{2} \right) - \tan \phi'_r \sin \left(\frac{\alpha}{2} \right) \right) +$$

$$M_2 \tan \phi'_b \left(\tan \phi'_b \sin \left(\frac{\alpha}{2} \right) - \tan \phi'_b \tan \phi'_r \cos \left(\frac{\alpha}{2} \right) + \tan \phi'_r \sin \left(\frac{\alpha}{2} \right) + \cos \left(\frac{\alpha}{2} \right) \right)$$

$$s_{P_{\text{win1}}} = M_1 \tan \phi'_b \left(\sin \left(\frac{\alpha}{2} \right) \cos \left(\frac{\alpha}{2} \right) - \tan \phi'_r \sin^2 \left(\frac{\alpha}{2} \right) \right) +$$

$$M_2 \tan \phi'_r \tan \phi'_b \left(-\cos^2 \left(\frac{\alpha}{2} \right) + \sin^2 \left(\frac{\alpha}{2} \right) - 2 \tan \phi'_b \cos \left(\frac{\alpha}{2} \right) \sin \left(\frac{\alpha}{2} \right) \right)$$

$$s_{P_{w2}} = M_1 \tan \phi'_b \cos \beta \left(\cos \left(\frac{\alpha}{2} \right) - \tan \phi'_r \sin \left(\frac{\alpha}{2} \right) \right) +$$

$$M_2 \tan \phi'_b \cos \beta \left(\cos \left(\frac{\alpha}{2} \right) - \tan \phi'_b \tan \phi'_r \cos \left(\frac{\alpha}{2} \right) + \tan \phi'_b \sin \left(\frac{\alpha}{2} \right) + \tan \phi'_r \sin \left(\frac{\alpha}{2} \right) \right)$$

$$s_{P_{w1}} = M_2 \tan^2 \phi'_b \left(\sin \left(\frac{\alpha}{2} \right) + \cos \left(\frac{\alpha}{2} \right) \tan \phi'_r \right)$$

$$\begin{aligned}
s_{P_{w2}} &= M_1 \tan \phi'_b \left(\tan \phi'_r \sin \left(\frac{\alpha}{2} \right) - \cos \left(\frac{\alpha}{2} \right) \right) + \\
M_2 \tan \phi'_b &\left(\tan \phi'_b \tan \phi'_r \cos \left(\frac{\alpha}{2} \right) - \cos \left(\frac{\alpha}{2} \right) \tan \phi'_r \sin \left(\frac{\alpha}{2} \right) - \tan \phi'_b \sin \left(\frac{\alpha}{2} \right) \right) \\
s_{u_{w1}} &= M_2 \tan^2 \phi'_b \left(\sin \left(\frac{\alpha}{2} \right) + \tan \phi'_r \cos \left(\frac{\alpha}{2} \right) \right) \\
s_{u_{w2}} &= M_1 \tan \phi'_b \tan \phi'_r \left(\sin \left(\frac{\alpha}{2} \right) - \cos \left(\frac{\alpha}{2} \right) \right) + \\
M_2 \tan \phi'_b &\left(\tan \phi'_b \tan \phi'_r \cos \left(\frac{\alpha}{2} \right) - \tan \phi'_b \sin \left(\frac{\alpha}{2} \right) - \tan \phi'_r \sin \left(\frac{\alpha}{2} \right) - \cos \left(\frac{\alpha}{2} \right) \right) \\
s_{c_r} &= M_1 \tan \phi'_b + \\
M_2 \tan \phi'_b &\left(-\sin^2 \left(\frac{\alpha}{2} \right) + \cos^2 \left(\frac{\alpha}{2} \right) + 2 \sin \left(\frac{\alpha}{2} \right) \tan \phi'_b \cos \left(\frac{\alpha}{2} \right) \right) \\
s_{dM_1 dt} &= -M_2 \tan \phi'_b \left(\tan \phi'_r \cos \left(\frac{\alpha}{2} \right) + \sin \left(\frac{\alpha}{2} \right) \right) \\
s_{dM_2 dt} &= M_1 \tan \phi'_b \left(\tan \phi'_r \cos \left(\frac{\alpha}{2} \right) - \sin \left(\frac{\alpha}{2} \right) \right) \\
s_{M_1} &= \tan \phi'_b \left(\cos \left(\frac{\alpha}{2} \right) - \tan \phi'_r \sin \left(\frac{\alpha}{2} \right) - \tan \phi'_b \sin \left(\frac{\alpha}{2} \right) - \tan \phi'_b \tan \phi'_r \cos \left(\frac{\alpha}{2} \right) \right) \\
s_{M_2} &= \tan \phi'_b \left(\cos \left(\frac{\alpha}{2} \right) - \tan \phi'_b \tan \phi'_r \cos \left(\frac{\alpha}{2} \right) + \tan \phi'_b \sin \left(\frac{\alpha}{2} \right) + \tan \phi'_r \sin \left(\frac{\alpha}{2} \right) \right) \\
s_{M_2} &= -\tan \phi'_b \cos \left(\frac{\alpha}{2} \right) \tan \phi'_r + \tan \phi'_b \sin \left(\frac{\alpha}{2} \right) + \cos \left(\frac{\alpha}{2} \right) + \sin \left(\frac{\alpha}{2} \right) \tan \phi'_r
\end{aligned}$$

CHAPTER 7

Canelles Landslide

During the summer of 2006, after a rapid drawdown (the drawdown velocity exceeded to 1 m/day), a very large landslide developed in the left margin of Canelles reservoir (Catalonia, Spain). Canelles dam, located in the Noguera Ribagorçana river, is 150 m high arch dam. This chapter describes the analysis made to define the movement and the reasons that led to the instability. The possible evolution of the landslide in the future is also discussed in the chapter.

The geometry of the slide could be established from the detailed analysis of the continuous cores recovered in deep borings and from the limited information provided by inclinometers. Deep piezometric records provided also valuable information on the pressure changes in the vicinity of the failure surface. These data, available for a significant time, allowed validating a flow-deformation coupled calculation model that took into account the changes in water level of the reservoir and external contributions (rainfall). The model indicates that the most likely reason for failure is the rapid drawdown that took place during the summer of 2006.

This chapter studies the causes of the observed failure and analyses the conditions that could lead to a rapid acceleration of the slide in the future.

7.1 BACKGROUND

During the summer of 2006, a continuous crack was detected in the left margin of Canelles reservoir. It was interpreted as the upper limit of a large slide that probably began in the submerged area of the reservoir. An analysis of the reservoir level

evolution indicated high values of drawdown velocities in the period July-August 2006. In fact, during the first days of August 2006, the velocity was greater than 1 m/day reaching a maximum value of 1.20 m/day. It is quite likely that the motion that caused the crack took place around this date. Water level elevation reduced from 440 m to 430 m. Never before, from 1986 to 2009, had drawdown velocities reached such high levels and neither had the water level elevation been so low.



Figure 7.1 Detail of the tensile crack at the foot of the jump limiting the southern boundary of the landslide. The lack of deformation, due, for instance, to surface tilting of the displaced soil (left to the crack), suggests an essentially translational movement. The remnants of the old village of Blancafort can be seen in the background of the photograph.

7.1.1 Description of the failure

The instability of the northern slope of Sierra de Blancafort, which took place most probably in the summer of 2006, became evident by the presence of a continuous crack, a few decimetres in width (10-20 cm) and more than one kilometre long (in a direction parallel to the Noguera Ribagorçana River). The crack (Fig. 7.1) is located at a slope foot with an apparent scarp of more than 4-5 m. This jump limits the southern part of the landslide (Figs. 7.2 and 7.3). This geomorphologic feature was interpreted as an indication that the slide is not a first failure, but the reactivation of a movement whose dating is unknown. In fact, it can be observed in aerial photographs taken in

1956. The straightness of the upper scar and the fact that the soil near the crack does not indicate any surface tilt suggests a translational type of slide.

In the northern zone of the Blancafort Sierra (Fig. 7.3) neither geological nor geomorphological evidence of landslide activity was found. The valley slope is a structural surface of Campanian marl and Maastricht sandstone, in which the draining network was embedded without anomalies. The development of the drainage network took a long-period of time to form (millenary scale), so it can be concluded that the slide is limited by the mentioned crack located on the lower part of the valley slope.



Figure 7.2 Overview crown scarp of the slide on the left bank at the foot of the developed tension crack 2006.

Geological setting and location of the sliding plane

This section describes the stratigraphy and the structure of materials located around the reservoir following the study performed by Corominas and Moya (2009).

The northern slope of the Sierra de Blancafort consists of sedimentary rocks whose age ranges from late Cretaceous to Paleocene. Six groups of materials have been distinguished in the bedrock. These units have been defined by means of surface observation and the stratigraphic columns provided by the borings performed. Figure 7.4 shows the geological map of the area and Figure 7.5-7.7, representative geological profiles.



Figure 7.3 Orthophotograph of Canelles reservoir, Blancafort Sierra and the slide under study (in yellow). To the south of the slide, the northern slope of Blancafort Sierra presents a well-developed drainage network on a rock substratum (cemented marls and sandstones), showing no additional failure scars. A perfect lateral continuity can be observed in the contacts among strata. The sliding volume was estimated at 40 millions of m^3 .

At the beginning of the field investigation, it was thought that the information furnished by deep inclinometers would provide a precise position of the failure surface. Under favourable conditions (slide undergoing some movement), the inclinometer data should be enough to identify the sliding surface or surfaces. However, inclinometers did not provide but slight indications, in some cases, of the existence of movements. The slide essentially did not move since the onset of the crack in the summer of 2006. As an alternative, the location on the sliding surface was determined by means of a detailed analysis of the rock massif quality and the identification of shearing planes in boring cores.

Since the movement corresponds to a translational slide, there exists probably a level or layer that favours the development of a failure surface (stratum, fault area, etc.). Given the strong dip of strata at the bottom of the valley, the aim of the analysis was to search for shearing surfaces, especially in the weakest levels. A priori, the lithological formations most likely to produce failure surfaces are the clayey ones. In particular the following two formations, which are favourably orientated and belong to the Garumn complex:

- (a) orange sandstone unit with interbedded sandy and clayey silts
- (b) wine-red clay and silt strata

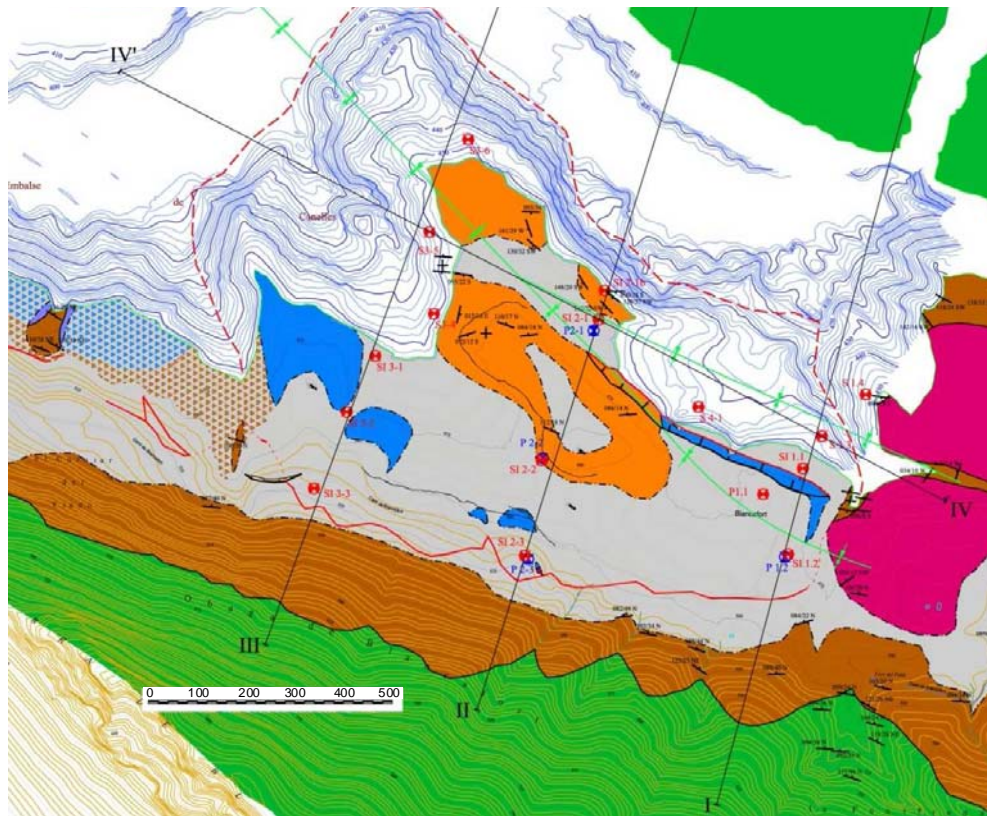
are good candidates to locate the failure surface.

The arrangement of the silty and the red-wine clay strata allows defining the initial hypothesis: the failure surface develops at those weaker levels without crossing other stronger strata.

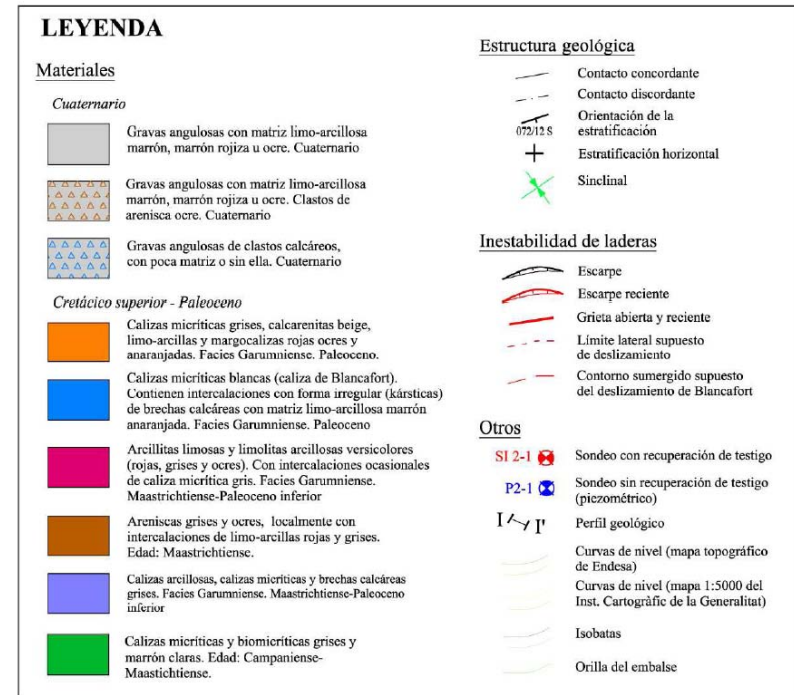
In the sliding plane, it is quite usual to find well-developed and continuous shearing surfaces. Nevertheless, the shearing surfaces can also have a tectonic origin with no direct relationship with the slide. During the alpine orogenesis of Blancafort Sierra, the site suffered relative movement among strata, wedging some layers and creating progressive discordances. The relative movement among strata generated extensive and continuous shearing surfaces (Fig. 7.8). For these reasons, it was necessary to search for additional specific criteria to identify shearing surfaces associated with the landslide.

The identification of the sliding plane was based on several indicators:

- Presence of frequent shearing planes. These planes can be easily identified due to the existence of slickensides or polished surfaces.
- Continuity and parallelism of shearing planes with respect to the potential sliding plane.
- Degree of core recovery and quality of the samples above the shearing plane. In case of sliding, the movement can break the most rigid strata and produce a massif of less quality when compared with non-slid rock samples.
- Degree of core recovery and quality of the samples above the shearing plane. In case of sliding, the movement can break the most rigid strata and produce a massif of less quality when compared with non-slid rock samples.
- The interpolation of the sliding plane among borings cannot be inconsistent.
- Finally, the correlation with inclinometric records.



(a)



(b)

Figure 7.4 (a) Geological map of the northern slope of the Sierra de Blancafort. Black continuous lines indicate the profiles examined and used in the analysis; (b) map legend (Corominas and Moya, 2009).

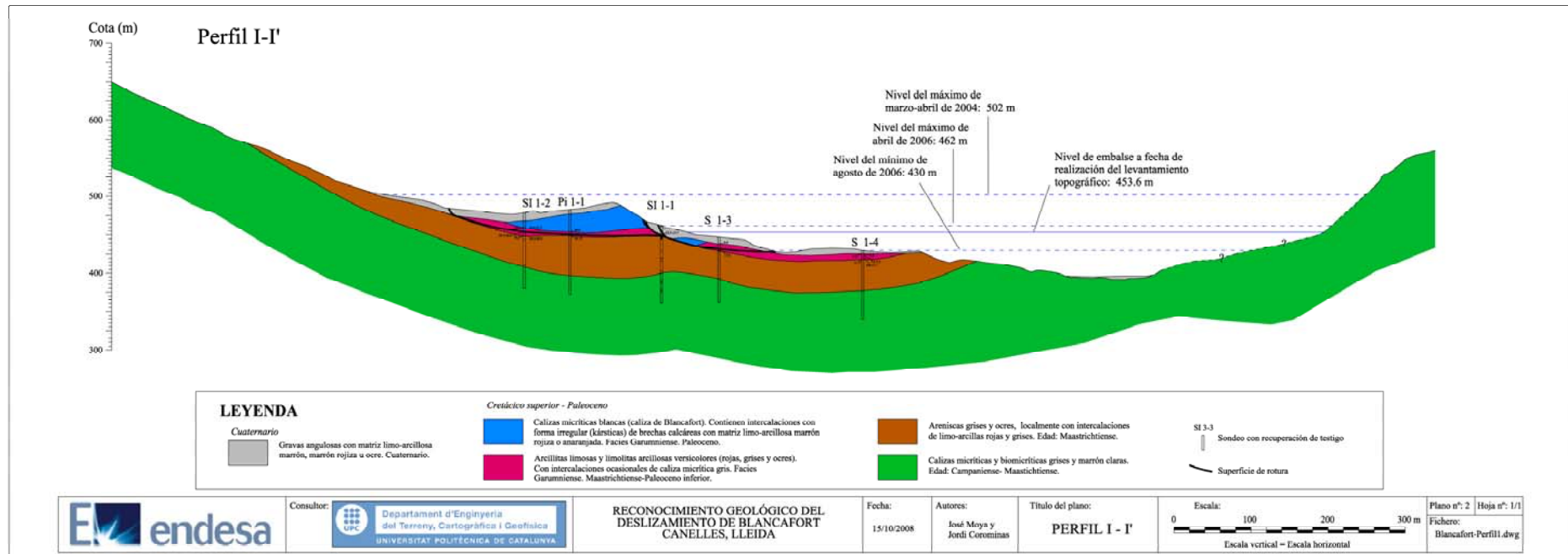


Figure 7.5 Geological Profile I (Corominas and Moya, 2009)

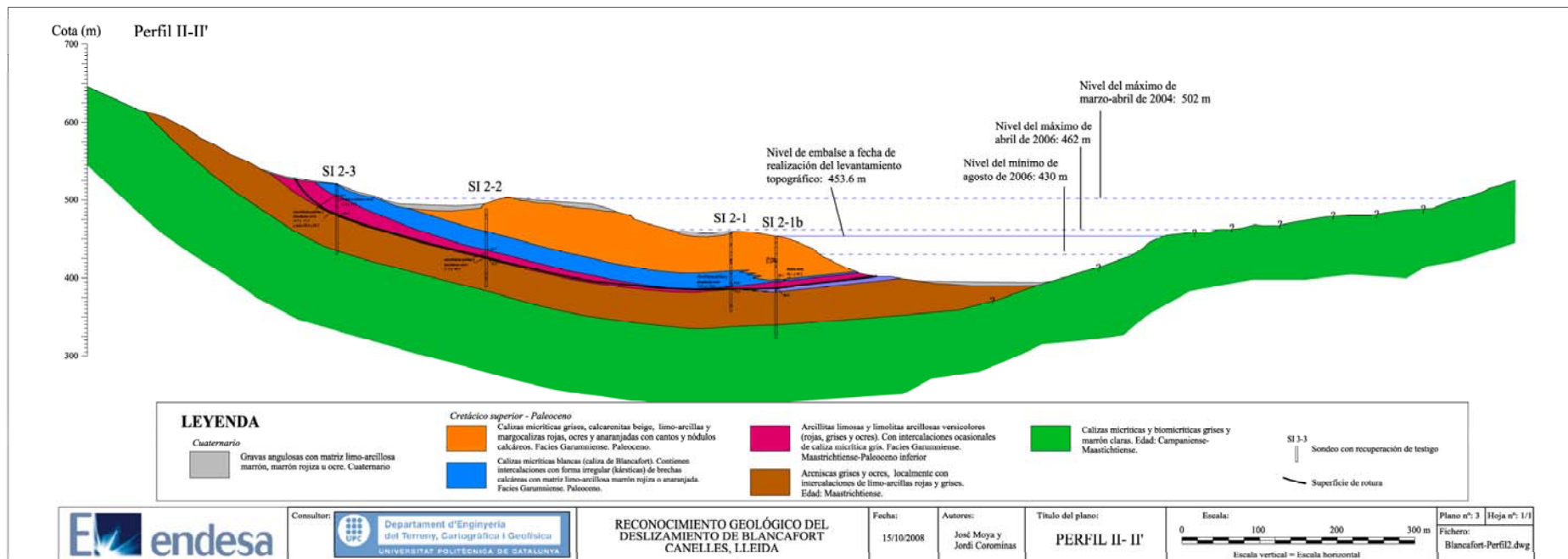


Figure 7.6 Geological Profile II (Corominas and Moya, 2009)

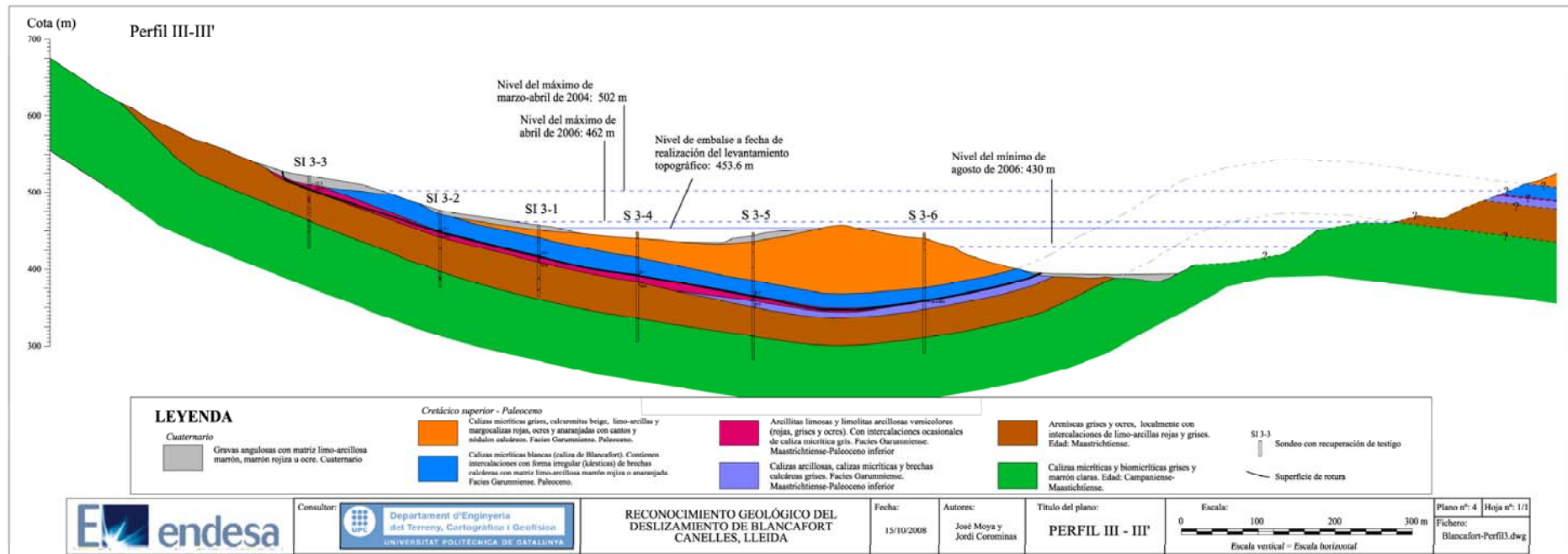


Figure 7.7 Geological Profile III (Corominas and Moya, 2009)



Figure 7.8 Shearing surface in the Maastricht brown sandstone formation located 58.75 deep in boring SI-1-1.

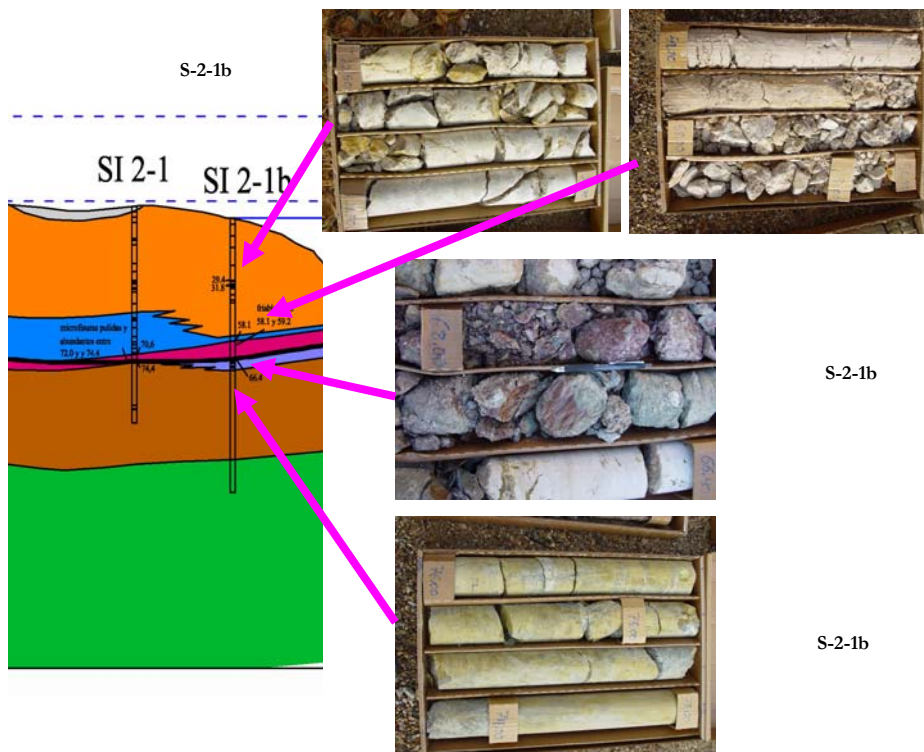


Figure 7.9 Sliding surface identified by the presence of frequent shearing surfaces located at elevations 66.40 to 68.80 m. Above this depth, the marl levels from the Garumn complex are either cracked or completely broken. Below this depth, sandstones and marls show a massive appearance and high RDQ.

7.2 LABORATORY TESTS

This section summarises the results obtained in the laboratory on samples of natural and remoulded material taken from the Garumn clayey stratum where the failure surface is located. The natural conditions of the samples indicate densities ranging from 1.71 to 1.88 T/m³, which correspond to void ratios of 0.96-0.68. Water content in most cases is close to 20% (saturation degree of 70%) or more in some samples. Garumn clay is quite plastic ($w_L = 54-57\%$; $PI = 26-31\%$)(CH). 40% of the particles are smaller than 2 μm .

Since the landslide is a reactivated slide, the residual strength was measured on remoulded samples in the ring shear equipment. The measured angle ($\phi'_{res} = 12-13^\circ$) is consistent with the clay plasticity.

Taking into account the discussion given as a result of the sensitivity analysis presented in Chapters 4 and 6 about the relevant parameter controlling the acceleration of a landslide if thermal effects are considered, the permeability to water was also measured in two samples subjected to a vertical stress of 300 kPa. Permeability showed values of 4.2×10^{-10} and 4.9×10^{-11} m/s. The reason for the variation of one order of magnitude between these two values can be due to different locations of the specimens within the clay stratum.

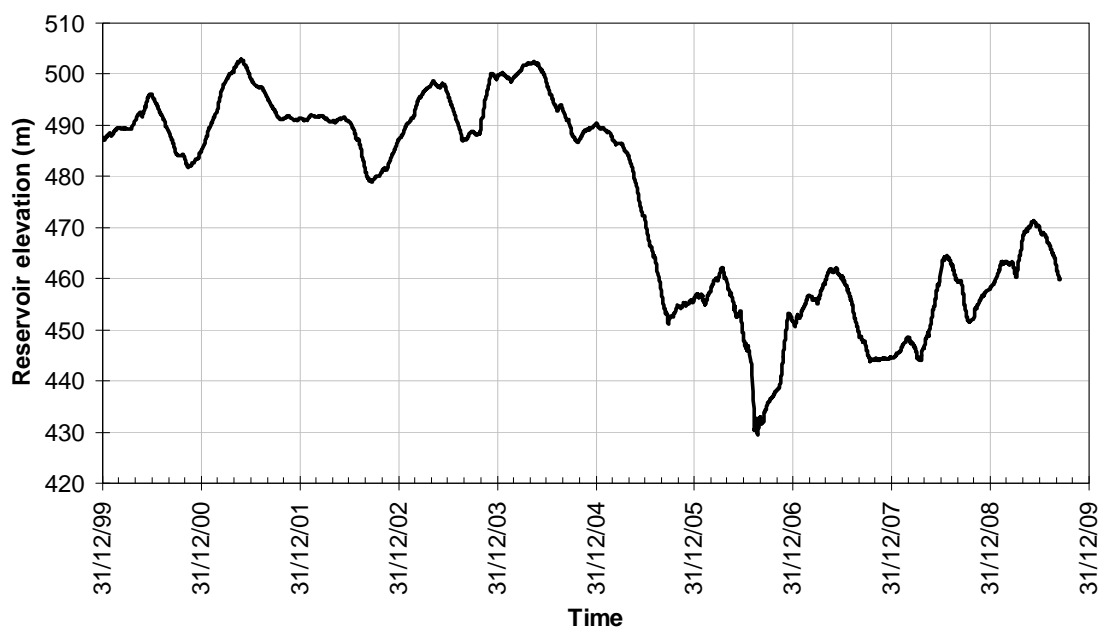


Figure 7.10 Evolution in time of the water level elevation of reservoir.

7.3 WATER LEVEL AND PIEZOMETER MEASUREMENTS

7.3.1 Water level elevation

Figure 7.10 shows the evolution in time of the water level elevation in the reservoir from January 1987 until 2009. The crack in the left valley slope of the reservoir was observed at the end of summer 2006, after the water level elevation dropped to elevation 430 (absolute minimum value since 1987, according to available data). The average daily drawdown velocity, before failure, was around 0.25 m/day and the daily maximum velocities were higher than 1 m/day during the last drawdown period. Note that the 2006 drawdown followed a long period (1992-2004) in which the level was consistently located above elevation 480. This period probably allowed reaching water pressures corresponding to high water elevations, even in those strata with lower permeability. This previous history should be taken into account when estimating the water pressure during drawdown.

7.3.2 Piezometers

Figure 7.11 indicates the location in plan view of the piezometers installed. Several piezometers (three or four) were installed in each bore hole at different depths. Piezometers were installed around the clayey layer where the failure surface was most likely located.

The piezometer records are shown in Figures 7.12–7.16. The recorded water pressures in the sandstone stratum follow the water level elevation in the reservoir. The response is fast in all the piezometers except for the piezometers located in SI 2-3. On the contrary, the piezometers located in the clayey stratum maintain high pressures, which in some cases exceed the pressures corresponding to the current water reservoir elevation. Note, in particular, the value of the pressures recorded in SI 1-2 and SI 2-2 in the piezometer located within the clayey Garumn stratum. The pressure in this case remains constant and independent to the water level elevation. This result confirms the low permeability of the clay stratum, in contrast to the higher permeability of the sandstone and marls located below. The pressure in the upper part of the slide (SI 2-3) seems not to be directly connected to the reservoir. High pressure values are measured in the rock layer (Fig. 7.16). These values of water pressure probably are a consequence of direct infiltration from rainfall or perhaps the results of other sources of water no well defined, linked to the geological structure of the area.

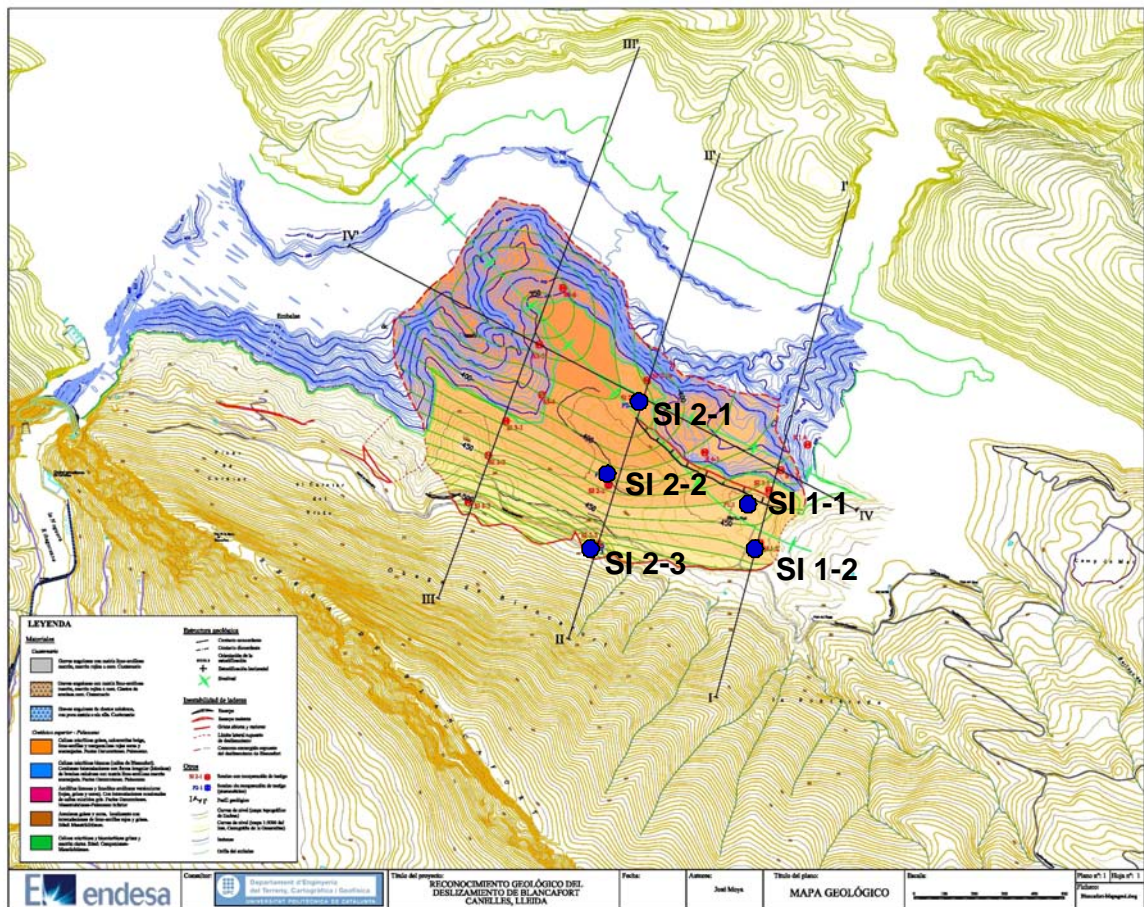


Figure 7.11 Position of piezometers installed after the failure.

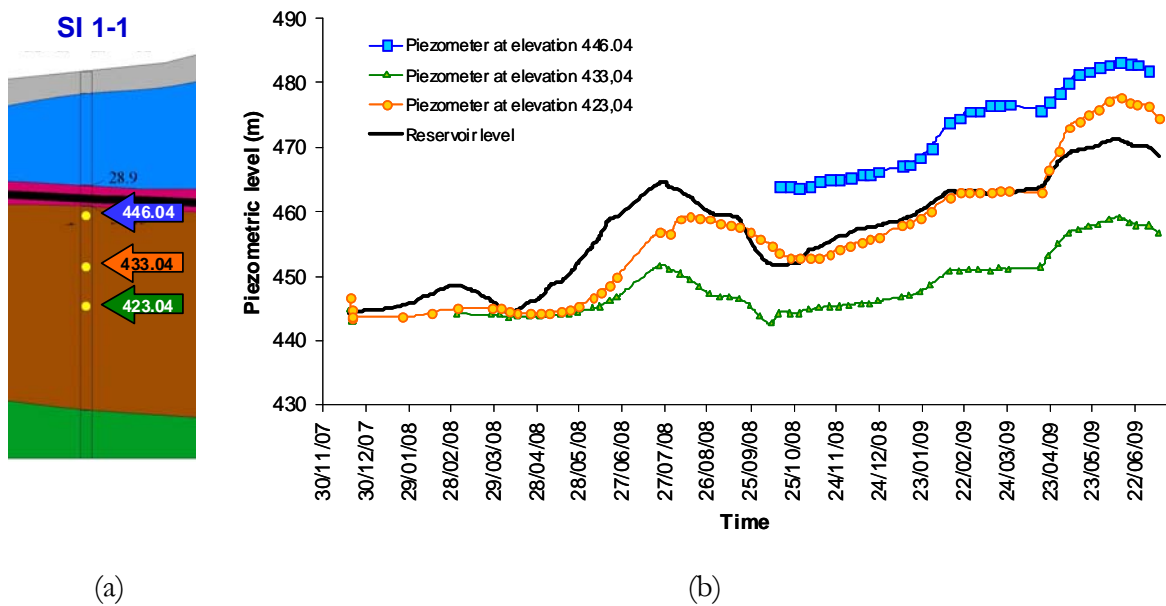


Figure 7.12 (a) Position of piezometers in borehole SI 1-1 (see Fig. 7.11); (b) piezometer records and reservoir elevation.

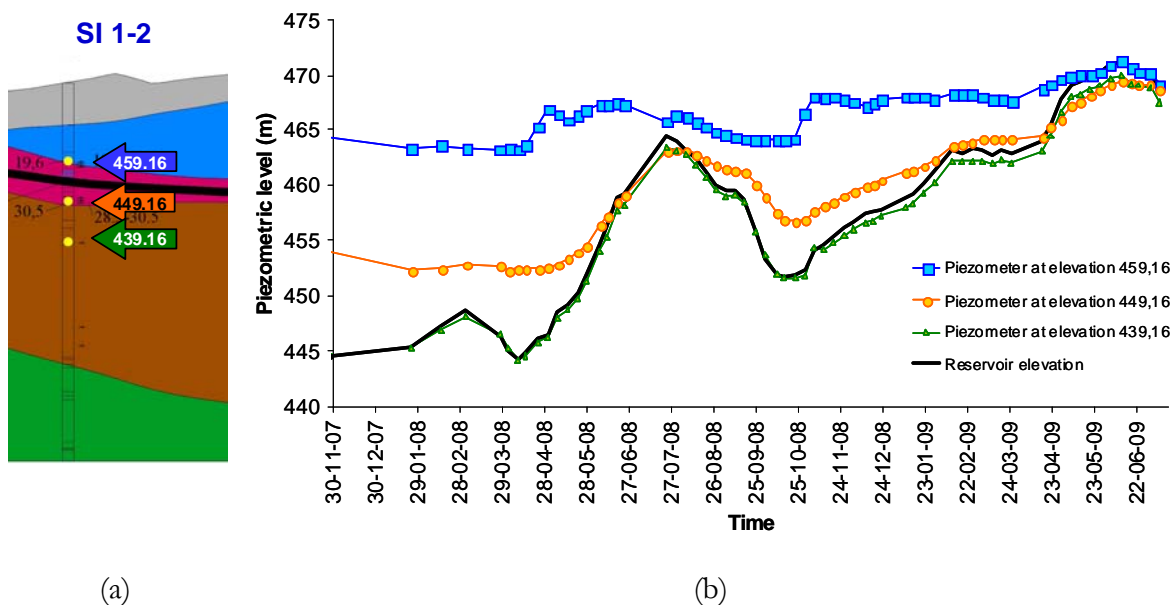


Figure 7.13 (a) Position of piezometers in borehole SI 1-2 (see Fig. 7.11); (b) piezometer records and reservoir elevation

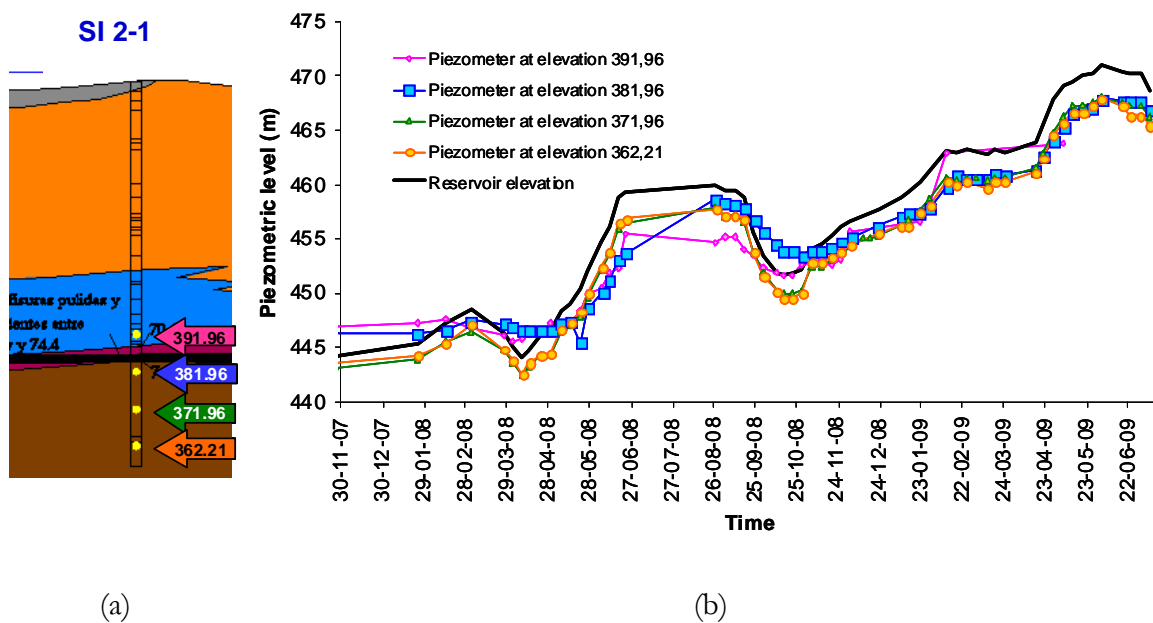
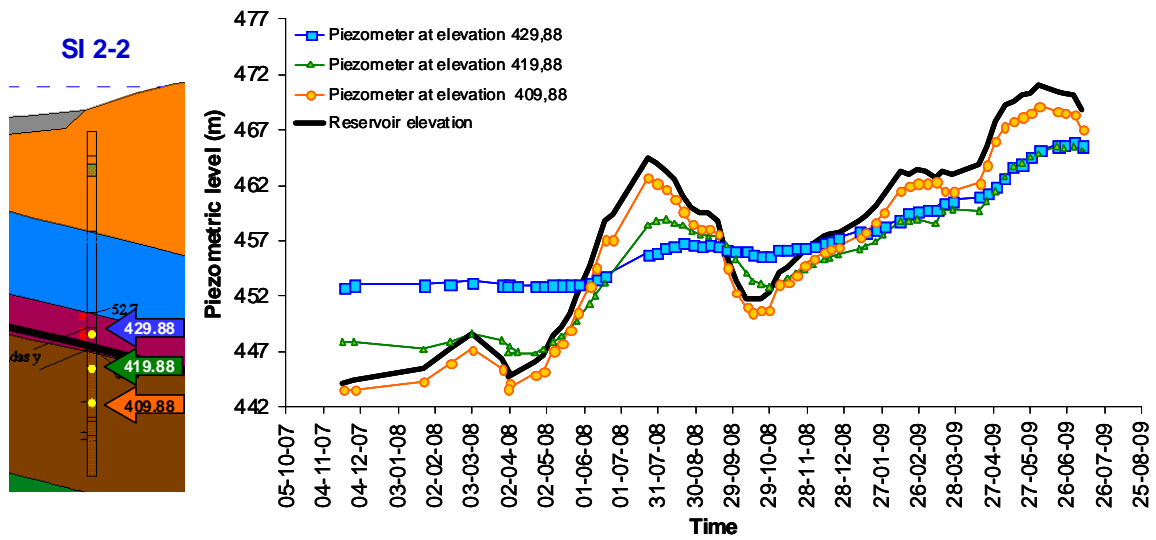
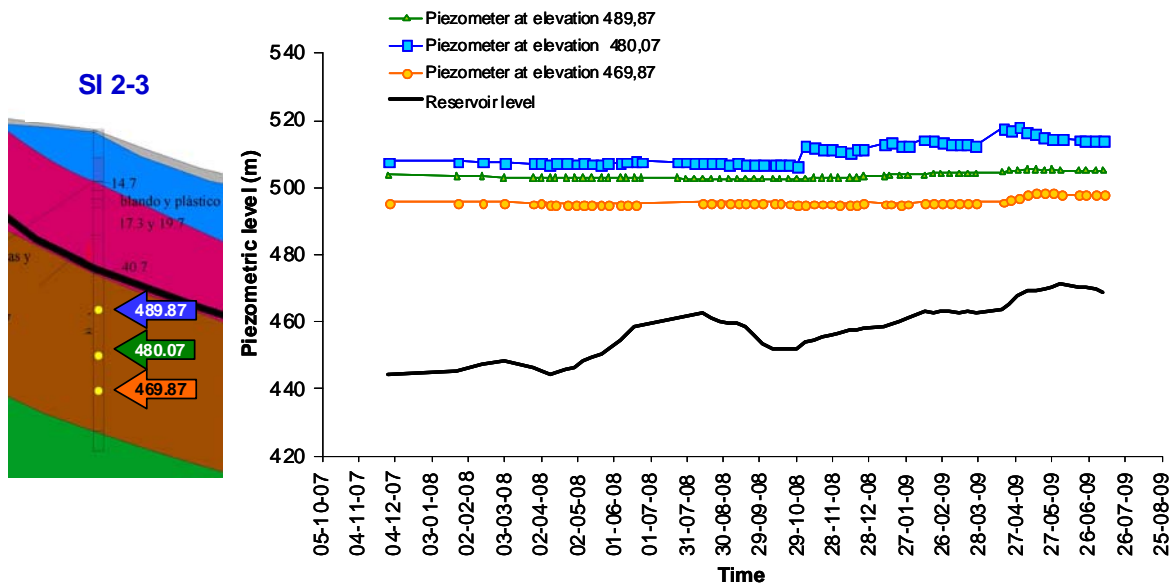


Figure 7.14 (a) Position of piezometers in borehole SI 2-1 (see Fig. 7.11); (b) piezometer records and reservoir elevation



(a) (b)
 Figure 7.15 (a) Position of piezometers in borehole SI 2-2 (See Fig. 7.11); (b) piezometer records and reservoir elevation



(a) (b)
 Figure 7.16 (a) Position of piezometers in borehole SI 2-3 (See Fig. 7.11); (b) piezometer records and reservoir elevation

As a summary, the examination of piezometer measurements leads to the following conclusions:

- The hydraulic behaviour of the Garumn clay stratum seems to be independent from the lower sandstone stratum.

- The pressures in the sandstone stratum, except for the upper part of the slide, follows immediately the water level elevation in the reservoir. This behaviour is an indication of the high permeability of the sandstone.
- Pressures remain essentially constant in the clay and independent from water level elevation mainly during the first seven months of measurements when reservoir elevation was lower than 460 m. This is an indication of the difficulty to dissipate or increase water pressures within clayey layers where the sliding surface is located. It also points out the low “in situ” permeability of this clay level.

7.4 PORE WATER PRESSURE CALCULATION

The characterisation of the slide, the laboratory tests performed and piezometric measurements seem to indicate that the cause of the sliding was the high water pressures that remained within the low permeability clayey stratum, together with the absence of the stabilising effect of reservoir water due to the drawdown. Rapid drawdown is a complex problem which integrates unloading of the reservoir’s water weight, soil deformation and water flow under saturated/unsaturated conditions. It has been discussed in Chapter 2.

The analysis presented here was carried out by means of the finite element code Code_Bright, which can solve coupled flow/deformation problems in saturated/unsaturated media.

The calculation model is shown in Figure 7.18. The figure also shows a linear quadrilateral element mesh. Nodes have three degrees of freedom (water pressure and vertical and horizontal displacement). The mesh had to be refined mainly in the thinner clay stratum to ensure the correct calculation of water flow through materials in direct contact having values of permeability widely different among them. In order to simplify the model, the sequence of detailed stratification above the Garum clay level has not been specified in detail. The mobilised rock above the clay mainly consists of sandstone levels.

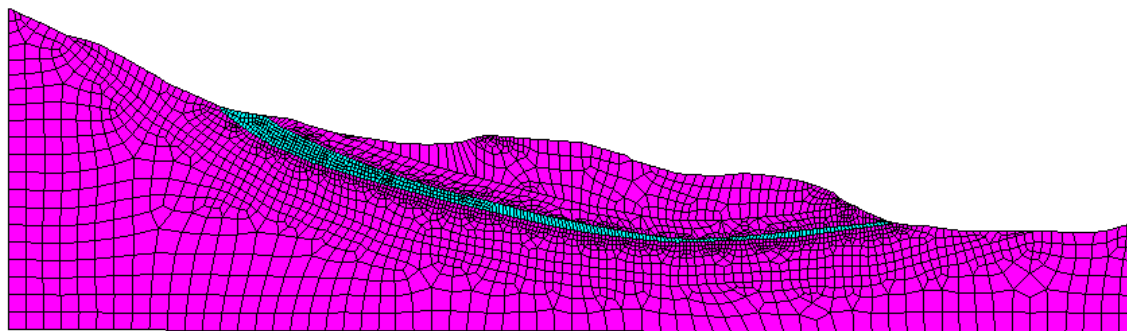


Figure 7.18 Finite element calculation model.

Table 7.1 Parameters for coupled hydro-mechanical calculations

Parameter and unit	Clay	Rock
Young modulus (MPa)	500	2500
Poisson's coefficient	0.3	0.3
Saturated permeability (m/s)	$4.9 \cdot 10^{-11}$	10^{-5}
Van Genuchten parameters:		
P_0	0.3	0.03
λ	0.33	0.33
$S_{r\ max}$	1	1
$S_{r\ max}$	0	0

The stress-strain behaviour of the materials was characterised by means of a linear elastic law defined by Young's modulus and Poisson's ratio. Elasto-plastic considerations have limited effect when estimating drawdown-induced pore water pressure. This result was discussed in Chapter 2 and it is explained because the drawdown mainly results in an elastic stress path. In addition, the involved materials are highly overconsolidated rocks. Thus the elasticity hypothesis seems sufficient in this case. Table 7.1 shows the elastic values chosen, as well as the saturated permeability. Clay parameters were derived from laboratory tests, while rock parameters were estimated according to typical values due of lack of precise data.

The analysis requires the characterisation of materials under unsaturated conditions. The retention curves introduced in the calculations use the Van Genuchten model having the parameters indicated in Table 7.1 and plotted in Figure 7.19. Relative permeability is defined according to the cubic law ($k = k_{sat} k_{rel} = k_{sat} S_r^3$ where k_{sat} is the saturated permeability and S_r is the degree of saturation) for both materials.

The known history of water level elevation, was modelled during the four years prior to the drawdown that probably caused the failure (October, 2002 until July, 2009) (Fig. 7.20). This allows establishing the pressures acting on the failure surface with the purpose of analyzing the stability at any time. In addition, the measurements taken in the piezometers installed in November 2007 could be compared with calculations in an effort to validate the numerical model. The initial pore water pressure assumed in the calculation is a horizontal hydrostatic profile.

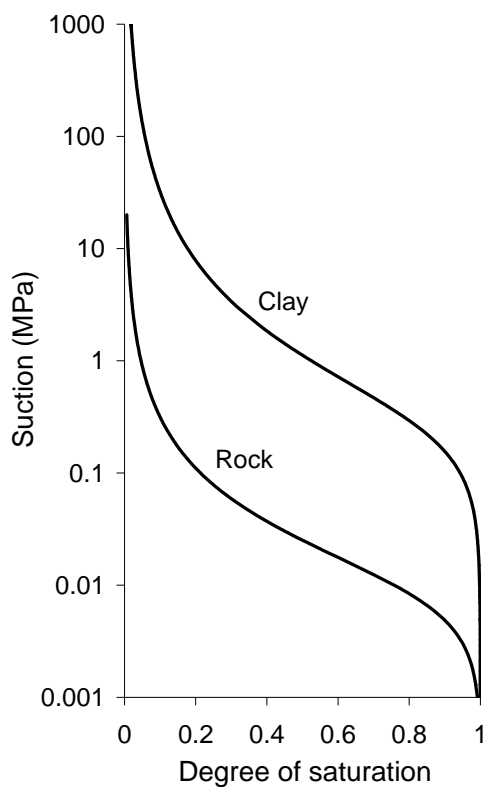


Figure 7.19 Retention curves used in calculation.

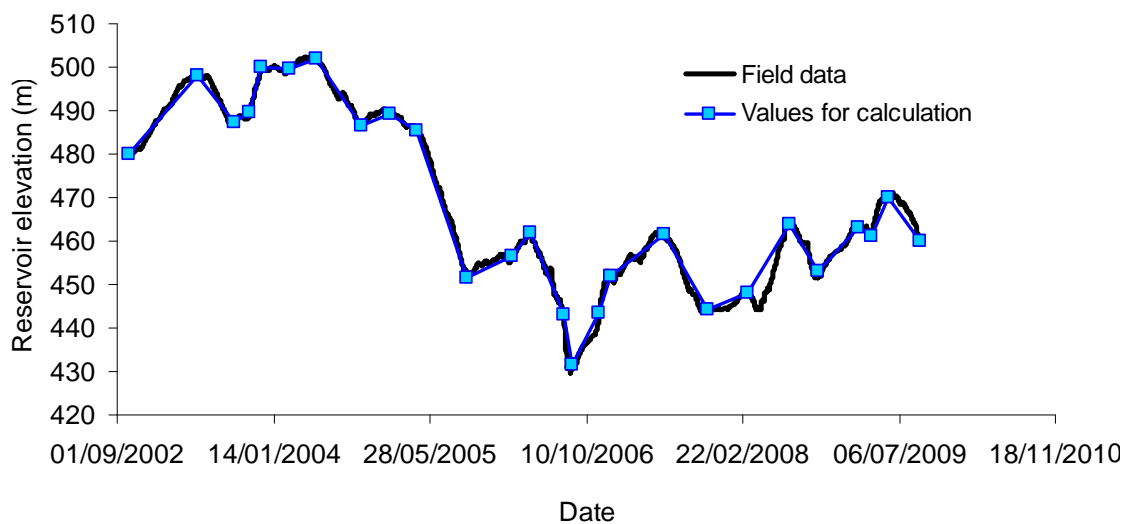


Figure 7.20 Time variation of reservoir level.

The effect of rainfall has been incorporated in the simulation in order to model the water inflow through the upper part of the slope, which is approximately equal to the average value of the rainfall recorded in the region (400 l/m²/year).

Figures 7.21 and 7.22 show the water pressure contours calculated for the 26th September, 2005 and 21st August, 2006, when water elevation of the reservoir reached elevations 451 and 431 m. This last elevation corresponds to the minimum values reached in the period 1986 – August 2006. The effect of the low permeability of the clay layer and its continuity can be observed by the abrupt change of the contours. This can be clearly observed in Figure 7.22 that shows the calculated pore water pressure along a vertical profile located in the position of SI 2-2.

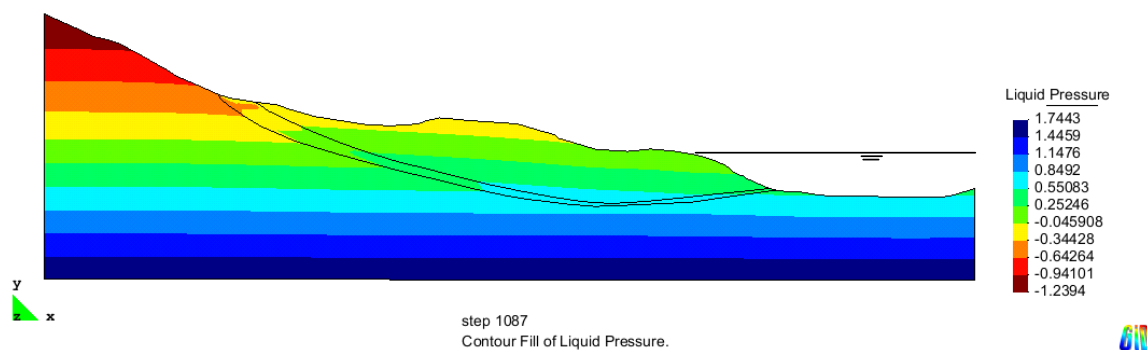


Figure 7.21 Calculated pore water pressure distribution on September 26, 2005 when reservoir elevation was at 451 m (see Fig. 7.20).

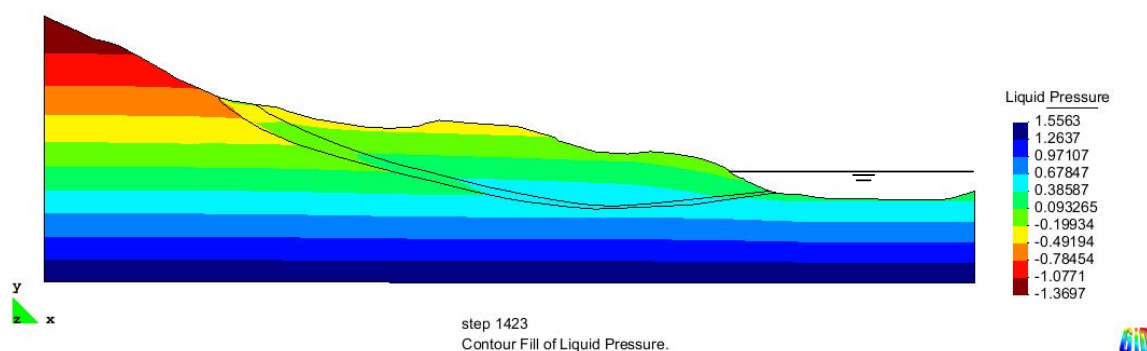


Figure 7.22 Calculated pore water pressure distribution on August 21, 2006 when reservoir elevation was at 431 m (see Fig. 7.20).

The pore water pressure distribution given in Figures 7.21 and 7.22 has been introduced in the calculation of the safety factors, by means of a limit equilibrium procedure to analyse the stability in the most critical situations previous to the failure.

However, before the analysis the failure is presented, the calculated pore water pressure will be compared with piezometer measurement recorded after the failure in order to check the reliability of results. Figures 7.24 to 7.26 show such a comparison for the piezometers installed in Profile II (see their position in Figs. 7.4, 7.6 and 7.14a – 7.16a).

Pore water pressure measured within the lower sandstone in SI 2-1 and SI 2-2, which follow precisely the reservoir elevation evolution, are well captured by the

calculation. This is a consequence of a correct choice for sandstone permeability. Pressure measurements within the impervious clayey layer in SI 2-2, which are especially important for the subsequent calculation of safety factor, have been simulated quite satisfactorily. Pressures are lightly overestimated when the reservoir reaches low levels.

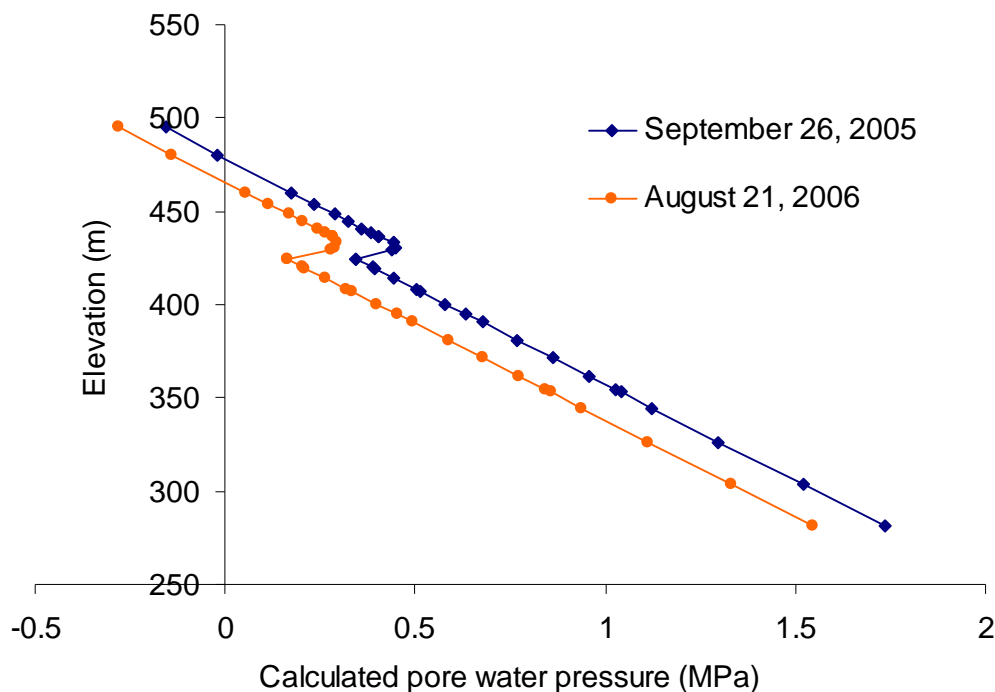
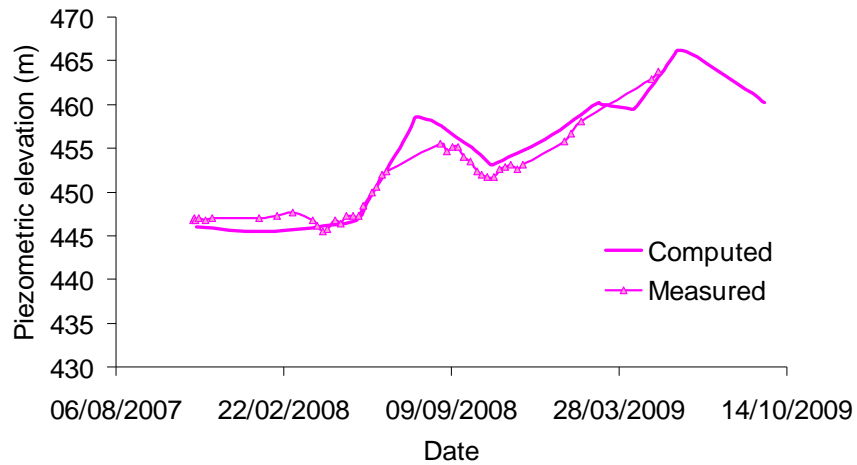
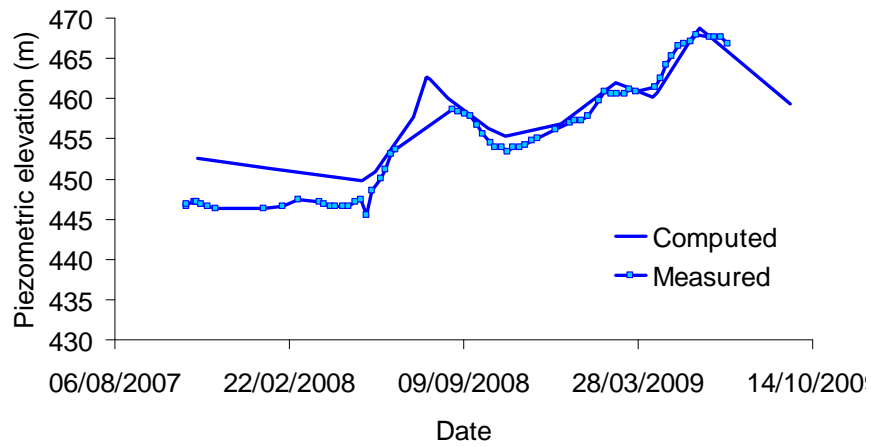


Figure 7.23 Calculated pore water pressure distribution along vertical profile located at the position of SI1-2 (see Fig. 7.6) on September 26, 2005 and August 21, 2006 when reservoir elevation was at 451 and 431 m, respectively (see Fig. 7.20).

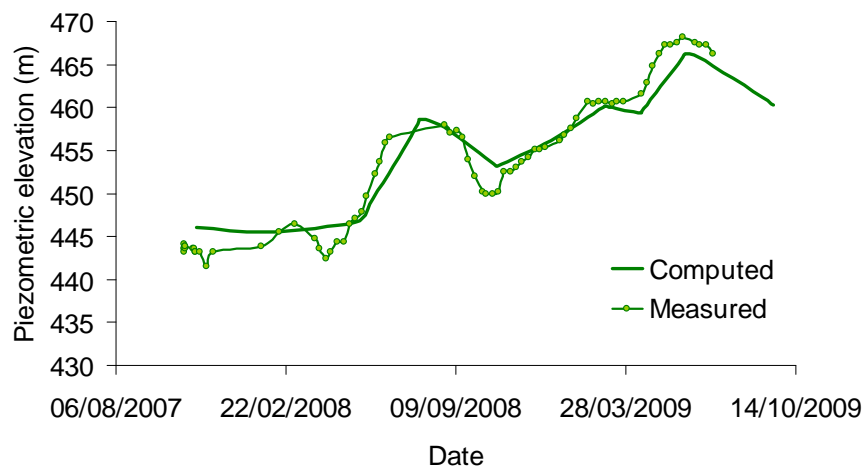
The major discrepancy appears in piezometers installed in SI 2-3. Reservoir level was always below the elevation of piezometers located in SI 1-3. In addition, the high sandstone permeability allows a rapid flow of rainfall infiltration towards the reservoir level. As a result, no positive pore pressures above the piezometer positions are calculated. Field measurements show a totally different response. In fact, water columns in excess of 15–25 m over the piezometers location are measured. This is probably a consequence of the external infiltration and a different local geological structure of pervious/impervious materials at the head of the slide. In subsequent stability calculations, this field information will also be considered.



(a)

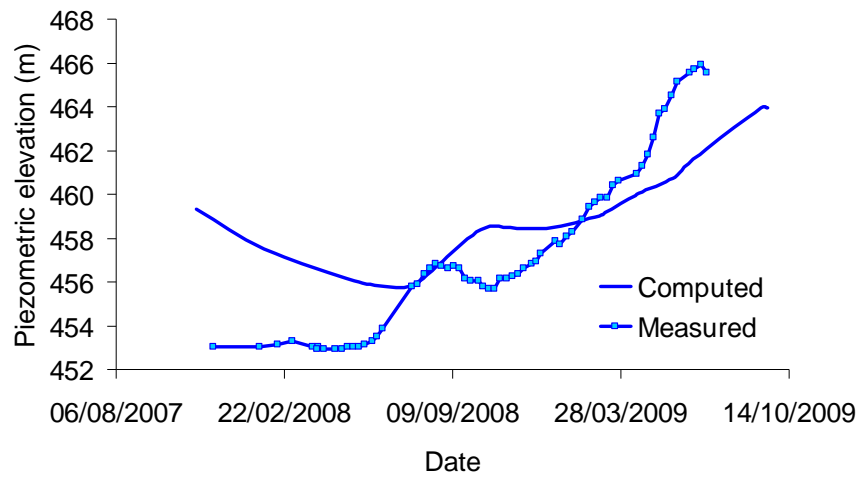


(b)

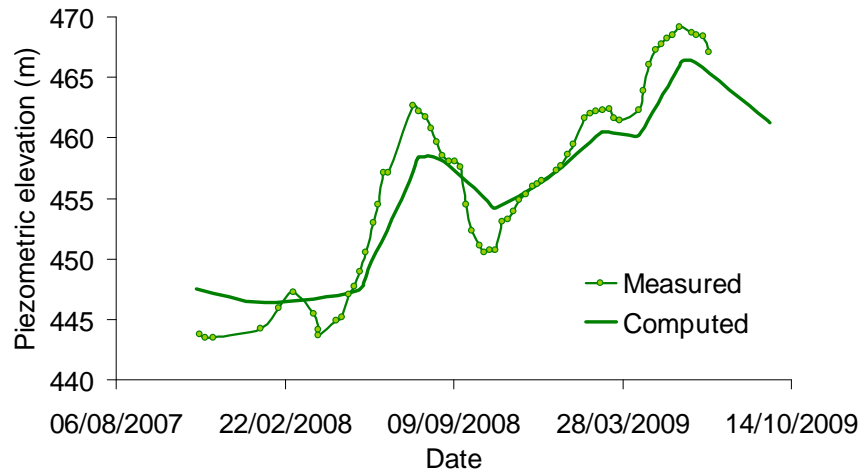


(c)

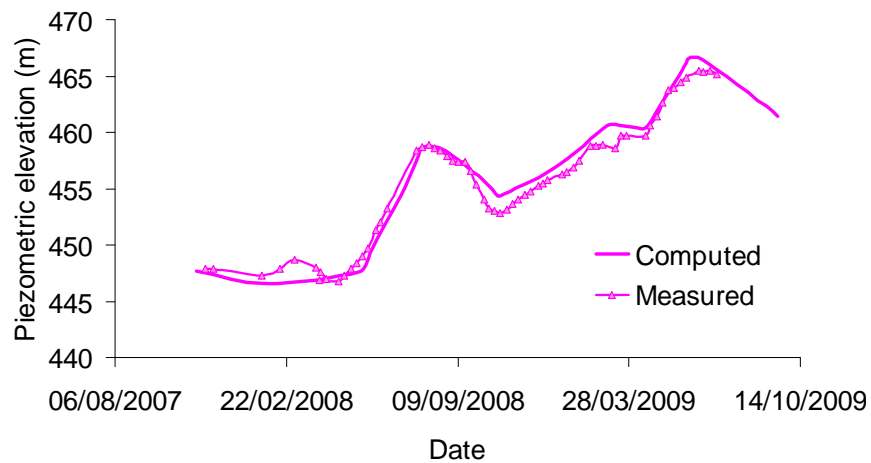
Figure 7.24 Comparison of calculated and measured pore water pressure in piezometers located in boring SI 2-1 at elevation (a) 391.96 m; (b) 381.96 m; (c) 371.96 m.



(a)

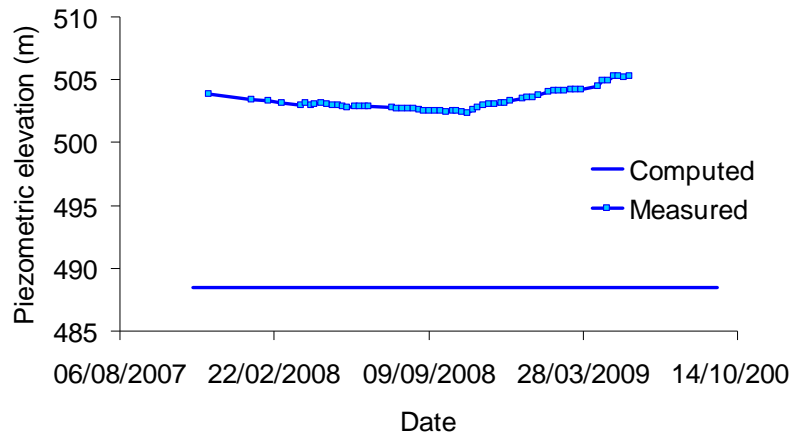


(b)

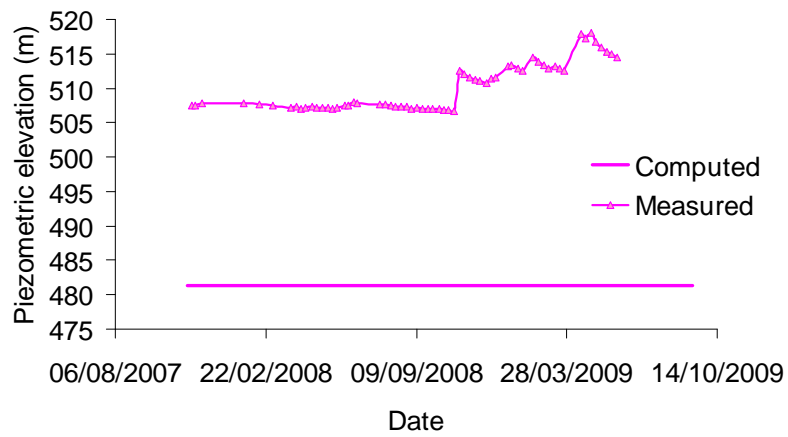


(c)

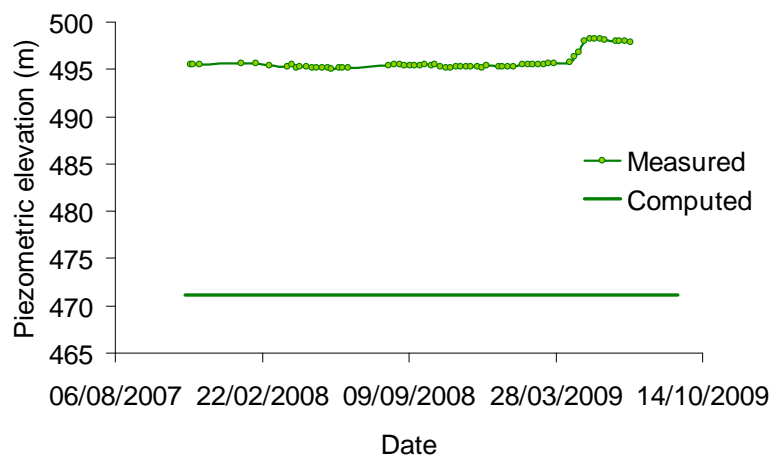
Figure 7.25 Comparison of calculated and measured pore water pressure in piezometers located in boring SI 2-2 at elevation (a) 429.88 m; (b) 419.88 m; (c) 409.88 m.



(a)



(b)



(c)

Figure 7.26 Comparison of calculated and measured pore water pressure in piezometers located in boring SI 2-3 at elevation (a) 489.87 m; (b) 480.07 m; (c) 469.87 m.

7.5 SAFETY FACTOR CALCULATION

The failure surface seems to be located entirely in the Garumn clay stratum. Therefore, the analysis of limit equilibrium only requires the definition of the soil densities above the failure surface, the strength properties of clay and the pore water pressure acting on the failure surface. The density of the mobilized mass has been estimated equal to 21 kN/m³.

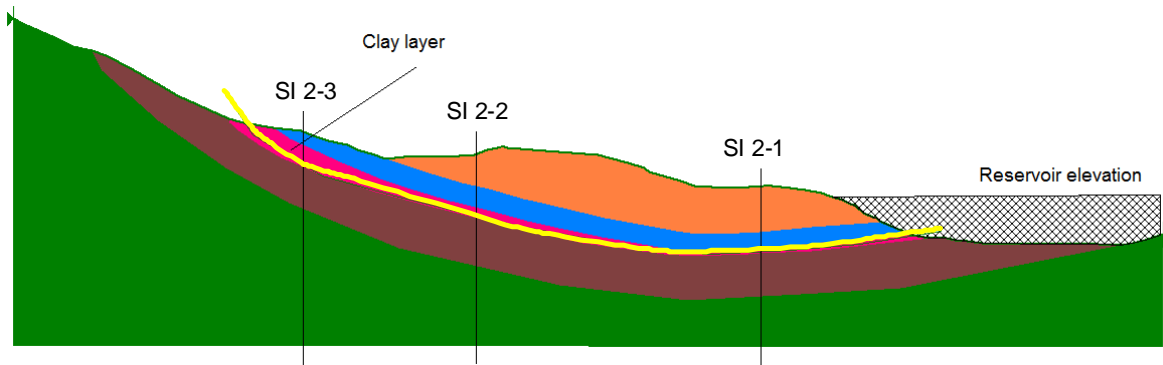


Figure 7.27 Calculation section for limit equilibrium analysis and pre-established failure surface in yellow.

The strength available on the failure surface was defined by a Mohr-Coulomb law. Since the slide is the reactivation of an ancient slide, the residual angle and a null effective cohesion should be used. The ring shear tests carried out in the laboratory indicate a residual angle of 12° under vertical effective stresses ranging from 100 to 250 kPa. Nevertheless, the vertical effective stresses on the failure surface range from 100 to 1500 kPa (some 800 kPa in average). Generally, the friction angle decreases with effective normal stress. On the other hand, during the geological history of the slide the failure surface probably underwent larger than current stresses. Later, once unloaded until reaching the current initial situation, the remaining friction angle would correspond to the lowest value in the past. This hypothesis would lead to a friction angle lower than the value measured in the laboratory (12°) and most likely close to 10° (Stark and Eid, 1994; Alonso, 2005). Both values will be considered in calculation.

The water pressures obtained by these calculations were introduced in the calculation of safety factor by limit equilibrium with the program GeoSlope. The model used is shown in Figure 7.27. The failure surface has been predefined following the geological interpretation. It is entirely located within the clay layer. Pore water pressure on the failure surface is imposed following the results obtained previously in the coupled analysis (results given in Figs. 7.21 and 7.22). The increase in strength due to suction was neglected in the unsaturated area.

The two critical drawdown events (September, 2005 and August, 2006) have been analysed. The safety factors obtained are indicated in Table 7.2 for two clay friction angles, 10° and 12°. The values obtained for $\phi' = 10^\circ$ are very close to 1. Both

drawdown situations were quite critical. However, the calculated safety factors are higher than 1 in both cases. Several factors can explain this discrepancy. It is uncertain if the analysed section is the most critical one. On the other hand, piezometers measurements indicate higher pore water pressure values in the upper part of the landslide. They were not introduced in the analysis reported in Table 7.2. If these measured values are introduced in the limit equilibrium analysis, maintaining the remaining values obtained in the calculation of pore water pressure, a safety factor equal to 1.01 is obtained for the situation in August.

Table 7.2 Safety factors calculated by limit equilibrium analysis

	September 26 th , 2005. Reservoir elevation: 451 m	August 21 st , 2006. Reservoir elevation: 431 m
$\phi' = 12^\circ$	1.25	1.31
$\phi' = 10^\circ$	1.04	1.09

7.6 ANALYSIS OF RAPID SLIDING

An additional risk is the possibility of rapid sliding which will result in the impact of the sliding mass against the reservoir water and the subsequent generation of uncontrolled destructive waves. A clear reference is the Vaiont slide in northern Italy in 1963 (Chapter 5). Other cases have been described in the Introduction.

The phenomena that may lead to this rapid acceleration were discussed in Chapter 3. The coupled thermo-hydro-mechanical problem has been solved in a representative cross section of Canelles landslide consisting of two blocks. The failure surface was simplified by means of two planes: one under the upper block, which dips 18° , and another one under the lower block, next to the reservoir, which is horizontal (Fig. 7.28). This geometry allows taking into consideration that as the slide progresses towards the reservoir, the deformed mass becomes, in principle, more stable. In fact, during sliding, the soil mass increases in the more stable lower block and decreases in the unstable upper block.

The analysis requires some thermo-hydro-mechanical properties of the clay stratum, where the failure surface is located. Table 7.3 provides the calculation parameters. The values selected for water and solid particles correspond to well-accepted values found in handbooks of physico-chemical constants. The specific properties of the shearing band material (Garumn clay) were defined previously. The coefficient of compressibility was calculated through the Young modulus used previously (500 MPa) and $\nu = 0.3$.

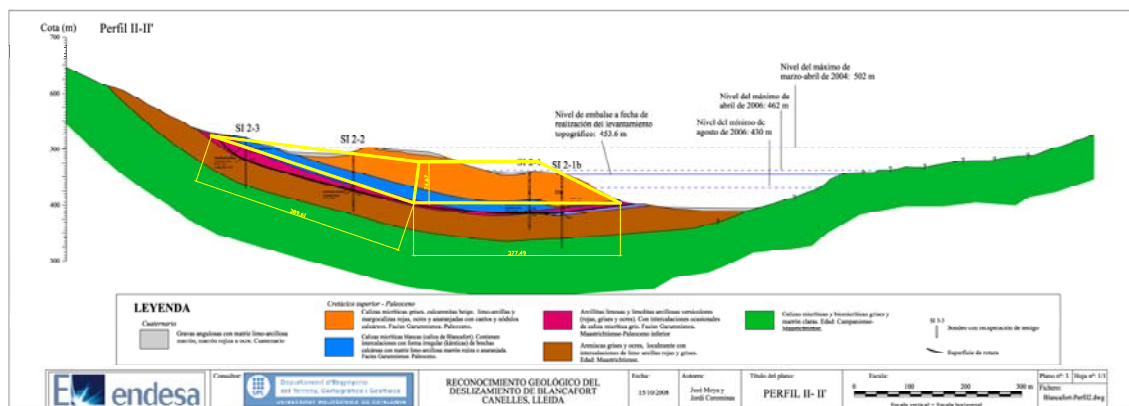


Figure 7.28 Calculation section considered for the thermo-hydro-mechanical analysis.

Table 7.3 Properties of the materials.

Parameters	Symbol	Value	Unit
Water			
Density	ρ_w	1000	kg/m ³
Compressibility coefficient	α_w	$5 \cdot 10^{-10}$	
Thermal expansion coefficient	β_w	$3.42 \cdot 10^{-4}$	
Specific heat	c_w	$4.186 \cdot 10^3$ 1.0	J/kg · °C kg · °C
Solid particles			
Density	ρ_s	2700	
Thermal expansion coefficient	β_s	$3 \cdot 10^{-5}$	
Specific heat	c_s	$8.372 \cdot 10^2$ 0.20	cal/ kg · °C
Material of the shearing band			
Porosity	n	0.2	-
Permeability	k	$4.9 \cdot 10^{-11}$	m/s
Compressibility coefficient	m_v	$2.1 \cdot 10^{-9}$	1/Pa
Friction angle (residual)	ϕ'	10	
Slid material			
Density	ρ_r	2200	kg/m ³

It is difficult to estimate accurately the thickness of the shearing band, even if recovered samples are examined. In general, the thickness of the shearing band is related to the size of the soil particles. In this case, the failure is located in a clayey soil with $D_{50} = 0.01$ mm (aperture diameter of the mesh through which 50 % of the material passes). For this value, a thickness of 5 mm is estimated for the shearing band.

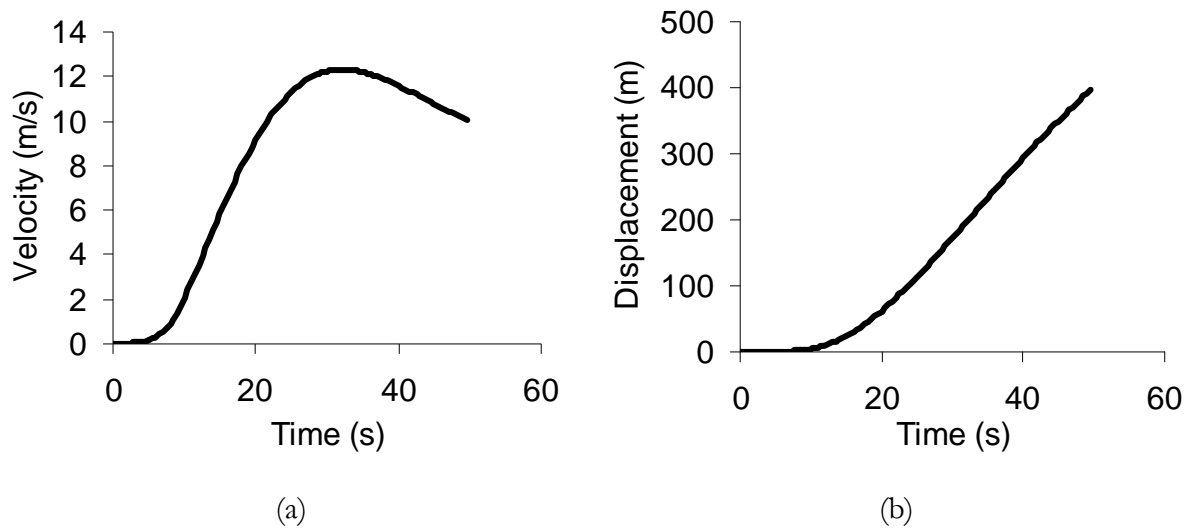


Figure 7.29 Calculated evolution of sliding velocity and displacement considering the thermo-hydro-mechanical effects.

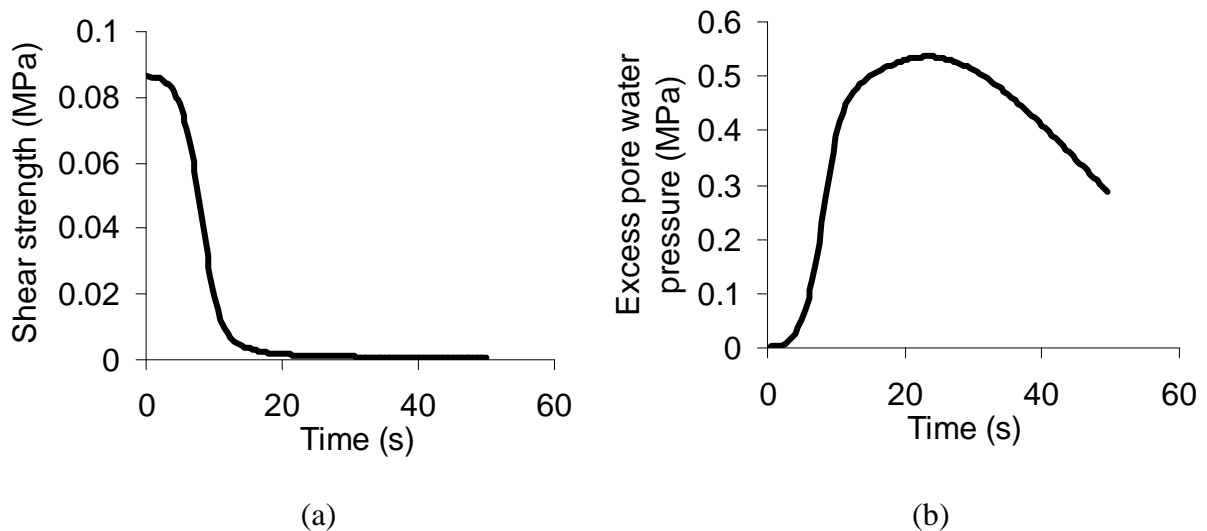


Figure 7.30 Evolution of (a) the frictional effective strength and (b) water pressure in the failure surface under the lower block.

The initial position of the slide considered for calculations corresponds to a water level elevation 470 m. For the dynamic analysis performed the water pressures on the failure surface are calculated under the simple hypothesis of hydrostatic distribution.

The effect of water weight on stresses on the slope is also taken into account. Under these conditions, according to limit equilibrium calculations, Canelles slope was strictly stable and instability takes place whenever higher pressures develop in the clay stratum. The initiation of the movement (safety factor lightly higher than 1) was simulated by setting a pressure increase of 0.09 MPa throughout the failure surface of the lower block.

Figure 7.29 plots the evolution of velocity in time during a displacement of 200 m. According to calculations, the slide would accelerate, reaching 12 m/s in a few seconds, after travelling some 300 m inside the reservoir. At the beginning, the sliding velocity remains low, close to a few millimeters per second. During the first seconds, the excess pore pressure accumulated in the shear band is not enough to significantly reduce the effective frictional strength.

Figure 7.30 shows the evolution of strength and the excess in water pressure during the same period of time. When pore pressure in the shear band increases (up to 0.5 MPa), shearing strength decreases and drops to values close to 0. This explains the high velocities reached by the slide.

If the effects of heat are neglected, the maximum velocity reached by the slide becomes significantly lower (12 cm/s). The velocity at $t = 40$ s is null, after travelling 3 m towards the dam.

7.7 CONCLUSIONS

This chapter presents the static and dynamic analysis of a 40 millions m^3 slide which was reactivated as a result of a sharp decrease of the water level in Canelles reservoir. A methodology to analyze the landslide, based on field work, laboratory testing and “in situ” measurements, is described. The model was based on a representative 2D central cross-section, on the shape and position of the failure surface, and on the changes in water level elevations during the 4 years prior to the development of the crack.

The intensity and distribution of pore pressures on the failure surface is critical to explain the initial failure.

The studies carried out demonstrate that the failure surface of the slide lies within the high plasticity clay stratum, which has a low permeability ($5 \cdot 10^{-11}$ m/s). According to previous work, this permeability value indicates that the slide can accelerate and reach high velocities in case of instability. The potential acceleration of the slide is analysed with the help of the theory discussed and developed in Chapter 3 and the program developed in Chapter 6. A calculation geometry based on the profile studied (Profile II) was defined by means of blocks of variable geometry (a triangular upper block and a trapezoid lower one).

Due to the low permeability of clay strata, where the failure surface is located, Canelles slide is potentially rapid. The slide is estimated to accelerate reaching a velocity equal to 12 m/s in 300 m of displacement.

One of the main limitations of this work, and, in particular, in the model applied to Canelles slide, is the difficulty to interpret, by means of the calculation model, slow slope movements prior to the accelerated and catastrophic movement. The fact that the slope did not accelerate during the August 2006 slide, does not necessary imply that it will not become potentially fast. This is also one of the lessons derived from Vaiont slide.

CHAPTER 8

Conclusions and Future Research

This Thesis deals with a particular class of fast landslides: those which slide on a well-defined shearing surface and, at the same time, do not experience a major degradation of the moving mass. In addition, the work has concentrated in a triggering action associate with the impoundment of the slope toe or rapid drawdown, a situation which is common in reservoirs and, to a less extent, in river valleys and fjords.

The review made in the introductory Chapter 1 reveals that the number of case histories described in the literature is quite limited. This is an important drawback to validated theories and models and indicates that well documented case studies is probably the first requirement for the advancement of knowledge. Ideally, a good case history should combine a comprehensive field information and laboratory testing program paying special attention to the geometry, mineralogy and shearing behaviour of the sliding surface material and knowledge of the past history of the slide. Unfortunately, these conditions are rarely met and even the well known reference of Vaiont landslide suffers from insufficiently known data for a proper understanding of the phenomenon.

The mechanisms of rapid drawdown are currently well understood. The available coupled flow and deformation models are a powerful tool to investigate the slope response against fast changes in water level. In practice, the combination of a fully coupled code and a procedure to determine the current safety factor would be of interest. Again, well documented case histories are not easily available and further

validation of existing models against real cases would improve our confidence in available tools.

The discussion on the basic phenomena leading to the fast acceleration of a landslide is today very active and far from achieving a consensus. In this work, the relevance of thermal effects on the sliding surface and its role to increase fast the local pore water pressure has been favoured as a rational mechanism to explain the slide acceleration. Other mechanisms leading to a loss of shear strength are the strain softening and the rate effects. Unfortunately, some available experiments to demonstrate the strain rate effects could also be interpreted a thermal-induced mechanism. Strain rate effects lack form a fundamental physical explanation. The framework behind thermal effects is perhaps better organized but in both cases there is a need for a more complete set of basic experiments at laboratory scale. A major difficulty is that the shearing strain rates achieved in reality are difficult to match in the laboratory. In addition, a proper understanding would require information on temperatures and water pressure being developed in a band where shearing strains localize. Testing shearing effects at a rate matching field conditions is still an important challenge for future experimental work.

The models developed may be also extended and developed further for a more comprehensive and precise analysis. The following improvements are mentioned:

- *Generalization of the landslide geometry.* A relatively straightforward step would be to adjust the geometrical description of slides typical of limit equilibrium models (slide described by interacting finite blocks) to a kinematically acceptable mechanism. Then, thermal effects should be introduced at any shearing surface. SPH meshless model (Augarde and Heaney, 2009; Pastor *et al.*, 2009) offer an interesting possibility to handle the problem. As well as, the developments of mixed finite element-particle method such as the Material Point Method (Sulsky and Schreyerb, 1996; Zabala and Alonso, 2010) offer an interesting potential.
- *Improved consideration of the effect of temperature on soil constitutive behaviour.* In this Thesis, the role of skeleton reaction to temperature changes was formulated in a simple manner through a simple coefficient. It was further argued that thermal effects on the skeleton reaction in the case of heavily overconsolidated and indurated clayey rocks (typically found in practice) was quite limited especially for moderate changes in temperature. In fact, the simulation of Vaiont does not require the consideration of thermal effect on the skeleton performance to achieve acceptable results.

But there is certainly a way to improve models by introducing generalized constitutive models of thermal behaviour. They would typically require a thermo-plastic formulation. Thermo-elastic constitutive models for soils have

been reported by: Hueckel and Borsetto, 1990; Hueckel *et al* (1998), Cui *et al.* (2000), Laloui (2001).

Available experimental data typically concentrate in temperatures within the range 20-90°, which may be insufficient for real cases involving very large landslide. In fact, some of the calculations reported indicate that, a under specific combination of shear band thickness, permeability and stiffness, temperatures may increase to vey high values (hundreds of degrees). Then fundamental changes in the mineralogical constituents of the clay shear band and its shearing behaviour is to be expected. This is also an open field for future research work.

The question of water vaporization when temperature increase beyond 100°C deserves also attention. The simple experiment reported in the Chapter 3 of this Thesis heating Opalinus clay indicates that available phase diagrams for “free” water are of very limited use in the case of water adsorbed in clay minerals. It is felt that more experimental information on the behaviour of clays under (high) temperature is needed before appropriate models are formulated.

- *Accurate representation of some nonlinearities of dependent variables.* The models would benefit also from a more accurate representation of some nonlinearities which have been simplified to linear relationships. This is the case of the thermal expansion coefficient of water (β_w) and solids (β_s), which depend on temperature. Date on the dependence β_w on temperature is available and could be introduced at a limited computational effort.

REFERENCES

- Akai , K., Ohnishi, Y., Murakami, T. and Horita. M. (1979) Coupled stress flow analysis in saturated/unsaturated medium by finite element method. *Proc. 3rd Int. Conf. Num. Meth. Geomech.* 1, 241-249.
- Alcantara-Ayala, I., Dominguez-Morales, L. (2008) The San Juan de Grijalva catastrophic landslide, Chiapas, Mexico: lessons learnt. *Web Proceedings of the First World Landslide Forum*. International Consortium on Landslides. United Nations International Strategy for Disaster Reductions. Nicola Casagli, Riccardo Fanti, Veronica Tofani (eds.). Tokyo, Japan, 96-99.
- Alonso, E., Gens, A. and Josa, A. (1990) A constitutive model for partially saturated soil. *Géotechnique* 40 (3), 405-430.
- Alonso, E.E (2005) Parámetros de Resistencia en cálculos de estabilidad. *VI Simposio Nacional sobre Taludes y Laderas Inestables*. Valencia, 21 – 24 June 2005. Alonso, E., Corominas, J., Jordà, L., Romana, M. and Serón, J.B. (eds.), 1131-1195.
- Alonso, E.E, Gens, A, Lloret, A. (1993) The landslide of Cortes de Pallas, Spain. *Géotechnique* 43 (4), 507-521.
- Alonso, E.E. (2000) Cuttings and natural slopes. General report. *The Geotechnics of Hard Soils-Soft Rocks*. Evangelista and Picarelli (eds.). Balkema, Rotterdam.
- Alonso, E.E. and Gens, A. (2006) Aznalcóllar dam failure. Part I: Field observations and material properties. *Géotechnique* 56 (3) 165-183

- Alonso, E.E. and Romero, E (2003) Collapse behaviour of sand. *Proceedings of the 2nd Asian Conference on Unsaturated Soils*. Osaka. 325-334.
- Alonso, E.E., Olivella, S. and Pinyol, N.M. (2005) A review of Beliche Dam. *Géotechnique*, 55 (4), 267-285.
- Andrews, D.J. (2002) A fault constitutive relation account for thermal pressurization of pore fluid. *J. Geophys. Res.* 107 (B12), 2363.
- Atkinson, J.H. and Richardson, D. (1987) The effect of local drainage in shear zones on the undrained strength of overconsolidated clay. *Géotechnique* 37, 393-403.
- Baker, R, Rydman, S. and Talesnick, M (1993) Slope stability analysis for undrained loading conditions. *Int. Jnl. Num. and Anal. Methods Geomech.* 17, 14-43.
- Baldi, G., Hueckel, T. and Pellegrini, R. (1988) thermal volume changes of mineral water system in low porosity clay. *Canadian Geotechnical Journal* 25 (4), 807-825.
- Barton, N. (2007) *Rock Quality, Seismic Velocity, Attenuation and Anisotropy*. Taylor and Francis. London.
- Barton, N. and Choubey, V. (1977) The shear strength of rock joints in theory and practice. *Rock Mechanics* 10, 1-54.
- Belloni, L.G. and Stefani, R. (1987) The Vajont slide: Instrumentation-Past experience and the modern approach. *Engineering Geology* 24, 445-474.
- Berilgen, M. (2007) Investigation of stability of slopes under drawdown conditions. *Computer and Geotechnics* 34, 81-91.
- Biscarini, C. (2010) Computational fluid dynamic modelling of landslide generated water waves. *Landslides* 7, 117-124.
- Bishop, A.W. (1954) The use of pore pressure coefficients in practice. *Géotechnique* 4 (4), 148-152.
- Bishop, A.W. (1967) Progressive failure – with special reference to the mechanism causing it. *Proc. Geotech. Conf. Oslo*, 2, 142-150.
- Bishop, A.W. (1971) The influence of progressive failure on the choice of the method of stability analysis. *Géotechnique* 21, 168-172.
- Bjerrum, L. (1967) Progressive failure in slopes of overconsolidated plastic clays and clay shales. *Journal Soil Mech. Found. Div. ASCE* 93, 3-49.
- Bock, K. (2001) Rock Mechanics Analyses and Synthesis: RA Experiment. Rock Mechanics Analyses and Synthesis: Data Report on Rock Mechanics. *Mont Terri Technical Report 2000-02*. Q+S Consult

- Bossart, P., Meier, P.M., Moeri, A., Trick, T. and Mayor, J.C. (2002) Geological and hydraulic characterisation of the excavation disturbed zone in the Opalinus Clay of the Mont Terri Rock Laboratory. *Engineering Geology* 66 (1-2), 19-38.
- Bracegirdle, A., Vaughan, P. and Hight, D. (1991) Displacement prediction using rate effects on residual shear strength. *Proc. 6th Int. Symp. Landslides, Christchurch, N.Z.* 1, 143-347.
- Brahma, S. P. and Harr, M.E. (1962) Transient development of the free surface in a homogeneous earth dam. *Géotechnique* 12, 283-302.
- Bridgwater, J. (1980) On the width of failure zone. *Géotechnique* 30, 533-536.
- Broili, L. (1967) New knowledge on the geomorphology of the Vaiont Slide slip surface. *Rock Mechanics and Engr. Geol., Journal Int. Soc. Rock Mechanics*. Vol. V (1), 38-88.
- Burland, J.B., Longworth, T.I. and Moore, J.F.A. (1977) A study of ground movement and progressive failure caused by a deep excavation in Oxford clay. *Géotechnique* 27 (4), 557-591.
- Campanella, R.G. and Mitchell, J.K (1968) Influence of temperature variation on soil behaviour. *Journal of the Soil Mechanics and Foundation Division ASCE* 94(SM3), 709-734.
- Capone, T. (2009) SPH numerical modelling of impulse water waves generated by landslides. *PhD Thesis*. University of Rome, La Sapienza.
- Casagrande, A. (1940) *Seepage through dams. Contributions to soil mechanics, 1925-1940*. Boston Society of Civil Engineers.
- Cedergren, H.R. (1967) *Seepage, drainage and flow nets*, edited by Wiley, New York.
- Cekerevac, C and Laloui, L. (2004) Experimental study of thermal effects on the mechanical behaviour of a clay. *Int. Jnl. Num. and Anal. Methods Geomech.* 28, 209-228.
- Chamot, P. (1993) El deslizamiento La Josefina en el Valle del Tío Paute: *Zurich, report to the United Nations*, 16p.
- Chandler, R.J. and Skempton, A.W. (1974) The design of permanent slopes in stiff fissured clays. *Géotechnique* 24, 457-464.
- Chigira, M. (1989) Chemical weathering of mudstones in mountainous areas. Abstracts. *Proc. Assoc. Eng. Geol. Annual Meeting, Vail, Colorado*, 56.
- Cividini, A. and Gioda, G. (1984), Approximate F. E. analysis of seepage with a free surface. *International Journal for Numerical and Analytical Methods in Geomechanics* 8 (6), 549-566.

- Cooley, R.L. (1971) A finite difference method for unsteady flow in variable saturated porous media: Application to a single pumping well. *Water Res. Res.*, 7 (6), 1607-1625.
- Cooper, M.R., Bromhead, E.N., Petley, D.J. and Grant, D.I. (1998) The Selborne cutting stability experiment. *Géotechnique* 48, 83-101.
- Corominas, J. and Moya, J. (2010) Informe del deslizamiento de la margen izquierda del embalse de Canelles. *Internal Report*.
- Coussy O. *Poromechanics*. Wiley: New York, 2004; 1-14.
- Cui, Y.J., Sultan, N. and Delage, P. (2000) A thermomechanical model for saturated clays. *Canadian Geotechnical Journal* 37, 607-620.
- Dai, F.C, Deng, J.H., Tham, L.G., Law, K.T. and Lee, C.F. (2004) A large landslide in Zigui County, Three Gorges area. *Canadian Geotechnical Journal* 41, 1233-1240.
- Davis, R.O and Smith, N.R. (1990) Pore fluid frictional heating and stability of creeping landslides. *Int. J. for Numer. Anal. Meth. Geomech.* 14, 424-443.
- Davis, R.O. and Smith, N.R. (1990) Pore fluid frictional heating and stability of creeping landslides. *Int. J. Numer. Analyt. Meth. Geomech.* 14, 427-443.
- Delage, P., Cui, Y.J. and Sultan, N. (2004). On the *thermal behaviour of Boom clay*. *Proceedings Eurosafe 2004 Conference*, Berlin, Germany.
- Delage, P., Sultan, N. and Cui, Y.J. (2000) On the thermal consolidation of Boom clay. *Canadian Geotechnical Journal* 37, 343-354.
- Demars, K.R. and Charles, R.D. (1982) Soil volume changes induced by temperature cycling. *Canadian Geotechnical Journal* 19, 188-194.
- Desai, C.S. (1972) Seepage analysis of earth banks under drawdown. *Jnl. of the Soil Mech. and Found. Div.*, ASCE, n° SM11: 1143-1162.
- Desai, C.S. (1977) Drawdown analysis of slopes by numerical method. *Jnl. of the Soil Mech. and Found. Div.*, ASCE, n° GT7: 667-676.
- Desai, C.S. and Shernan Jr., W.C. (1971) Unconfined transient seepage in sloping banks. *Jnl. of the Soil Mech. and Found. Div.*, ASCE, n° SM2: 357-373.
- Desrues, J. (1984) Sur l'application de la stéréophotogrammétrie à la mesure des grandes déformations. *Revue Française de Mécanique* 3, 55-63.
- Desrues, J., Chambon, R., Mokni, M. and Mazerolle, F. (1996) Void ratio evolution inside shear bands in triaxial sand specimens studied by computed tomography. *Géotechnique* 46 (3), 529-546.

- Dikay, R., Brundsen, D., Schrott, L. and Ibsen, M.L. (1996) *Landslide recognition*. John Wiley and Sons, Chichester.
- DIT-UPC (2002) CODE_BRIGHT. *A 3-D program for thermo-hydro-mechanical analysis in geological media. USER'S GUIDE*. Centro Internacional de Métodos Numéricos en Ingeniería (CIMNE), Barcelona.
- Dounias, G.T., Potts, D.M. and Vaughan, P.R. (1996) Analysis of progressive failure and cracking in of British dams. *Géotechnique* 46 (4), 621-640
- Dudoignon, P., Pantet, A., Carrara, L. and Velde, B. (2001) Maco-micro measurement of particle arrangement in sheared kaolinic matrices. *Géotechnique* 51 (6), 493-499.
- Elnaggar, H.A. and Flint, N.K. (1976) Analysis and design of high-way cuts in rocks. *Report*. Univ. of Pittsburgh to Pennsylvania Dept. of Transportation.
- EUR (2006) Heater Experiment: Rock and bentonite thermo-hydro-mechanical (THM) processes in the near-field of a thermal source for development of deep underground high-level radioactive waste repositories. Project FIS5-2001-00024. Project funded by the European Community under the 5th EURATOM Framework Programme (1998-2002). 106 pp.
- Fell, R., Macgregor, P., Stapledon, D. and Bell, G. (2005) *Geotechnical Engineering of Dams*. Taylor & Francis Group. London.
- Freeze, R.S. (1971) Three dimensional transient saturated-unsaturated flow in a groundwater basin. *Water Res. Res.*, 7 (2): 347-366.
- Ganerød, G., Nilsen, B. and Sandven, R. (2009) Shear strength estimation of Ankes sliding area in western Norway. *International Journal of Rock Mechanics and Mining Sciences*, 46, 479-488.
- Ganerød, G.V., Grøneng, G., Rønning, J.S., Dalsegg, E., Elvebakk, H, Tønnesen, J.F., Kveldsvik, V., Eiken, T., Blikra, L.H. and Braathen, A. (2008) Geological model of the Åknes rockslide, western Norway. *Engineering Geology* 102, 1-18.
- Ghabezloo, S. and Sulem, J. (2008) Stress dependent thermal pressurization of a fluid-saturated rock. *Rock Mechanics and Rock Engineering* 42, 1-24.
- Gogue, J. (1978) Scale-dependent rockslide mechanism, with emphasis on the role of pore fluid vaporization. *Developments in geotechnical engineering*. Vol. 14a. Rockslides and avalanches. Voight, B. (eds.). Elsevier. 693-705.
- Graham, J., Tanaka, N., Crilly, T. and Alfaro, M. (2001) Modified Cam-clay modelling of temperature effects in clays. *Canadian Geotechnical Journal* 38, 608-621.

- Habib, P. (1967) Sur un mode de glissement des massifs rocheux. *C.R. Hebd. Seanc. Acad. Sci.*, Paris 264, 151-153.
- Hamel, J.V. (2004) Discussion of “Residual shear strength mobilized in first-time slopes failures” by G. Mesri and M. Shahien. *Journal of Geotechnical and Geoenvironmental Engineering, ASCE* 130 (5), 544-546.
- Harbitz, C.B., Pedersen and G., Gjevik, B. (1993) Numerical simulations of large water waves due to landslide. *Journal of Hydraulic Engineering, ASCE* 133 (2), 208-216.
- Harden, C.P. (2004) Book review: The 1993 landslide dam at La Josefina in Southern Ecuador: A review of Sin Plazo Para La Esperanza. *Engineering Geology* 74 (1), 157-161.
- Hawkins, A.B., Lawrence, M.S. and Privett, K.D. (1988) Implications of weathering on the engineering properties of the Fuller’s Earth formation. *Géotechnique*, 38 (4), 517-532.
- Hendron, A. and Patton, F.D. (1985) The Vaiont slide, a geotechnical analysis based on new geologic observations of the failure surface. *Technical Report GL-85-5*. Department of the Army US Army Corps of Engineers, Washington, DC.
- Hendron, A.J. and Patton, F.D (1987) The Vaiont slide. A geotechnical analysis based on new geologic observations of the failure surface. *Engineering Geology* 24, 475-491
- Henkel, D.J. (1960) The shear strength of saturated remoulded clays. *Proc. ASCE Research Conference on Shear Strength of Cohesive Soils*, Boulder: 533-554.
- Hernández-Madrigal, V., Mora-Chaparro, J. and Garduño-Monroy (2010) Large block slide at San Juan Grijalva, Northwest, Chiapas, Mexico. *Landslides* 7 (3). Published online.
- Hoek, E. (2007) Practical Rock Engineering
<http://www.rocscience.com/hoek/PracticalRockEngineering.asp>
- Howard, K. (1973) Avalanche mode of motion: implication from lunar examples. *Science*, N.Y. 180, 1052-1055.
- Hromadka, T.V. and Guymon, G.L. (1980) Some effects of linearizing the unsaturated soil moisture transfer diffusivity model. *Water Resources Research* 16 (4), 643-650.
- Hsu, K. J. (1975). Catastrophic debris streams (Sturzstroms) generated by rock falls. *Geol. Soc. Am. Bull.* 86, 123-140.
- Hueckel and Pellegrin, (1991) Effective stress and water pressure in saturated clays during heating-cooling cycles. *Workshop on Stress Partitioning in Engineering Clay Barriers*. Durham, United Kingdom.

- Hueckel, T. and Baldi, G. (1990) Thermoplasticity of saturated clays: experimental constitutive study. *J. Geotech. Eng. ASCE* 116.
- Hueckel, T. and Borsetto, M. (1990) Thermoplasticity of saturated soils and shales: constitutive equations. *Journal of Geotechnical Engineering, ASCE* 116 (12), 1765-1777.
- Hueckel, T., Pellegrini, R. and Olmo, C. (1998) A constitutive study of thermo-elasto-plasticity of deep carbonatic clays. *Int. J. Numer. Anal. Meth. Geomech.* 22, 549-574.
- Hungr, O., Salgado, F.M. and Byrne, P.M (1989). Evaluation of a three-dimensional method of slope stability analysis. *Canadian Geotechnical Journal*, 26, 679-686.
- Hutchinson, J.N. (1986) A sliding-consolidation model for flow slides. *Can. Geotech. J.* 23 (2), 115-126.
- Hutchinson, J.N., (1988) Morphological and geotechnical parameters of landslides in relation to geology and hydrogeology. *Proc. 5th Int. Symp. on Landslides*, Lausanne, Switzerland. Vol. 1. pp. 3-35.
- ICOLD (1980) Deterioration of dams and reservoirs. Examples and their analysis. ICOLD, Paris. Balkema, Rotterdam.
- ICOLD (2002) Reservoir landslides-guidelines for investigation and management. International Commission on Large Dams. Paris *Bulletin* 124.
- Jaeger, C. (1965a). The Vaiont rockslide. Part I. *Water Power*. March, pp. 110-111.
- Jaeger, C. (1965b). The Vaiont rockslide. Part II. *Water Power*. April, pp. 142-144.
- Jardine, R.J., Gens, A., Hight, D.W. and Coop, W.R. (2004) Developments in understanding soil behaviour. Advances in geotechnical engineering. *The Skempton Conference*. London, UK. Jardine, Potts & Higgins (eds). Thomas Telford. 1, 103-206.
- Jian, W, Wang, A. and Yin, K. (2009) Mechanism of the Anlesi landslide in the Three Gorges reservoir, China. *Engineering Geology* 108, 86-95.
- Kenney, T. C. (1967). Stability of the Vajont valley slope, discussion of a paper by L. Müller (1964) on the rock slide in the Vajont valley. *Rock Mechanics and Engr. Geol.*, Journal of the Int. Soc. Rock Mechanics. Vol. 5, 10-16.
- Koerner, H.J. (1977) Flow mechanisms and resistance in the debris streams of rock slides. *Bull. Int. Assoc. Engng. Geol.* 16, 101-104.
- Lachenbruch, A.H. (1980) Frictional heating, fluid pressure and the resistance to fault motion. *J. Geophys. Res.* 85, 6097-6122.
- Laloui, L. (2001) Thermo-mechanical behaviour of soils. *Environmental Geomechanics* 5, 809-843.

- Lane, P.A. and Griffiths, D.V. (2000) Assessment of stability of slopes under drawdown conditions. *Jnl. Geotech. and Geoenv. Engng.* 126 (5): 443-450.
- Lawrence Von Theen, J. (1985) San Luis dam upstream slide. *Proc. 11th Int. Conf. on Soil Mech. and Found. Engng.* San Francisco. Vol. 5, 2593-2598.
- Lee, T-C and Delaney P.T. (1987) Frictional heating and pore pressure rise due to a fault slip. *Geophysical Journal of the Royal Astronomical Society* 88 (3), 569-591.
- Lemos, L.J.L. (1986) The effect of rate on the residual strength of soil. *PhD Thesis.* University of London, London, United Kingdom.
- Leonards, G.A. (1987) International workshop on dam failures - overview and personal commentary. Proceedings of the International Workshop on Dam Failures. Special issue of *Engineering Geology* 24, 577-612.
- Lo, K. Y., Lee, C.F. and Gelinas, P. (1972) Alternative interpretation of the Vaiont slide. *Stability of Rock Slopes: Proc. 13th Symp. on Rock Mechanics*, Univ. of Illinois, Urbana, ASCE, New York, 595-623.
- Lowe, J. and Karafiath, L. (1980) Effect of anisotropic consolidation on the undrained shear strength of compacted clays. *Proc. Research Conf. on Shear Strength of Cohesive Soils.* Boulder: 237-258.
- Lupini, J.F., Skinner, A.E. and Vaughan, P.R. (1981) The drained residual strength of cohesive soils. *Géotechnique* 31 (2), 181-213.
- Mase, C.W and Smith, L. (1985) Pore-fluid pressure and frictional heating on a fault surface. *Pure Appl. Geophys.* 122, 583-607.
- Mencl, V. (1966) Mechanics of landslides with non-circular slip surfaces with special reference to the Vaiont Slide. *Géotechnique* 19 (4), 329-337.
- Mesri, G. and Shahien, M. (2003) Residual shear strength mobilized in first-time slope failures. *Journal of Geotechnical and Geoenvironmental Engineering, ASCE* 129, 12-31.
- Mitchell, J.K. (1960) Fundamental aspects of thixotropy in soils. *J. Soil Mech. Fdn Engng Am. Soc. Civ. Engrs* 86, SM3, 19-52.
- Morgenstern N.R. (1963) Stability charts for earth slopes during rapid drawdown. *Géotechnique* 13 (1), 121-131.
- Morgenstern N.R. and Tchalenko J.S. (1967) Microscopic structure in koalin subjected to direct shear. *Géotechnique* 17, 309-328.
- Morgenstern N.R. and Tchalenko J.S. (1987) Microstructural observations of shear zones from slips in natural clays. *Proceedings Geotechnical Conference Oslo*, 147-152.

- Morgenstern, N.R. and Price, V.E. (1965) The analysis of the stability of general slip surfaces. *Géotechnique* 15, 79-93.
- Mühlhaus, H-B. and Vardoulakis I.G. (1987) The thickness of shear bands in granular materials. *Géotechnique* 37, 271-283.
- Müller, L. (1964). The rock slide in the Vajont Valley. *Rock Mechanics and Engr. Geol.* Vol. 2, 148-212.
- Müller, L. (1987) The Vaiont catastrophe -A personal review. *Engineering Geology*, 24 (1-4), 423-444.
- Muir Wood, D. (2002) Some observations of volumetric instabilities in soil. *International Journal of Solids and Structures*, 3426-3449.
- Muñoz, J.J. (2007) Thermo-hydro-mechanical analysis of soft rock. Application to large scale heating and ventilation tests. *Doctoral Thesis*. Universitat Politècnica de Catalunya. Barcelona.
- Nakamura, S. (1990) *Applied numerical methods with software*. Prentice-Hall.
- Nemcok, A., Pasek, J. and Ryber, J. (1972) Classification of landslides and other mass Movements. *Rock Mechanics* 4, 71-78.
- Neumann, S.P. (1973) Saturated-unsaturated seepage by finite elements. *Jnl. Hydraul. Div., ASCE*, 99, HY12: 2233-2250.
- Noda, E. (1979) Water waves generated by landslides. *Harb. and Coast. Engineering Division*, ASCE 96 (4), 835-855.
- Nonveiller, E. (1967) Shear strength of bedded and jointed rock of landslides with noncircular surfaces with special reference to Vajont slides. *Proc. Geotechnical Conference*, Oslo. Vol. 1, pp. 289-294.
- Nonveiller, E. (1987) The Vajont reservoir slope failure. *Engineering Geology* 24, 493-512.
- Oda, M. and Kazama, H. (1998) Microstructure of shear bands and its relation to the mechanism of dilatancy and failure of dense granular soils. *Géotechnique* 48 (4), 465-481.
- Oldecop, L. and Alonso, E.E. (2001) A model for rockfill compressibility. *Géotechnique* 51 (2), 127-139
- Olivella, S., Carrera, J. Gens, A. and Alonso, E.E. (1994) Nonisothermal multiphase flow of brine and gas through saline media, *Transport in Porous Media*, 15, 271-293.
- Olivella, S., Gens, A., Carrera, J., Alonso, E.E. (1996) Numerical formulation for a simulator (CODE BRIGHT) for the coupled analysis of saline media. *Engineering Computations* 13 (7), 87-112.

- Osipov, V.I., Nikolaeva, S.K. and Sokolov, V.N. (1984) Microstructural changes associated with thixotropic phenomena in clay soils. *Géotechnique* 34 (2), 293-303.
- Paaswell, R.E. (1967) Temperature effects on clay soil consolidation. *Journal of the Soil Mechanics and Foundation Engineering Division, ASCE* 93, 9-22.
- Pastor, M., Herreros, I., Fernández Merodo, J.A., Mira, P., Haddad, B., Quecedo, M., González, E., Álvarez-Cedrón, C. and Dempetic, V. (2009) *Engineering Geology* 109, 124-134.
- Paton, J. and Semple, N.G. (1961) Investigation of the stability of an earth dam subjected to rapid drawdown including details of pore pressure recorded during a controlled drawdown test. *Pore Pressure and Suction in Soils*, 85-90. Butterworths, London.
- Pauls, G.J., Karlsauer, E., Christiansen, E.A. and Wigder, R.A. (1999) A transient analysis of slope stability following drawdown after flooding of highly plastic clay. *Can. Geotech. Jnl.* 36, 1151-1171.
- Picarelli, L. (1990) Discussion: The general and congruent effects of structure in natural soils and weak rocks. *Géotechnique* 40 (3), 407-488.
- Pinyol, N.M. (2004) Anàlisi i modelització del comportament geotècnic de la presa de Beliche (Portugal). *Degree Thesis*. Universitat Politècnica de Catalunya, Spain.
- Plaza-Netos, G. and Zevallos, O. (1994) The La Josefina rockslide. In *The 1993 La Josefina Rockslide and Río Paute Landslide Dam. Ecuador: Landslides News* 8, 4-6.
- Plum, R.L. and Esrig, M.I. (1969) Some temperature effects on soil compressibility and pore water pressure. Effects of temperature and heat on engineering behaviour of soils. Highway Research Board, Special Report 103, 231-242.
- Potts, D.M., Dounias, G.T. and Vaughan, P.R. (1990) Finite element analysis of progressive failure of Carsington embankment. *Géotechnique* 40, 79-101.
- Qi, S., Yan, F., Wang, S. and Xu, R. (2006) Characteristics, mechanism and development tendency of deformation of Maoping landslide after commission of Geheyuan reservoir on the Qingjiang River, Hubei Province, China. *Engineering Geology* 86, 37-51.
- Reinius, E. (1954) The stability of the slopes of earth dams. *Géotechnique* 5, 181-189.
- Rice, J.R. (2006) Heating and weakening of faults during earthquake slip. *J. Geophys. Res.*, 111, B05311, doi:10.1029/2005JB004006.
- Richards, B.G. and Chan, C.Y. (1969) Prediction of pore pressures in earthdams. Proc. 7th Int. Conf. S.M.F.E., 2, 355-362. Mexico.

- Robiner, J.C., Rahbou, A., Plas, F. and Lebon, P. A constitutive thermomechanical model for sautrated clays. *Engineering Geology* 41, 1-4, 145-169.
- Rodríguez-Ortiz and Prieto (1980) Personal communication in Alonso (2005).
- Romero, E. (1999) Characterisation and THM behaviour of unsaturated Boom clay. *PhD Thesis*. Universitat Politècnica de Catalunya, Spain.
- Roscoe, K.H. (1970) The influence of strains in soil mechanics. *Géotechnique* 20, 129-170.
- Rubin, J. (1968) Theoretical analysis of two-dimensional transient flow of water in unsaturated and partly saturated soils. *Soil Sci. Soc. Am. Proc.* 32 (5), 607-615.
- Sassa, K., Fokuoka, H., Scarascia-Mugnozza, D. and Evans, S. (1996) Earthquake-induced landslides: distribuion motion and mechanism. *Special Issue of Soils and Foundation*, JAN, 53-64.
- Scarpelli, G. and Wood, D.M.. (1982) Experimental observations of shear band patterns in direct shear tests. *Proceedings of the IUTAM Conference on Def. Fail. Gran. Media*, Ed. Balkema, Delf, 473-484.
- Schuster, R.L., Salcedo, D.A. and Valenzuela, L. (2002) Overview of catastrophic landslides of South America in the twentieth century. In *Catastrophic Landslides: Effects, Occurrenes and Mechnism*. Evans, S.G. and DeGraff, J.V. (eds.) Geological Society of America.
- Seed, H.B. (1968) Landslides during earthquakes due to soil liquefaction. *J. Soil Mech. Fdn Engng Am. Soc. Civ. Engrs* 94, SM5, 1053-1122.
- Seed, H.B. and Chan, C. (1957) Thixotropic characteristics of compacted clays. *J. Soil Mech. Fdn Engng Am. Soc. Civ. Engrs* 83, SM4, 1-35.
- Semenza, E. (2001) *La Storia del Vaiont Raccontata del Geologo Che ha Scoperto la Frana*. Tecomproject. Editore Multimediale. Italia.
- Semenza, E. and Ghirotti, M. (2000) History of the 1963 Vaiont slide: the importance of geological factors. *Bull. Eng. Geol. Env.* 59, 87-97.
- Shelton, J.S. (1966) *Geology Illustrated*. W.H. Freeman and Company, San Francisco.
- Sherard, J.L., Woodward, R.J., Gizienski, S.F. and Clevenger, W.A. (1963) *Earth and earth-rock dams*. John Wiley and Sons, New York.
- Sitar, N. and MacLaughlin, M. (1997) Kinematics and discontinuous deformation analysis of landslide movement. *Invited Keynote Lecture. II Paramerican Symposioum on Landslides*. Río de Janeiro, Brasil.

- Sitar, N.M., MacLaughlin, M.M. and Doolin, D.M. (2005) Influence of Kinematics on Landslide Mobility and Failure Mode. *Journal of Geotechnical and Geoenvironmental Engineering*. ASCE 131 (6), June 1, 716-728.
- Skempton A.W., Petley, F.R.S and Petley, D.J. (1967) The strength along structural discontinuities in stiff clays. *Proc. of Geotechnical Conference*. Oslo, Norwegian.
- Skempton, A.W. (1954) The pore pressure coefficients A and B. *Géotechnique* 4 (4), 143-147.
- Skempton, A.W. (1964) Long-term stability of clay slopes. *Géotechnique* 14, 77-101.
- Skempton, A.W. (1966) Bedding-plane slip, residual strength and the Vaiont landslide. Correspondence to *Géotechnique* 16 (2), 82-84.
- Skempton, A.W. and Hutchinson, J.N. (1969) Stability of natural slopes. *Proc. 7th Int. Conf. Soil Mech. and Found. Eng.*, Mexico D.F., 4, 291-340.
- Skempton, A.W., Leadbeater, A.D. and Chandler, R.J. (1989) The Mam Tor Landslide, North Derbyshire. *Phil. Tans. R. Soc. Lond.* A329, 503-547.
- Stark, T.D. and Eid, H.T. (1994) Slope stability analyses in stiff fissured clays. *Journal of Geotechnical and Geoenvironmental Engineering* 123 (4), 335-343.
- Stephenson, D. (1978) Drawdown in embankments. *Géotechnique* 28 (3), 273-280.
- Sulem, J., Lazar, P. and Vardoulakis, I. (2007) Thermo-poro-mechanical properties of clayey gouge and application to rapid fault shearing. *Int. J. for Numer. Anal. Meth. Geomech.* 31, 523-540.
- Sulsky, D. and Schreyer, H.L. (1996) Axisymmetric form of the material point method with applications to upsetting and Taylor impact problems. *Comput. Methods Appl. Mech. Engrg.* 139, 409-429
- Sultan, N. (1997) Étude du comportement thermo-mécanique de l'argile de Boom : expériences et modélisation. *PhD Thesis*. École Nationale de Ponts et Chaussées, Paris, France.
- Tanakata, N. Graham, J. and Crilly, T. (1997) Stress-strain behaviour of reconstituted illitic clay at different temperatures. *Engineering Geology* 47, 339-350.
- Terzaghi, K. (1956) Varieties of submarine slope failures. *Proc. 8th Texas Conf. Soil Mech.*, New York, 1-15.
- Terzaghi, K. and Peck, R.B. (1967) *Soil Mechanics in Engineering Practice* (2nd edition). John Wiley. New York.

- Thury, M. and Bossart, P. (1999) Mont Terri rock laboratory, a new international research project in a Mesozoic shale formation, in Switzerland. *Engineering Geology* 52 (3-4), 347-359.
- Tika, T.E. (1989) The effect of rate of shear on the residual strength of soil. PhD Thesis, University of London, London, United Kingdom.
- Tika, T.E. and Hutchinson, J.N. (1999) Ring shear test on soil from the Vaiont landslide slip surface. *Géotechnique* 49 (1), 59-74
- Tika, Th.E., Vaughan, P.R. and Lemos, L.J. (1996) Fast shearing of pre-existing shear zones in soil. *Géotechnique* 46 (2), 197-233.
- Towhata, I., Kuntiwattanakul, P. and Kobayashi, H. (1993) A preliminary study on heating of clay to examine possible effects of temperature on soil-mechanics properties. *Soil and Foundations* 33 (4), 184-190.
- Towhata, I., Kuntiwattanakul, P., Seko, I. and Ohishi, K. (1993) Volume change of clays induced by heating as observed in consolidation tests. *Soil and Foundations* 33 (4), 170-183.
- Uriel Romero, S. and Molina, R. (1977) Kinematic aspects of Vaiont slide. *Proceedings of the 3rd International Conference of the ISRM*, Vol. 2B, Denver, 865-870
- USCOLD (1988) *Lessons from dam incidents. USA-II*. American Society of Civil Engineers. New York.
- Vardoulakis, I. (1980) Shear band inclination and shear modulus of sand in biaxial tests. *International Journal for Numerical and Analytical Methods in Geomechanics* 4, 103-119.
- Vardoulakis, I. (2000) Catastrophic landslides due to frictional heating of failure plane. *Mech. of Cohes.-Fric. Mater.* 5, 444-467.
- Vardoulakis, I. (2002) Dynamic thermo-poro-mechanical analysis of catastrophic landslides. *Géotechnique* 52 (3), 157-171.
- Varnes, D.J. (1978) Slopes movement types and processes. In *Landslides-Analysis and Control* (Schuster, R.L. and Krizek, R.J. Transportatoin Research Board Special Report, 176, National Academia of Sciences, pp. 11-33.
- Vaughan, P.R., Hight, D.W., Sodha, V.G. and Walbancke, H.J. (1978) Factors controlling the stability of clay fills in Britain. *Clay Fills, Institution of Civil Engineers*, London, 203-217.
- Voigt, B. and Faust, C. (1982) Frictional heat and strength loss in some rapid landslides. *Géotechnique* 32 (1) 43-54.

- Walder, J.S., Watts, P., Sorensen, O.E. and Janssen, K. (2003) Tsunamis generated by subaerial mass flows. *Journal of Geophysical Research* 108 (B5), 2236.
- Wang, F., Zhang, Y., Huo, Z., Peng, X., Wang, X. and Yamasaki, S. (2008) Mechanism for the rapid motion of the Qianjiangping landslide during reactivation by the First impoundment of the Three Gorges dam reservoir, China. *Landslides* 5, 379-386.
- Wang, F.W., Zhang, Y.M., Huo, A.T., Matsumoto, T. and Huang, B.T. (2004) The July 14, 2003 Qianjiangping landslide, Three Gorges Reservoir, China. *Landslides* 1, 157-162.
- Wang, G. and Sassa, K. (2002) Post-failure mobility of saturated sands in undrained load controlled ring shear tests. *Canadian Geotechnical Journal* 34 (4), 821-837.
- Wen, B.P., Aydin, A., Duzgoren-Aydin, N.S., Li, Y.R., Chen, H.Y. and Xiao, S.D. (2007) Residual strength of slip zones of large landslides in the Three Gorges area, China. *Engineering Geology* 93, 82-98.
- Wood, D.M. (2002) Some observations of volumetric instabilities in soils. *Int. J. Solids and Structures* 39, 3429-3449.
- Zabala, F. and Alonso, E.E. (2010) Progressive failure of Aznalcóllar dam using the Material Point Method. *Géotechnique*. Accepted for publication.